

Spray Impact on and Carry-Over from Complex Shaped Surfaces

Liam Robert Gray

SUBMITTED IN ACCORDANCE WITH THE REQUIREMENTS FOR THE DEGREE OF
DOCTOR OF PHILOSOPHY

THE UNIVERSITY OF LEEDS

EPSRC CENTRE FOR DOCTORAL TRAINING IN FLUID DYNAMICS

MAY 2023

Declaration

The candidate confirms that the work submitted is his own. Appropriate credit has been given where reference has been made to the work of others. This copy has been supplied on the understanding that it is copyright material and that no quotation from this thesis may be published without proper acknowledgement.

The right of Liam Robert Gray to be identified as Author of this work has been asserted by Liam Robert Gray in accordance with the Copyright, Designs and Patents Act 1988.

*Though much is taken, much abides; and though
We are not now that strength which in old days;
Moved earth and heaven, that which we are, we are,
One equal temper of heroic hearts,
Made weak by time and fate, but strong in will
To strive, to seek, to find, and not to yield.*

ALFRED LORD TENNYSON,

ULYSSES - 1842

Acknowledgements

I would first like to express incredible thanks to my supervisors Prof. Nikil Kapur, Prof. Andrew Bayly and Dr. Amirul Khan, whose guidance, suggestions and expertise throughout the PhD have been invaluable.

I would like to thank the centre for doctoral training (CDT) in fluid dynamics for the support throughout and my entire cohort for the fruitful discussions and great times.

I would like to thank the Engineering and Physical Sciences Research Council (EPSRC) for funding this work.

I would like to thank Unilever for their financial support and to thank Louise McMaster for their discussions and insight into the complexities of personal care products.

I would like to thank the thermodynamic laboratory team at the University of Leeds, Samuel Flint, Max Pepper and Peter Grieve for their useful discussions and assistance with the experimental setups.

Most importantly I would like to thank my fiancée Robyn Gill whose support and love throughout has kept me guided in completing this journey.

Thank you all.

Abstract

Personal care products are pervasive. A common mechanism for transporting products to the desired target is via spray application, a method capable of efficiently breaking the product into droplets and creating coverage of a surface. The work presented in this thesis focuses on (i) experimentally investigating sprays generated from deodorant-type aerosol cans and (ii) generating a validated numerical model to aid in both understanding the mechanisms and predicting the fate of the generated droplets.

To do this, spray generation from nine different aerosol cans, with varying formulation and nozzle type, are investigated using three experimental setups: high-speed schlieren imaging; particle size measurement using laser diffraction; and a thermocouple array. Schlieren imaging gives insight into the two-phase nature of the spray and allows the spray angle to be measured, with measurements varying from 16.3° - 22.2° . Particle size measurements show that a log-normal distribution is able to represent the initial sizes generated by an aerosol can. Centreline temperature measurements reveal that temperatures can drop as low as -41°C due to the evaporation of the alkane-based propellants used to carry the product. The formulation and the nozzle type have a strong influence on these parameters.

A carrier-jet CFD model is created, finding that the realizable $k-\varepsilon$ turbulence model performs best at predicting momentum decay and propellant dispersion. One-way coupling modelling is used to capture the movement of droplets as they approach a surface and the resulting capture efficiency is determined. The surface is parameterised in terms of standoff distance and degree of curvature. Model predictions show that flatter surfaces result in a reduced capture efficiency and that the release position of the droplets significantly impacts their efficiency. An extension of the model to two-way coupling of droplets with the carrier-jet shows that incorporating droplet latent heat due to vaporisation is important for capturing the spray temperature.

Both the developed methods and the results give new insights into the complex behaviours of aerosol sprays which remains a relatively unstudied area.

Contents

List of Figures	x
List of Tables	xxiii
Nomenclature	xxvii
1 Introduction	1
1.1 Background and Motivation	1
1.2 Project Aims	2
1.3 Thesis Outline	3
2 Literature Review	5
2.1 Introduction	5
2.2 Aerosol Cans	7
2.2.1 Fundamentals	7
2.2.2 Flash Atomization	12
2.3 Jet Physics	15
2.3.1 Carrier Jets	15
2.3.2 Liquid Jet Breakup	19
2.3.3 Primary Atomization	25
2.3.4 Nozzle Types and Influence	29
2.4 Droplet Physics	33
2.4.1 Secondary Atomization	33
2.4.2 Droplet Trajectories	36
2.4.3 Droplet Collisions	39

2.4.4	Droplet Evaporation	42
2.4.5	Droplet-Wall Interaction	47
2.5	CFD Modelling	49
2.5.1	Conservation of Mass and Momentum	51
2.5.2	Turbulence Modelling	52
2.5.3	Near-Wall Modelling	59
2.5.4	Species Transport	62
2.5.5	Energy Equation	62
2.6	Summary	64
3	Experimental Study of Spray Generation	67
3.1	Introduction	67
3.2	Methodology	69
3.2.1	Schlieren Imaging	69
3.2.2	Determining Droplet Size	89
3.2.3	Spray Temperature Measurements	102
3.3	Results	108
3.3.1	Schlieren Imaging Results	108
3.3.2	Determining Droplet Size Results	120
3.3.3	Spray Temperature Measurements Results	143
3.4	Summary	148
4	Species Transport of a Single Phase Gaseous Jet	151
4.1	Introduction	151
4.1.1	Problem Motivation	152
4.2	Relevant Physics	152
4.3	Turbulence Model Study	154
4.3.1	Geometry Generation	155
4.3.2	Boundary Conditions	156
4.3.3	Numerical Schemes	159

4.3.4	Mesh Independence	160
4.3.5	Results	165
4.3.6	Boundary Condition and Parameter Studies	172
4.3.7	Conclusion	177
4.4	Aerosol Can Carrier Jet	178
4.4.1	Geometry Generation	178
4.4.2	Mesh Generation	179
4.4.3	Boundary Conditions	181
4.4.4	Results	183
4.5	Summary	189
5	Spray Impingement and Droplet Carry-Over	193
5.1	Introduction	193
5.2	Droplet Dynamics	194
5.2.1	Governing equations	194
5.2.2	Numerical Implementation	197
5.2.3	Verification	200
5.2.4	Results	202
5.2.5	Coupling Discrete and Continuous Phases in Fluent	208
5.3	Capture Efficiency and Carry-Over	213
5.3.1	Design Of Experiments	214
5.3.2	Surrogate Modelling	215
5.3.3	Mesh Generation and Sensitivity	217
5.3.4	Results	225
5.4	Summary	234
6	Conclusions and Outlooks	237
6.1	Summary	237
6.1.1	Chapter 3 - Experimental Study of Spray Generation	238
6.1.2	Chapter 4 - Species Transport of a Single Phase Gaseous Jet	240

6.1.3	Chapter 5 - Spray Impingement and Droplet Carry-Over	241
6.2	Future Work	243
	Bibliography	245

List of Figures

2.1	The spray generation process from a deodorant-type aerosol can towards a human axilla (not to scale). The 6 processes of interest are labelled: 1) Primary breakup, 2) Turbulent droplet transport, 3) Secondary breakup and Coalescence, 4) Droplet heat and mass Transfer, 5) Droplet impingement and 6) Droplet carry-over.	6
2.2	Cross-section of an aerosol can and labelling of key components. Left: Unactuated aerosol can, Right: Actuated aerosol can. Image adapted from BAMA (2023)	8
2.3	The saturation vapour pressure against temperature (293.15 K - black line) for (a) pure substances Propane, Isobutane and Butane, (b) Mixtures of different mole fractions of Propane and Butane. (c) Saturation vapour pressure (log contours) at 293.15 K for different mole fractions of Propane, Butane and Isobutane.	11
2.4	Example Pressure-Volume Diagram taken from Blander and Katz (1975) showing the saturation and spinodal curves for liquid and vapour, and the isotherm at the critical temperature (T_c) and a real-type isotherm below it.	14
2.5	The development of a free jet. The regions of development shown are: the potential core (initial) region, transitional region and the self-similar fully developed region. Figure taken from Greco (2018)	16
2.6	A basic representation of a (a) shadowgraph and (b) schlieren setup taken from Settles (2012)	18

2.7	Experimental photographs showing the breakup of a viscous jet for a perturbation wavelength of (a) $\lambda = 0.268$, taken from Donnelly and Glaberson (1966) and (b) $\lambda = 0.683$, taken from Rutland and Jameson (1971).	19
2.8	(a) Breakup regimes with respect to the density of the ambient gas and Reynolds number. Adapted from Kadocsa (2007). (b) Qualitative look at the four jet breakup regimes, adapted from Schneider (2003).	23
2.9	(a) The intact core present in the atomization regime, taken from Bianchi et al. (2007). (b) Liquid core approximation with “blobs” and the resulting primary atomization. Taken from Ansys (2009). . .	27
2.10	(a) Side schematic of a simple orifice nozzle taken from Marinescu et al. (2013) and (b) a front on schematic of a pressure-swirl taken from Lefebvre and McDonell (2017).	30
2.11	Cavitation regimes taken from Sou et al. (2007) for water, showing no-cavitation, cavitation on-set, super cavitation and hydraulic flip. .	30
2.12	The five different regimes of droplet breakup classified in terms of Weber number. Figure taken from Pilch and Erdman (1987).	34
2.13	The collision of two droplets with different sizes P_s and P_L . The lateral displacement of the droplets’ centroids is denoted by b and the relative velocity within the plane as U_{rel} . Figure taken from Sommerfeld and Pasternak (2019).	40
2.14	An example of a collision phase diagram where the Weber number is plotted against the impact parameter. The four different collision regimes along with an example of their regime-dividing lines can be seen. Taken from Sommerfeld and Pasternak (2019)	41
2.15	Regimes of droplet impact, figure adapted from Bai and Gosman (1995)	47
2.16	Droplet-wall collision model taken from Sommerfeld et al. (2021). . .	49

2.17	Turbulent energy spectrum showing the amount of turbulent energy modelled and resolved by the RANS, LES and DNS approach. Figure adapted from Argyropoulos and Markatos (2015)	53
2.18	Plot of dimensionless velocity (U^+) against dimensionless wall distance (y^+) showing the viscous sublayer, buffer layer and fully turbulent layer. Taken from Mehta et al. (2018)	60
3.1	Schematic drawing (not to scale) of the z-type schlieren setup used. 1) Light source, 2) 6" parabolic mirrors, 3) Generated spray, 4) Iris, 5) Knife cut off and 6) Camera.	70
3.2	Schlieren image taken of can 1D for (a) the first setup showing background disturbances and turbulent structures, (b) the second setup showing the improvements over background disturbances but reduction in pixel density, (c) the third setup showing no background disturbances and improved pixel quality over the second setup.	73
3.3	Experimental schlieren setup showing the light source, two parabolic mirrors, positioned aerosol can, Weller extraction tube and knife cut off.	75
3.4	(a) A typical frame taken from a schlieren video (b) Application of Otsu's automatic thresholding technique and a search algorithm for the row and column indices to identify the bounds of the mirror's field of view.	77
3.5	Histogram of pixel intensities along with the inter-class variance for a frame taken from the schlieren experiments.	78
3.6	(a) Original image captured from the schlieren experiments, (b) Convolution of the original image with the horizontal Prewitt kernel, (c) Convolution of the original image with the vertical Prewitt kernel, (d) Magnitude of the gradients.	81
3.7	Gradient Magnitude resulting from the convolution with (a) Prewitt, (b) Sobel, (c) Roberts and (d) Canny filter with $\sigma = 0.036$	82

3.8	Edges detection using a threshold determined by Otsu's method. The edges for the different filters resulting from the convolution with (a) Prewitt, (b) Sobel, (c) Roberts and (d) Canny filter with $\sigma = 0.036$.	83
3.9	Number of total zeroes plotted against frame number for aerosol can 1D. Blue noisy line represents raw count of each frame. Orange line shows smoothed data after applying Savitzky-Golay smoothing filter.	85
3.10	Greyscale image of (a) the mid frame of aerosol can 1D (b) averaged frame of aerosol can 1D.	86
3.11	Important image into ImageJ with angle measuring lines for (a) the mid frame of aerosol can 1D (b) averaged frame of aerosol can 1D.	87
3.12	Images of the spraytec setup (a) the positioning of the spraytec device and clamp stand (b) the aligning process of the aerosol can.	90
3.13	(a) Detector 0 transmission signal and scattering signal when all detectors are used. (b) Resultant volume based particle size distribution from signal shown in (a).	91
3.14	Cumulative volume distribution from varying lower detector number of the Spraytec device.	94
3.15	Distributions for the detector range 10-36, blue histogram showing particle size distribution and red line showing cumulative distribution.	94
3.16	Particle size distribution for different low detector number limit of, 14, 15,16 and 17.	95
3.17	Cumulative distribution for varied averaging periods within a 5 second spray: 0-1 s, 1-2 s, 2-3 s, 3-4 s, 4-5 s and 0-5 s.	96
3.18	The measured volume frequency and cumulative frequency from the Spraytec device for aerosol can 1D at 1cm. The D_{50} , $D_{3,2}$ and $D_{4,3}$ are also plotted.	98
3.19	The CSD measured by the Spraytec device at the different axial positions tested: [1, 2, 5, 10, 15, 20] cm for can 1C.	98

3.20	Original measured distribution from aerosol can 1C at 2 cm Vs the normalised distribution isolating the main mode.	100
3.21	A comparison of the mineral insulated T-Type thermocouple (top) with the bare T-Type thermocouple (bottom).	102
3.22	The thermocouple setup for (a) insulated T type thermocouples (b) exposed T type thermocouples.	103
3.23	T-type thermocouple readings for three runs with thermocouples axially positioned at 1cm, 5cm, 10cm, 15cm and 20cm after actuation of can 1D. Bold line is the first run, dashed line is the second run and dotted line the third run.	105
3.24	Mean minimum thermocouple temperature for nozzle position at the tip (Red) of the thermocouple or 1 cm below (Blue), with the first thermocouple positioned at either 1 cm from the nozzle (Solid) or 5 cm (dashed) using can 1D.	107
3.25	(a) Full time series of temperature measurements for both insulated (solid) and bare (dashed) T-type thermocouples using can 1D. (b) Mean minimum values of temperature from a set of 3 experiments with both bare and insulated T-type thermocouples at different axial positions using can 1D.	108
3.26	The spray generation phase for aerosol cans (a) 1A, (b) 1B, (c) 1C, (d) 1D, (e) 2A, (f) 2B, (g) 2C, (h) 2D and (i) 2E.	115
3.27	The fully activated phase for aerosol cans (a) 1A, (b) 1B, (c) 1C, (d) 1D, (e) 2A, (f) 2B, (g) 2C, (h) 2D and (i) 2E.	117
3.28	The collapse phase for aerosol cans (a) 1A, (b) 1B, (c) 1C, (d) 1D, (e) 2A, (f) 2B, (g) 2C, (h) 2D and (i) 2E.	119
3.29	Axial distance evolution of D_{32} for the different aerosol cans tested. The swirl nozzle cans are represented in black and the simple orifice nozzles represented in red.	122

3.30	Axial distance evolution of distribution Span for the different aerosol cans tested. The swirl nozzle cans are represented in black and the simple orifice nozzles represented in red.	123
3.31	Axial distance evolution of D_{50} for the different aerosol cans tested. The swirl nozzle cans are represented in black and the simple orifice nozzles represented in red.	124
3.32	Axial distance evolution of D_{43} for the different aerosol cans tested. The swirl nozzle cans are represented in black and the simple orifice nozzles represented in red.	125
3.33	The CSD variation at varying axial positions of 1, 2, 5, 10, 15, 20 cm for the cans (a) 1A, (b) 1C, (c) 1D, (d) 2A, (e) 2B, (f) 2C, (g) 2D and (h) 2E.	128
3.34	The CSD variation for aerosol cans 1A, 1D, 2A and 2E axial positions (a) 1 cm, (b) 2 cm, (c) 5 cm, (d) 10 cm , (e) 15 cm and (f) 20 cm Black lines represent swirl nozzle and red lines a simple orifice nozzle. Solid lines are propellant formulations and blue circles are product formulations.	130
3.35	For aerosol can 1D at axial position of 1cm the (a) Normalised PDF plotted with fitted distributions Rosin-Rammler ($k_r = 2.52, \lambda = 21$), Log-normal ($\mu = 2.92, \sigma = 0.535$), Gamma ($k_g = 0.535, \theta = 4.42$); (b) Normalised PDF for repeated experiments plotted with mean parameter distributions Rosin-Rammler ($k_r = 2.48, \lambda = 0.67$), Log-normal ($\mu = 2.95, \sigma = 0.54$), Gamma ($k_g = 4.34, \theta = 4.70$).	133
3.36	Normalised PDF for aerosol can 1A (Propellant) showing each repeat and the mean parameter fits of the Rosin-Rammler, Log-Normal and Gamma Distributions for axial distances (a) 1 cm, (b) 2 cm, (c) 5 cm, (d) 10 cm, (e) 15 cm, (f) 20 cm.	134

3.37	Normalised PDF for aerosol can 1C (Alcohol + Propellant) showing each repeat and the mean parameter fits of the Rosin-Rammler, Log-Normal and Gamma Distributions for axial distances (a) 1 cm, (b) 2 cm, (c) 5 cm, (d) 10 cm, (e) 15 cm, (f) 20 cm.	135
3.38	Normalised PDF for aerosol can 1D (Full Product) showing each repeat and the mean parameter fits of the Rosin-Rammler, Log-Normal and Gamma Distributions for axial distances (a) 1 cm, (b) 2 cm, (c) 5 cm, (d) 10 cm, (e) 15 cm, (f) 20 cm.	136
3.39	Normalised PDF for aerosol can 2A (Propellant) showing each repeat and the mean parameter fits of the Rosin-Rammler, Log-Normal and Gamma Distributions for axial distances (a) 1 cm, (b) 2 cm, (c) 5 cm, (d) 10 cm, (e) 15 cm, (f) 20 cm.	137
3.40	Normalised PDF for aerosol can 2B (D5 + Propellant) showing each repeat and the mean parameter fits of the Rosin-Rammler, Log-Normal and Gamma Distributions for axial distances (a) 1 cm, (b) 2 cm, (c) 5 cm, (d) 10 cm, (e) 15 cm, (f) 20 cm.	138
3.41	Normalised PDF for aerosol can 2C (Active + Propellant) showing each repeat and the mean parameter fits of the Rosin-Rammler, Log-Normal and Gamma Distributions for axial distances (a) 1 cm, (b) 2 cm, (c) 5 cm, (d) 10 cm, (e) 15 cm, (f) 20 cm.	139
3.42	Normalised PDF for aerosol can 2D (Slurry + Propellant) showing each repeat and the mean parameter fits of the Rosin-Rammler, Log-Normal and Gamma Distributions for axial distances (a) 1 cm, (b) 2 cm, (c) 5 cm, (d) 10 cm, (e) 15 cm, (f) 20 cm.	140
3.43	Normalised PDF for aerosol can 2E (Full Product) showing each repeat and the mean parameter fits of the Rosin-Rammler, Log-Normal and Gamma Distributions for axial distances (a) 1 cm, (b) 2 cm, (c) 5 cm, (d) 10 cm, (e) 15 cm, (f) 20 cm.	141

3.44	Normalised PDF for aerosol can 1D at 1cm and the resultant PDFs after sampling from the fitted Rosin-Rammler, Log-Normal and Gamma distributions with (a) 100, (b) 1000, (c) 10000 and (d) 100000 uniformly distributed points.	142
3.45	Time series of bare thermocouples for aerosol cans (a) 1A swirl nozzle with propellant and (b) 2A plain nozzle with propellant.	144
3.46	Average centreline temperature profile and their standard deviations at axial positions: 1, 3, 5, 7, 10, 13, 15, 17, 20 and 22 cm for aerosol cans 1A (Blue) and 2A (Orange).	145
3.47	Centreline temperature at different axial positions for all the aerosol cans tested.	145
4.1	Cut through schematic of the square wind tunnel used in the Schefer (1987) , not to scale.	153
4.2	The geometry generation process: 1) The problem to be simulated, 2) The full geometry created, 3) The splitting of the geometry by symmetry planes, 4) The final geometry used, 5) The assignment of regions and dividing lines, 6) The resulting mesh. Further detail can be found within section 3.4.1.	157
4.3	Starting at Update properties, the pressure-based solution algorithm employed in Ansys Fluent v19.2.	159
4.4	Symmetry plane view of the meshes generated for the carrier jet mesh sensitivity study, top to bottom: Coarse, Medium and Fine. A close up of the nozzle mesh region for the coarse (red), medium (blue) and fine (green) meshes.	161
4.5	Residuals for the coarse mesh from iterations 7000-7500.	163
4.6	The axial velocity [(a),(c),(e)] and propane mass fraction [(b),(d),(f)] values along the centreline and for axial positions $X_d = 4$ and 30. Values are shown for the the coarse (red), medium (blue) and fine (green) mesh.	164

4.7	Velocity contours and vectors for the different turbulence models investigated, top to bottom: standard, RNG and realizable $k - \varepsilon$ and $k - \omega$ and $k - \omega$ SST.	166
4.8	Propane mass fraction contours for the different turbulence models investigated, top to bottom: standard, RNG and realizable $k - \varepsilon$ and $k - \omega$ and $k - \omega$ SST.	167
4.9	Velocity [(a),(c),(e)] and mixture fraction [(b),(d),(f)] profiles for the tested turbulence models and experimental results of Schefer (1987) . Data is plotted for axial positions $x_d = 4, 15$ and 30 . $k - \varepsilon$ turbulence models are in red and $k - \omega$ turbulence models in blue.	169
4.10	Centerline velocity (a) and propane mass fraction (b) for the investigated turbulence models and experimental data from Schefer (1987) . Shear Reynolds stress profiles $(\overline{u'v'})$ [(c),(d),(e)] for the investigated turbulence models and the experimental data of Schefer (1987) at the axial positions $x_d = 4, 15$ and 30 . $k - \varepsilon$ turbulence models are in red and $k - \omega$ turbulence models in blue.	170
4.11	Propane mixture fractions plotted for varying turbulent Schmidt number ranging from $Sc_t=0.5$ to $Sc_t=0.9$. Mixture fractions are plotted (a) along the centreline, and radially at axial distances (b) $x_d = 4$, (c) $x_d = 15$ and (d) $x_d = 30$	174
4.12	(a) Radial velocity profiles for both the Wall and No-Wall case at axial positions $X_d = 4, 15$ and 30 (b) Radial propane mass fraction profiles for both Wall and No-Wall cases at the same axial positions. .	175

4.13	(a) Data fit for the centerline decay within the transitional region. Here the decay rate is given as $\beta \approx 5.8$ and the virtual origin $x_0 \approx 2.6$. The core level is denoted by the black line and the fit to scaled axial velocity is denoted by the dashed green line. (b) The self similar profiles of the numerical solution for a range of axial positions $x_D = 30, 40, 50$ and 100 . The Gauss error function with $\beta = 5.8$ and $x_0/D = 2.6$ is also plotted for comparison and is given by the dashed line.	176
4.14	Domain schematic showing lengths and boundary conditions applied. Note this is not to scale.	179
4.15	Illustration to show the separation of the 2D axisymmetric domain into five rectangles.	180
4.16	The computational mesh constructed and zoom in of the near-nozzle region for the axisymmetric domain.	180
4.17	Relative humidity contours plotted for four different combinations of ambient temperature (T) and relative humidity (RH), top to bottom: T=20 °C RH=40% (case 1), T=40 °C RH=20% (case 2), T=40 °C RH=40% (case 3), T=40 °C RH=80% (case 4).	185
4.18	(a) Comparison of the CFD predicted propane mass fraction field to a mean schlieren frame for aerosol can 1A. (b) Radial propane mass fraction profile at an axial position of 10 cm.	186
4.19	Centreline temperature predicted by the axisymmetric CFD models with initial jet temperature of T=241 K and T=231 K compared to the the measured centreline temperature for aerosol cans 1D (Deo) and 1A (Prop).	188
5.1	X velocity and Y velocity plot against time for the release of different size droplets with initial velocity $u = 1 \text{ ms}^{-1}$ prescribed in the x-direction into quiescent air.	201
5.2	Relative error of the implemented model predictions to the settling velocity Eq. (5.19) for droplets sizes 10-100 μm	201

5.3	For a 12 μm diameter water droplet within a quiescent environment with an ambient temperature of 293.15 K and RH=50%, (a) d^2 against time and (b) droplet temperature (T) against time.	202
5.4	For a 12 μm diameter water droplet within a quiescent environment with an ambient temperature of 293.15 K and RH=50%, (a) droplet diameter (d) against time and (b) droplet temperature (T) against time are plotted for both the Maxwell (diffusion) model and Stefan-Fuchs (advection-diffusion) model.	203
5.5	Plots against time of (a) droplet diameter and (b) the droplet vertical velocity. Droplets evaporate with an assumed constant temperature of 293.15 K in an ambient of temperature 293.15 K and 50% RH. . .	204
5.6	Plots against time of (a) droplet diameter and (b) the droplet vertical velocity. Droplets evaporate allowing with an initial temperature of 293.15 K in an ambient of temperature 293.15 K and 50% RH, droplet temperature is allowed to change.	205
5.7	A water droplet of initial diameter 12 μm is initialised with a temperature of 293.15 K into a quiescent ambient with (a) fixed ambient temperature of 293.15 K but varying relative humidity (RH) or (b) a fixed RH of 50% with varying ambient temperature.	206
5.8	Log-log plot of droplet diameters against time for a water droplet and propane droplet initialised at 10 K less than the liquids' boiling points (-52°C and 90°C respectively).	207
5.9	Minimum droplet temperature achieved against the ambient saturation fraction due to propane droplet vaporisation in an ambient temperature of 231.15 K.	208
5.10	Contours of velocity magnitude for the continuous phase as well as particle trajectories coloured by particle diameter top: without turbulent dispersion and bottom: with turbulent dispersion.	211

5.11	Centreline temperature predicted by the axisymmetric CFD models with initial jet temperature of $T=241$ K and $T=231$ K with the inclusion of propane droplet vaporisation, compared to the the measured centreline temperature for aerosol cans 1D (Deo) and 1A (Prop).	213
5.12	Axisymmetric domain with a curved impingement surface at a stand-off distance (D) away from the nozzle, radius of curvature (R) and surface height (H).	215
5.13	The design space coverage for surface height (H) and standoff distance (D) resulting from a design of experiments.	217
5.14	Mesh zones	218
5.15	Schematic of the geometry split into mesh zones, and a zoom in of the mesh near the nozzle region and near the curved impingement surface for the fine mesh.	219
5.16	For droplets of size $15 \mu\text{m}$ the droplet efficiency is measured against the total number of droplets injected into the domain (N).	220
5.17	Monitor point locations (crosshairs) within the axisymmetric impingement simulation domain.	221
5.18	(a) Propane mass fraction at the monitor point locations plotted against log scale of iteration number, (b) Residual levels from iterations 60000-70000.	222
5.19	Velocity contours with log scaling for the, top to bottom: Coarse, Medium and Fine mesh for left: $R=7.5$ cm case and right: $R=600$ cm case.	223
5.20	Propane mass fraction contours with log scaling for the, top to bottom: Coarse, Medium and Fine mesh for left: $R=7.5$ cm case and right: $R=600$ cm case.	224
5.21	Mesh sensitivity of capture efficiency for the coarse, medium and fine mesh for both cases where $R=7.5$ cm and $R=600$ cm.	224

5.22	Response surfaces of capture efficiency (E) from varying the standoff distance (D) and surface height (H) for a surface with radius of curvature 75 mm generated for monodisperse sizes of (a) 10 μm , (b) 15 μm , (c) 20 μm and (d) 25 μm	228
5.23	Response surfaces of capture efficiency (E) from varying the standoff distance (D) and surface height (H) for a surface with radius of curvature 75 mm generated for (a) droplets injected along the centreline, $y=0$ mm (b) injected at the nozzle edge, $y=0.25$ mm.	229
5.24	Injected particle size distribution for both the edge and centreline injections for design points (H,D) cm (a) (4.1,18.4) cm, (b) (4.3, 10.3) cm, (c) (4.6,15) cm, (d) (5,19.8) cm, (e) (5.4,16.7) cm, (f) (5.7,12) cm, (g) (6.7,16) cm, (h) (6.2,14) cm (i) (6.7,16) cm and (j) (6.9, 12.8) cm.	233

List of Tables

2.1	Antoine equation coefficients, A, B and C taken from the NIST Web-Book (Linstrom and Mallard, 2001). The temperature ranges (Kelvin) used and the sources of data used to generate the coefficients are given.	12
2.2	Analogy of spring-mass forces to that fluid forces governing droplet breakup in the TAB breakup model.	35
3.1	The contents of the cans separated into swirl atomizer nozzles (group 1) and simple orifice nozzles (group 2). D5 represents cyclopentasiloxane and AACH the active aluminum chlorohydrate.	68
3.2	For each aerosol can the component mass (g), separated into propellant and base, and their respective mass fractions (%) are given.	68
3.3	Different camera setups for the Schlieren Experiments detailing both camera and lens specifications.	75
3.4	The probability distribution function (PDF) and cumulative distribution function (CDF), including their parameters, for the Rosin Rammler, Log-normal and Gamma distributions.	99
3.5	Nozzle position and first thermocouple position for the four different setups tested.	106
3.6	Mean spray angle (μ) and standard deviation (σ) for an individual frame (single) and mean frame (mean) of schlieren videos for nine different formulations and two nozzle types.	109

3.7	The arithmetic mean (μ) and standard deviation (σ) of temperature (T), relative humidity (RH) and mass sprayed (within 2 seconds) (ΔM) for the Spraytec experiments for all aerosol cans.	120
3.8	Fit parameters averaged over for their means and standard deviations for the Rosin-Rammler, Log-Normal and Gamma distributions for aerosol cans 1A, 1C, 1D, 2A, 2B, 2C, 2D, 2E at axial positions of 1 cm, 2 cm, 5 cm, 10 cm, 15 cm and 20 cm.	132
4.1	This table shows the number of cells (N_{cells}), average cell skewness, average orthogonal quality and average aspect ratio for each of the three meshes generated. The number of divisions for the geometrical regions are also included in the table.	162
4.2	This table shows the errors between the coarse, medium and fine meshes. The percentage error for axial velocity is shown on the left hand side and the mean absolute error for the mass fraction on the right hand side. The errors are calculated for along the centerline and at axial positions $X_d = 4$ and 30.	165
4.3	Horizontal (H) and vertical (V) cell sizings defined on the five rectangular regions along with the corresponding bias factors.	180
4.4	Ambient temperature and relative humidity conditions for the four cases simulated.	182
5.1	Morsi and Alexander (1972) coefficients a_i determined by the value of the Reynolds number.	195
5.2	Thermophysical properties at approximately 293 K for water, propane and butane.	197
5.3	Horizontal and vertical edge sizings (mm) for the six mesh zones for the coarse, medium and fine mesh.	218
5.4	Information on simulation time for the coarse medium and fine mesh for both the curved surface cases.	221

- 5.5 Cubic equation coefficients p_{ij} for the capture efficiency response surfaces predicted for monodisperse droplet sizes and polydisperse droplet sizes initialised at the centre or at the edge of the carrier jet. . 225

Nomenclature

List of Abbreviations

Symbol	Description
AACH	Aluminium Chlorohydrate
CDF	Cumulative Distribution Function
CDT	Centre for Doctoral Training
CFD	Computational Fluid Dynamics
CFL	Courant-Freidrichs-Lewy
CSD	Cumulative Size Distribution
D5	Cyclopentasiloxane
DNS	Direct Numerical Simulation
DoE	Design of Experiments
DRW	Discrete Random walk
FVM	Finite Volume Method
ID	Inner Diameter
KH	Kelvin Helmholtz
LDV	Laser Doppler Velocimetry

LES	Large Eddy Simulation
LPG	Liquefied Petroleum Gas
MMAD	Mass Median Aerodynamic Diameter
OD	Outer Diameter
PCC	Phantom Camera Control
PDF	Probability Distribution Function
PISO	Pressure-Implicit with Splitting of Operators
PIV	Particle Image Velocimetry
PSD	Particle Size Distribution
RANS	Reynolds Averaged Navier-Stokes
RH	Relative Humidity
RMS	Root Mean Square
RNG	Re-Normalisation Group
RR	Rosin-Rammler
RSM	Reynolds Stress Model
RT	Rayleigh Taylor
SIMPLE	Semi-Implicit Method for Pressure Linked Equations
SIMPLEC	Semi-Implicit Method for Pressure Linked Equations-Consistent
SMD	Sauter Mean Diameter
SOP	Standard Operating Procedure
SST	Shear Stress Transport

SVP	Saturation Vapour Pressure
TDR	Turbulent Dissipation Rate
TKE	Turbulent Kinetic Energy
VOF	Volume Of Fluid
VPT	Vapour Phase Tap

Aerosol Cans

Symbol	Description
1A	Swirl nozzle with propellant
1B	Swirl nozzle with propellant and water
1C	Swirl nozzle with propellant and alcohol
1D	Swirl nozzle with full product
2A	Simple orifice nozzle with propellant
2B	Simple orifice nozzle with propellant and D5
2C	Simple orifice nozzle with propellant and AACH
2D	Simple orifice nozzle with propellant and slurry
2E	Simple orifice nozzle with full product

Dimensionless Numbers

Symbol	Description	Definition
Ja	Jakob Number	$\frac{c_p(T_w - T_{sat})}{h_{fg}}$
Nu	Nusselt Number	$\frac{hL}{k}$
Oh	Ohnesorge Number	$\frac{\mu}{\sqrt{\rho\sigma L}}$

Pr	Prandtl Number	$\frac{\nu}{\alpha}$
Re	Reynolds number	$\frac{\rho UL}{\mu}$
Sc	Schimdt Number	$\frac{\nu}{D_m}$
Sc _t	Turbulent Schimdt Number	$\frac{\nu_t}{D_t}$
Sh	Sherwood Number	$\frac{hL}{D_m}$
St	Stokes Number	$\frac{t_0 U}{L}$
We	Weber Number	$\frac{\rho U^2 L}{\sigma}$

Greek Symbols

Symbol	Description	Units
β	Decay constant	[-]
δ_{ij}	Kronecker delta	[-]
γ	Surface tension	[N m ⁻¹]
λ_μ	Rosin-Rammler distribution parameter 2 mean	[-]
λ_σ	Rosin-Rammler distribution parameter 2 standard deviation	[-]
μ_μ	Log-Normal parameter 1 mean	[μm]
μ_σ	Log-Normal parameter 1 standard deviation	[μm]
μ_l	Liquid dynamic viscosity	[Pa s]
μ_{mean}	Mean spray angle from a mean frame	[deg]
μ_{single}	Mean spray angle from a single frame	[deg]
μ_t	Turbulent viscosity	[m ² s ⁻¹]

ν	Kinematic viscosity	$[\text{m}^2 \text{s}^{-1}]$
ω	Specific dissipation rate	$[\text{s}^{-1}]$
ρ	Density	$[\text{kg m}^{-3}]$
ρ_g	Gas density	$[\text{kg m}^{-3}]$
ρ_l	Liquid density	$[\text{kg m}^{-3}]$
$\sigma_{k,\varepsilon}$	Model constants for the transport equations of k and $v\varepsilon$	$[-]$
σ_{mean}	Standard deviation of spray angle from a mean frame	$[\text{deg}]$
σ_{SB}	Stefan-Boltzman Constant, 5.6704×10^{-8}	$[\text{W m}^{-2} \text{K}^{-1}]$
σ_{single}	Standard deviation of spray angle from a single frame	$[\text{deg}]$
θ	Gamma Distribution parameter 2	$[-]$
θ	Surface radius of curvature	$[\text{deg}]$
θ_μ	Gamma Distribution parameter 2 mean	$[-]$
θ_σ	Gamma Distribution parameter 2 standard deviation	$[-]$
θ_R	Radiation temperature	$[\text{K}]$
ε	Turbulent dissipation rate	$[\text{m}^2 \text{s}^{-3}]$
ε_p	Particle emissivity	$[-]$

Roman Symbols

Symbol	Description	Units
a	Measure of attraction between particles	$[\text{N m}^4 \text{mol}^{-2}]$

A_p	Particle/Droplet surface area	$[\text{m}^2]$
b	Volume excluded by a mole of particles	$[\text{m}^3 \text{ mol}^{-1}]$
B_m	Spalding mass number	$[-]$
C_s	Surface vapour concentration	$[\text{kg kmol}^{-1}]$
$C_{1,2,3\varepsilon}$	Model constants 1, 2 and 3 for the transport equation for the turbulent dissipation rate	$[-]$
C_∞	Ambient vapour concentration	$[\text{kg kmol}^{-1}]$
C_μ	Boussinesq's eddy viscosity constant	$[-]$
$C_{b,d,k,F}$	TAB model constants	$[-]$
C_L	Levich Constant	$[-]$
c_p	Specific heat capacity	$[\text{J kg}^{-1} \text{ K}^{-1}]$
D	Standoff distance	$[\text{m}]$
d_0	Orifice Diameter	$[\text{m}]$
d_0	Nozzle Diameter	$[\text{m}]$
D_{10}	10 th percentile	$[\mu\text{m}]$
$D_{3,2}$	Sauter Mean Diameter	$[\mu\text{m}]$
$D_{4,3}$	Volume Mean Diameter	$[\mu\text{m}]$
D_{50}	50 th percentile	$[\mu\text{m}]$
D_{90}	90 th percentile	$[\mu\text{m}]$
$D_{m,i}$	Mass diffusion coefficient of species i	$[\text{m}^2 \text{ s}^{-1}]$
d_p	Particle/Droplet diameter	$[\mu\text{m}]$

$D_{T,i}$	Soret coefficient of species i	$[\text{K}^{-1}]$
H	Surface height	$[\text{m}]$
I	Inner region	$[-]$
J	Rate of Momentum Flow	$[\text{kg m s}^{-2}]$
k	Turbulent kinetic energy	$[\text{m}^2 \text{s}^{-2}]$
k_c	Mass transfer coefficient	$[\text{m s}^{-1}]$
$k_{g\mu}$	Gamma distribution parameter 1 mean	$[-]$
$k_{g\sigma}$	Gamma distribution parameter 1 standard deviation	$[-]$
k_{GD}	Gladstone-Dale Coefficient	$[\text{m}^3 \text{kg}^{-1}]$
k_g	Gamma distribution parameter 1	$[-]$
$k_{r\mu}$	Rosin-Rammler distribution parameter 1 mean	$[-]$
$k_{r\sigma}$	Rosin-Rammler distribution parameter 1 standard deviation	$[-]$
k_r	Rosin-Rammler distribution parameter 1	$[-]$
L	Length Scale	$[\text{m}]$
l	Flow length scale	$[\text{m}]$
M	Middle region	$[-]$
$m_{p,in}$	Mass of droplet entering cell	$[\text{kg}]$
$m_{p,out}$	Mass of droplet leaving cell	$[\text{kg}]$
m_p	Particle/Droplet mass	$[\text{kg}]$
M_w	Molecular weight	$[\text{kg kmol}^{-1}]$

N	Nozzle region	[-]
n	Amount of a substance	[mol]
N_{End}	Frame number for Start of the collapse regime	[-]
n_{ind}	Refractive index	[-]
N_{Mid}	Middle of fully activated spray regime	[-]
N_{start}	Frame number for start of the fully activated spray regime	[-]
O	Outer region	[-]
P	Pressure	[Pa]
P_b	Production term for turbulent kinetic energy due to buoyancy	[kg m ⁻¹ s ⁻³]
P_k	Production term for turbulent kinetic energy	[kg m ⁻¹ s ⁻³]
$P_{Par,i}$	Partial pressure of component i	[Pa]
$P_{Sat,i}$	Saturation vapour pressure of component i	[Pa]
P_{Tot}	Total Pressure	[Pa]
P_{Vap}	Vapour Pressure	[Pa]
Q_p	Particle Mass flow rate	[kg s ⁻¹]
R	Co-flow region	[-]
R	Ideal gas constant, 8.314	[J K ⁻¹ mol ⁻¹]
r_0	Orifice Radius	[m]
r_j	Jet Radius	[m]

S_ε	Source term for turbulent dissipation rate	[kg m ⁻¹ s ⁻⁴]
S_k	Source term for turbulent kinetic energy	[kg m ⁻¹ s ⁻³]
T	Temperature	[K]
t_0	Particle relaxation time	[s]
T_c	Critical temperature	[K]
T_l	Liquid temperature	[K]
$T_{p,in}$	Temperature of droplet entering cell	[K]
$T_{p,out}$	Temperature of droplet leaving cell	[K]
T_p	Particle/Droplet temperature	[K]
U	Velocity Scale	[m s ⁻¹]
u', v', w'	Turbulent velocity fluctuations	[m s ⁻¹]
U_i	Initial jet velocity	[m s ⁻¹]
u_{ijk}	Velocity in the i j or k direction	[m s ⁻¹]
x_0	Virtual origin	[m]
x_{ijk}	Spatial coordinate in the i j or k direction	[m]
X_i	Mole Fraction of component i	[mol/mol]
x_p	Particle/Droplet x position	[m]
Y_∞	Mass fraction of species in the ambient	[kg/kg]
Y_i	Mass fraction of species i	[kg/kg]

Y_m	Dissipation term for turbulent kinetic energy due to compressible dilation	$[\text{kg m}^{-1} \text{s}^{-3}]$
y_p	Particle/Droplet y position	[m]
Y_s	Mass fraction of species at droplet surface	[kg/kg]
E	Capture Efficiency	[-]
N	Number of injected droplets	[-]
N_{Imp}	Number of impinged droplets	[-]

Chapter 1

Introduction

1.1 Background and Motivation

The use of sprays in both industrial and commercial applications is ubiquitous, with examples such as diesel sprays, spray drying, paint sprays, pesticides and irrigation, fire suppression systems, inhalers, personal care products and more [(Kong et al., 1999), (Mezhericher et al., 2009), (Andersson et al., 2013), (Fogliati et al., 2006), (Dong et al., 2015), (Hoffman et al., 1989), (Marshall and di Marzo, 2004), (Hochrainer et al., 2005), (Longest and Hindle, 2008)]. For each application specific spray devices are used, taking a product/fluid and breaking it into droplets for the desired application. This can include fine droplets for an increased product surface area, large spray angle for wider coverage or deeper penetration for further coverage over distance. The properties of the fluid, the spray device and the ambient play a key role in the breakup of the liquid and the resulting droplet sizes. Most spray research has focused on optimising sprays within fuel injectors, looking to increase their efficiency and improve cost. Other prominent applications are discussed in the work of Nasr et al. (2013) with only two out of approximately 500 pages discussing aerosol cans, the main focus of this work.

Over 8 billion aerosol cans were made in the year 2018 alone (AEROBAL, 2022) reaching a record high. In 2020 and in 2021 over 5 billion aerosol cans were produced in Europe, with over 50% produced for personal care products (Aerosol, 2022) demonstrating the continuing high demand for aerosol can products. However, to the author's knowledge, little published research has been done investigating the spray generation from propellant-based aerosol cans and the resultant carry-over (fate of droplets from impinging a target surface). Personal care products contribute a large proportion of aerosol cans used due to the quick and easy method of application. The high usage and limited scientific study on personal care product sprays means that this area presents great potential for academic investigation.

1.2 Project Aims

The work presented in this thesis aims to provide an experimental data set for various spray properties (e.g. spray angle, particle size and temperature) of sprays generated from personal care product type aerosol cans. The work also aims to provide an experimentally validated numerical model able to predict the spray carry-over of propellant-based aerosol cans. Using this model we aim to investigate both ambient and impingement surface topology effects on spray carry-over and provide a tool for further development. The main objectives of the work are set out as follows:

1. To perform a literature review of the current numerical and experimental methodologies of modelling and quantifying spray generation and the resultant droplet transport.
2. Carry out schlieren, Spraytec and thermocouple experiments to provide a data set in order to validate the carrier jet and droplet transport components of the numerical model.
3. Investigate 2-equation Reynolds Averaged Navier-Stokes (RANS) based turbu-

lence models for carrier jet generation and validate the simulated flow field and species fraction fields with experiments and work found within the literature.

4. Numerically model the trajectory, heat and mass transfer of the complex droplets generated from aerosol cans and the effects of ambient conditions on their transport.
5. Coupling the carrier jet and droplet dynamics work, perform a parametric study on convex surface topology to investigate capture efficiency for personal care products and droplet carry-over.
6. Investigate the effects of ambient conditions (relative humidity and temperature) on spray development.

1.3 Thesis Outline

The thesis is presented such that each chapter attempts to focus on one of the main objectives. Chapter 2 reviews the literature, detailing fundamentals of the spray generation procedure such as flash atomization, liquid jet breakup, secondary atomization and droplet impingement on a target surface. Chapter 3 details the methodology and results of the schlieren, Spraytec and thermocouple experiments. It also details the post-processing of the schlieren imaging to capture spray angle; fitting of particle size distributions to the spraytec measurements; and investigates the impact of formulation on centreline temperature profiles. Chapter 4 sets out the single-phase carrier jet model and its validation with the schlieren results and work found within the literature. This model is then used to investigate variations of ambient properties such as temperature and relative humidity. Chapter 5 brings the final objectives together, modelling the droplet transport including heat and mass transfer. Coupling of the phases within the numerical model is detailed as well as a parametric study of the effect of surface topology on capture efficiency. Chapter 6 concludes the key results from the work and provides an outlook for future work.

Chapter 2

Literature Review

2.1 Introduction

The aim of this review is to give a comprehensive exploration of the physics involved in spray formation (carrier jet, jet breakup, atomization, and droplet dynamics) and investigate the current stage of research in this area. [Lefebvre and McDonell \(2017\)](#), [Sirignano \(2010\)](#) and [Ashgriz \(2011\)](#) are examples of similar such reviews. [Lefebvre and McDonell \(2017\)](#) gives detailed explanations on the different types of atomisers used and droplet sizing methods; [Sirignano \(2010\)](#) performs a thorough review on droplet vaporisation from single component to multi-component droplets at sub-critical and critical conditions; and [Ashgriz \(2011\)](#) provides an overview of droplet dynamics including droplet-droplet interaction and droplet-wall interaction, primary and secondary atomization models, spray atomizers and their applications.

The experimental approaches available to measure spray characteristics will be discussed for each area of the spray formation process. An example of a review, primarily on experimental techniques for aerosol size and composition measurements, is given in [Kulkarni et al. \(2011\)](#). The experimental techniques, and the fundamentals of aerosol dynamics needed for their application, are given in great

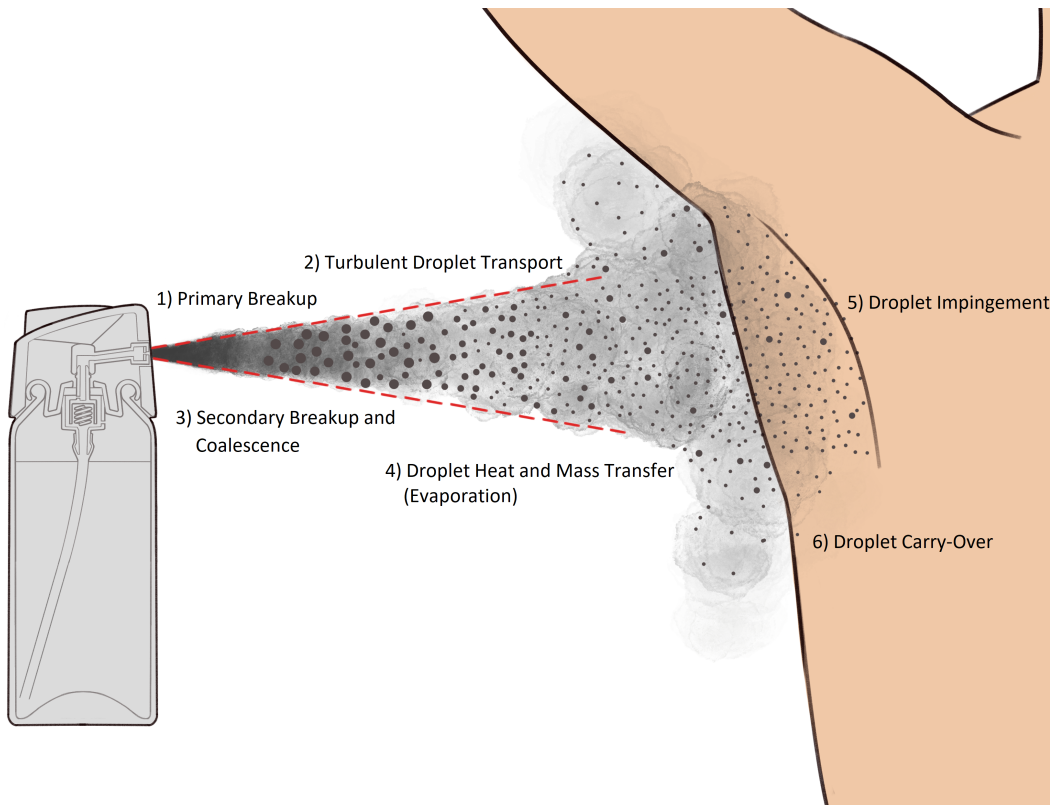


Figure 2.1: The spray generation process from a deodorant-type aerosol can towards a human axilla (not to scale). The 6 processes of interest are labelled: 1) Primary breakup, 2) Turbulent droplet transport, 3) Secondary breakup and Coalescence, 4) Droplet heat and mass Transfer (Evaporation), 5) Droplet impingement and 6) Droplet carry-over.

detail in [Kulkarni et al. \(2011\)](#).

This review is set out to cover the key areas of the spray generation process shown in [Figure 2.1](#). The review starts by looking within the aerosol can, detailing the main components and the actuation procedure. Then it moves up to the nozzle, where the main atomization type, flash atomization, is discussed. After leaving the aerosol can, the physics relevant to spray generation are detailed, starting with the carrier jet dynamics and breakup of liquid into droplets (primary atomization). The droplet physics are then detailed at each stage including: turbulent transport, thermodynamics including heat and mass transfer within the spray, and finally the impingement of droplets and the fate of these droplets after interacting with the target impingement surface (carry-over).

2.2 Aerosol Cans

The physics that underpins spray generation is highly complex. Before even beginning to understand how sprays are generated, the fundamentals of aerosol cans need to be understood. This section looks to give a comprehensive introduction to the fundamentals of aerosol cans and touch on flash atomization, the main form of atomization that occurs before the product propellant mix leaves the aerosol can.

2.2.1 Fundamentals

Aerosol cans provide one of the easiest and quickest methods of application for domestic products. Aerosol cans are typically designed as seen in Figure 2.2. Actuating the can is achieved by pressing down on the actuator located at the top of the can. This action lowers the stem through the gasket, compressing the internal spring, and opening a hole/valve between the bottom of the stem and the housing. The pressure difference with the external air causes the product concentrate and liquefied propellant to rise up the dip tube and exit through the insert/nozzle at the top of the aerosol can. To finish spraying, the actuator is released, which results in the spring relaxing and in turn raising the stem which closes the stem hole, stopping the spray. Some manufacturers include a vapour phase tap (VPT) in the housing to allow for some of the gaseous propellant mixture to mix into the liquid product/propellant mixture. The inclusion of the VPT aids in the breakup of the liquid and results in finer droplet production ([Nasr et al., 2013](#)).

The make-up of the propellant has been changed to alkane-based propellants (a blend of alkanes such as propane and butane also referred to as liquefied petroleum gas (LPG)), where before chlorofluorocarbons (CFCs) were used. This change was pushed due to CFCs' ozone-depleting properties and their link to global warming ([Grundmann, 2000](#)). Currently alkane-based formulations are the stan-

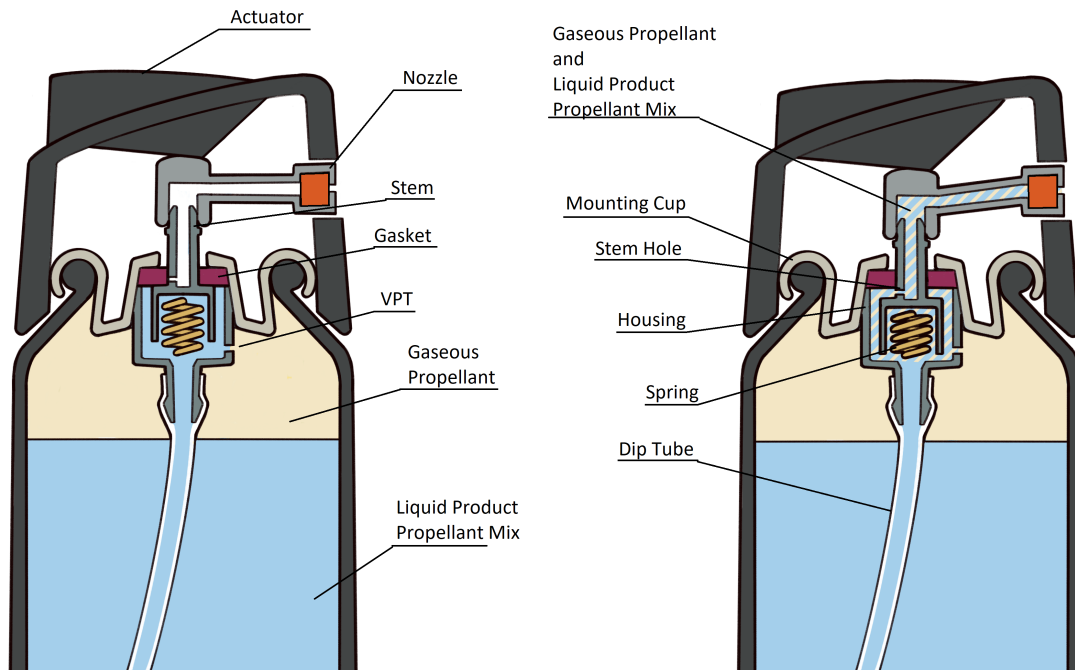


Figure 2.2: Cross-section of an aerosol can and labelling of key components. Left: Unactuated aerosol can, Right: Actuated aerosol can. Image adapted from [BAMA \(2023\)](#).

dard, however, these still have a negative environmental impact. That said, recent advances have been made to further reduce this with investigations into pressurising aerosol cans with nitrogen ([Nourian et al., 2015](#)). A key drawback with nitrogen-based aerosol cans, however, is that as the aerosol can is used the internal pressure decreases, whereas for alkane-based propellants, after spraying, the volatile propellant evaporates filling the space at the top of the can and maintaining the desired internal pressure. As the use of alkane-based aerosol cans is so widespread they will be the propellant of interest for this work.

Aerosol cans typically have an internal pressure of around 5 atm ([Nasr et al. \(2013\)](#)) depending on the blend of propellants. The pressure inside the can is mostly governed by the vapour pressure generated from the mixture of volatile propellants within the can. For many pure substances the saturation vapour pressure (SVP, P_{Sat}) can be plotted against temperature following the Antoine equation ([Thomson,](#)

1946), a semi-empirical correlation taking the form,

$$\log(P_{Sat}) = A - \frac{B}{C + T}. \quad (2.1)$$

Surface curvature at the liquid-vapour interface can also impact the vapour pressure. This influence is captured by the Kelvin effect. The change in vapour pressure (P_{Vap}) due to surface curvature is given by the Kelvin equation (Heidenreich and Bttner, 1995), which for a spherical droplet of radius r is

$$P_{Vap}(r) = P_{Sat} \exp\left(\frac{2\gamma M_w}{RT\rho_g r}\right), \quad (2.2)$$

where γ is surface tension, M_w the molecular weight of the substance, R the ideal gas constant (8.314 J/K/mol), T the temperature and ρ_g the density of the vapour. The equation shows that as the radius of the droplet decreases the vapour pressure at the interface increases and moves away from the saturation pressure. This effect can be neglected where the radius of the droplet is sufficiently large and can be important when the droplet is submicron in size.

For the typical propellants used in a deodorant-type aerosol can, the alkanes have constants A , B and C for specific temperature ranges given in Table 2.1, which are taken from Linstrom and Mallard (2001). The resultant Antoine equations are plotted for the three alkanes: propane, butane and isobutane, and can be seen in Figure 2.3a. At room temperature (293.15 K, 20°C) propane has the largest SVP (≈ 8.5 atm) followed by isobutane (≈ 3 atm) and then butane (≈ 2 atm). Following Raoult's law, taking an ideal mixture (a mixture of ideal gases) the partial pressure of each component is proportional to the mole fraction (X_i) of the component and its SVP (Smolkov-Keulemansov and Feltl, 1991),

$$P_{Par,i} = P_{Sat,i}X_i. \quad (2.3)$$

Dalton's law of partial pressures states that the total pressure of a mixture of N gases is equal to the sum of the partial pressures of the N components,

$$P_{Total} = \sum_{i=1}^N P_{Par,i}. \quad (2.4)$$

Combining Eqs. (2.3), (2.4) gives

$$P_{Total} = \sum_{i=1}^N P_{Sat,i} X_i. \quad (2.5)$$

Following this, and assuming an ideal mixture, the total pressure inside an aerosol can is then subject to the different mole fractions of the LPG components and their respective saturation vapour pressures. Assuming room temperature and taking Antoine's equation with constants from Table 2.1, the saturation vapour pressure of component i is calculated as well as the resultant total pressure using Eq. 2.5, and these values plotted in Figure 2.3c. Figure 2.3c shows the potential pressure inside an aerosol can depending on the blend of LPG used. Note that these propellants are not fully described by the ideal gas law and the different components of the mixture may exert higher or lower partial pressure contributions. These assumptions are adequate however to demonstrate how the internal pressure varies with changes in blend of LPG.

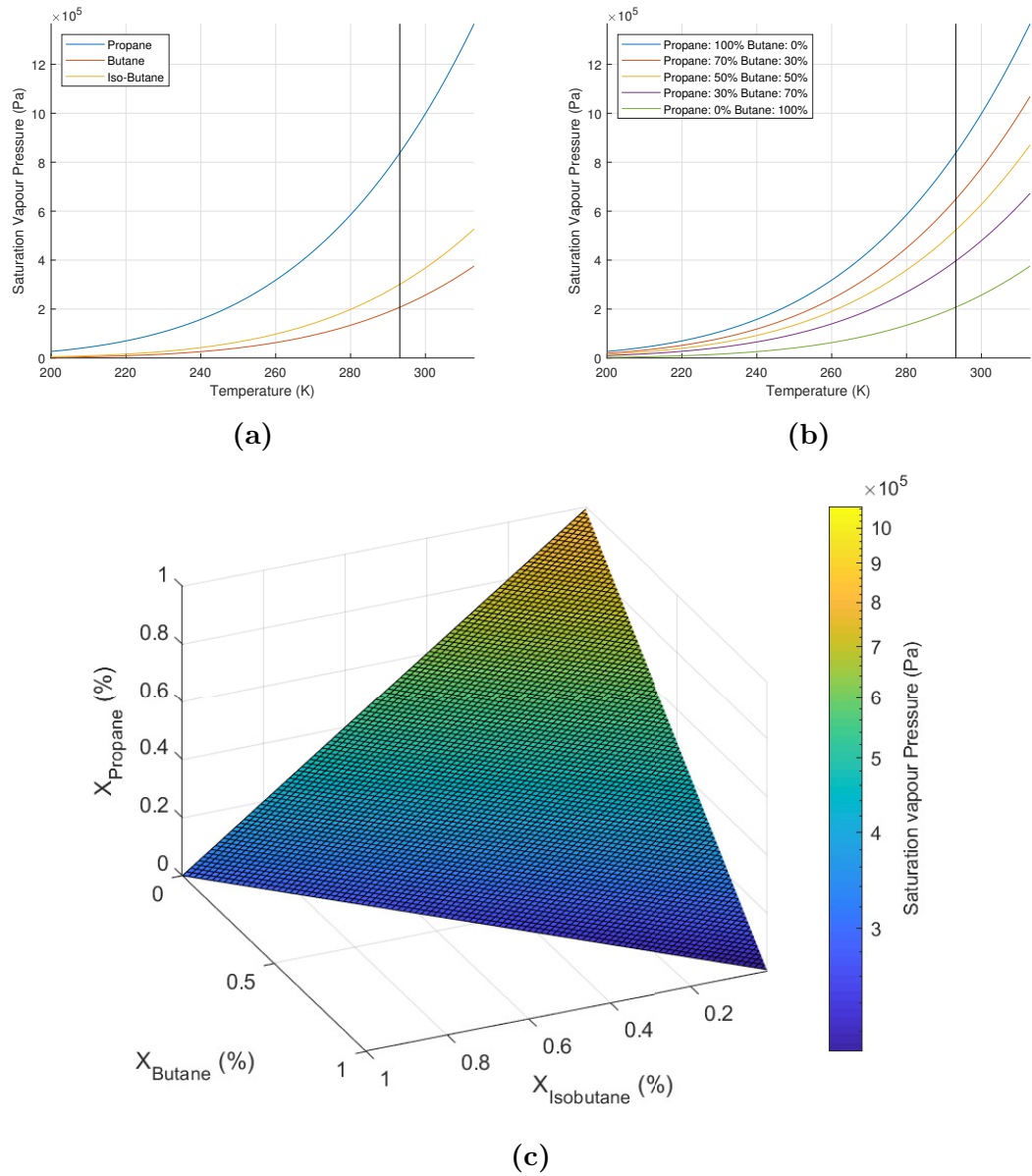


Figure 2.3: The saturation vapour pressure against temperature (293.15 K - black line) for (a) pure substances Propane, Isobutane and Butane, (b) Mixtures of different mole fractions of Propane and Butane. (c) Saturation vapour pressure (log contours) at 293.15 K for different mole fractions of Propane, Butane and Isobutane.

		A	B	C
Propane	Helgeson and Sage (1967) 166 < T < 230.6	4.01158	834.26	-22.763
	Rips (1963) 230.6 < T < 320.7	3.98292	819.296	-24.417
	Kemp and Egan (1938) 320.7 < T < 360.8	4.53678	1149.36	24.906
Butane	Carruth and Kobayashi (1973) 135.42 < T < 212.89	4.70812	1200.475	-36.146
	Aston and Messerly (1940) 212.89 < T < 272.66	3.85002	909.65	-36.146
	Das et al. (1973a) 272.66 < T < 425	4.35576	1175.581	-2.071
Isobutane	Aston et al. (1940) 188.06 < T < 261.31	3.94417	912.141	-29.808
	Das et al. (1973b) 261.32 < T < 408.12	4.3281	1132.108	0.918

Table 2.1: Antoine equation coefficients, A, B and C taken from the NIST Web-Book (Linstrom and Mallard, 2001). The temperature ranges (Kelvin) used and the sources of data used to generate the coefficients are given.

2.2.2 Flash Atomization

The atomization of the product and thus the generation of alkane propellant-based aerosol sprays is driven primarily by flash atomization. Here flash atomization occurs due to a rapid decrease in pressure as the liquid propellant travels from within the can to the external ambient pressure. The vaporising propellant results in bubble nucleation and rapid bubble growth within the fluid, which then collapse when the bubbles touch (Sher and Elata, 1977). The explosive collapse of the bubbles then tears the liquid product propellant mix into small droplets.

Bubble nucleation can be classed as either homogeneous or heterogeneous nucleation (Blander and Katz, 1975). Homogeneous nucleation is when nucleation occurs completely within the liquid bulk and heterogeneous nucleation is nucleation which occurs at an interface. The type of nucleation depends on the liquid properties such as the initial liquid temperature, its critical temperature (T_c , the temperature at the critical point), the ambient pressure and also the rate of pressure drop. A higher

nucleation rate in general results in a finer and more uniform spray. Essential criteria for homogeneous nucleation to occur is that the initial temperature of the liquid is high, $T_l \gg 0.9T_c$ (Avedisian, 1985), and that the pressure drop is sufficiently large, $\frac{dP}{dt} > 400$ MPa/s (Skripov et al., 1974).

For an ideal gas, the ideal gas law (Borgnakke and Sonntag, 2022) gives an approximation to their behaviour,

$$PV = nRT \quad (2.6)$$

where P is the pressure, V the volume, n the amount of the substance, R the ideal gas constant and T the temperature. The dashed line BF shown in Figure 2.4 does not capture the true behaviour exhibited. If the inter-molecular forces are taken into account an alternative equation of state, the Van der Waals equation of state (Poling et al., 2001) for example,

$$P = \frac{RT}{V_m - b} - \frac{a}{V_m^2} \quad (2.7)$$

can be used. Here $V_m = \frac{V}{n}$; a is the measure of attraction between particles; and b is the volume excluded by a mole of particles. This equation of state is able to capture the true isotherm shape given by BCDEF. Here fluid enters the metastable region, where the ambient pressure is less than the vapour pressure. C is the point between this metastable state and the unstable state. The particular isotherm temperature where this point C is at the ambient pressure is given at the thermodynamic limit of superheat which can be determined by taking $dP/dV=0$. An accurate equation of state is needed to determine this point.

The Redlich-Kwong equation of state (Poling et al., 2001) is an improvement over the Van der Walls equation of state but still suffers from capturing liquid density and vapour-liquid equilibrium. Other cubic equations of state are the Soave equation of state and the Peng Robinson equation of state (Poling et al., 2001) which

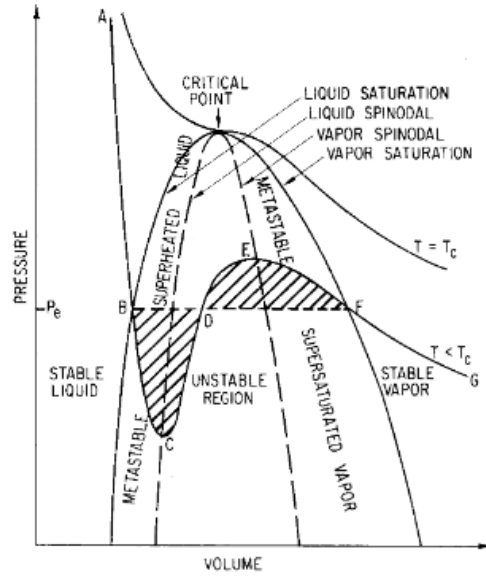


Figure 2.4: Example Pressure-Volume Diagram taken from Blander and Katz (1975) showing the saturation and spinodal curves for liquid and vapour, and the isotherm at the critical temperature (T_c) and a real-type isotherm below it.

improved capture of the vapour-liquid equilibrium but still struggle with capturing the liquid phase properties such as saturation liquid density.

Once bubbles have been nucleated an understanding of their growth is needed. The work of Sher and Elata (1977) derived a mathematical model for the growth of bubbles. They also experimentally investigated droplet sizes generated from spraying a mixture of Freon-22 and toluene, and the effects of varying both the internal pressure (1-5.5 ata) and operating temperature (15-60°C). Droplet sizes were measured by dyeing the spray and measuring deposited droplets on a sampling plate which were then microscopically counted. Sher and Elata (1977) found that by increasing the operating pressure a decrease in droplet size was observed. At high operating pressures, the change in droplet size decreased with an increase in operating pressure.

Loureiro et al. (2020) performed Direct Numerical Simulation (DNS) to understand the flash-boiling atomization process at a microscale. The motivation was for atomization within rocket thrusters. Loureiro et al. (2020) was able to demonstrate qualitatively the breakup processes that occur. This is not possible to

do experimentally due to the small length and time scales these processes occur over. The cases investigated took a minimum computational time of 1.18×10^3 core hours. DNS fully resolves all scales and as a consequence is incredibly computationally expensive.

The review of [Bhatia and De \(2019\)](#) details some of the recent modelling work on flash atomization, aiming to determine the drawback of models for bubble nucleation, growth and collapse. Other examples of reviews of flash atomization include those of [Sher et al. \(2008\)](#) and [Polanco et al. \(2010\)](#).

2.3 Jet Physics

As previously mentioned sprays generated from typical aerosol cans consist of an alkane-based propellant. The propellant contributes the largest component proportionally of the complex product which is atomized during the spray generation process. The propellant vapour forms what is known as a carrier jet. To understand this fully, a distinction between gaseous jets and liquid jets is made. This section will start with the gaseous carrier jet, looking at the jet regions, an analytic solution and the schlieren methodology for capturing this gas phase. This will then be followed by a detailed analysis of the physics involved with liquid jet formation and breakup. A detailed review of liquid jet breakup is performed as the physics present are important for understanding the generation of ligaments and subsequent droplet generation.

2.3.1 Carrier Jets

Gaseous jets are one type of jet generated by a spray. They are utilised in many industrial applications including ventilation, burners, cooling and gas turbines. Jets are formed when a fluid is injected through an orifice into a surrounding medium,

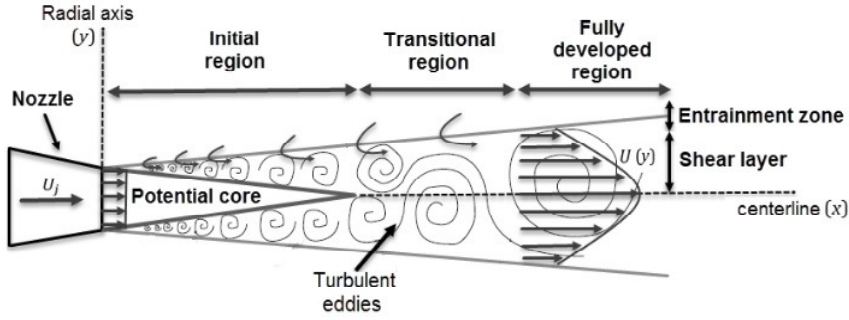


Figure 2.5: The development of a free jet. The regions of development shown are: the potential core (initial) region, transitional region and the self-similar fully developed region. Figure taken from Greco (2018).

with the injected fluid's momentum being relatively greater than that of the medium itself.

The formation of jets can be broken into three regions: the potential core (initial region), transitional region and self-similar (fully developed region), as shown in Figure 2.5. The potential core region for free round jets is usually in the range of $0 \leq \frac{x}{d} \leq 6d$ (Sivakumar et al., 2012) where x is the axial distance and d the nozzle diameter. Sivakumar et al. (2012) used hot wire anemometry to investigate the influence of initial velocity on jet spreading within the jet core region. Sivakumar et al. (2012) showed that scaling the velocity by the mean centerline velocity showed little deviation for radial velocity plots. The transitional region is within the range of $6d \leq \frac{x}{d} \leq 20d$ and the self-similarity region is the final region before the jet eventually becomes unstable and inertial effects cause the jet to collapse.

The decay of the jet can be examined by using momentum conservation to show that the decay of the centerline velocity U_c can be given as,

$$\frac{U_c}{U_i} = \beta \frac{d}{x - x_0}, \quad (2.8)$$

(Hussein et al. (1994), Zou (2001)) where U_i is the initial jet velocity, β the decay constant and x_0 the virtual origin. The decay constant can be found from experimental data and can vary depending on the initial jet conditions including velocity profile and nozzle geometry (Antoine et al., 2001). For a uniform initial profile a

decay constant of $\beta = 6.5$ has been found to fit and for a developed profile the decay constant can be $\beta = 5.6$ (Xia and Lam, 2009).

The self-similar region is coined as such due to the jet velocity profiles having a self-similar Gauss error function form, which was first proposed by Reichardt (1942). The profile is given by

$$\frac{U}{U_c} = e^{-\ln(2)\zeta^2}, \quad \text{with} \quad \zeta = \beta \frac{y}{x - x_0} \sqrt{\frac{2}{\ln 2}}, \quad (2.9)$$

with the self-similar variable being $\frac{y}{x-x_0}$. The self-similar solution is independent of nozzle diameter and so it is considered to have lost all memory of the nozzle.

Visualising these gaseous jets experimentally can be difficult as some gases are transparent and thus invisible to the naked eye. Optical experimental techniques such as shadowgraph and schlieren provide a tool to capture these small non-uniformities in the gas phase. As light passes through non-uniform mediums it is distorted. These distortions can be measured by a refractive index $n_{ind} = \frac{c}{c_0}$ with c_0 the speed of light in a vacuum and c the speed of light through the medium. The refractive index can be related to the density of the medium through the Gladstone-Dale relation,

$$n_{ind} - 1 = k_{GD}\rho \quad (2.10)$$

where k_{GD} is the Gladstone-Dale coefficient and ρ the density of the medium. Assuming an ideal gas medium, Eq. 2.6 shows that the density is dependant on other properties such as temperature and pressure and therefore this Gladstone-Dale coefficient will vary even for a single medium.

Refraction of light beams as they pass through a medium can be described by the beam curvature following

$$\frac{\partial^2 x}{\partial z^2} = \frac{1}{n_{ind}} \frac{\partial n_{ind}}{\partial x} \quad \text{and} \quad \frac{\partial^2 y}{\partial z^2} = \frac{1}{n_{ind}} \frac{\partial n_{ind}}{\partial y} \quad (2.11)$$

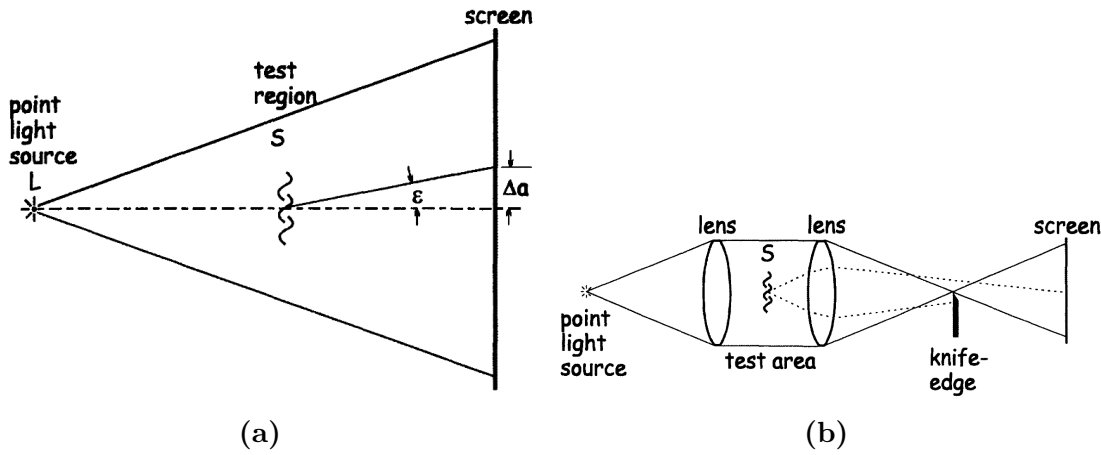


Figure 2.6: A basic representation of a (a) shadowgraph and (b) schlieren setup taken from [Settles \(2012\)](#).

where x and y are perpendicular to the direction of initial ray propagation z . These equations show that the beam curvature, or refraction, is dependant on the gradients of refractive index and forms the basis for the shadowgraph and schlieren techniques.

Shadowgraph experiments capture a shadow whereas schlieren experiments captures a focused image. The key difference between shadowgraph and schlieren is the presence of a knife cut off for schlieren setups, where some of the refracted light is blocked. Schlieren is also more preferable for capturing small details. An example of the setups can be seen in [Figure 2.6](#).

[Settles \(2012\)](#) gives one of the most thorough reviews of shadowgraph and schlieren techniques, describing the different types of setups as well as extensions to the simple methods to allow for capture of further flow details. The review of [Settles and Hargather \(2017\)](#) provides detail on the newest additions to schlieren including background-oriented schlieren, the use of colour filters and schlieren image velocimetry. Schlieren image velocity is where turbulent eddies within the gas jet provide tracers which enable the calculation of the jet velocity. As newer technologies develop, measurements of more intricate spray features are becoming possible.

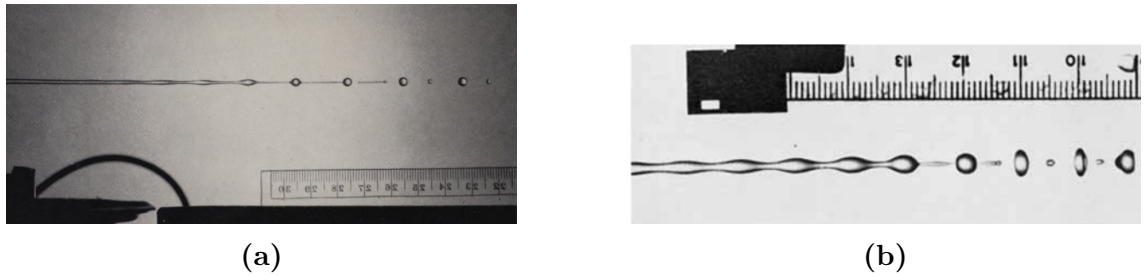


Figure 2.7: Experimental photographs showing the breakup of a viscous jet for a perturbation wavelength of (a) $\lambda = 0.268$, taken from [Donnelly and Glaberson \(1966\)](#) and (b) $\lambda = 0.683$, taken from [Rutland and Jameson \(1971\)](#).

2.3.2 Liquid Jet Breakup

The study of liquid jets can be dated back to 1510, with Leonardo da Vinci’s Codex Leicester ([Da Vinci, 1510](#)). Da Vinci noted that under certain conditions jets can undergo breakup, resulting in droplet formation. In particular, Da Vinci stated that for a running tap, droplet formation occurs when the gravitational forces overcome the “cohesive forces”. These “cohesive forces” are known as surface tension (γ) and are crucial to understanding the pinch-off and hence stability of the jet ([Plateau, 1850](#)).

The work from [Young \(1805\)](#) qualitatively discussed several phenomena linked to surface tension including meniscus within a tube and attraction of floating bodies, but this theory was not formalised mathematically until [Laplace \(1805\)](#), giving the Young-Laplace equation:

$$\Delta p = \gamma \left(\frac{1}{R_1} + \frac{1}{R_2} \right).$$

Here the pressure difference across the interface of two fluids (Δp) is related to the shape of the interface, which can be described by the interface’s axial and radial curvature R_1 and R_2 . The breakup of jets is dominated by the radial curvature ([Eggers and Villermaux, 2008](#)), tending the system to a state of lower surface area. This results in a decreasing radius and eventually results in droplet pinch-off.

The breakup of jets has since been studied extensively. Linear stability analysis has been used to study the effect of perturbations on a jet's stability. [Rayleigh \(1878\)](#) was able to identify critical wavelengths (λ) from which the surface energy increases and therefore breakup occurs fastest. High speed photography was utilised by [Rayleigh \(1891\)](#) to investigate the stability experimentally and allow for observation of the breakup for particular wavelength perturbations. This method was used because breakup occurs spontaneously and is unable to be captured by "ordinary means of observation" ([Rayleigh, 1891](#)). A similar approach was used more recently by [Donnelly and Glaberson \(1966\)](#) and [Rutland and Jameson \(1971\)](#). Here an audio speaker was used to generate specific wavelengths. An example of the breakup can be seen in [Figure 2.7a](#). The breakup shows how the ligaments between swells detach and the swells become spherical droplets. Similarly, [Van Hoeve et al. \(2010\)](#) used high speed photography, which was then compared with a numerical lubrication approximation, showing good agreement between the size of the droplets generated.

The nozzle type and cavitation effects (where local pressure drops below the vapour pressure of the liquid) have also been shown to affect the jet that is generated ([Soteriou et al., 1995](#)). Shear forces from the rough nozzle walls can induce initial instabilities along the jet's surface, which then grow from the interaction with the ambient gas, resulting in jet breakup and droplet generation.

The typical size of the droplets generated from jet breakup can be grouped into four different regimes. These regimes, as detailed in [Reitz \(1978\)](#), are given as (I) Rayleigh, (II) first wind, (III) second wind and (IV) atomization regime. The original classification of these regimes was given by [Ohnesorge \(1936\)](#) and improved to include the distinction between first and second wind regimes ([Reitz, 1978](#)) as seen in [Figure 2.8a](#). These regimes are typically classified in terms of three dimensionless parameters which are fundamental for jet breakup and the resulting dynamics:

- The Reynolds number $\mathbf{Re} = \rho_l \frac{UL}{\mu_l}$, which represents the ratio of inertial to

viscous forces. This is a classical dimensionless parameter arising in many fluid flow problems. A larger Reynolds number corresponds to inertial terms dominating over viscous ones.

- The Weber number $\mathbf{We}_{l,g} = \frac{\rho_{l,g} U^2 L}{\gamma}$, which shows the ratio of inertial to surface tension forces, widely used when looking at droplet dynamics and important when classifying the breakup regimes of a liquid jet. We use the liquid Weber number to classify liquid jet breakup because it captures the dominant inertial effects present.
- The Ohnesorge number $\mathbf{Oh} = \frac{\sqrt{\mathbf{We}}}{\mathbf{Re}} = \frac{\mu_l}{\sqrt{\rho_l \gamma L}}$, which is given as the ratio of viscous to surface tension forces. A larger Ohnesorge number shows that viscous forces have more influence than surface tension forces.

These dimensionless parameters are dependent on fluid and kinematic properties. Here ρ is the density of the fluid, U the characteristic velocity scale (typically the jet's mean velocity), L the characteristic length scale (typically the diameter of the nozzle) and μ the dynamic viscosity of the fluid. Note subscripts l and g indicate liquid and gas phase respectively. The four regimes are detailed below:

I. Rayleigh Regime

The Rayleigh regime typically occurs for jets with a small velocity, resulting in surface tension having the greatest contribution to the breakup of the jet. The jet breaks up due to axisymmetric oscillations along the jet surface (Reitz, 1978) and occurs away from the nozzle. The breakup length has been shown to depend linearly on the jet velocity (Rayleigh, 1878). The resulting droplet size is typically slightly larger than the diameter of the jet (Lefebvre and McDonell, 2017).

II. First Wind Regime

The first wind breakup also occurs away from the nozzle. If we increase jet velocity while keeping the other properties constant (and so increase the Weber number) then the inertial/aerodynamic forces increase (Gordillo and Prez-Saborid, 2005). This change results in a static pressure distribution along the jet surface due to the gas medium and thus enhances the breakup of the jet (Reitz, 1978). The droplets generated are smaller than those of the Rayleigh regime, and are the size of the jet diameter.

III. Second Wind Regime

The second wind breakup occurs closer to the nozzle and is sometimes considered to be the start of the atomization regime. In this regime the aerodynamic forces dominate and create more disturbances along the jet's surface due to the difference in viscosity of the jet and the ambient. The instability generation is known as the Yih instability (Yih, 1967) but commonly attributed to the Kelvin-Helmholtz instability (Kadocsa, 2007). Within this regime the droplets produced from the breakup are much smaller than the diameter of the jet.

IV. Atomization Regime

The final regime is the atomization regime which occurs directly after the jet leaves the nozzle. The mechanisms behind this regime are not fully understood. Originally it was thought that the interaction with the ambient gas was the dominant factor for atomization (Castleman, 1932). For high pressure diesel sprays it has been shown that cavitation and inner nozzle velocity fluctuations dominate the initial jet breakup (Smallwood and Gulder, 2000), which was proposed by Reitz and Bracco (1982). The droplets within this regime are much smaller than the diameter of the jet.

Eggers and Villermaux (2008) cover the physics of jet atomization with the Rayleigh and first wind regimes in great detail, providing derivations of the dispersion relation for capillary instabilities. This aids in understanding the growth of different modes and insight into the fastest growing instability. Control of this breakup is crucial for limiting satellite droplet generation in applications such as ink jet printing.

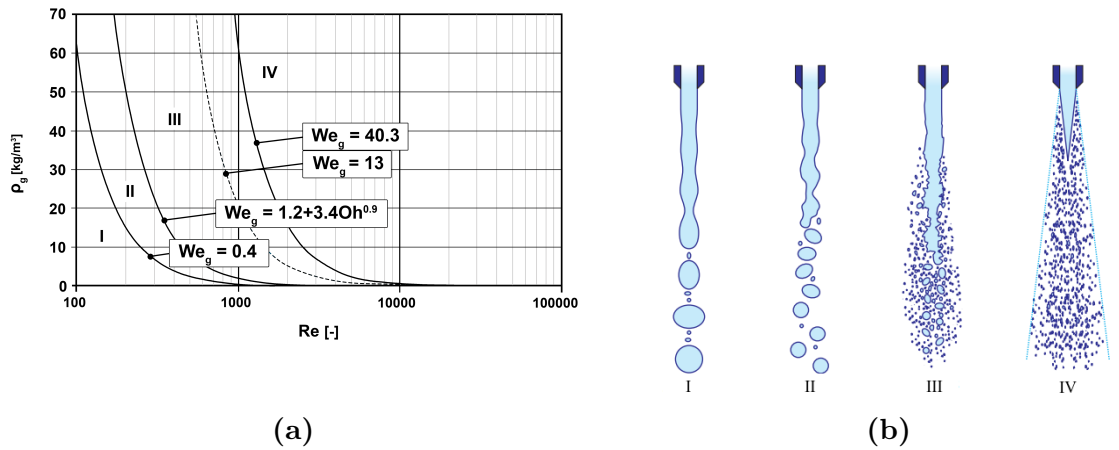


Figure 2.8: (a) Breakup regimes with respect to the density of the ambient gas and Reynolds number. Adapted from Kadocsa (2007). (b) Qualitative look at the four jet breakup regimes, adapted from Schneider (2003).

Figure 2.8a shows a visual representation of the liquid jet breakup regimes and the influence the ambient gas density has on the breakup. With increasing density and a fixed Reynolds number the jet breakup moves towards the higher order regimes due to the greater inertial effects of the ambient gas. This is an important factor within engines due to temperature and pressure variations, and can lead to gas densities in the range of 60-90 kg/m^3 (Imperato et al., 2016). The research to be conducted within this project will be looking at spraying into air with a density of 1.225 kg/m^3 , the approximate density of air at room temperature.

For an aerosol can the diameter of the nozzle is given by $L \approx 0.0005$ m and the jet velocity is approximated to be $U \approx 30$ m/s. The exact properties of

the product within the can are not easily measured due to the complex mixture of propellant and base. This makes it difficult to determine source conditions at the nozzle exit. The two-phase mixture may have a variable density at the nozzle exit influencing the flow rate. Assuming the contents of the can to be alcohol gives liquid jet Reynolds and Ohnesorge numbers of $Re \approx 20000$ and $Oh \approx 0.005$, therefore if the aerodynamic breakup was only considered the jet breakup would be within the atomization regime. These classifications do not consider the flash atomization contribution, which is assumed to dominate, but it appears that assuming the atomization is well within the fully atomized regime is appropriate for sprays generated from deodorant cans.

2.3.3 Primary Atomization

Primary atomization is a complex multi-phase flow phenomenon. Understanding it is crucial to understanding spray generation and the dynamics thereafter. One contribution to primary atomization is the aerodynamic shear interaction with the ambient gas, resulting in Kelvin-Helmholtz instabilities along the jet surface. This instability competes with other factors effecting the jet stability, such as the surface tension of the liquid and the turbulence of the jet (Bower et al., 1988). Much work has been done to investigate the size of the droplets generated from this initial breakup. Rayleigh’s work focused on the Rayleigh regime (Rayleigh, 1879), where the droplets produced from the breakup are relatively uniform (due to surface tension).

Quantitatively the higher order regimes have been investigated to determine the droplet sizes generated and showing that surface tension has less of an effect than in the Rayleigh regime. Merrington and Richardson (1947) experimentally investigated the “mean droplet diameter” generated for a variety of different liquids, noting however that it was not possible to measure the exact droplet size immediately after breakup if in the atomization regime.

There exist several ways of interpreting the “mean droplet diameter”. Within Merrington and Richardson (1947) this “mean droplet diameter” was defined as the droplet size which represents the highest fraction of liquid discharge and is therefore a type of volume-weighted diameter. Other methods found within the literature include the arithmetic mean diameter (D10) (the average of all the droplet diameters); the volume mean diameter (D30) (the diameter of a droplet which represents the total volume of the sample divided by the number of droplets); the mass median aerodynamic diameter (MMAD) (the diameter at which 50% of droplets (by mass) are larger); the Sauter mean diameter (SMD, D32) (the diameter of a sphere with a volume to surface area ratio as a particle of interest); and the De

Brouckere diameter (D43), another volume-weighted mean diameter.

Within the atomization regime the resulting aerosols are typically polydisperse, meaning droplets of different sizes, which is typical of most aerosols (Hinds, 2012). The droplets generated from standard atomisers can be in the range of 1-500 μm (Lefebvre and McDonell, 2017). Typical aerosol nozzles are built in order to generate droplets which are greater than 10 μm . This is due to the fact that if they are less than 10 μm the droplets belong to what is called the thoracic region (US EPA National Center for Environmental Assessment, 1997), where the droplets are capable of passing the larynx and can potentially reach the alveoli of the lungs. Experimental results of Brown et al. (2013) found that the cut off value of 5 μm was more accurate for a child, showing that the bound of 10 μm is a cautious limit. The design of asthma inhalers are designed in such a way that the droplets generated are smaller than this bound. This is because some of the drugs need to be transported deep within the lungs.

Measuring the size of droplets within sprays is not trivial but has been made considerably easier with the advancement of technology and development of new devices. The device used to measure droplet size is however dependent on the size of the droplets intended to be captured. Kulkarni et al. (2011) gives a comprehensive guide of what to use for the various ranges of droplet sizes. Issues can arise when trying to link the measurements from multiple techniques into one measurement and so care is needed when doing so.

Numerical models have also been developed for the different breakup regimes, capturing the breakup of the intact jet into liquid ligaments and then the polydisperse droplets. A thorough analysis by Gorokhovski and Herrmann (2008) identifies the main challenges when modelling primary atomization, with one major problem being the high CPU resources required in order to resolve the multiple length and time scales which are present. The atomization regime is different to the other regimes with the main difference being that the breakup occurs directly at the noz-

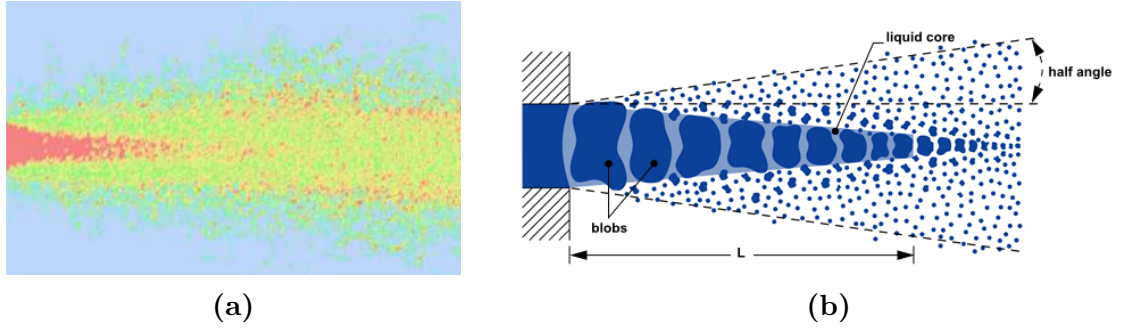


Figure 2.9: (a) The intact core present in the atomization regime, taken from [Bianchi et al. \(2007\)](#). (b) Liquid core approximation with “blobs” and the resulting primary atomization. Taken from [Ansys \(2009\)](#).

zle exit and so no intact jet is present. What is present however is a liquid core which was proposed by [Reitz and Bracco \(1982\)](#). The intact liquid core is present because it has not come into contact with the aerodynamic forces from the ambient gas. The intact liquid core length can be found from [Levich \(1962\)](#),

$$L = C_L d_0 \sqrt{\frac{\rho_l}{\rho_g}}, \quad (2.12)$$

with C_L the Levich constant and d_0 the nozzle diameter.

The numerical models by [de Villiers et al. \(2004\)](#) and [Bianchi et al. \(2007\)](#) aimed to better understand the dominant effects involved in primary atomization. They modelled the nozzle cavitation and turbulence, and captured the jet breakup using the volume of fluid (VOF) method, a method for tracking the interface between immiscible fluids. The work of [de Villiers et al. \(2004\)](#) found that the primary atomization is caused by wave growth on the surface of the jet from the Kelvin-Helmholtz instability. The initial instability however is caused by nozzle turbulence and interface acceleration.

A simpler approach in modelling primary atomisation is to assign turbulence parameters at the nozzle outlet, as done by [Menard et al. \(2006\)](#), and so the inner nozzle flow is not modelled. This method allows for adjustment of the turbulence parameters to achieve different droplet formations but lacks the fully-informed

spray generation (where upstream nozzle flows are modelled). [Menard et al. \(2006\)](#) uses DNS to solve the breakup of the jet which although accurate is too computationally expensive for large parameter studies.

Another approach is to not fully model the primary atomization but instead approximate the initial breakup by applying turbulence parameters, similar to that in [Menard et al. \(2006\)](#), and to then initialise polydisperse droplets at the nozzle exit. This approach can be seen in [Figure 2.9b](#) and is discussed in [Shinjo \(2018\)](#). As the liquid jet is approximated as droplets, a droplet breakup model is used, in particular the Kelvin-Helmholtz Rayleigh-Taylor (KH-RT) model. The jet core instability is described by the WAVE model developed by [Reitz and Bracco \(1982\)](#). Here the solution to the dispersion relation gives the maximum growth rate Ω_{KH} and corresponding wavenumber Λ_{KH} as,

$$\frac{\Lambda_{KH}}{r_j} = 9.02 \frac{(1 + 0.45\text{Oh}^{0.5}) (1 + 0.4\text{Oh}^{0.7}\text{We}_g^{0.35})}{(1 + 0.87\text{We}_g^{1.67})^{0.6}}, \quad (2.13)$$

$$\Omega_{KH} = \left(\frac{\gamma}{\rho_l r_j^3} \right)^{0.5} \frac{0.34 + 0.38\text{We}_g^{1.5}}{(1 + \text{Oh}) (1 + 1.4\text{Oh}^{0.6}\text{We}_g^{0.3})}. \quad (2.14)$$

where r_j is the jet radius. The RT instability is described in a later droplet breakup section.

A distribution function can be used to approximate the sizes of droplets in a polydisperse aerosol and is both cheap (computationally) and requires few parameters. The normal (Gaussian) distribution is the most well-known distribution, but if any bias is present in the droplet sizes this distribution will fail to capture it as it is a purely random distribution. The log-normal distribution occurs widely in nature ([Grnholm and Annala, 2007](#)) and has been shown to give accurate approximations for the size of atmospheric aerosol particles, making it widely accepted in that field ([Heintzenberg, 1994](#)). The gamma distribution has also shown good fits to spray data as seen in [Villermaux \(2006\)](#) and [Almohammed and Breuer \(2019\)](#). The Rosin-Rammler (RR) distribution was first used for powders by [Rosin and Rammler](#)

(1933) but has since been used in atomization models to approximate the size of the droplets generated (Beji et al., 2017), (Ansys, 2009). A method which uses a distribution function for the inlet conditions requires informed spray features and so predicting the flow without prior knowledge of these becomes difficult.

Delmaar and Bremmer (2009) measured droplet sizes from 23 different consumer products in order to validate a chemical exposure model called ConsExpo. Three measurement techniques were used to capture particles of different sizes: laser diffraction using a Mastersizer S (0.5-900 μm), an aerodynamic particle sizer (0.3-20 μm) and an electric low pressure impactor (0.05 - 10 μm). Three of the products of interest were deodorant products. The Mastersizer took measurements 30 cm away from the nozzle and found that droplets within the size range 10-20 μm had the largest volume fraction for two of the three cans. A log-normal distribution was fit and for deodorant cans the mean and standard deviation were found to be 8.3 μm and 0.84 μm respectively.

2.3.4 Nozzle Types and Influence

For different applications a specific type of nozzle atomizer is used. An effective nozzle should work across a range of flow rates providing good quality atomization. Some typical nozzle types include the simple/plain-orifice, simplex/pressure-swirl, fan, rotary, air-assist, air-blast, effervescent atomizers and more (Lefebvre and McDonell, 2017). For deodorant type aerosol cans a simple orifice nozzle and pressure-swirl atomizer are the most standard (Nasr et al., 2013) with basic schematics seen in Figure 2.10.

Simple orifice nozzles work by passing fluid through a small circular opening. As this happens a phenomenon known as cavitation may occur when the local pressure falls below the vapour pressure of the fluid. As mentioned previously, the internal nozzle flows impact the sprays generated and therefore cavitation also influ-

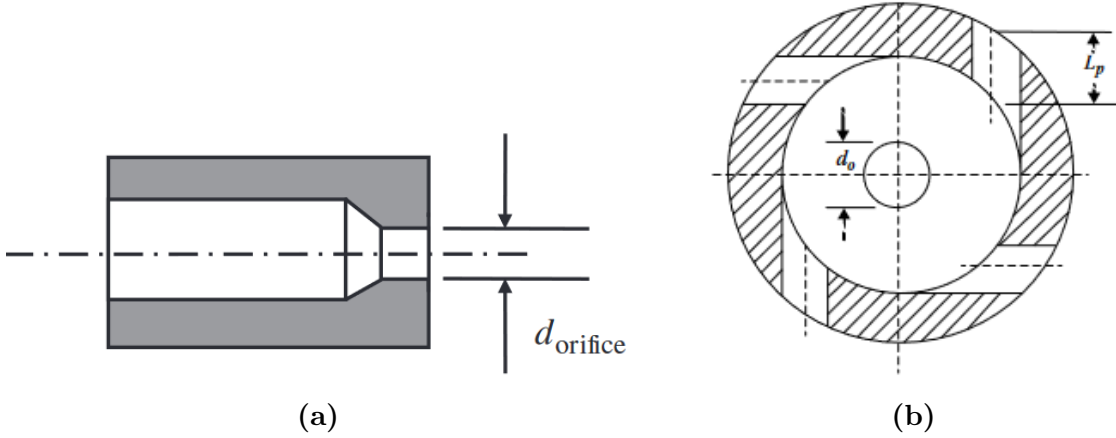


Figure 2.10: (a) Side schematic of a simple orifice nozzle taken from [Marinescu et al. \(2013\)](#) and (b) a front on schematic of a pressure-swirl taken from [Lefebvre and McDonell \(2017\)](#).

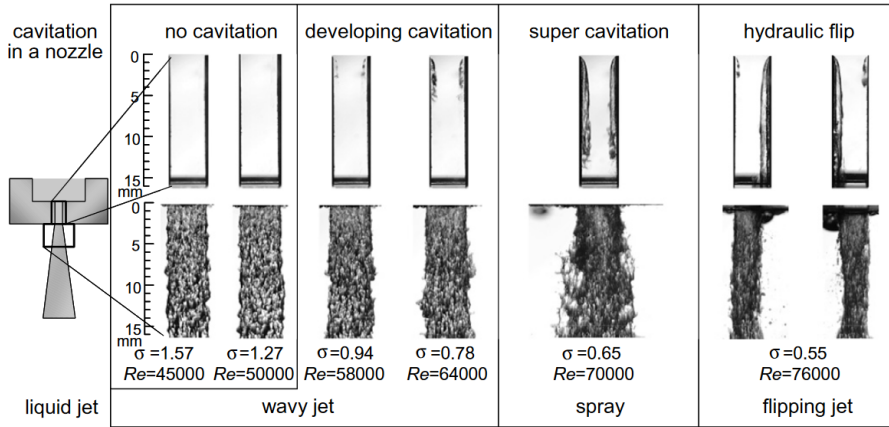


Figure 2.11: Cavitation regimes taken from [Sou et al. \(2007\)](#) for water, showing no-cavitation, cavitation on-set, super cavitation and hydraulic flip.

ences the discharge from the nozzle and the spray generated. There are four stages to cavitation shown in [Figure 2.11](#). Cavitation is determined to occur when the cavitation parameter (K) satisfies $K < -1$, where

$$K = \frac{P_{loc} - P_{amb}}{P_{amb} - P_v} \quad (2.15)$$

with P_{loc} the local pressure, P_{amb} the ambient pressure and P_v the vapour pressure. Once the cavitation reaches the nozzle exit, hydraulic flip occurs (see [Figure 2.11](#)).

The change in nozzle discharge can be determined by the discharge coefficient C_d , the ratio of mass flow rate to the maximum mass flow rate ([Sun et al.](#),

2019),

$$C_d = \frac{\dot{m}}{A\sqrt{2\rho_l(P_{inj} - P_{amb})}}, \quad \text{with } \dot{m} = U\rho_l A, \quad (2.16)$$

where A is the nozzle area, P_{inj} the upstream injection pressure and U the flow velocity. The contraction of the liquid cross-sectional area due to cavitation can be found using the fit of [Nurick \(1976\)](#)

$$C_{con} = \left(\frac{1}{C_{ct}^2} - \frac{11.4r_{cur}}{d_0} \right)^{-\frac{1}{2}} \quad (2.17)$$

with r_{cur} the radius of curvature of the internal nozzle opening and $C_{ct} = 0.611$ the constant for a fully flipped nozzle flow. [Schmidt and Corradini \(1997\)](#) found that the exit velocity U for cavitating nozzles and fully flipped nozzles can be described as

$$U_{cav} = \frac{2C_{con}P_{inj} - P_{amb} + (1 - 2C_{con})P_v}{C_{con}\sqrt{2\rho_l(P_{inj} - P_v)}} \quad \text{and} \quad U_{flip} = \frac{\dot{m}}{\rho_l C_{con} A} \quad (2.18)$$

respectively where C_{con} is the contraction relation of [Nurick \(1976\)](#).

Pressure-swirl atomizers result in a different structure at the nozzle exit. Here a thin circular film forms around an air core, due to the centrifugal motion. The mass flow rate of pressure-swirl nozzles is calculated using

$$\dot{m} = \pi\rho_l U l_{film} (d_0 - l_{film}) \quad (2.19)$$

where l_{film} is the film thickness. Here the exit velocity (U_{exit}) depends on the nozzle structure and is not trivially calculated. The formula from [Han et al. \(1997\)](#) gives the exit velocity as

$$U_{exit} = k_v \sqrt{\frac{2(P_{inj} - P_{amb})}{\rho_l}} \quad (2.20)$$

where the velocity coefficient k_v is dependant on nozzle characteristics and pressure differences ([Lefebvre and McDonell, 2017](#)). Before cavitation occurs, a value of $k_v = 0.78$ has been found appropriate whereas a value of 0.6-0.7 is appropriate

during cavitation (Lichtarowicz et al., 1965).

Lefebvre and McDonell (2017) discuss many simple correlations for predicting the SMD of droplets generated from different nozzle types, including that of plain office nozzles and pressure swirl nozzles. Merrington and Richardson (1947) experimentally found that for fluids injected through a plain circular orifice into a quiescent ambient, that the SMD can be given by,

$$SMD = \frac{500d_0^{1.2}\nu^{0.2}}{U}, \quad (2.21)$$

with d_0 the orifice diameter and U the jet velocity. As the velocity of the release decreases the correlation was shown to break down and a limiting droplet size was reached.

Further correlations have been generated for other nozzle types and also to take into account ambient conditions and pressure drop (Lefebvre and McDonell, 2017). Care is needed when using SMD correlations as they are fit to specific conditions and therefore use outside those conditions is not advised.

2.4 Droplet Physics

The physics of transporting droplets is critical to understanding the final carry-over phase. Examples of the different physical components that might play a role when modelling the spray procedure include droplet trajectories, droplet collisions, evaporation and wall-impact.

2.4.1 Secondary Atomization

Secondary atomization looks at the breakup of the droplets generated from the primary atomization phase. This secondary breakup has been found to be important to the spray dynamics and overall structure of the spray (O'Rourke and Amsden, 1987). Droplets will deform if the aerodynamic forces exceed the surface tension forces (Bower et al., 1988) where the ratio of forces, as mentioned in section 2.1, can be represented by the Weber number. Once the Weber number exceeds $We > 1$ deformation of the droplet can be seen.

One of the first experiments that looked at droplet breakup was that of Lane (1951). Here droplets ranging from 0.5 mm to 5 mm fell under gravity through a vertical wind-tunnel and the breakup identified was described as “a hollow bag anchored to a rim” (Lane, 1951). A range of experiments were conducted after those of Lane, looking at variations in flow and droplet sizes (e.g Nicholls and Ranger (1969), Temkin and Mehta (1982)). Pilch and Erdman (1987) collected data from the related literature and identified five different regimes of breakup which can be seen in Figure 2.12. The description of the droplet breakup from Lane (1951) can be identified as being in the bag breakup regime. Further experimental work was performed and found agreement with the regions and the breakup type (Liu et al., 1993).

The transition point at which droplet breakup occurs was also identified

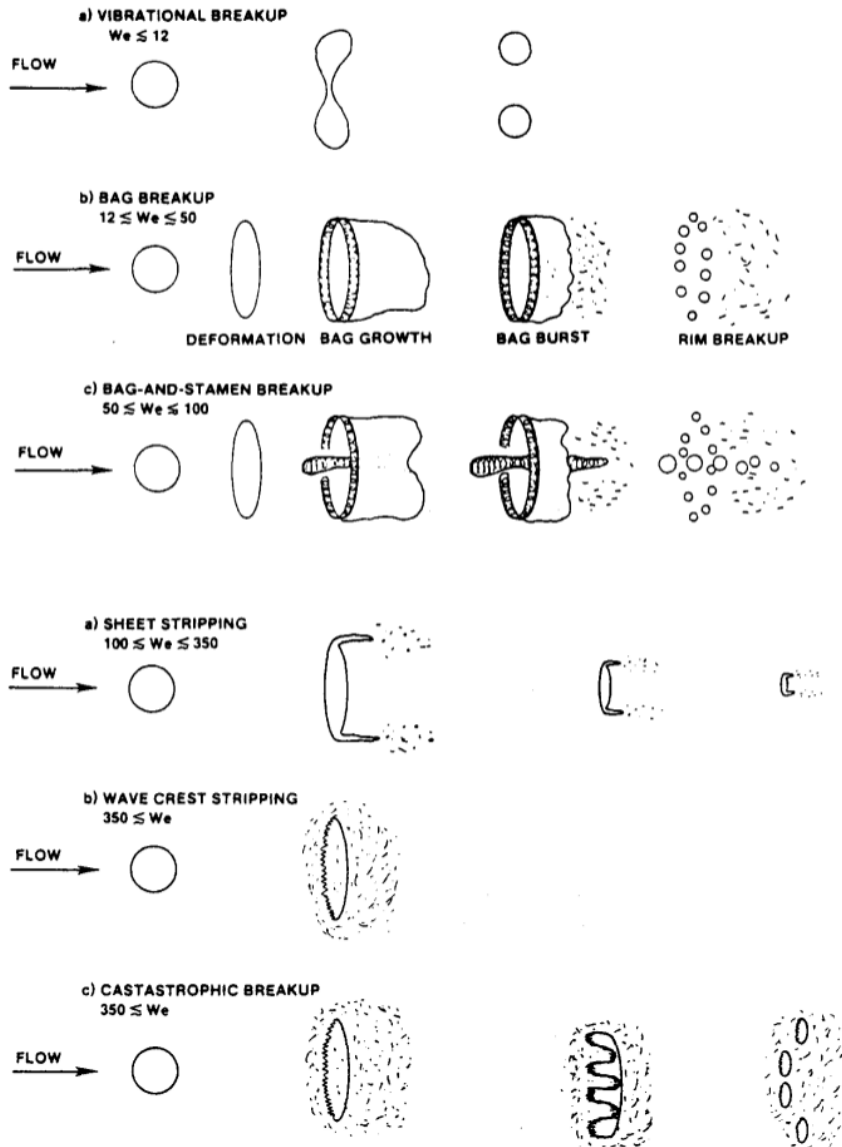


Figure 2.12: The five different regimes of droplet breakup classified in terms of Weber number. Figure taken from [Pilch and Erdman \(1987\)](#).

by [Pilch and Erdman \(1987\)](#) and is known as the critical Weber number (We_C). [Majithia et al. \(2008\)](#) investigated viscous effects on this critical Weber number and found that for an increase in Ohnesorge number there was an increase in the critical Weber number, agreeing with Brodkey's correlation and the theoretical work of [Hinze \(1955\)](#). Viscosity therefore plays a part in secondary atomization.

There exist several models for secondary atomization. The Taylor analogy breakup (TAB) model of [O'Rourke and Amsden \(1987\)](#) was one of the first breakup models developed. The TAB model claims that the breakup of a droplet is analogous

Spring-mass system	Droplet breakup
External forces (F)	Droplet drag forces
Restoring force (kx)	Surface tension forces
Damping force ($d\dot{x}$)	Viscous forces

Table 2.2: Analogy of spring-mass forces to that fluid forces governing droplet breakup in the TAB breakup model.

to that of an oscillating spring and is governed by the spring-mass damped oscillator equation,

$$F - kx - d\dot{x} = m\ddot{x}, \quad (2.22)$$

which was first proposed by [Taylor \(1963\)](#). The analogous components of the two systems can be seen in [Table 2.2](#). The variable x is defined as the distance the droplet's equator has moved from its equilibrium state and the constants are defined as,

$$\frac{F}{m} = C_F \frac{\rho_g u_d^2}{\rho_l r}, \quad \frac{k}{m} = C_k \frac{\gamma}{\rho_l r^3} \quad \text{and} \quad \frac{d}{m} = C_d \frac{\mu_l}{\rho_l r^2}, \quad (2.23)$$

where u_d is the relative droplet velocity and r the droplet radius. The values of the dimensionless constants $C_{k,d,F}$ are taken to fit experimental results and also the theoretical results of [Lamb \(1932\)](#) with $C_k = 8$, $C_d = 5$ and $C_F = \frac{1}{3}$. A droplet is then said to breakup if the oscillations grow to a size of $x > C_b r$, where C_b is taken to equal 0.5.

The model constants are sometimes varied for the application, with [Ashgriz \(2011\)](#) describing a value of $C_k = 6$ being more appropriate for gasoline injection applications. [Joshi et al. \(2021\)](#) investigated the influence of varying these constants, subject to the theoretical constraints of [Lamb \(1932\)](#), and investigated the influence on breakup time and daughter droplet velocity. [Joshi et al. \(2021\)](#) provides a way of selecting values for the constants for the given application suggesting care is needed when selecting the model constants.

By performing a change of variables $\left(y = \frac{x}{C_b r}\right)$ on [\(2.22\)](#) and substituting

the coefficients in (2.23) an equation for the non-dimensional distortion y is obtained,

$$\frac{d^2 y}{dt^2} = \frac{C_F \rho_g u^2}{C_b \rho_l r^2} - \frac{C_k \sigma}{\rho_l r^3} y - \frac{C_d \mu_l}{\rho_l r^2} \frac{dy}{dt}. \quad (2.24)$$

The size of the resulting droplets is calculated by equating the energy of the parent droplet to the total energy of the resulting daughter droplets. The velocity of the daughter droplets is then prescribed a normal contribution dependent on the current velocity of the parent droplet. For high Weber ($We > 100$) number flows the interaction with the ambient gas becomes very important, resulting in other oscillation modes other than the fundamental mode playing a major role. This makes the spring analogy fail for large Weber number spray systems.

A secondary atomization model which incorporates the disturbances along the surface of the droplets is the Kelvin-Helmholtz Rayleigh-Taylor (KH-RT) breakup model by [Beale and Reitz \(1999\)](#) and [Patterson and Reitz \(1998\)](#). This model builds on the primary atomization WAVE model of [Reitz and Bracco \(1982\)](#), described previously. The KH-RT model derives similar maximum growth rate (Ω_{RT}) and corresponding wavenumber (Λ_{RT}) relations due to the RT instabilities, generated due to the acceleration of the droplets into the ambient. These relations are given by,

$$\Lambda_{RT} = \sqrt{\frac{-g_t (\rho_p - \rho_g)}{3\gamma}}, \quad \Omega_{RT} = \sqrt{\frac{2 (-g_t (\rho_p - \rho_g))^{1.5}}{3\sqrt{3\gamma} (\rho_p + \rho_g)}}. \quad (2.25)$$

The KH-RT model models the core breakup based on the KH instabilities whereas outside the core both the KH and RT instabilities are taken into account. Typically for high Weber numbers, the fastest growing wave is due to the RT instability.

2.4.2 Droplet Trajectories

This section introduces some of the typical approaches used to model a particle/droplet-laden flow, the type of flow generated from a deodorant type aerosol can. It also

introduces the particle force balance equation, which is fundamental in predicting the trajectories of the droplets generated. A particle/droplet-laden flow is a two-phase flow system where one phase is continuous and the other can be thought of as a particle/droplet phase. The continuous phase or carrier flow is seen in an Eulerian framework where the flow is analysed through space and time. The particle phase is typically seen in a Lagrangian framework where the individual droplets are tracked. The interactions of the droplets between themselves and with the carrier flow then govern the trajectories of individual droplets. These interactions can be considered in terms of various couplings: one-way, two-way and four-way.

One-way coupling considers a droplet phase which is only influenced by the Eulerian phase and so the droplets can be considered as tracer particles for the continuous phase. Two-way coupling allows both phases to interact with one another through their interface. Here the continuous phase is subject to influence due to the presence of the droplets. Four-way coupling is the most advanced, where the droplets now interact with one another whilst also considering the effects from two-way coupling. The effect of the droplets on the turbulence is also important and is detailed in [Elghobashi \(1994\)](#) for the different types of coupling.

Higher order couplings increase the computational cost of the simulation, this is because more interactions between the continuous and discrete phase are accounted for. Similarly, by including droplet-droplet interactions (four-way coupling) there are a possible $\mathcal{O}(N^2)$ interactions to account for. Typically with large droplet count systems four-way coupling is not viable or an efficient algorithm is needed to reduce the number of droplet-droplet calculations. This is discussed further in §2.4.3.

The velocity of a particle can be found by integrating the particle force balance equation,

$$\frac{du_i^p}{dt} = F_D(u_i - u_i^p) + g_i \frac{(\rho_p - \rho)}{\rho_p} + \frac{F_i}{\rho_p}. \quad (2.26)$$

Here the inertia of the droplet is equated to the forces acting on the droplet. The terms on the right-hand side (from left to right) are the drag, gravitational and additional forcing terms with u_i^p and u_i the particle velocity and carrier flow velocity in the i^{th} direction, F_D the drag force on the droplet, g_i the i^{th} component of gravity and ρ_p and ρ the particle and carrier flow density. The particle trajectory is then found by integrating the force balance equation with respect to time,

$$\frac{d\mathbf{x}_p}{dt} = \mathbf{u}_p. \quad (2.27)$$

The drag force for spherical particles is given as,

$$F_D = \frac{18\mu C_D \text{Re}}{\rho_p d_p^2} \frac{C_D \text{Re}}{24} \quad \text{with} \quad \text{Re} = \frac{\rho |\mathbf{u} - \mathbf{u}_p| d_p}{\mu} \quad (2.28)$$

Here ρ_p is the density of the particle, d_p the particle's diameter, Re the droplet Reynolds number (with length scale as the droplet diameter and velocity scale as the relative velocity of the carrier flow and droplet) and C_D the drag coefficient. The drag coefficient has been shown to be highly dependent on Reynolds number and the shape of the droplet. For a fixed Reynolds number of $\text{Re} = 10^6$ the drag coefficient is 0.47 for a smooth sphere and 1.28 for a 3D flat plate perpendicular to the flow direction. If we take the body to be a smooth sphere then by varying the Reynolds number from $10^5 - 10^6$ the drag coefficient ranges from 0.1 - 0.47. This variation in drag coefficient must be taken into account. For a smooth spherical droplet the drag coefficient can be approximated by,

$$C_D = a_1 + \frac{a_2}{\text{Re}} + \frac{a_3}{\text{Re}^2} \quad (2.29)$$

where the coefficients a_i for $i=1,2,3$ are taken from [Morsi and Alexander \(1972\)](#).

For sub-micron droplets the Cunningham correction factor ([Cunningham and Larmor, 1910](#)) for the drag must be taken into account. This is because the

Knudsen number (Kn - the ratio of mean free path to a representative physical length scale) becomes too large, $\text{Kn} > 10$ (Laurendeau, 2005). This is when the continuum approximation begins to fail and the no-slip condition on the droplets is no longer appropriate. The Cunningham correction factor is given as

$$C_c = 1 + \frac{2\lambda}{d} \left(A_1 + A_2 e^{-\frac{A_3 d_p}{\lambda}} \right) \quad (2.30)$$

with λ the mean free path and experimentally derived constants, A_1, A_2 and A_3 equal to 1.257, 0.4 and 0.55 respectively. The Stokes-Cunningham drag law should be employed for sub-micron droplets with the drag force given as

$$F_D = \frac{18\mu}{d_p^2 \rho_p C_c}. \quad (2.31)$$

Deformation of the droplet results in changes to the forces acting on the droplet and, in particular, the drag force. If the Weber number is sufficiently large the droplets become so distorted that they appear as disks. A dynamic drag model has to then be implemented to account for this distortion. Liu et al. (1993) use a drag coefficient given as,

$$C_D = C_{D,sphere} (1 + 2.632y), \quad (2.32)$$

where y is the droplet distortion governed by the TAB distortion equation (2.24).

2.4.3 Droplet Collisions

The literature is not scarce of work on droplet collisions. The effects of droplet collisions within clouds and within diesel sprays have been heavily researched (Testik et al. (2011), Ashgriz and Poo (1990)), and give great insight into the physics of these systems, aiding in the development of sophisticated numerical models. Typically collisions involving just two droplets are investigated and form the basis of many

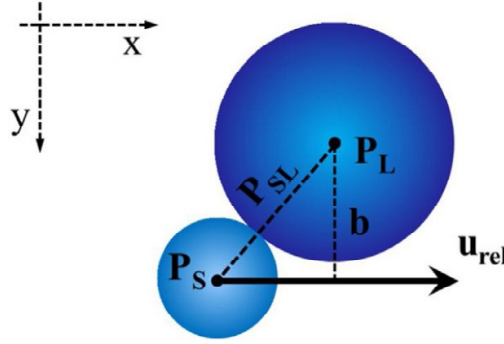


Figure 2.13: The collision of two droplets with different sizes P_s and P_L . The lateral displacement of the droplets' centroids is denoted by b and the relative velocity within the plane as U_{rel} . Figure taken from [Sommerfeld and Pasternak \(2019\)](#).

numerical models. The non-dimensional numbers important for droplet collisions are the Reynolds, Ohnesorge and Weber numbers. The characteristic velocity and length scales however are now different. The important velocity scale is the relative velocity between the colliding droplets and the length scale used is the size of the smallest droplet. Other important parameters are the impact parameter (B) and the ratio of the colliding droplets' diameters, which are given as

$$B = \frac{2b}{d_S + d_L} = \sin \phi \quad \text{and} \quad \Delta = \frac{d_S}{d_L} \quad (2.33)$$

respectively. Here b denotes the lateral displacement of the droplets' centroids as seen in Figure 2.13. During the transportation of the product the droplets generated have a probability of colliding with one another. By increasing the number of droplets, naturally the rate of collisions increases.

When droplets collide there are four main regimes: bouncing, coalescence, stretching separation and reflexive separation. A collision map example can be seen in Figure 2.14. Here the dividing lines between regimes are found either theoretically or experimentally. Alkanes have been found to change this collision map with an extra “slow” coalescing region for $B < 0.6$ and $We < 5$ ([Sommerfeld and Pasternak, 2019](#)). Experimental studies have been performed to determine each region, such as those of [Ashgriz and Poo \(1990\)](#) and [Al-Dirawi and Bayly \(2020\)](#).

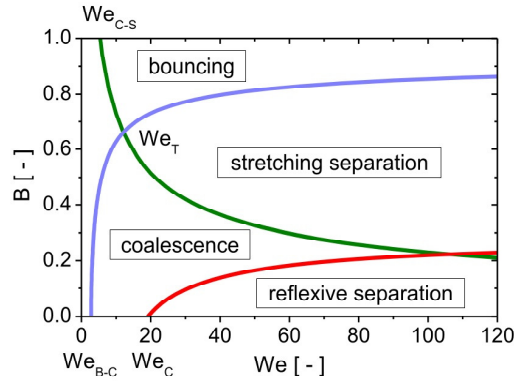


Figure 2.14: An example of a collision phase diagram where the Weber number is plotted against the impact parameter. The four different collision regimes along with an example of their regime-dividing lines can be seen. Taken from [Sommerfeld and Pasternak \(2019\)](#)

For spray regions near the nozzle, where high inertial forces can be seen, the Weber numbers are so high that coalescing has a low probability of occurring. Moving further downstream or even after impacting onto the surface, the different regimes play particular importance in the fate of the droplets.

For numerical models the effect of droplet collisions is needed when considering a four-way coupled system and therefore the theoretical understanding of colliding droplets is needed. There are three main groups of collision models: deterministic, stochastic and deterministic-stochastic. Each of these models must detect the collision and determine the type of collision.

A deterministic model considers the size and the trajectories of the droplets, checking for an intersection during the current simulation time-step. The droplets are then said to collide and criteria for the type of collision can be prescribed using theory from the literature. The deterministic models are very time consuming for systems with large numbers of droplets. This is because each pair of droplets must be inspected giving $O(N^2)$ calculations. Deterministic-stochastic models like that of [O'Rourke \(1981\)](#) track parcels rather than individual droplets. These models use a random number criteria to determine if two parcels within the same mesh cell collide. This model is clearly sensitive to the resolution of the mesh used and clustering of

parcels on the corners of cells has been observed (Sommerfeld and Pasternak, 2019). Stochastic models do not require knowledge of neighbouring parcels but instead use local droplet properties. Random number criteria is again used to determine if a collision occurs. The main benefit of these models is their increased efficiency over the deterministic models.

2.4.4 Droplet Evaporation

During the entire spray procedure of deodorant type aerosol cans the mixture of propellant and product is evaporating. Evaporation is considered a phase transition from a liquid to a gas. The liquid molecules gain enough energy to overcome their inter-molecular forces and thus escape into the ambient medium. This process involves both heat and mass transfer at the interface of the droplet. Some factors that influence the evaporation of droplets include the vapour pressure, temperature and relative velocity with the ambient gas. Understanding evaporation is important as it enhances the breakup of liquid jets (Eggers and Villermaux, 2008) and alters spray features. Experimentally it has been seen that a single droplet will heat up until a steady state is reached, at which point the square of the diameter decays linearly with time (Lefebvre and McDonell, 2017). This can be modelled by the d-squared law,

$$d_0^2 - d^2(t) = \beta_v t, \quad (2.34)$$

where d_0 is the initial diameter and β_v the evaporation constant.

Convective and diffusive transport of the evaporated mass are the two important modes of vapour transport. This coupled with heat effects give the important dimensionless parameters for evaporation as:

- The Nusselt number $\mathbf{Nu} = \frac{h}{L/k}$, the ratio of convective heat transfer to conductive heat transfer, where h is the convective heat transfer coefficient, L the

characteristic length scale and k the thermal conductivity of the outer fluid. The Nusselt number appears in spray cooling (Hnizdil et al., 2016) and in areas where heat transfer across an interface is observed (Herwig, 2016).

- The Sherwood number $\mathbf{Sh} = \frac{k_c}{D/L}$, the ratio of convective mass transfer rate to diffusive rate, with k_c the convective mass transfer coefficient and D the mass diffusivity. The Sherwood number appears in sediment flows and flows involving the transport of mass (Murzin and Salmi, 2005).
- The Schmidt number $\mathbf{Sc} = \frac{\mu}{\rho D}$, the ratio of viscous diffusion rate to the mass diffusion rate. Here μ is the dynamic viscosity and ρ the fluid density.
- The Prandtl number $\mathbf{Pr} = \frac{c_p \mu}{k}$, the ratio of momentum diffusivity to thermal diffusivity, with c_p the specific heat of the fluid.

For dense regions of sprays where clusters of droplets are located it has been shown that diffusion effects dominate evaporation. For regions with fewer clusters convection plays a more significant role (Bellan and Harstad, 1987).

Models for evaporation can vary over several degrees of complexity. Ashgriz (2011) summarises the different evaporation models found in Sirignano (2010) into six groups:

1. The temperature of the droplet is kept constant during evaporation.
2. The temperature of the droplet changes while remaining uniform across the droplet.
3. The heating throughout the droplet is considered time-dependent.
4. The conductivity inside the droplet is taken into account.
5. The heating is affected by the internal flow of the droplet.
6. Solutions of the Navier-Stokes equations are used.

The level of complexity is important for modelling the evaporation of the droplets in numerical models and the physics relevant to the scenario of interest. Sprays have a large number of droplets resulting in an additional consideration, the computational cost of the model.

[Sazhin \(2014\)](#) details two of the simplest models, Maxwell's evaporation model and the Stefan-Fuchs model. Maxwell models mass transfer for a spherical droplet when considered purely diffusive, and is given by,

$$\frac{dm_p}{dt} = -A_p M_w N \quad (2.35)$$

with: m_p the droplet mass; $A_p = 4\pi r_d^2$ the droplet's surface area; M_w the molecular weight of the evaporating species; $N = k_c (C_s - C_\infty)$ the difference in species vapour concentration at the surface of the droplet (C_s) and in the bulk of the ambient medium (C_∞); and k_c the convective mass transfer coefficient. Note when the ambient vapour concentration is greater than the surface vapour concentration the rate of change of droplet mass is positive leading to condensation onto the droplet. Similarly when $C_s > C_\infty$ the rate of change of droplet mass is negative and thus evaporation occurs. The vapour concentrations ($C = \frac{n}{V}$) can be found from the ideal gas law $pV = nRT$ giving,

$$C_s = \frac{p_{sat}(T_p)}{RT_p}, \quad C_\infty = X \frac{p}{RT_\infty}.$$

where p is the local ambient pressure, $R = 8.314$ J/mol/K the universal gas constant, X the mole fraction of the species in the bulk, and the partial pressure at the surface of the droplet is assumed to be the saturation vapour pressure (P_{sat}).

Here the convective mass transfer coefficient can be found by the Ranz-Marshall correlation ([Ranz and Marshall, 1952](#)) given by:

$$\text{Sh} = \frac{d_p k_c}{D_m} = 2 + 0.6 \text{Re}_d^{\frac{1}{2}} \text{Sc}^{\frac{1}{3}},$$

giving,

$$k_c = \frac{D_m}{d_p} \left(2 + 0.6 \text{Re}_d^{\frac{1}{2}} \text{Sc}^{\frac{1}{3}} \right),$$

where D_m is the mass diffusivity.

Considering a droplet of a volatile liquid, and thus one where the evaporation rate is large, results in the diffusion model not accurately capturing the change in droplet mass. The evaporation model must also account for the advection of species vapour away from the surface of the droplet. This advection is known as Stefan flow. The mass transfer equation taking into account Stefan flow is then given by

$$\frac{dm_p}{dt} = -k_c A_p \rho \ln(1 + B_m) \quad (2.36)$$

where B_m is the Spalding mass number given by,

$$B_m = \frac{Y_s - Y_\infty}{1 - Y_s}. \quad (2.37)$$

Here Y_s is the mass fraction of species at the surface of the droplet, and Y_∞ the mass fraction of species in the ambient. This is known as the Stefan-Fuchs evaporation model.

As the droplet evaporates energy is used in changing phase resulting in cooling of the droplet. This is known as latent heat. Other thermal factors which may affect the temperature of the droplet are heat exchanges with the ambient and possible radiative effects. Taking these factors into account allows the droplet temperature T_p to be governed by the ODE,

$$m_p c_p \frac{dT_p}{dt} = \underbrace{h A_d (T_\infty - T_p)}_{\text{Convective}} + \underbrace{\varepsilon_d A_d \sigma_{SB} (\theta_R^4 - T_p^4)}_{\text{Radiation}} + \underbrace{\frac{dm_d}{dt} h_{fg}}_{\text{Latent loss}} \quad (2.38)$$

where m_d is the mass of the particle, c_p the heat capacity of the droplet, A_d the surface area of the droplet, T_∞ the local continuous phase temperature, h the convective heat transfer coefficient, ε_d the particle emissivity, σ_{SB} the Stefan-Boltzmann

constant, θ_R the radiation temperature and h_{fg} the latent heat. The governing ODE lacks any internal resistance of the droplet to changes in temperature so a uniform droplet temperature is assumed, falling into group 2 of evaporation models.

The convective heat transfer coefficient can be found from the Ranz-Marshall correlation of the Nusselt number ([Ranz and Marshall, 1952](#)),

$$\text{Nu} = \frac{hd_p}{k} = 2 + 0.6\text{Re}^{1/2}\text{Pr}^{1/3},$$

giving,

$$h = \frac{k}{d_p} \left(2 + 0.6\text{Re}^{1/2}\text{Pr}^{1/3} \right).$$

2.4.5 Droplet-Wall Interaction

Spray-wall impact is critical in many applications such as spray coating, combustion and cleaning. The carry-over of droplets from the surface is determined by the prior impact onto the target surface and the flow field the droplet re-enters. To understand how sprays impact onto walls and thus understand carry-over one must first understand how the individual droplets impact onto walls. Droplets can exhibit several impact types such as depositing, bouncing and splashing. The impact type is determined by several properties: the droplet's viscosity, surface tension, density, velocity, temperature and size, as well as the wall's temperature, wetting and roughness.

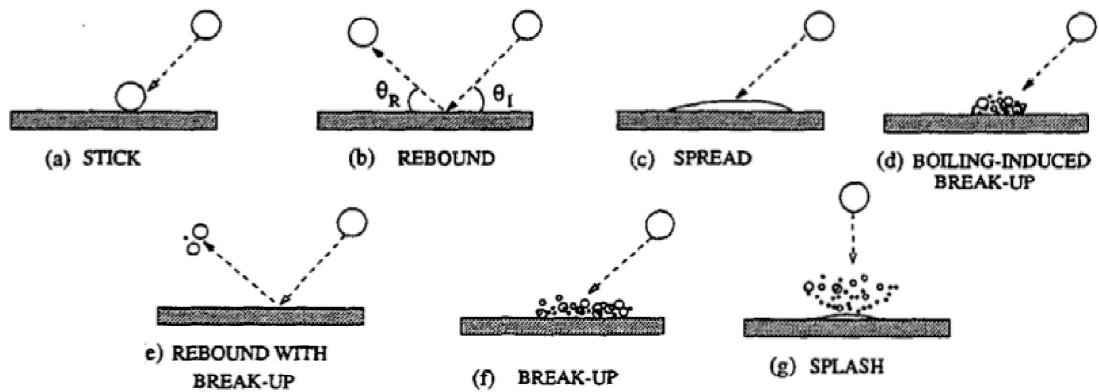


Figure 2.15: Regimes of droplet impact, figure adapted from [Bai and Gosman \(1995\)](#)

[Josserand and Thoroddsen \(2016\)](#) present a detailed review of droplet impacts on solid surfaces and [Yarin \(2006\)](#) gives a review on droplet impact on liquid surfaces. The main regimes can be classified as shown in Figure 2.15. The critical parameters used to determine the regime are the impact energy (E) and wall temperature (T_{wa}). For dry walls the regimes and criteria are taken from [Bai and Gosman \(1995\)](#) and are as follows:

- a. The droplet **sticks** to the wall when the impact energy is small and the temperature of the wall is below the adhesion temperature.

- b. The droplet will **bounce** if a vapour film is present between the droplet and the wall. This occurs if the wall temperature is greater than the defined rebound temperature.
- c. **Spreading** occurs when the impact energy of the droplet is greater than the stick energy and the temperature of the wall is less than the adhesion temperature.
- d. The droplet will breakup from **boiling** if the wall reaches a temperature corresponding to its maximum evaporation rate.
- e. The droplet will **rebound with break-up** if the droplet rebounds off a hot surface and then undergoes breakup.
- f. The droplet will **break up** if the droplet spreads on the wall and thermo-instabilities result in droplet breakup.
- g. The final breakup is **splash** which occurs for droplets with larger impact energies.

Other examples of droplet impact models are the Stanton-Rutland model ([Rutland and Jameson, 1971](#)), where impact energy and wall temperature are also used to determine the impact regime, and the Kuhnke model ([Kuhnke, 2004](#)), where a non-dimensional parameter based on fluid properties and the wall temperature are used to determine the breakup regimes.

One of the simplest of models for droplet wall interaction is the inelastic collision model where rebound is calculated but the other more physically complicated regimes are not. For inelastic collision models detail of the coefficients of restitution are needed. Figure [2.16](#) shows the impacting and rebounding velocities of a droplet impacting a flat wall. Given coefficients of restitution ($R_{N,T,v,\alpha}$), which are critical to this inelastic collision modelling approach, the impact velocity (subscript

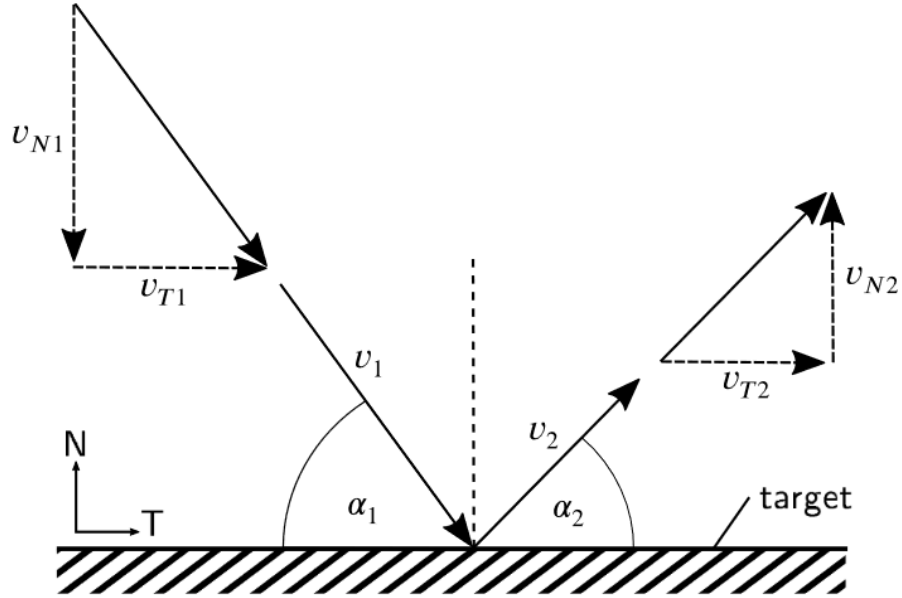


Figure 2.16: Droplet-wall collision model taken from [Sommerfeld et al. \(2021\)](#).

1) can be related to the rebound velocity (subscript 2) by,

$$R_N = \frac{v_{N2}}{v_{N1}}, \quad R_T = \frac{v_{T2}}{v_{T1}}, \quad R_v = \frac{v_2}{v_1}, \quad \text{and} \quad R_\alpha = \frac{\alpha_2}{\alpha_1}. \quad (2.39)$$

These coefficients are typically determined by experiments. [Sommerfeld et al. \(2021\)](#) details an experimental approach of calculating coefficients of restitution. Here particle image velocimetry (PIV) was used to calculate the particle velocities.

2.5 CFD Modelling

CFD (Computational Fluid Dynamics) modelling has become a vastly researched area following improvements in computational power, efficiency and numerical techniques. These improvements have allowed for simulation of highly complex flows in both 3D and, where simplifications are possible, 2D. CFD has been used to model a wide range of fluid flow problems, in particular spray systems, with some examples previously mentioned. It is possible to apply CFD modelling to the problem of deodorant-type sprays, modelling both the continuous phase of the carrier jet and

the discrete phase of the droplets generated. This section describes some of the available CFD techniques for modelling these spray systems.

The typical process of generating a functional CFD model is to first identify the problem of interest as well as relevant physics and governing equations. A representative geometry of the problem is then generated for the computational domain. Once the geometry is generated a computational mesh is constructed which splits the domain into small control elements on which the governing equations are solved. Generating a suitable mesh, which resolves the important physics at the necessary length scales, can be a time-consuming process. Typically the mesh generation procedure will go through several iterations of solving the governing equations and improving the quality of the mesh until the necessary mesh refinements are made.

There are several commercial CFD packages available to solve the governing equations, examples include Fluent, CFX, STARCCM+, COMSOL, SIMSCALE, FLOW3D and more. There are benefits and drawbacks for each, and some of the software provide a full suite of geometry generation, mesh generation, equation solving and post-processing capabilities. An example of a piece of open source CFD software is OpenFOAM where the main benefit is the easy accessibility to the program and no need for license fees, however, OpenFOAM has a steep learning curve and open source packages can be developed in an uncontrolled environment. ANSYS Fluent is one of the most commonly used CFD packages. Fluent v19.2 is the particular version used in this study on sprays generated from deodorant-type aerosol cans.

2.5.1 Conservation of Mass and Momentum

The incompressible Navier-Stokes equations are fundamental equations for modelling the mass and momentum conservation of fluid flows. They are given as

$$\frac{\partial \rho}{\partial t} + \nabla \cdot (\rho \mathbf{u}) = S_m, \quad (2.40)$$

and

$$\frac{\partial \mathbf{u}}{\partial t} + (\mathbf{u} \cdot \nabla) \mathbf{u} = -\frac{1}{\rho} \nabla P + \nu \nabla^2 \mathbf{u} + \mathbf{F} \quad (2.41)$$

with ρ the density of the fluid, \mathbf{u} the velocity field of the fluid, P the pressure field, ν the kinematic viscosity and S_m and \mathbf{F} any mass source terms and external forcing terms respectively.

Fluid flow can be classed as either laminar, turbulent or transitional (Versteeg and Malalasekera, 2007). A typical criteria for characterising turbulent flow is the magnitude of the Reynolds number, where higher Reynolds numbers correspond to more turbulent flow. Chaotic fluid motion is a characteristic of turbulent flow, where the velocity will fluctuate in both direction and magnitude. These turbulent length scales vary in size from the largest eddies cascading down to the smallest, with the smallest scale, the Kolmogorov length scale (η), being fundamental in the dissipation of turbulent kinetic energy into heat. Here $\eta = \left(\frac{\nu^3}{\varepsilon}\right)^{\frac{1}{4}}$ where ν is the kinematic viscosity of the fluid and ε the turbulent dissipation rate. To accurately solve for the entire fluid flow, a computational mesh must be generated which is fine enough to resolve this length scale. For a 3D domain the number of mesh points (N^3) scales with turbulent Reynolds number (Pope, 2000), following

$$N^3 \sim 4.4 \text{Re}^{\frac{9}{4}}. \quad (2.42)$$

As well as length scales, the relevant time scales must also be resolved.

The Kolmogorov time scale $\tau_\eta = \left(\frac{\nu}{\epsilon}\right)^{\frac{1}{2}}$ is the time scale associated with the turnover of the smallest of the turbulent eddies. For numerical convergence the Courant-Friedrichs-Lewy (CFL) number is typically used as a necessary convergence criteria. For resolving turbulent flow the CFL number is defined as,

$$CFL = \frac{u' \Delta t}{h} \quad (2.43)$$

where u' is the turbulent velocity fluctuation, Δt is the time step size and h the mesh grid size. The time scale here can be associated with the time to resolve a fluid parcel travelling across a mesh cell. Direct numerical simulation (DNS) of the entire range of length and time scales is costly for flows with large Reynolds numbers and thus turbulent flows. A 3D flow with a $Re=10^5$ would require a computational domain with at least 10^9 computational cells. This method is impractical for optimisation studies where a large number of simulations are needed. A balance must then be found between resolving the full range of length and time scales and modelling the flow turbulence.

2.5.2 Turbulence Modelling

Two of the main turbulence modelling approaches are the Large Eddy Simulation (LES) and family of Reynolds averaged Navier Stokes (RANS) turbulence models. Figure 2.17 shows the level of turbulent energy resolved and modelled by these approaches, with DNS fully resolving all scales, LES resolving a fraction of the turbulent energy and RANS modelling the entire spectrum.

Large Eddy Simulation

Large Eddy Simulation (LES) was first proposed by (Smagorinsky, 1963) and is a turbulence modelling approach where the governing equations are spatially filtered by a defined cut-off length scale. Here the turbulent eddies larger than this

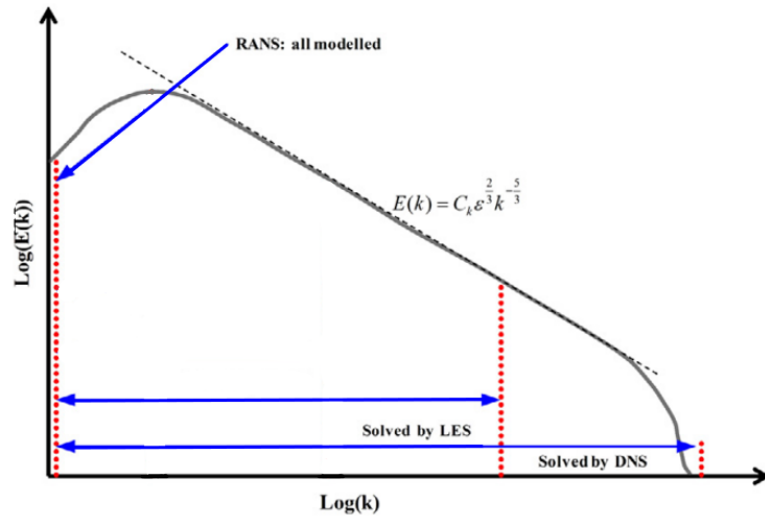


Figure 2.17: Turbulent energy spectrum showing the amount of turbulent energy modelled and resolved by the RANS, LES and DNS approach. Figure adapted from [Argyropoulos and Markatos \(2015\)](#).

scale are resolved and the more computationally expensive smaller eddies are modelled using a subgrid-scale model. This approach is less computationally expensive than DNS as only the largest of the eddies are being resolved and therefore a coarser grid sizing can be used as well as a larger time step. LES is still considerably more computationally expensive relative to fully modelling the turbulent scales through a RANS approach.

Reynolds Averaged Navier-Stokes

A Reynolds Averaged Navier-Stokes (RANS) approach for the conservation of momentum is the beginning of many turbulence models. Following Reynolds decomposition, the instantaneous velocity field is decomposed into a mean velocity component $\bar{\mathbf{u}}$ and fluctuating component \mathbf{u}' which represent the turbulent fluctuations away from the mean velocity,

$$\mathbf{u} = \bar{\mathbf{u}} + \mathbf{u}'. \quad (2.44)$$

By making this substitution into Equation (2.41) the RANS equations are derived,

$$\rho \bar{u}_j \frac{\partial \bar{u}_i}{\partial x_j} = \rho \bar{f}_i + \frac{\partial}{\partial x_j} \left(-\bar{p} \delta_{ij} + \mu \left[\frac{\partial \bar{u}_i}{\partial x_j} + \frac{\partial \bar{u}_j}{\partial x_i} \right] - \overline{\rho u'_i u'_j} \right), \quad (2.45)$$

where the subscript i represents the i^{th} Cartesian component of the velocity field, j the index for Einstein summation notation and $\delta_{i,j}$ the Kronecker delta function. A consequence of using this approach is the presence of the turbulent fluctuations seen in the final term of the RHS, also known as the Reynolds stresses. For closure of the Reynolds stresses ($\overline{\rho u'_i u'_j}$) additional equations are needed and here a suitable turbulence model is used for closure of the Reynolds stresses. Choosing a turbulence model which allows for accurate flow predictions while remaining computationally inexpensive is the challenge many CFD models face. There exist too many turbulence models with individual nuances to detail them all in full here, but the ones relevant to this work will be discussed. The following turbulence model equations can be found in [Ansys \(2009\)](#).

Standard $k - \varepsilon$ turbulence model

The standard $k - \varepsilon$ turbulence model developed by [Launder and Spalding \(1974\)](#), [Jones and Launder \(1972\)](#) and [Launder and Sharma \(1974\)](#) was one of the first turbulence models developed. In its formulation, Boussinesq's turbulent viscosity¹ (μ_t) is used to relate the Reynolds stress to the deformation of the mean flow,

$$-\overline{\rho u'_i u'_j} = \mu_t \left(\frac{\partial \bar{u}_i}{\partial x_j} + \frac{\partial \bar{u}_j}{\partial x_i} \right) - \frac{2}{3} (\rho k) \delta_{ij}, \quad (2.46)$$

where $\mu_t = \rho C_\mu \frac{k^2}{\varepsilon}$, with C_μ a model constant.

The standard $k - \varepsilon$ model is a 2-equation model for the transport of tur-

¹For a detailed historical look at Boussinesq's eddy viscosity please see [Schmitt \(2007\)](#)

bulent kinetic energy (TKE) k and turbulent dissipation rate (TDR) ε :

$$\begin{aligned}\frac{\partial}{\partial t}(\rho k) + \frac{\partial}{\partial x_i}(\rho k u_i) &= \frac{\partial}{\partial x_j} \left[\left(\mu + \frac{\mu_t}{\sigma_k} \right) \frac{\partial k}{\partial x_j} \right] + P_k + P_b - \rho \varepsilon - Y_m + S_k, \\ \frac{\partial}{\partial t}(\rho \varepsilon) + \frac{\partial}{\partial x_i}(\rho \varepsilon u_i) &= \frac{\partial}{\partial x_j} \left[\left(\mu + \frac{\mu_t}{\sigma_\varepsilon} \right) \frac{\partial \varepsilon}{\partial x_j} \right] + C_{1\varepsilon} \frac{\varepsilon}{k} (P_k + C_{3\varepsilon} P_b) - C_{2\varepsilon} \rho \frac{\varepsilon^2}{k} + S_\varepsilon.\end{aligned}\quad (2.47)$$

Here P_k is the production of TKE and P_b is the production of TKE due to buoyancy, given as,

$$P_k = -\rho \overline{u'_i u'_j} \frac{\partial u_j}{\partial x_i}, \quad P_b = -\frac{1}{\rho} \left(\frac{\partial \rho}{\partial T} \right)_p g_i \frac{\mu_t}{\text{Pr}_t} \frac{\partial T}{\partial x_i}. \quad (2.48)$$

Y_m is the effect of compressible dilation on the dissipation of TKE; S_k a user defined source of TKE and S_ε a user defined source of TDR. The effect due to compressible dilation is given as,

$$Y_m = 2\rho\varepsilon M_t^2 \quad (2.49)$$

where $M_t = \sqrt{\frac{k}{\alpha}}$ is the turbulent Mach number with α the speed of sound. For incompressible flows this term is negligible.

$C_{1\varepsilon}$, $C_{2\varepsilon}$, $C_{3\varepsilon}$, σ_k and σ_ε are model constants found from data fitting (Launder and Spalding, 1974). These model constants are typically taken as, 1.44, 1.92, -0.33, 1 and 1.3 respectively, and $C_\mu = 0.09$. These model constants are sometimes tuned for applications but care is needed that the tuning is not compensating for other limitations of the model.

From left to right the terms can be interpreted as: the rate of change of k or ε ; the transport of k or ε due to convection; the transport of k or ε due to diffusion; the rate of production of k or ε and the rate of destruction of k or ε .

Since the development of the standard $k - \varepsilon$ model there have been many other 2-equation turbulence models developed. Ones of interest in this work are the RNG $k - \varepsilon$, realizable $k - \varepsilon$, $k - \omega$ and $k - \omega$ SST models.

RNG $k - \varepsilon$ turbulence model

The RNG model was developed by [Yakhot et al. \(1992\)](#) using Re-Normalisation group (RNG) methods (methods which investigate changes in a system when viewed from different scales). The model has been used to investigate sprays ([Han and Reitz, 1995](#)) ([Ailaboina and Saha, 2022](#)). A different transport equation for the TDR is created with the main change coming from the production term. The equations for transport of TKE and TDR are given as,

$$\begin{aligned} \frac{\partial}{\partial t}(\rho k) + \frac{\partial}{\partial x_i}(\rho k u_i) &= \frac{\partial}{\partial x_j} \left(\alpha_k \mu_{\text{eff}} \frac{\partial k}{\partial x_j} \right) + P_k + P_b - \rho \varepsilon - Y_m + S_k, \quad (2.50) \\ \frac{\partial}{\partial t}(\rho \varepsilon) + \frac{\partial}{\partial x_i}(\rho \varepsilon u_i) &= \frac{\partial}{\partial x_j} \left(\alpha_\varepsilon \mu_{\text{eff}} \frac{\partial \varepsilon}{\partial x_j} \right) + C_{1\varepsilon} \frac{\varepsilon}{k} (P_k + C_{3\varepsilon} P_b) - C_{2\varepsilon}^* \rho \frac{\varepsilon^2}{k} + S_\varepsilon. \end{aligned}$$

Here the main change of the TDR equation is found in the $C_{2\varepsilon}^*$ term where it is given by

$$C_{2\varepsilon}^* = C_{2\varepsilon} + \frac{C_\mu \eta^3 \left(1 - \frac{\eta}{\eta_0}\right)}{1 + \beta \eta^3} \quad \text{with} \quad \eta = S \frac{k}{\varepsilon}, \eta_0 = 4.38 \quad \text{and} \quad \beta = 0.012. \quad (2.51)$$

From this new form of the TDR reduction term, when $\eta < \eta_0$ there is an increase in the destruction of TDR due to this parameter. Similarly, where $\eta > \eta_0$ there is a decrease. This allows the RNG model to perform better when there are changes in strain rates and has been shown to capture reattachment lengths more accurately than the standard $k - \varepsilon$. Other improved applications have been found in [OrszagS et al. \(1993\)](#).

Some of the model constants are also different because they are found during the RNG method rather than data fitting. The model constants are given as $C_{1\varepsilon} = 1.42$ and $C_{2\varepsilon} = 1.68$ and for high Reynolds number flows the turbulent viscosity is the same as that used in the standard model but with $C_\mu = 0.0845$. The RNG model also has a low Reynolds number correction available close to the wall.

Realizable $k - \varepsilon$ turbulence model

The realizable $k - \varepsilon$ model of [Shih et al. \(1995\)](#) gives a different approach to calculating the turbulent viscosity (μ_t) using a variable C_μ , unlike the standard model where the model parameter is set as $C_\mu = 0.09$. The standard turbulent viscosity approach allows for the normal stresses to become negative in cases where the flow exhibits larger mean strain rate, and so using a model with a variable C_μ insures realizability.

Another difference between the models is how the turbulent dissipation rate is modelled. Unlike other models the turbulent dissipation rate is derived from the mean-square vorticity fluctuations ($\overline{\omega_i \omega_i}$), with $\varepsilon = \nu \overline{\omega_i \omega_i}$. The realisable $k - \varepsilon$ transport equations are given as,

$$\frac{\partial}{\partial t} (\rho k) + \frac{\partial}{\partial x_i} (\rho k u_i) = \frac{\partial}{\partial x_j} \left[\left(\mu + \frac{\mu_t}{\sigma_k} \right) \right] + P_k + P_b - \rho \varepsilon - Y_M + S_k, \quad (2.52)$$

$$\begin{aligned} \frac{\partial}{\partial t} (\rho \varepsilon) + \frac{\partial}{\partial x_i} (\rho \varepsilon u_i) = & \frac{\partial}{\partial x_j} \left[\left(\mu + \frac{\mu_t}{\sigma_\varepsilon} \right) \frac{\partial \varepsilon}{\partial x_j} \right] + \rho C_1 S \varepsilon \\ & - \rho C_2 \frac{\varepsilon^2}{k + \sqrt{\nu \varepsilon}} + C_{1\varepsilon} \frac{\varepsilon}{k} C_{3\varepsilon} P_b + S_\varepsilon. \end{aligned} \quad (2.53)$$

with

$$C_1 = \max \left(0.43, \frac{\eta}{\eta + 5} \right), \quad \eta = S \frac{k}{\varepsilon}, \quad S = \sqrt{2 S_{ij} S_{ij}}$$

and turbulent viscosity given as

$$\mu_t = \rho C_\mu \frac{k^2}{\varepsilon} \quad \text{where} \quad (2.54)$$

$$C_\mu = \frac{1}{A_0 + A_s \frac{k U^*}{\varepsilon}} \quad \text{with} \quad (2.55)$$

$$U^* \equiv \sqrt{S_{ij} S_{ij} + \tilde{\Omega}_{ij} \tilde{\Omega}_{ij}}, \quad \tilde{\Omega}_{ij} = \Omega_{ij} - 2 \epsilon_{ijk} \omega_k, \quad \Omega_{ij} = \bar{\Omega}_{ij} - \epsilon_{ijk} \omega_k, \quad (2.56)$$

$$A_0 = 4.04, \quad A_s = \sqrt{6} \cos \phi, \quad (2.57)$$

$$\phi = \frac{1}{3} \arccos \left(\sqrt{6} W \right), \quad W = \frac{S_{ij} S_{jk} S_{ki}}{\tilde{S}^3}, \quad \tilde{S} = \sqrt{S_{ij} S_{ij}}, \quad S_{ij} = \frac{1}{2} \left(\frac{\partial u_j}{\partial x_i} + \frac{\partial u_i}{\partial x_j} \right). \quad (2.58)$$

The transport equation for k is the same as the standard model but a different transport equation for ε can be seen in Equation (2.53). For the formulation of the eddy viscosity, S_{ij} is the strain rate tensor and $\bar{\Omega}_{ij}$ the mean rate of rotation tensor when viewed in a reference frame with angular velocity ω_k . Here it is clear to see that C_μ is variable and depends on the strain rate, rotation rate, reference frame angular velocity, k and ε . These dependencies result in an improved prediction for many types of flows (Kim et al., 1999). The realizable model has also been used to simulate sprays (Singhal et al., 2018) (Geng et al., 2020).

$k - \omega$ turbulence model

The $k - \omega$ model of Wilcox (1988) uses transport equations for TKE and the specific dissipation rate ω . The transport equations for k and ω are given as

$$\frac{\partial}{\partial t}(\rho k) + \frac{\partial}{\partial x_i}(\rho k u_i) = \frac{\partial}{\partial x_j} \left[\left(\mu + \frac{\mu_t}{\sigma_k} \right) \frac{\partial k}{\partial x_j} \right] + G_k - Y_k + S_k, \quad (2.59)$$

$$\frac{\partial}{\partial t}(\rho \omega) + \frac{\partial}{\partial x_i}(\rho \omega u_i) = \frac{\partial}{\partial x_j} \left[\left(\mu + \frac{\mu_t}{\sigma_\omega} \right) \frac{\partial \omega}{\partial x_j} \right] + G_\omega - Y_\omega + S_\omega. \quad (2.60)$$

Here G_k and G_ω represent the production of TKE and ω respectively and are given as

$$G_k = -\overline{\rho u_i' u_j'} \frac{\partial u_j}{\partial x_i} \quad \text{and} \quad G_\omega = \alpha \frac{\omega}{k} G_k. \quad (2.61)$$

Y_k and Y_ω , the dissipation of TKE and ω respectively, are given by

$$Y_k = \rho \beta_* f_{\beta^*} k \omega \quad \text{and} \quad Y_\omega = \rho \beta f_\beta \omega^2 \quad (2.62)$$

and S_k and S_ω are defined source terms of TKE and ω respectively. The eddy viscosity is now defined as $\mu_t = \rho \alpha^* \frac{k}{\omega}$, where α^* is the low-Reynolds number correction to the turbulent viscosity given by,

$$\alpha^* = \alpha_\infty^* \left(\frac{0.024 + \frac{\rho k}{6\mu\omega}}{1 + \frac{\rho k}{6\mu\omega}} \right). \quad (2.63)$$

At high Reynolds numbers $\alpha^* = 1$ and therefore the eddy viscosity is taken as $\mu_t = \rho \frac{k}{\omega}$.

$k - \omega$ SST turbulence model

The $k - \omega$ Shear Stress Transport (SST) model by [Menter \(1994\)](#) blends the near wall advantages of the $k - \omega$ and the fully turbulent flow advantages of the $k - \varepsilon$ model via a blending function. The ω transport equation gains an additional cross diffusive term (D_ω) to account for the blending of the two models. The $k - \omega$ SST model has been used in various spray studies ([Salvador et al., 2014](#)), ([Bhide and Abdallah, 2022](#)).

2.5.3 Near-Wall Modelling

A typical boundary condition at wall boundaries for viscous fluids is that the relative velocity of the fluid parcels in contact with the boundary is equal to zero. This condition is known as the no-slip boundary condition. Moving away from the wall boundary, the velocity of a turbulent flow follows what is known as the ‘‘Law of the wall’’ found by [Von Karman \(1931\)](#). Here the dimensionless flow velocity ($u^+ = \frac{u}{u_\tau}$) can be divided into three regions, classified by a non-dimensional wall-distance,

$$y^+ = \rho \frac{u_\tau y}{\mu}, \quad (2.64)$$

where $u_\tau = \sqrt{\frac{\tau_w}{\rho}}$ is the shear velocity, with τ_w the wall shear, and y the distance away from the wall. The three regions are defined as the viscous/laminar sublayer, the buffer layer and the log-law layer. In the viscous sublayer, where $y^+ < 5$, the dimensionless velocity behaves linearly as it tends towards the zero velocity no-slip condition, with u^+ following $u^+ = y^+$. At the other extreme, in the log-law layer

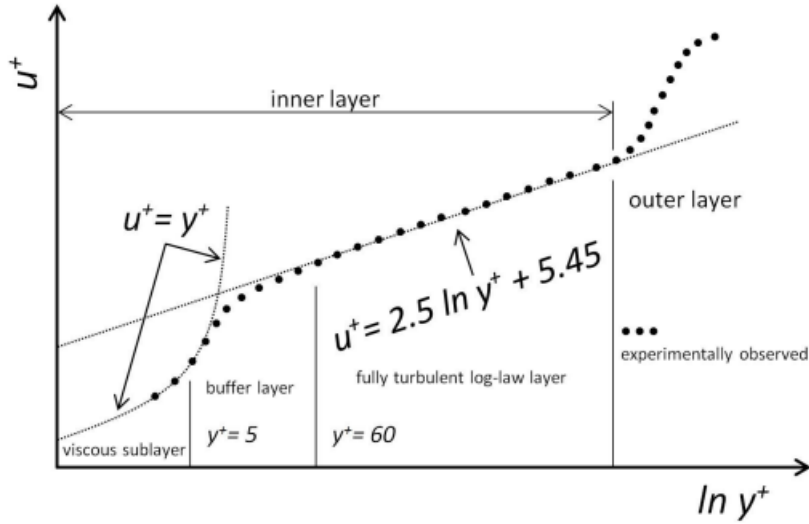


Figure 2.18: Plot of dimensionless velocity (U^+) against dimensionless wall distance (y^+) showing the viscous sublayer, buffer layer and fully turbulent layer. Taken from [Mehta et al. \(2018\)](#).

where $y^+ > 30$, the dimensionless velocity follows,

$$u^+ = \frac{1}{\kappa} \ln y^+ + C^+, \quad (2.65)$$

where κ is the von Kármán constant taken as $\kappa = 0.41$, but with other values close to 0.40 also used, and $C^+ \approx 5.5$ ([Versteeg and Malalasekera, 2007](#)). In the buffer layer, $5 < y^+ < 30$, the dimensionless velocity follows neither the linear profile or the log-law. The law of the wall can be seen in [Figure 2.18](#).

The near wall flow can either be resolved down to the wall with a sufficiently fine mesh or the viscous sub-layer and buffer layer can be modelled using a wall-function which is less computationally expensive. Some turbulence models like the standard $k - \varepsilon$ are not applicable close to the wall and are only for fully turbulent flows. The TDR is not well defined at boundaries so a wall function can be used. This has lead to some low-Reynolds number corrections to the turbulence models.

The standard wall function of [Launder and Spalding \(1974\)](#) takes a scaling

of the mean velocity and when $y^* > 11.225$ sets it as the log-law defined by

$$U^* = \frac{1}{\kappa} \ln(9.793y^*) \quad (2.66)$$

where the dimensionless velocity and wall-distance are given as,

$$U^* = \frac{U\rho C_\mu^{\frac{1}{4}} k^{\frac{1}{2}}}{\tau_w} \quad \text{and} \quad y^* = \frac{y\rho C_\mu^{\frac{1}{4}} k^{\frac{1}{2}}}{\mu}. \quad (2.67)$$

When $y^* < 11.225$ the mean velocity is set as,

$$U^* = y^*. \quad (2.68)$$

The accuracy of the standard wall function approach decreases as the mesh is refined near the wall. An alternative approach is to ensure that the wall function is y^* limited and is achieved with the use of the scalable wall function approach where the y^* is replaced with \tilde{y}^* where

$$\tilde{y}^* = \max(y^*, 11.225). \quad (2.69)$$

Where $y^* > 11.225$ the scalable approach is equivalent to the standard wall function approach.

Enhanced Wall Treatment

ANSYS Fluent offers an improved near-wall treatment which uses a blending function between the laminar viscous sub-layer and fully turbulent log-law layer (Ansys, 2009). Here the new function for normalised velocity is given by

$$u^+ = e^\Gamma u_{\text{laminar}}^+ + e^{\frac{1}{\Gamma}} u_{\text{Turbulent}}^+ \quad \text{with} \quad \Gamma = -\frac{a(y^+)^4}{1 + by^+} \quad (2.70)$$

where $a=0.01$ and $b=5$. For small y^+ this function tends to the laminar linear law and for large y^+ this function tends to the turbulent log-law. This gives a way

of modelling the momentum equation close to the wall from the viscous sub-layer, through the buffer layer and into the turbulent log-law layer.

2.5.4 Species Transport

Convection-diffusion equations for the i^{th} species' mass fraction (Y_i),

$$\frac{\partial}{\partial t} (\rho Y_i) + \underbrace{\nabla \cdot (\rho \mathbf{u} Y_i)}_{\text{convection}} = - \underbrace{\nabla \cdot \mathbf{J}_i}_{\text{diffusion}} + \underbrace{S_i}_{\text{source}} \quad (2.71)$$

are used to model the transport of species. In general, for N species only N-1 transport equations must be solved. The turbulent diffusive flux of species i is defined as,

$$\mathbf{J}_i = - \left(\rho D_{m,i} + \frac{\mu_t}{Sc_t} \right) \nabla Y_i - D_{T,i} \frac{\nabla T}{T}. \quad (2.72)$$

The terms from left to right are: the rate of change of species mass fraction, convection of species due to the flow, diffusion of species and source terms. Here $D_{m,i}$ and $D_{T,i}$ are the mass diffusion coefficient (defined by Ficks law) and Soret coefficient respectively. $Sc_t = \frac{\mu_t}{\rho D_t}$ is the turbulent Schmidt number, where D_t is the turbulent diffusivity. As this turbulent Schmidt number arises in the diffusion term its value will impact the diffusion of species. The default value typically used is $Sc_t = 0.7$. The source terms can be due to evaporating species from evaporating droplets.

2.5.5 Energy Equation

The energy equation, important for representing the change in energy of the system, is given by,

$$\frac{\partial (\rho E)}{\partial t} + \nabla \cdot (\mathbf{u} (\rho E + p)) = \nabla \cdot \left(k_{eff} \nabla T - \sum_j h_j \mathbf{J}_j + \tau_{eff} \cdot \mathbf{u} \right) \quad (2.73)$$

where the terms from left to right are: the change of energy with respect to time, the convection of energy by the flow, the energy transfer due to conduction, energy loss due to species diffusion and viscous dissipation respectively.

The thermal boundary layer close to the walls is modelled using a similar approach to that of the law of the wall for the momentum boundary layer following [Viegas et al. \(1985\)](#). The dimensionless temperature (T^*) is defined as

$$T^* = \frac{(T_w - T_p) \rho c_p C_\mu^{\frac{1}{4}} k_p^{\frac{1}{2}}}{\dot{q}} \quad (2.74)$$

where T_w is the temperature of the wall, T_p the cell temperature, c_p the fluid specific heat, \dot{q} the wall heat flux. The dimensionless temperature is defined as

$$T^* = \begin{cases} \text{Pr} y^* + \frac{1}{2} \rho \text{Pr} \frac{C_\mu^{\frac{1}{4}} k_p^{\frac{1}{2}}}{\dot{q}} U_p^2 & y^* < y_T^* \\ \text{Pr}_t \left[\frac{1}{\kappa} \ln(E y^*) + D \right] + \frac{1}{2} \rho \frac{C_\mu^{\frac{1}{4}} k_p^{\frac{1}{2}}}{\dot{q}} \left[\text{Pr}_t U_p^2 + (\text{Pr} - \text{Pr}_t) U_c^2 \right] & y^* > y_T^* \end{cases} \quad (2.75)$$

where D is given by,

$$D = 9.24 \left[\left(\frac{\text{Pr}}{\text{Pr}_t} \right)^{\frac{3}{4}} - 1 \right] \left[1 + 0.28 e^{-0.007 \frac{\text{Pr}}{\text{Pr}_t}} \right] \quad (2.76)$$

and the Prandtl number and turbulent Prandtl number are given as, $\text{Pr} = \frac{\mu C_p}{k_f}$ and $\text{Pr}_t = 0.85$ respectively.

2.6 Summary

This literature review shows the broad range of physics that are involved in the spray generation procedure. The review has attempted to give an introduction into the complexities and important parameters for each contribution to the spray process.

In summary:

- Sprays have been widely researched, however to date the main focus has been on fuel sprays within the automotive industry. Numerical models have thus been developed with this area in mind and as a result have not been extended to other areas of interest. The field of interest, “Spray generation from aerosol cans”, has not been studied to the same degree as fuel sprays and presents a big gap within the literature considering the wide commercial use.
- Primary atomization is a complex process and requires large amounts of computational power to fully resolve all of the features, including the internal nozzle disturbances and the breakup of the liquid jet. Simpler approaches have been employed and show promising results, like those detailed in [Shinjo \(2018\)](#). Primary atomization is not a key focus of this research but an understanding is needed in order to build a spray model able to capture droplet carry-over.
- Secondary atomization can contribute to the generation of the majority of the droplets that make up the dense spray region and could be an important part in the modelling of the problem. Determining the influence and deciding on a suitable model will be discussed when developing an accurate model.
- The conditions that the transporting droplets experience greatly affect the flow field and the neighbouring droplets. For aerosol cans the product-propellant mixture is inherently complex. In order to predict the fate of droplets an accurate numerical model for the carrier jet must be developed which is able to then

incorporate the droplet physics while remaining computationally inexpensive.

- There is limited experimental data for sprays generated from deodorant-type aerosol cans. An experimental dataset for droplet sizes, temperature and flow field of deodorant-type sprays is needed to validate any numerical model made. This is to ensure the reliability in the model predictions.
- To understand the carry-over of droplets the deposition of droplets onto a target surface and their interaction will be important for determining effectiveness of spray methods for application of a product.

The following chapters will detail the work carried out to capture spray features experimentally and the process of building a validated CFD model to investigate sprays generated from deodorant-type aerosol cans.

Chapter 3

Experimental Study of Spray Generation

3.1 Introduction

In this chapter the experimental methods used to investigate sprays generated from aerosol cans are discussed. To visualise the spray structure a schlieren approach is used due to its ability to capture the density variations between the ambient air and alkane propellants. To measure the temperature variations within the spray, thermocouples are positioned along the centreline of the spray cone. To capture the particle sizes generated from the aerosol cans and the change in particle size during flight a Malvern Spraytec is used at different axial locations. Each of the experimental setups, methodologies, results and post-processing are discussed in detail within this chapter.

For each experimental method, 9 cans of varying formulation are tested. The cans are separated into two groups classified by the nozzle type used, being either a swirl atomizer (group 1) or a simple orifice (group 2). The simple orifice atomiser is used for antiperspirant (AP) as the insert of swirl nozzles are prone

Group	A	B	C	D	E
1	Prop	Prop + Water	Prop + Alcohol	Full Product	N/A
2	Prop	Prop + D5	Prop + AACH	Prop + Slurry	Full AP Product

Table 3.1: The contents of the cans separated into swirl atomizer nozzles (group 1) and simple orifice nozzles (group 2). D5 represents cyclopentasiloxane and AACH the active aluminum chlorohydrate.

to clogging for such formulations (Ashgriz, 2011). The orifice diameter for both types is approximately of the order 0.5 mm. The label notation of the cans and their contents are given in Table 3.1 and Table 3.2 respectively. The label “Prop” refers to the propellant mixture used in all formulations which is an LPG blend of propane, butane and iso-butane with approximate mass fractions of 20%, 45% and 35% respectively and resulting in an internal pressure of 40 PSIG within the aerosol cans. To investigate how the nozzles and typical additional ingredients influence spray generation the can formulations are specifically made up to allow for testing. When referring to a can throughout this thesis, the group number (nozzle type) and associated letter are used, e.g propellant and water would be 1B and propellant and slurry would be 2D. It is to be noted that D5 refers to the fluid cyclopentasiloxane and AACH refers to the antiperspirant active aluminum chlorohydrate and are components not to be confused with the testing can labels.

Label	Content	Nozzle Type	Base (g)	Propellant (g)	% Base	% Prop
1A	Prop	Swirl	-	-	-	100
1B	Prop + Water	Swirl	3.41	81.94	4.00	96.00
1C	Prop + Alcohol	Swirl	38.01	57.02	40.00	60.00
1D	Full Product	Swirl	-	-	-	-
2A	Prop	Simple	-	-	-	100
2B	Prop + D5	Simple	11.52	83.85	12.08	87.92
2C	Prop + AACH	Simple	4.32	81.99	5.01	94.99
2D	Prop + Slurry	Simple	11.54	77.24	13.00	87.00
2E	Full Product	Simple	-	-	-	-

Table 3.2: For each aerosol can the component mass (g), separated into propellant and base, and their respective mass fractions (%) are given.

3.2 Methodology

3.2.1 Schlieren Imaging

Schlieren imaging is an optical technique able to capture density differences, or more precisely, first order refractive index gradients within flows (Settles, 2012). With the use of high speed photography, videos of a high temporal resolution are capable of capturing the spray's initiation, fully developed state and its collapse. The processing of these schlieren videos can provide both qualitative and quantitative insight into spray features.

This section details the setup of the schlieren experiment as well as the iterations taken to improve the quality of the results. The experimental methodology and image processing procedure is also described. Finally, the measurements of the spray angle produced by the different fluid types and the influence of nozzle type are discussed.

Experimental Setup

A z-type schlieren setup is one of the most common schlieren setups used, as mentioned in §2, and was the setup chosen for this study due to its advantages over other mirror type setups as well as equipment and space limitations. A z-type setup was constructed following guidance from Settles and Hargather (2017) where a clear description of the setup procedure and example equipment list is given. The guide also includes common set-up errors concerning knife edge positioning, and ways of reducing optical aberrations such as coma and astigmatism which can influence the quality of the recorded images.

A schematic of the z-type setup used can be seen in Figure 3.1. The light source is generated with a Dolan-Jenner MI-152 high intensity illuminator and

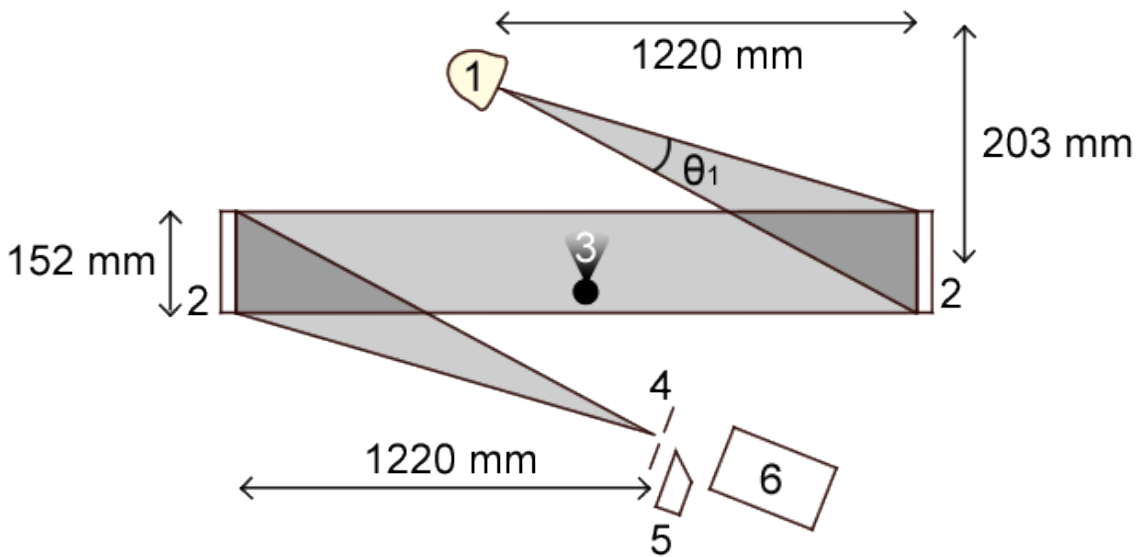


Figure 3.1: Schematic drawing (not to scale) of the z-type schlieren setup used. 1) Light source, 2) 6" parabolic mirrors, 3) Generated spray, 4) Iris, 5) Knife cut off and 6) Camera.

attached 0.191" ID fibre optic cable to generate a point-like light source. The light beam is directed towards a 6" aluminium coated parabolic mirror with focal length 1220 mm. This mirror directs the light to an identical mirror positioned 1750 mm away. The light reflecting off the second mirror is focused through an iris onto a knife edge and finally into a camera lens. The aerosol can is supported between the two parabolic mirrors by a clamp in order to hold the aerosol can in place at the correct height during actuation. To extract the spray a Weller fume extractor is positioned downstream of the aerosol can, so as to minimise any risk to the user from exposure to the sprays.

Regarding optical aberrations, coma occurs when the direction at which light is reflected is dependant on the point it reflects from. Coma gives rise to a tail like structure at the focal point. The z-type setup used, with identical mirrors and opposite angles, naturally eliminates coma. Astigmatism arises due to a difference in path length along the centreline and mirror periphery. Astigmatism cannot be eliminated entirely and so methods are used to minimise it. Long focal length mirrors help to do this, as well as small (setup dependent) mirror offset angles. To reduce astigmatism as much as possible f/8, 6" parabolic mirrors with a focal length

of 1220 mm are used in this study.

A metric for determining severity of astigmatism is by looking at the difference between the sagittal focus and tangential focus (Δf) of the setup (Speak and Walters, 1950) given by,

$$\Delta f = f \frac{\sin^2(\theta)}{\cos(\theta)} \quad (3.1)$$

where f is the focal length of the mirror and θ the offset angle.

To calculate the severity of astigmatism using Eq. (3.1) the focal length of the mirrors and their offset is needed. The focal length of the parabolic mirrors is approximately 1220 mm and the offset angle is calculated as,

$$\theta = \arctan\left(\frac{203}{1220}\right) / 2 = 0.0836 \text{ rad.} \quad (3.2)$$

Substituting these values into Eq. 3.1 the distance between foci is given as 4.79 mm. With such a small offset angle the equation can be simplified to $\Delta f = D^2/4f$ (Settles and Hargather, 2017), with D the mirror aperture. A focal length of 1220 mm and mirror aperture $f/8$ gives a focal deviation of $\Delta f = 4.73$ mm. Settles and Hargather (2017) deemed a deviation of 2.4 mm to have no problem with astigmatism and one of 38 mm very noticeable, thus astigmatism is deemed not to be a severe problem for this setup.

Setup Iterations

The schlieren setup went through three iterations in order to obtain clear images. The position of the light source, parabolic mirrors, and camera remained the same through each iteration, however, the camera type, lens type and angle of the aerosol can with the vertical axis changed. Here a description of the experimental procedure is given as well the reasons behind the changes for each setup. The ambient conditions, relative humidity and temperature, were also recorded using an ATP MT-903 Pocket Thermo-Hygrometer.

The first setup used a Basler ace acA1300-30um usb camera positioned behind the knife edge. The camera/software had a maximum recording frame rate of 25 fps. A frame taken from the first setup using the Basler camera can be seen in Figure 3.2a. Several issues were identified. The temporal resolution was too small to capture the development of the spray. The initial frame showed the actuation but the next frame showed that the spray had already crossed the entire field of view. This can be fixed by using a camera which can record at a higher frame rate. There was also uneven illumination of the background resulting in the lower region being darker than that of the top. This problem is discussed in [Settles and Hargather \(2017\)](#), where for this particular case, the knife edge is positioned too close to the parabolic mirror. To fix this in this setup the knife edge was positioned further away, which resulted in a more even illumination, however the problem wasn't eliminated entirely.

Background disturbances are also clearly present in Figure 3.2a which is due to the spray crossing the beam from the light source to the first parabolic mirror. In order to eliminate the background disturbance several possible alternatives were investigated. The first was to rotate the entire setup to a vertical z-type schlieren setup, but this was not investigated further due to the inherent sensitivity of the schlieren technique as well as the need to construct additional pieces of equipment to support the mirrors in a horizontal plane. The second alternative was to add an L-shaped adaptor to the dip tube of the can and attach the nozzle to the other end so as to direct the spray downward vertically. A third alternative idea was to spray vertically up or down through the central beam, however, this would require the can to be in a horizontal orientation and would potentially result in the dip tube within the can not being fully submerged, which could affect the generated spray as a result. The final option, and the simplest, was to rotate the can a small amount such that the dip tube was still submerged but the spray went under the initial beam between the light source and first parabolic mirror. This would make postprocessing more complicated as the spray was no longer directed along the horizontal axis, however

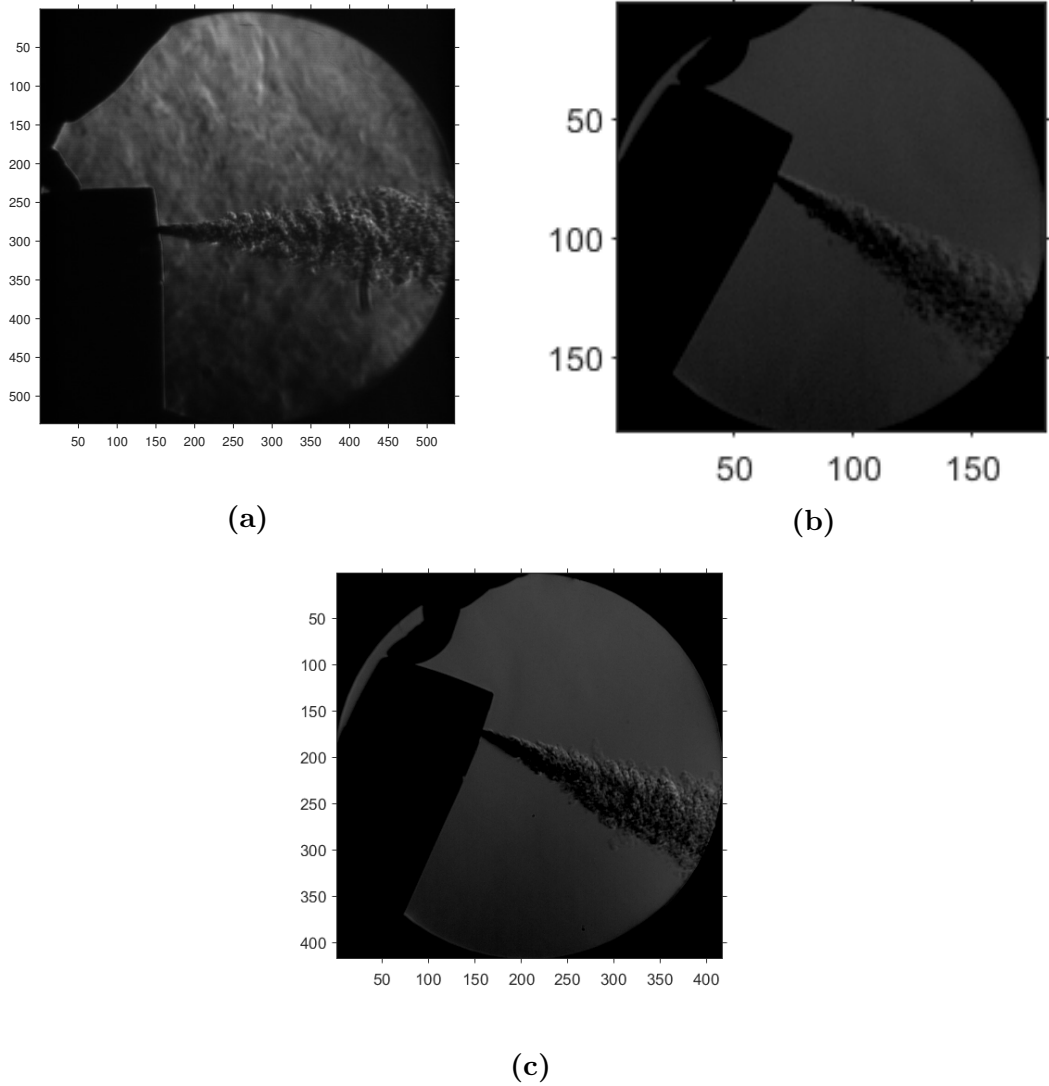


Figure 3.2: Schlieren image taken of can 1D for (a) the first setup showing background disturbances and turbulent structures, (b) the second setup showing the improvements over background disturbances but reduction in pixel density, (c) the third setup showing no background disturbances and improved pixel quality over the second setup.

this provided a cheap and simple solution.

The second iteration of the setup used a Phantom Miro M310 high speed camera with a 28 mm lens to improve the temporal resolution of the spray. The videos are recorded using Phantom Camera Control (PCC) V3.6 where the frame rate and exposure time are input. Here the frame rate was limited by the exposure time and the intensity of the illuminator. Recording at 2000 fps showed that the schlieren technique captured the initial generation of the spray when actuated, the continuous spray period and the collapse of the spray after releasing the actuator. A frame from the continuous spray period can be seen in Figure 3.2b. The improvements are clearly visible when comparing Figure 3.2a and 3.2b. The background disturbances are eliminated and a more even grading of background illumination is achieved by moving the knife cut off further away from the parabolic mirror. A disadvantage of this setup is the reduced spatial resolution of the schliere from $532px \times 532px$ to $181px \times 181px$, with a pixel density reduction from $3.49px/mm$ to $1.19px/mm$. The high speed camera also introduces a hot air flow towards the region of interest, due to the inbuilt cooling fan. Due to its lower density, this airflow is captured by the schlieren setup. To prevent this disturbance a perspex sheet was placed between the camera and the region of interest to direct the air flow away from the schlieren setup.

The final iteration of the setup aimed to improve the pixel density of the image by seeking to distribute the light across more of the camera's sensor. A camera lens with an improved focal length was used to achieve this. A Nikon AF Nikkor 28-70mm lens was used, increasing the focal length from 28 mm to 70 mm when compared to the second setup. This change increased the pixel density to $2.73px/mm$, a 129% increase over the second setup. Table 3.3 details the differences between the camera setups used for the different schlieren iterations. The third setup is then used and discussed for the remainder of this section.



Figure 3.3: Experimental schlieren setup showing the light source, two parabolic mirrors, positioned aerosol can, Weller extraction tube and knife cut off.

	Camera Model	Make	Lens	Exposure	Aperture	Focal Length	ISO	Frame rate
Setup 1	Ace acA1300-30um	Basler	Edmund Optics CFFL F1.4 f16mm 2/3"	...	f/1.4	16 mm	...	28 fps
Setup 2	Miro M310	Phantom	Nikkor 28 mm	1 μ s	f/2.8	28 mm	1600	2000 fps
Setup 3	Miro M310	Phantom	Nikkor 28-70 mm	3.5 μ s	f/5.6	70 mm	1600	2000 fps

Table 3.3: Different camera setups for the Schlieren Experiments detailing both camera and lens specifications.

Experimental procedure

The schlieren experimental procedure for each of the different formulations and nozzle types is as follows:

1. Shake the aerosol can for 5 seconds, this is to achieve a well-mixed formulation before spraying.
2. Place the aerosol can within the clamp and align with the central beam. This allows for even actuation and aids in repeatability of experiments.
3. Record the relative humidity and temperature, this is to provide the ambient conditions to accompany the experimental data.
4. Activate the recording software PCC. The software is set up before the run as no automatic activation mechanism was used.

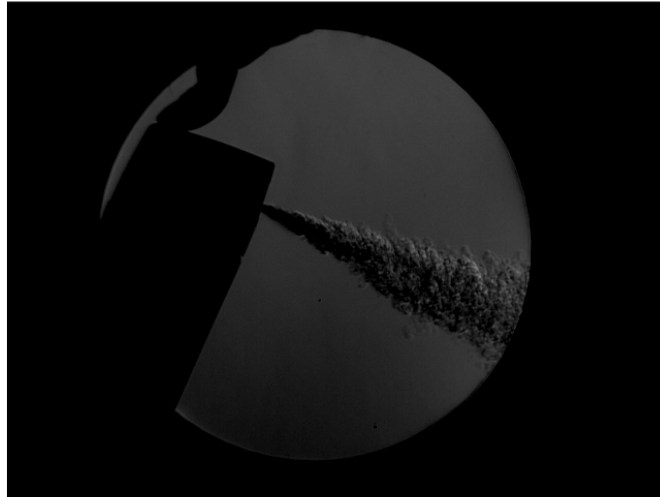
5. Manually actuate the aerosol can for 2-3 seconds. The aerosol can is actuated for a period long enough to capture the generation, continuous spray period and collapse of the spray. The internal memory of the cameras also limited how long a recording can be for a set frame rate.
6. Stop recording software to prevent unnecessarily large video files.
7. Repeat steps 1-6 for a total of 3 runs. This is to provide data on repeatability of experiments.

Image Processing

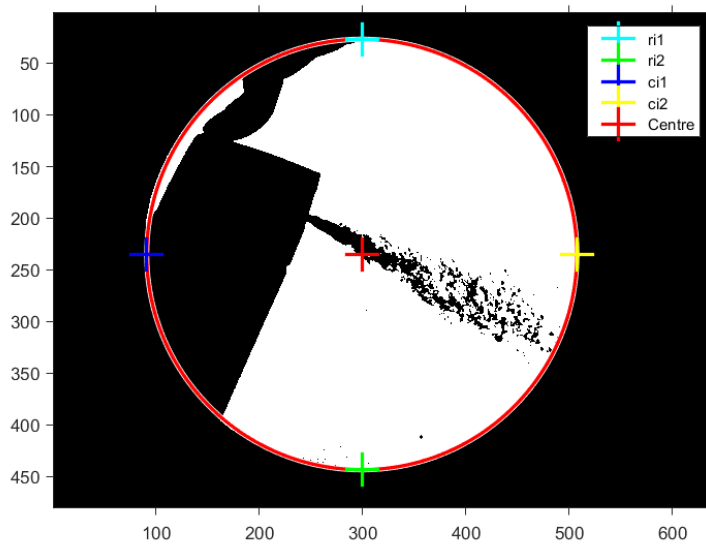
This section details the image processing procedures that were used to analyse the schlieren videos recorded. The videos are taken from PCC and exported in Audio Video Interleave (avi) format which are then imported into MATLAB R2018b where all the post-processing is performed.

Circle Identification

A typical frame taken from the schlieren experiments is shown in Figure 3.4a. The field of view is surrounded by black due to the exposure time being sufficiently small that those regions don't receive sufficient illumination. This allows for an easy reduction of the frame where a circle finding algorithm is applied, identifying the region of interest. First the image is converted to a black and white image where a threshold is determined using Otsu's automatic thresholding method (Otsu, 1979). Otsu's method looks to maximise the inter-class variance of pixel intensities. An example can be seen in Figure 3.5 where the histogram of pixel intensities and inter-class variance are plotted. This technique is suited where a bimodal distribution of pixel intensities can be observed. Figure 3.5 shows a large number of pixels with an intensity of 0, identifying the black region around the mirror's field of view, and a second mode centred at an approximate pixel intensity of 50, identifying the



(a)



(b)

Figure 3.4: (a) A typical frame taken from a schlieren video (b) Application of Otsu's automatic thresholding technique and a search algorithm for the row and column indices to identify the bounds of the mirror's field of view.

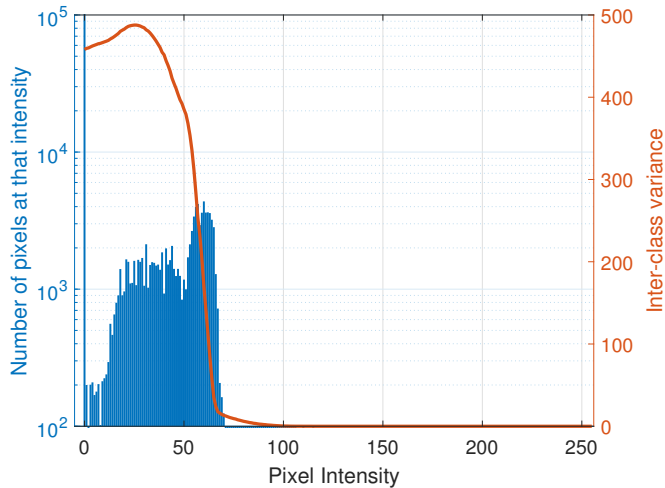


Figure 3.5: Histogram of pixel intensities along with the inter-class variance for a frame taken from the schlieren experiments.

variation seen in the mirror’s field of view. By applying this thresholding technique to a typical schlieren frame, the image can be separated into a matrix of 0s or 1s for black and white pixels respectively. The mirror field of view is then found by finding the first and last columns and rows with a non-zero sum. The row and column numbers provide the location of the coloured crosses seen in Figure 3.4b and thus the bounds of the view of interest.

Edge Detection

Using the reduced image, edge detection filters are applied to determine the spray region. The standard edge detection filters investigated include the Prewitt, Sobel, Robert’s cross and Canny filter. Each of the respective filters have a kernel associated with them. This kernel is then convolved (denoted by $*$) with an image piece (I , a subset of the image matrix). Kernels for the Prewitt, Sobel and Robert’s Cross methods are given in 3.3 where subscripts x and y denote horizontal and

vertical gradients respectively.

$$\begin{aligned}
K_x^{Prewitt} &= \begin{pmatrix} +1 & 0 & -1 \\ +1 & 0 & -1 \\ +1 & 0 & -1 \end{pmatrix}, & K_y^{Prewitt} &= \begin{pmatrix} +1 & +1 & +1 \\ 0 & 0 & 0 \\ -1 & -1 & -1 \end{pmatrix}, \\
K_x^{Sobel} &= \begin{pmatrix} +1 & 0 & -1 \\ +2 & 0 & -2 \\ +1 & 0 & -1 \end{pmatrix}, & K_y^{Sobel} &= \begin{pmatrix} +1 & +2 & +1 \\ 0 & 0 & 0 \\ -1 & -2 & -1 \end{pmatrix}, & (3.3) \\
K_x^{Robert} &= \begin{pmatrix} +1 & 0 \\ 0 & -1 \end{pmatrix}, & K_y^{Robert} &= \begin{pmatrix} 0 & +1 \\ -1 & 0 \end{pmatrix}.
\end{aligned}$$

The kernel form determines which gradient type is calculated and the weighting associated to the neighbouring pixels. The Prewitt kernel weights all edge and diagonal pixels equally whereas the Sobel kernels weight the edge pixels more heavily. This form of the kernels is predicting horizontal and vertical gradients. The Robert's cross kernels have a form which looks to predict diagonal gradients. Here horizontal and vertical refer to looking at edges that are at 45° (anti-clockwise) to the horizontal and vertical axis. The convolution of an $m \times n$ kernel K and matrix A is defined as:

$$\begin{aligned}
K * A &= \begin{pmatrix} k_{1,1} & k_{1,2} & \cdots & k_{1,n} \\ k_{2,1} & k_{2,2} & \cdots & k_{2,n} \\ \vdots & \vdots & \ddots & \vdots \\ k_{m,1} & k_{m,2} & \cdots & k_{m,n} \end{pmatrix} * \begin{pmatrix} a_{1,1} & a_{1,2} & \cdots & a_{1,n} \\ a_{2,1} & a_{2,2} & \cdots & a_{2,n} \\ \vdots & \vdots & \ddots & \vdots \\ a_{m,1} & a_{m,2} & \cdots & a_{m,n} \end{pmatrix} \\
&= \sum_{i=0}^{m-1} \sum_{j=0}^{n-1} k_{(m-i)(n-j)} a_{(1+i)(1+j)}
\end{aligned}$$

The kernels are used to find gradients in both the horizontal (x) and vertical (y) directions of image intensity.

The Canny algorithm is different to the other methods in that a Gaussian

filter,

$$G(x, y) = \frac{1}{\sqrt{2\pi}\sigma} e^{-\left(\frac{x^2+y^2}{2\sigma^2}\right)} \quad (3.4)$$

is first applied to remove noise within the image. The parameter σ is a measure of how much the image will be blurred, with higher values indicating a greater blur. Once the Gaussian filter is applied the gradients are calculated by convolving the respective gradient of the Gaussian filter;

$$K_x^{canny} = -\frac{x}{\sigma^2} G(x, y), \quad K_y^{canny} = -\frac{y}{\sigma^2} G(x, y) \quad (3.5)$$

with the image.

Taking the horizontal Prewitt kernel and performing convolution with an image piece we obtain a horizontal gradient image (G_x). A vertical gradient image (G_y) is also obtained using the vertical kernel. Convolving the two Prewitt Gradient kernels with a typical schlieren image (Figure 3.6a) gives the results seen in Figure 3.6b and Fig 3.6c. After obtaining both gradients a magnitude and direction can be calculated using $G_{mag} = \sqrt{G_x^2 + G_y^2}$ and $\Theta = \arctan\left(\frac{G_y}{G_x}\right)$. The magnitude can also be seen in Figure 3.6d. A comparison of the gradient magnitude for the different filters when convolved with the schlieren frame can be seen in Figure 3.7.

Once the gradient magnitudes are calculate a threshold of gradient intensity is defined to determine the presence of an edge. Possible values can be either user-defined, taken as the maximum of gradient intensity, or defined as the root mean square (RMS) of noise. An approximation of the RMS of noise is found in Pratt (2001), using the mean of the gradient magnitude squared. Using this method the pixel where values of gradient magnitude are less than the threshold are set to 0 and those greater are set to 1.

The edges detected by the different methods can be seen in Figure 3.8. The Prewitt and Sobel methods both use maximum gradient intensity and therefore detect the spray region in near identical forms, which is also expected due to the

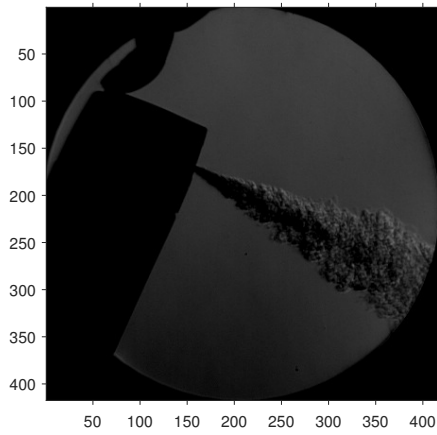
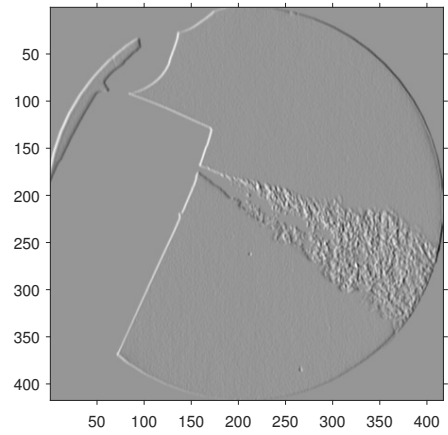
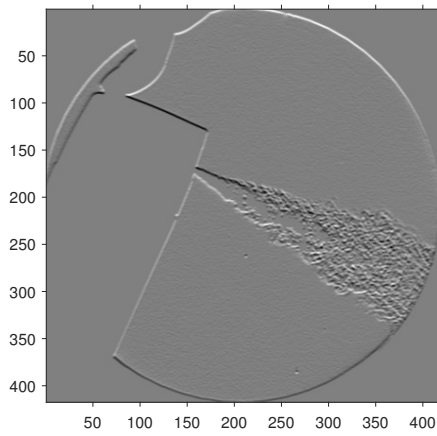
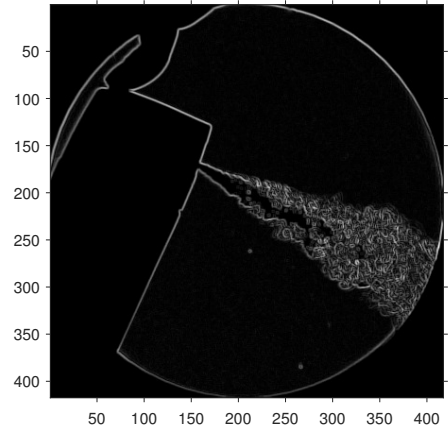
(a) Original Image (I)(b) Horizontal gradient: $G_x = K_x^{Prewitt} * I$ (c) Vertical gradient: $G_y = K_y^{Prewitt} * I$ (d) Gradient Magnitude: $G_{mag} = \sqrt{G_x^2 + G_y^2}$

Figure 3.6: (a) Original image captured from the schlieren experiments, (b) Convolution of the original image with the horizontal Prewitt kernel, (c) Convolution of the original image with the vertical Prewitt kernel, (d) Magnitude of the gradients.

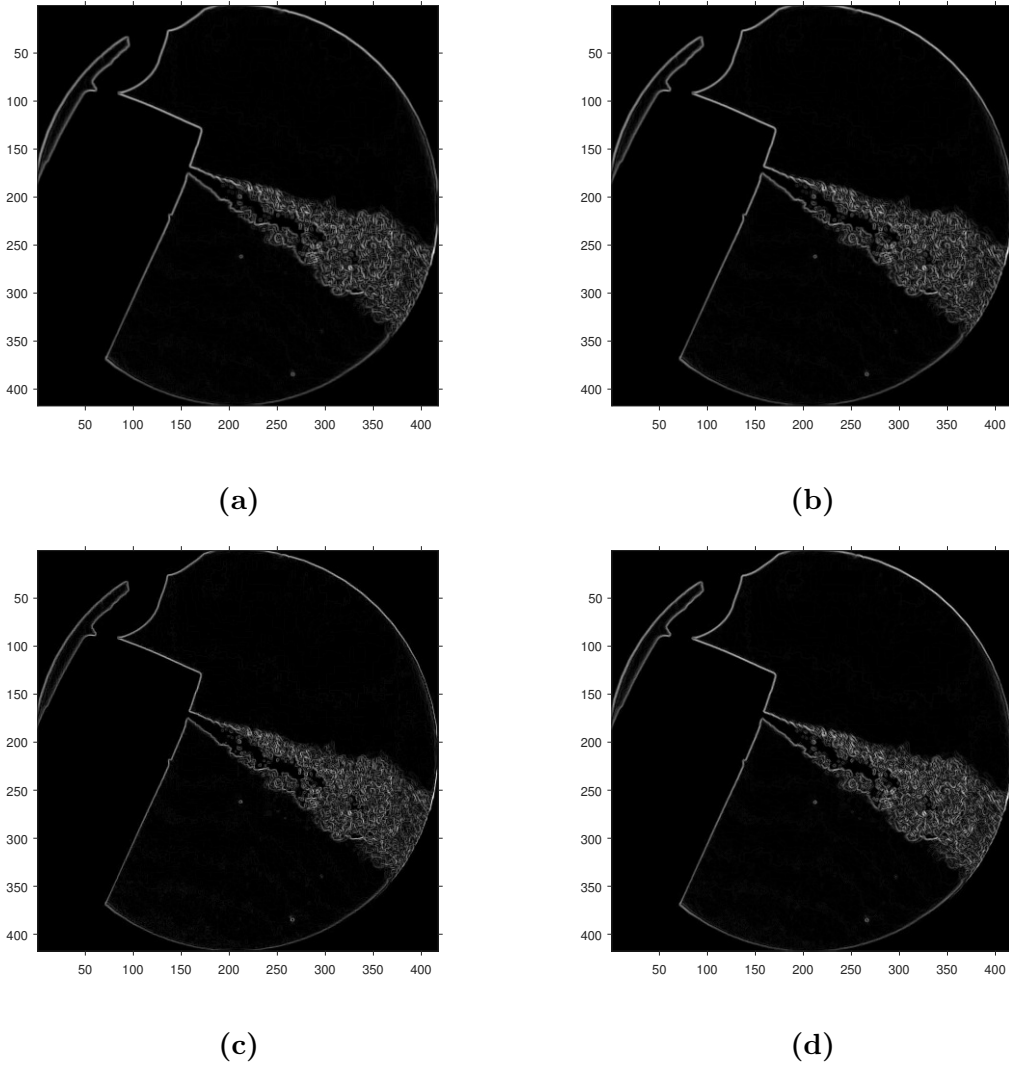


Figure 3.7: Gradient Magnitude resulting from the convolution with (a) Prewitt, (b) Sobel, (c) Roberts and (d) Canny filter with $\sigma = 0.036$.

similar kernel forms. The Robert's cross is also able to detect the spray region as it also uses maximum gradient intensity. The Canny method applied to our experiments is also able to identify the spray region, however it also detects the small differences in background lighting. This is due to the threshold selection and value of σ used within the filter. Due to the sensitivity of the Canny method and the comparable performance between the other filters the Sobel filter was arbitrarily chosen to determine the edge of the spray as there was no clear qualitative difference between the other three.

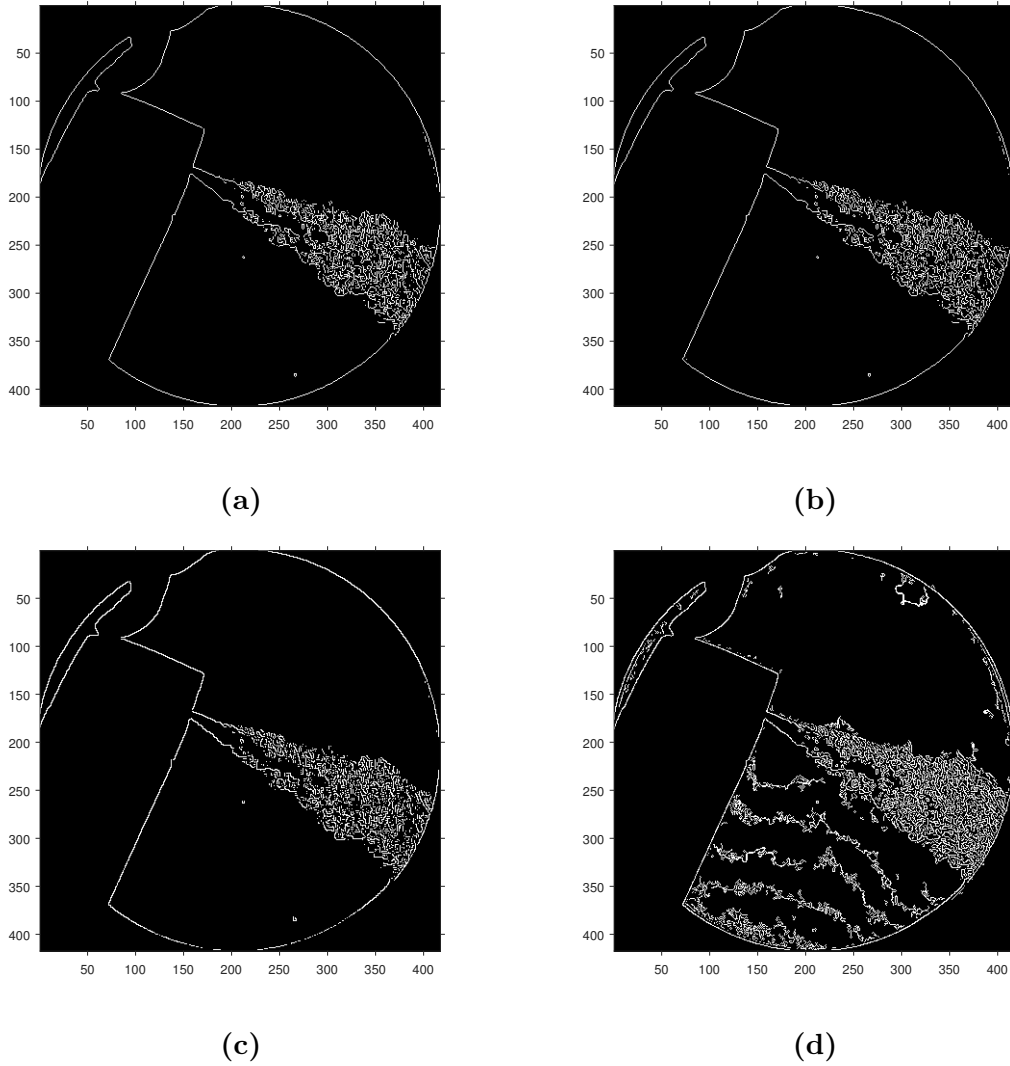


Figure 3.8: Edges detection using a threshold determined by Otsu's method. The edges for the different filters resulting from the convolution with (a) Prewitt, (b) Sobel, (c) Roberts and (d) Canny filter with $\sigma = 0.036$.

Spray Angle and Frame Averaging

During the fully activated spray period, pulsing of the spray can be observed in the videos. This is believed to be due to cavitation within nozzle with a repeating growth and collapse resulting from pressure variations from the evaporation of propellant. This phenomenon occurs more frequently for cans with the simple orifice nozzle, believed to be due to the internal flow dynamics where the swirl nozzles also entrain ambient air into the nozzle reducing this effect. To negate the influence of the pulsing on the fully activated spray period, pixel intensity values are averaged over for a number of frames to generate a time-averaged spray cone. Finding an average frame also provides a way of comparing with a steady carrier jet numerical model.

An automatic method for determining the spray region was created to allow for consistent frame selection and averaging. The circle locator algorithm is applied to the initial frame of the video, this provides the field of view of the mirror. A further reduction of the image is made where the spray region close to the nozzle is found, this is done by taking the position of the centre pixel and a region sufficiently large around it, approximately 1/4 of the frame's pixel width. Taking the spray region frame and applying Otsu's automatic thresholding algorithm provides a matrix of 1s and 0s. With this, the total number of zeros within the matrix is calculated. This process is applied for the entire video. The time series of total zero count is noisy due to the nature of the spray, therefore a Savitzky-Golay smoothing filter is applied convolving a set of 500 zero counts. The results for aerosol can 1D can be seen in Figure 3.9.

The smoothed zero count data provides a way of automatically detecting the spray generation and collapse. Taking the smoothed data, the maximum zero count within the first half of the total number of frames is determined to be where the fully activated spray region starts (N_{Start}) and the the maximum zero count in the final half is determined to be when the spray starts to collapse (N_{End}). The

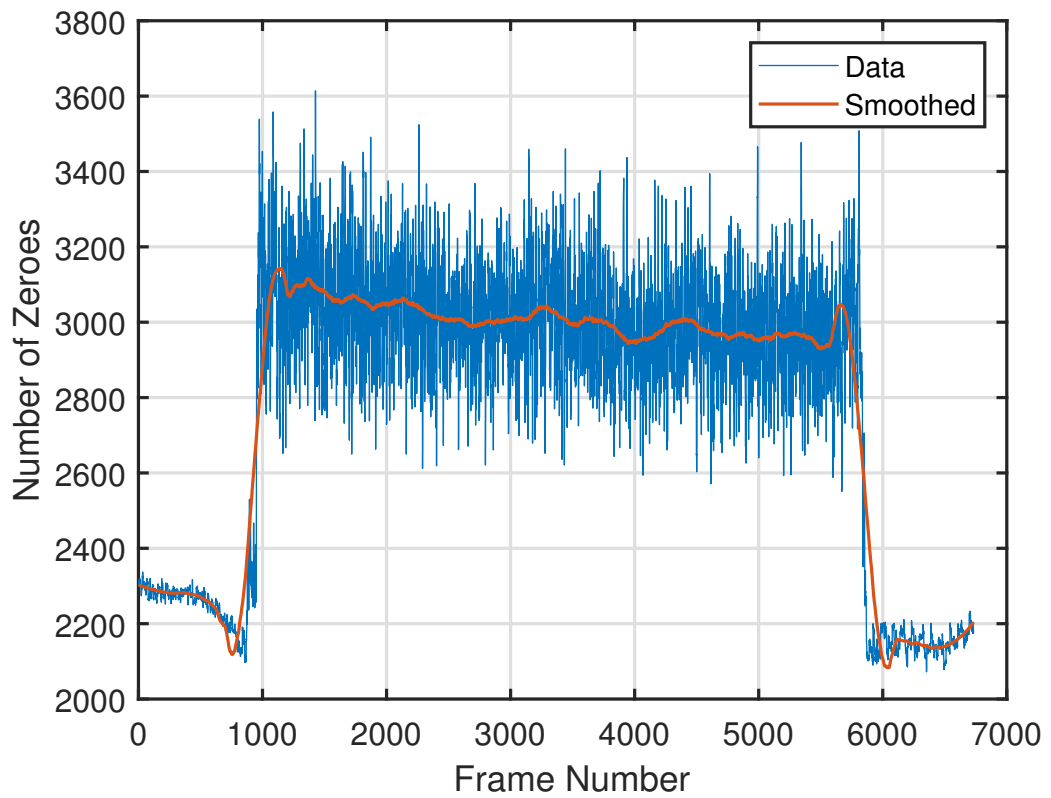


Figure 3.9: Number of total zeroes plotted against frame number for aerosol can 1D. Blue noisy line represents raw count of each frame. Orange line shows smoothed data after applying Savitzky-Golay smoothing filter.

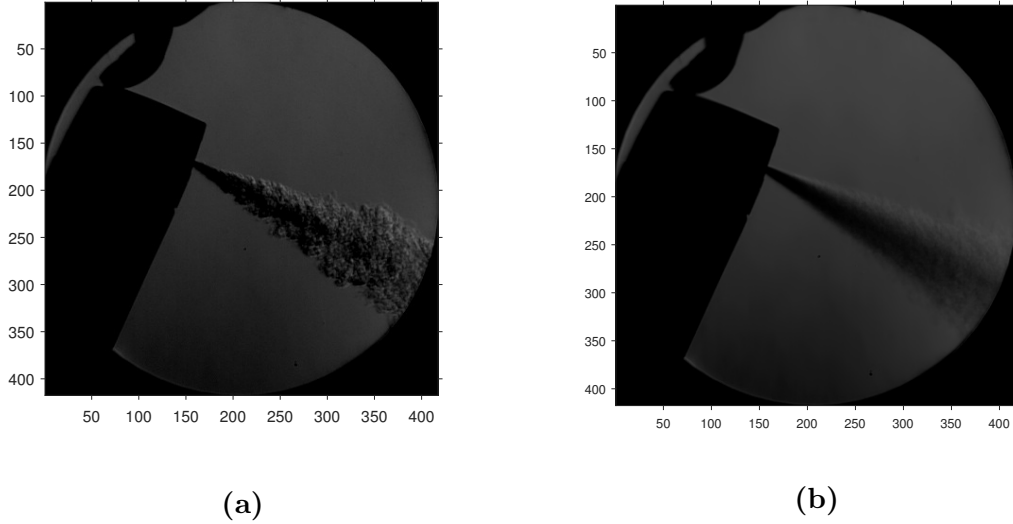


Figure 3.10: Greyscale image of (a) the mid frame of aerosol can 1D (b) averaged frame of aerosol can 1D.

middle frame of the spray is also determined as the average of the start and end of the fully activated spray region. More precisely these are defined as,

$$N_{Start} = \max(Zsm_i), i = 1, \dots, \frac{N_{Total}}{2} \quad (3.6)$$

$$N_{End} = \max(Zsm_i), i = \frac{N_{Total}}{2}, \dots, N_{Total} \quad (3.7)$$

$$N_{Mid} = \frac{N_{Start} + N_{End}}{2} \quad (3.8)$$

where Zsm_i is the smoothed zero count for frame i and the N_{Total} is the total number of frames of the video. From the middle frame of the fully activated spray region $\frac{N_{range}}{2}$ frames are taken before and after N_{Mid} . The greyscale intensity values of each pixel are averaged over a range of frames centered at the middle frame. This gives an averaged representation of the spray generated for that can. An example of the middle frame and averaged frame can be seen in Figure 3.10.

The spray angle is measured manually. Here the edge detected images are imported into ImageJ, an image processing software. ImageJ has an angle measuring tool where 3 points A,B and C are manually defined and the angle generated by ABC ($\angle ABC$) is measured. An example can be seen in Figure 3.11 for the middle frame

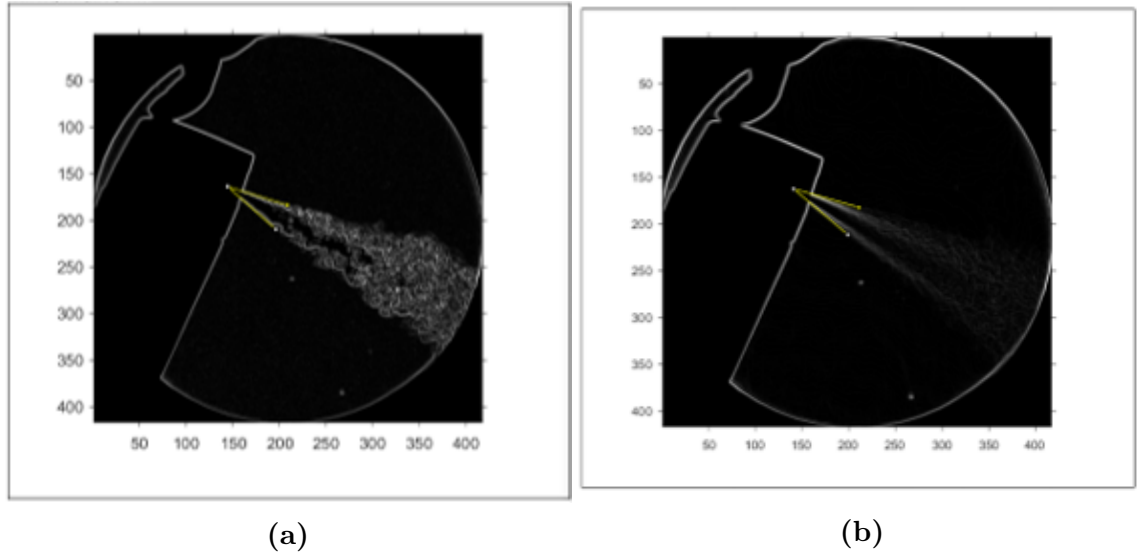


Figure 3.11: Important image into ImageJ with angle measuring lines for (a) the mid frame of aerosol can 1D (b) averaged frame of aerosol can 1D.

of aerosol can 1D and an averaged frame. The angle measured is sensitive to the positioning of the B point which represents the virtual origin of the spray. In order to ensure as consistent angle as possible, a repeatable routine was used to define the virtual origin. Two straight lines are generated manually, one for the top of the spray and the other for the bottom of the spray. For each line, two construction points are generated, one at the intersection of the aerosol can and spray, and the other at a point on the spray boundary. Once these lines are constructed their extruded intersection is deemed to be the virtual origin location for the spray angle calculation.

Spray Stages

After the initial actuation of the different aerosol cans there are 3 key spray stages which can be identified and observed in the experimental videos. The three stages are classified as the: generation stage, fully-developed stage and collapse stage. The generation stage captures the initial vapour release and subsequent product release which then transitions to the fully-developed stage. The fully-developed stage describes the main stage of the spray process where the aerosol can is fully actuated for the longest duration of the spray time and as such is the main stage

of interest, demonstrating the spray structure during the breakup and transport of the product. The spray collapse stage is the final stage of the process and shows the actuator release and the collapse of the spray due to the reduction in momentum and mass.

3.2.2 Determining Droplet Size

The initial sizes of droplets generated from spray devices are dependant on the breakup of the fluid, which itself is governed by the physical properties of the fluid, nozzle type and ambient conditions. Due to the limited data on droplet sizes generated from aerosol cans, Spraytec experiments are performed. This section details the Spraytec device and its applications. The experimental procedure undertaken is detailed and finally the fitting procedure of different particle size distributions is reported and discussed for the different nozzles and fluid blends found in Table 3.1.

Spraytec Device

The Malvern Spraytec is a laser diffraction system which allows for rapid measurements of particle sizes of spray systems to be taken. The device is able to measure sizes ranging from 0.1-2000 μm at a rate of 2.5 kHz (increasing to 10 kHz with a software key). A Helium-Neon laser is transmitted from the transmitter module to the detector module. As the droplets pass the laser the laser light is diffracted. This diffracted light is then measured at a range of angles using a series of detectors. Using the Fraunhofer approximation and Mie theory the diffraction patterns detected provide the droplet sizes which have passed the laser. The droplet size distribution generated is volume based, where droplets are binned by diameter with volume fractions of the total volume.

Experimental Setup

The aim of this experiment is to measure the particle size distribution (PSD) at different axial positions throughout the spray cone. The axial positions investigated are 1 cm, 2 cm, 5 cm, 10 cm, 15 cm and 20 cm from the nozzle orifice. The cans are held in place using a clamp and vertically positioned such that the nozzle is vertically inline with the laser. The axial distance is measured using a ruler,

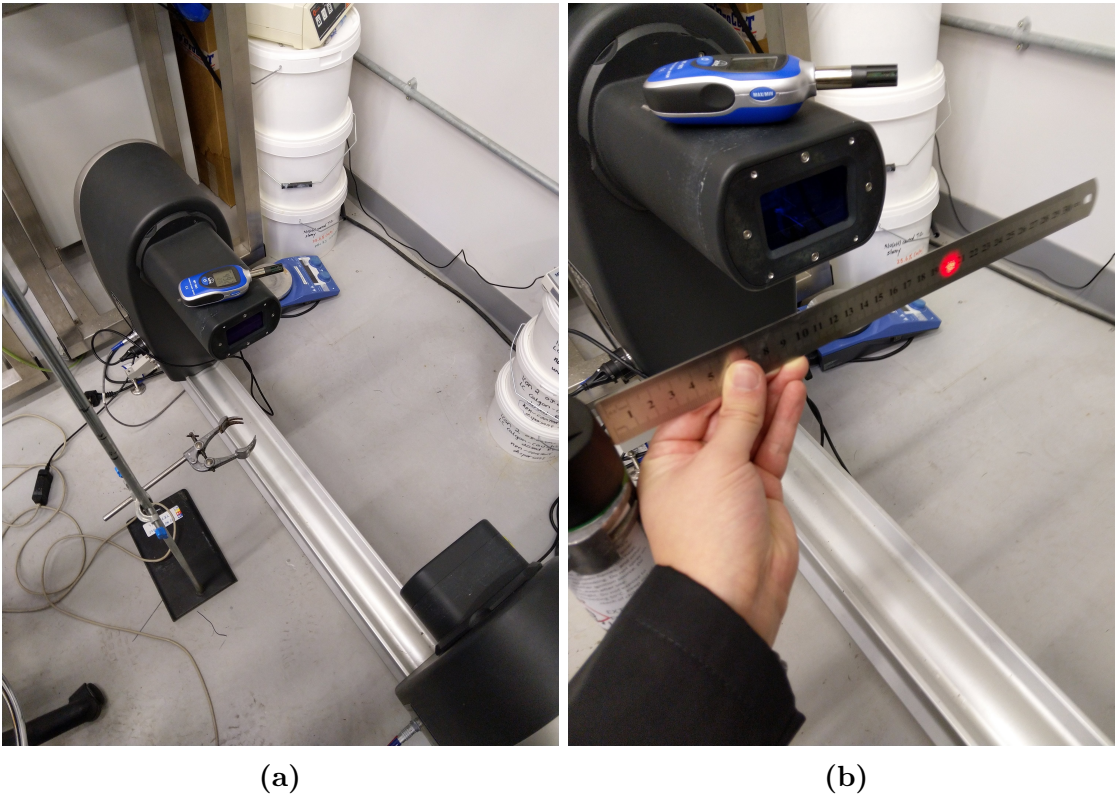


Figure 3.12: Images of the spraytec setup (a) the positioning of the spraytec device and clamp stand (b) the aligning process of the aerosol can.

positioning one end against the aerosol can orifice and moving the clamp stand until the laser meets the axial distance required, as seen in Figure 3.12b. Once the can is positioned it is taken out of the clamp and shaken for approximately 5 seconds to mix the formulation, after which the can is placed back into the clamp at the preset position. The humidity and temperature are then recorded using an ATP MT-903 Pocket Thermo-Hygrometer. These conditions were not controlled throughout the experiments but were measured to provide environmental data. The can is then actuated until the Spraytec software has recorded 2 seconds of data.

Spraytec software V4.0 is used where a Standard Operating Procedure (SOP) is generated. This provides quick and consistent setup of the Spraytec recording software. The data acquisition is set to rapid, which allows for the highest sampling rate of 2.5 kHz. The lens type is set to 300 mm, this is because the droplets generated are expected to be within the range 0.1-900 μm and this lens captures those sizes. The measurement trigger is set such that when the transmission level

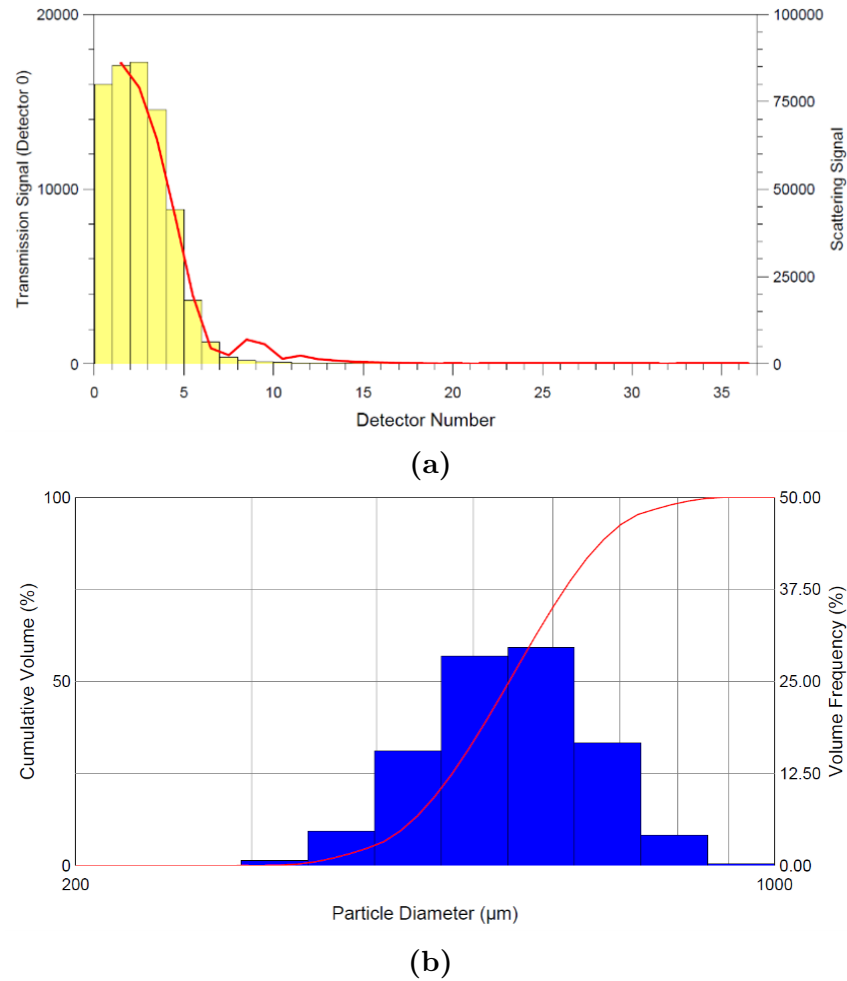


Figure 3.13: (a) Detector 0 transmission signal and scattering signal when all detectors are used. (b) Resultant volume based particle size distribution from signal shown in (a).

drops below 80%, the software begins to record. The termination time is also set to 2 s to record for the desired period of time.

The angle of diffraction is dependant on the size of the droplet. Large droplets have a smaller diffraction angle whereas small droplets have a greater one (Lefebvre and McDonell (2017)). An issue with using laser diffraction methods for measuring sprays generated from alkane-based propellants is the refraction of the laser. In this case refraction occurs due to changes in density from the ambient air to the denser propellants. Whereas this made the schlieren technique viable, here it presents a problem.

Experimental Procedure

For each run the following procedure was followed:

1. Calibrate/activate spraytec device, this is to ensure the lens is clean and calculate any potential background noise. If the detector light measurements do not show an inverse log decay then the lens is cleaned appropriately.
2. Measure the initial mass of the aerosol can, this provides an initial measurement to later determine the average mass flow rate of the can.
3. Align the aerosol can and clamp stand for the required axial position, this is done to ensure correct axial measurements for each run.
4. Measure the RH and temperature of the ambient to provide ambient conditions of the experimental measurements.
5. Shake aerosol can for 5 seconds to adequately mix the product/propellant mixture within the aerosol can.
6. Reposition the aerosol can in the clamp stand, this is the final position for the experiment.
7. Actuate the aerosol can, here the Spraytec trigger will start the recording software after the transmission to the zeroth detector drops below 80%.
8. Stop actuation after the 2 seconds of Spraytec recording is complete.
9. Measure the final mass of the aerosol can, this is to provide the necessary measurement for calculating the mass flow rate over the 2 second period.
10. Repeat steps 1-9 for each aerosol can for a total of 3 runs per axial position desired.

Beam Steering Issues

As the laser passes through the spray it is refracted, resulting in the detectors close to the centre reading a larger intensity of light due to the laser's refraction. This is known as beam steering. The refraction of light to the central detectors increases the intensity of the light measured there. As large droplets have a smaller refraction angle the calculation of PSD is considerably overestimated for the larger droplets. An example of the resulting scattering signal from spraying aerosol can 1D at an axial position of 5 cm can be seen in Figure 3.13a where the scattering signal is dominated by detectors 1-5. The scattering signal observed in Figure 3.13a results in a size distribution shown in Figure 3.13b where the cumulative distribution is shown as the red line and volume fraction for sizes is shown in the histogram. The particle sizes predicted as shown in Figure 3.13b are considerably larger than the expected D_{50} of $15 - 25\mu m$ stated in Nasr et al. (2013). This is an indication that beam steering is an issue here.

Wittner et al. (2018) addresses beam steering and discusses the standard approach of shutting off detectors, as well as an approach of fitting a multimodal log-normal distribution to isolate the non beam steering part of the distribution. Due to the considerably high levels of beam steering observed here, the method opted for in this case is the standard approach of switching off detector numbers near the centre.

To investigate the influence of detector number range, the cumulative distribution is plotted for a range of detector starting numbers up to the final detector number of 36. The resulting cumulative distributions can be seen in Figure 3.14.

By taking the entire detector range the line 1-36 shows the cumulative distribution generated and the effects of beam steering. The considerable over-prediction of the droplet size is observed. As the lower limit of detector number is increased, the distribution transitions from a unimodal distribution to a trimodal distribution observed for the range 10-36, seen in 3.15.

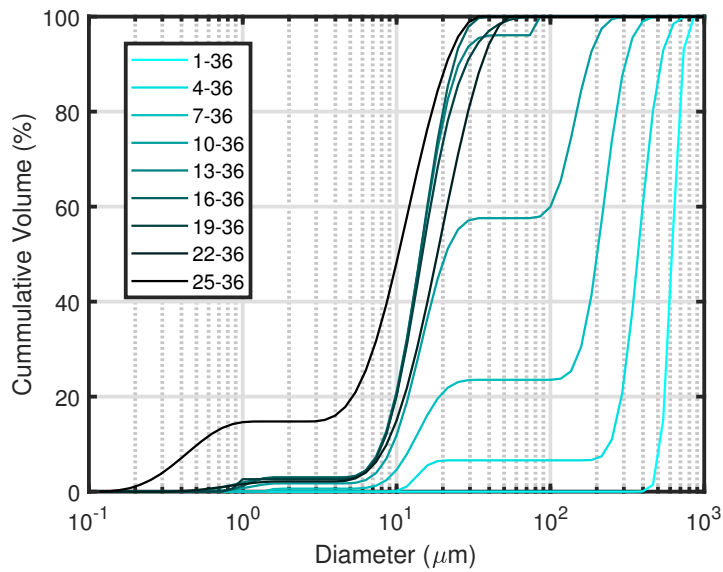


Figure 3.14: Cumulative volume distribution from varying lower detector number of the Spraytec device.

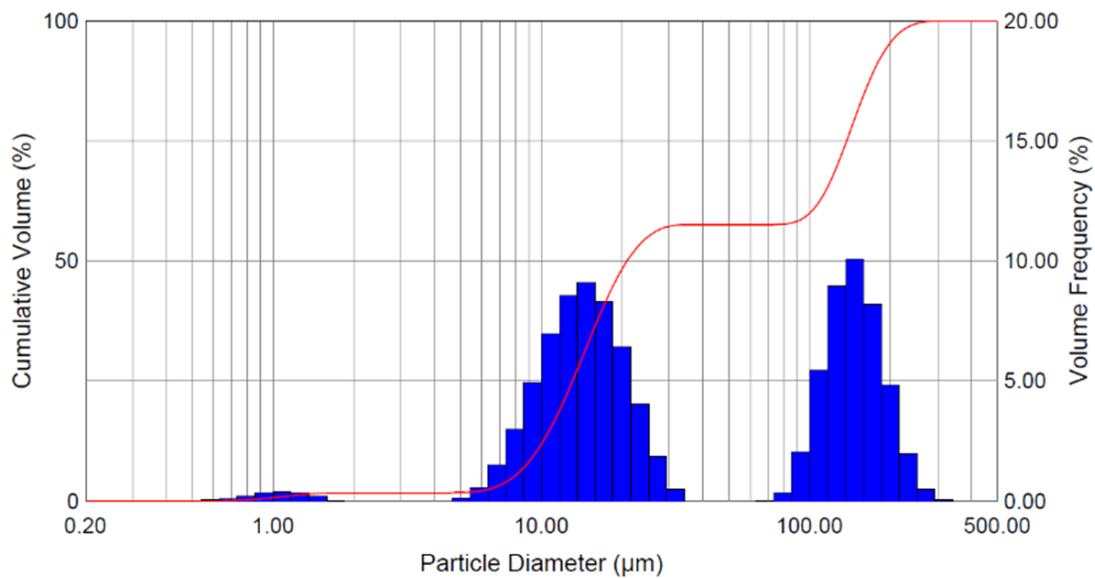


Figure 3.15: Distributions for the detector range 10-36, blue histogram showing particle size distribution and red line showing cumulative distribution.

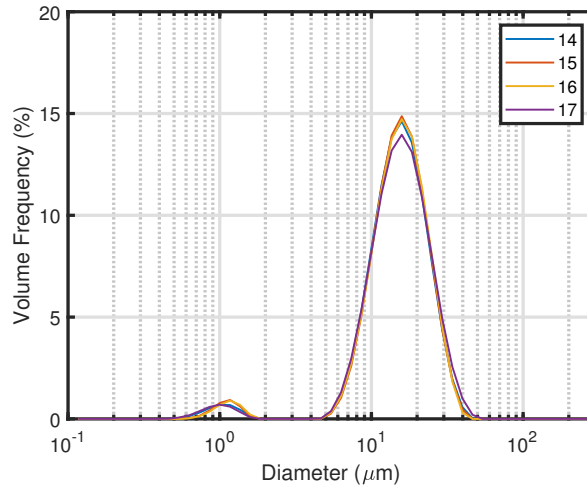


Figure 3.16: Particle size distribution for different low detector number limit of, 14, 15,16 and 17.

One of the three modes in this distribution is considered to be representative of the droplet sizes generated from the aerosol can. The large mode is considered to be an impact of beam steering, resulting in a need for a further increase in lower detector number. The lower mode is assumed to be due to dust and other airborne particulates which are being entrained into the spray during measurements. The middle mode is considered to represent the droplets generated from the aerosol can, with size ranges in agreement with [Nasr et al. \(2013\)](#). The work of [Bertholon et al. \(2015\)](#) found a mass median aerodynamic diameter (MMAD) between 0.3-2.79 μm for air freshener aerosol cans, which fit within the lower mode here. However, air fresheners are designed to generate droplets small enough to stay suspended in the air over longer time periods which accounts for this discrepancy.

As the lower limit is increased, there exists a range at which the important central mode dominates, as seen in [Figure 3.14](#). Between detector ranges 14-36 and 17-36 the contribution due to beam steering is eliminated. The lower mode however is present intermittently during the measurements and cannot be eliminated entirely without further data manipulation. [Figure 3.16](#) shows the volume particle size distribution for lower limits 14,15,16 and 17. The lower mode is still present but is still considered to be due to entrainment of ambient contaminants. Detector

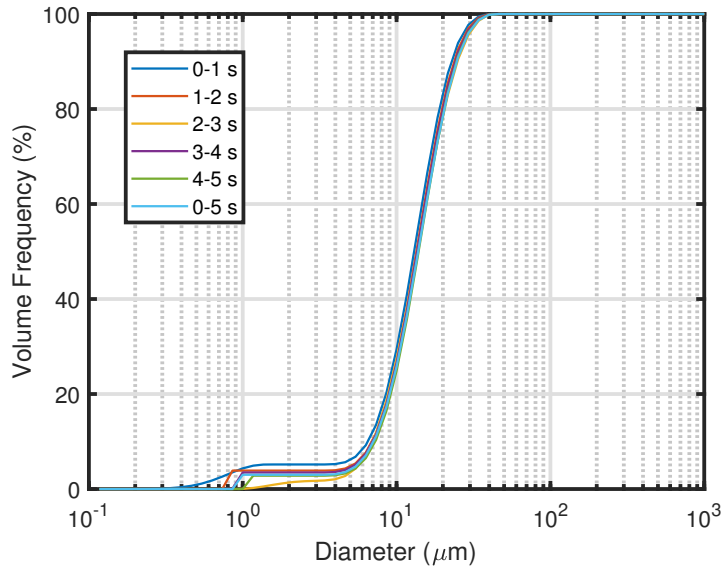


Figure 3.17: Cumulative distribution for varied averaging periods within a 5 second spray: 0-1 s, 1-2 s, 2-3 s, 3-4 s, 4-5 s and 0-5 s.

lower limits of 14,15 and 16 give comparable results, therefore a lower limit of 15 was chosen for the Spraytec experiments.

Time Averaging Sensitivity

A 5 second spray was measured for aerosol can 1D at an axial position 1 cm to determine the influence of when the averaging process is taken. The resulting distributions were averaged over five 1 second intervals for the entire 5 second spray period, resulting in 5 separate averages. The average over the entire spray period was also calculated. The resulting cumulative volume distribution can be seen in Figure 3.17. The resulting distributions show some variation between them with increasing droplet size as the spray time increases. This is likely due to the slight drop in pressure in the can during actuation. The variation seen is not considered significant and averaging within the 2 second spray period is therefore considered appropriate for capturing a representation of droplet sizes at the given axial positions.

Particle Statistics

To fully understand the data produced, several typical measures are used which provide additional detail and insight into the size distributions measured. The particle statistics measured are the 10, 50 and 90 percentiles (D_{10} , D_{50} , D_{90}), span, Sauter mean diameter (SMD, $D_{3,2}$) and volume mean diameter ($D_{4,3}$). The percentiles are defined as the diameter at which below the given percent of the spray volume lies. The span gives a representation of the spread of the distribution and is defined as

$$span = \frac{D_{90} - D_{10}}{D_{50}}. \quad (3.9)$$

The $D_{3,2}$ and $D_{4,3}$ are defined as:

$$D_{p,q}^{p-q} = \frac{\sum_i d_i^p n_i}{\sum_i d_i^q n_i} \quad (3.10)$$

where d_i is the representative diameter for class i and n_i is the number of droplets in class i .

The data acquired provides a particle size distribution (PSD) along with the cumulative size distribution (CSD). An example for aerosol can 1D is shown in Figure 3.18. The PSD exhibits a right-tailed log-normal shape where the largest volume fractions are measured close to the particle statistic measures. Figure 3.18 also shows the D_{50} , $D_{3,2}$ and $D_{4,3}$ for this data. D_{50} crosses where the cumulative distribution is at 50% which holds by definition. The other measures, $D_{3,2}$ and $D_{4,3}$, can be seen below and above the D_{50} respectively. The data is exported from Spraytec Software V4.0 and imported into MATLAB R2018b where all post-processing is performed.

Repeatability

Figure 3.19 shows the CSD measured by the Spraytec device for aerosol can 1C at the axial positions investigated. The repeatability of the different runs

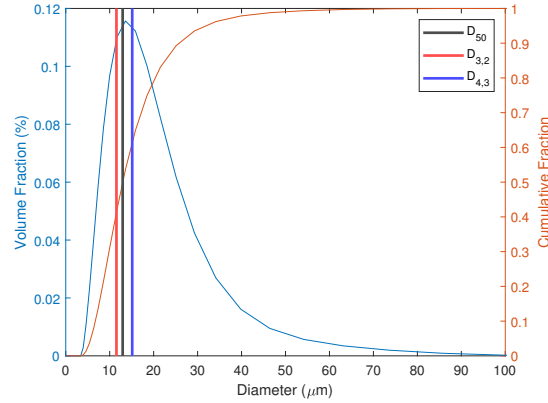


Figure 3.18: The measured volume frequency and cumulative frequency from the Spraytec device for aerosol can 1D at 1cm. The D_{50} , $D_{3,2}$ and $D_{4,3}$ are also plotted.

is demonstrated with nearly all of the distributions measured falling close to the other measurements at each axial distance. One example where significant variation

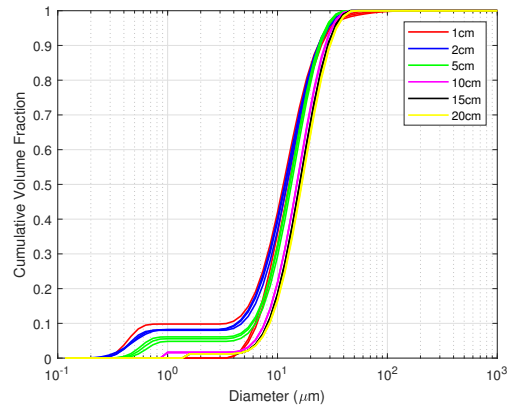


Figure 3.19: The CSD measured by the Spraytec device at the different axial positions tested: [1, 2, 5, 10, 15, 20] cm for can 1C.

is observed, however, is for the CSD measured at 1 cm. When the small mode is present this impacts the point where the initial fraction is observed. For two of the runs at 1 cm the smallest mode isn't observed. This shows some sensitivity to the measurements and care is therefore needed for when this small mode appears in the measured distributions.

Fitting Distributions

Fitting a distribution to particle data provides a way of representing the data with respect to a Probability Distribution Function (PDF) and Cumulative

Distribution Function (CDF). Depending on the distribution used it is possible to reduce the information needed to represent the entire data set down to a number of parameters. The Rosin-Rammler (Rosin and Rammler, 1933) and Log-normal (Lefebvre and McDonell, 2017) are two popular two-parameter distributions which are used extensively for representing particle size distributions of sprays. The work of Villermaux (2006) has shown that the Gamma distribution also provides a good fit to droplet sizes generated from sprays, therefore these three are the distributions investigated. The form of the PDF and CDF as well as the distribution parameters are given in Table 3.4.

	PDF	CDF	Parameters
Rosin-Rammler	$f(x) = \frac{k_r}{\lambda} \left(\frac{x}{\lambda}\right)^{k_r-1} e^{-\left(\frac{x}{\lambda}\right)^{k_r}}$	$F(x) = 1 - e^{-\left(\frac{x}{\lambda}\right)^{k_r}}$	k_r, λ
Log-normal	$f(x) = \frac{1}{x\sigma\sqrt{2\pi}} \exp\left(-\frac{(\ln(x)-\mu)^2}{2\sigma^2}\right)$	$F(x) = \frac{1}{2} + \frac{1}{2} \operatorname{erf}\left(\frac{\ln(x)-\mu}{\sqrt{2}\sigma}\right)$	μ, σ
Gamma	$f(x) = \frac{1}{\Gamma(k_g)\theta^{k_g}} x^{k_g-1} e^{-\frac{x}{\theta}}$	$F(x) = \frac{1}{\Gamma(k_g)} \gamma\left(k_g, \frac{x}{\theta}\right)$	k_g, θ

Table 3.4: The probability distribution function (PDF) and cumulative distribution function (CDF), including their parameters, for the Rosin Rammler, Log-normal and Gamma distributions.

In Table 3.4 the Gamma distribution contains both the Gamma function ($\Gamma(k_g)$) and the lower incomplete Gamma function ($\gamma(k_g, \frac{x}{\theta})$). These functions take the form

$$\Gamma(k) = \int_0^{\infty} t^{k-1} e^{-t} dt \quad \text{and} \quad \gamma(k_g, \frac{x}{\theta}) = \int_0^{\frac{x}{\theta}} t^{k_g-1} e^{-t} dt.$$

From the exported data if the small mode is present then those size bins are set to zero to avoid any issues of attempting to fit a unimodal distribution to it. As the distributions being fit are normalised (the integral over the size range equals unity) the same has to be done for the measured distributions. To achieve this the bin frequency is divided by the total area of the PSD which is found by integrating over the measured distribution using the trapezium rule. The manipulation to isolate

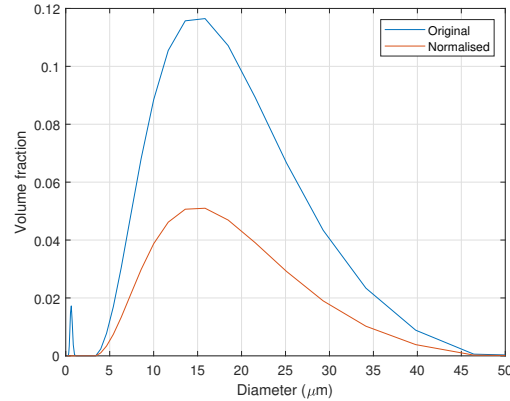


Figure 3.20: Original measured distribution from aerosol can 1C at 2 cm Vs the normalised distribution isolating the main mode.

the main mode and to normalise the data is performed for each of the runs. An example of the distribution before and after manipulation can be seen in Figure 3.20. Here any contribution from the lower mode is eliminated but the shape of the main mode is preserved.

The normalised data is passed into MATLAB R2018b. The PDFs to fit are defined within fit types using the `wblpdf`, `lognpdf` and `gampdf` inbuilt functions. The fit types and normalised data are passed into the `fit` function from the Curve fitting toolbox. Here a non-linear least squares method is used with the trust-region algorithm described in Coleman and Li (1996) to stop once a tolerance of 10^{-12} is reached or, to prevent infinite loops, setting the maximum number of iterations to 10^4 .

Sampling From Fitted Distributions

Taking the distributions generated, the inverse CDF is then used to sample from the fitted distributions. This is done by first generating a set of N numbers uniformly distributed from 0 to 1 and passing the set through the inverse CDF of the distributions. To generate the set of N numbers the MATLAB function `rand` is used which generates the set of N uniformly distributed pseudorandom numbers. The inverse CDF functions within MATLAB, `wblinv`, `logninv` and `gaminv` are then

used to generate the set of droplet sizes sampled from the distribution.

3.2.3 Spray Temperature Measurements

The temperature field of a spray plays an important role in the evaporation of the droplets and the resultant impact and carry-over. This section looks to detail the experimental procedure of measuring the temperature along the centreline of the sprays generated by the different fluids and nozzle types. From [Camp et al. \(2003\)](#) and [Lacour and Coultre \(1991\)](#) the temperatures generated from alkane propellant based aerosol cans is expected to reach around -40°C , believed to be due to the boiling point of propane at -42.2°C . T-Type thermocouples are used here, because of their accuracy and that they can record temperatures in the region of the predicted minimum temperature. The experimental methodology is first discussed, looking at measurements and the sensitivity of both mineral insulated T-type thermocouples and exposed T-type thermocouples (thermocouples as seen in Figure 3.21). Then a comparison of the results for the different contents and nozzle types are discussed.



Figure 3.21: A comparison of the mineral insulated T-Type thermocouple (top) with the bare T-Type thermocouple (bottom).

Experimental Setup

To support the thermocouples, a stand of length 25 cm and height 15 cm is constructed. Five thermocouples are then taped in place with a distance of 1cm from the first thermocouple to the nozzle, 4 cm between the first two thermocouples and a distance of 5 cm between each of the remaining thermocouples. These distances

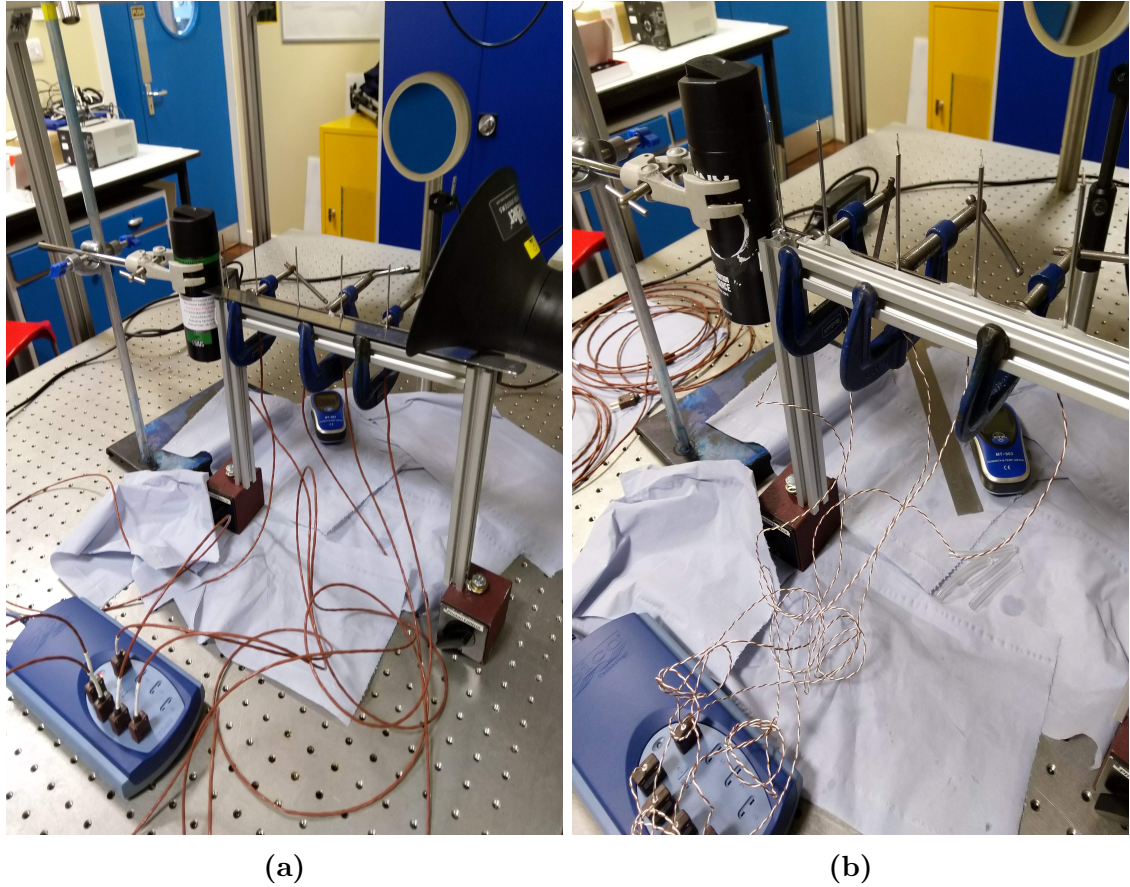


Figure 3.22: The thermocouple setup for (a) insulated T type thermocouples (b) exposed T type thermocouples.

were chosen to ensure an even spread along the spray centreline. A final support is clamped to the other side of the thermocouples to fix them in place, in the event the adhesive of the tape is dissolved by the spray. Downstream of the aerosol can a Weller extractor is positioned to prevent the risk of user exposure to the sprays. This set up can be seen in Figure 3.22. The temperature data is logged by a Pico TC-08 thermocouple data logger to which the five thermocouples are connected. Using the Picolog software the data is recorded at a rate of 10 Hz for each of the thermocouples. The humidity and temperature of the room were also measured at the beginning of each run before spray actuation using an ATP MT-903 Pocket Thermo-Hygrometer.

Experimental Procedure

The thermocouple experimental procedure follows the steps:

1. Shake aerosol can and position 1 cm from the first thermocouple and align vertically. This is the starting point of each run and allows for a good mixture of the can contents.
2. Start the recording software. Due to actuating the aerosol cans manually the recording software is started in advance.
3. Actuate the aerosol can until the thermocouple readings become steady. Looking at the continuous output from the recording software provides the point at which the readings become approximately steady and the point at where to release the aerosol can's actuator.
4. Stop recording software after a warmup period of approximately 1-2 minutes. This provides additional data of the warmup period of the thermocouples.
5. Allow thermocouples to reach the starting room temperature again and wipe off any residue that has deposited onto the thermocouples. By cleaning the thermocouples after each run it minimises any product which has impinged on the thermocouples thus potentially impacting their thermal conduction and outputs.
6. Repeat steps 1-5 three times. This is to provide repeatability statistics for the experiments.

Data Processing

The results are exported from the Picolog software and post-processed in MATLAB R2018b. An example plot of a set of three runs can be seen in Figure 3.23. Here the point of actuation is found by determining the point at which the gradient ($^{\circ}C/s$)

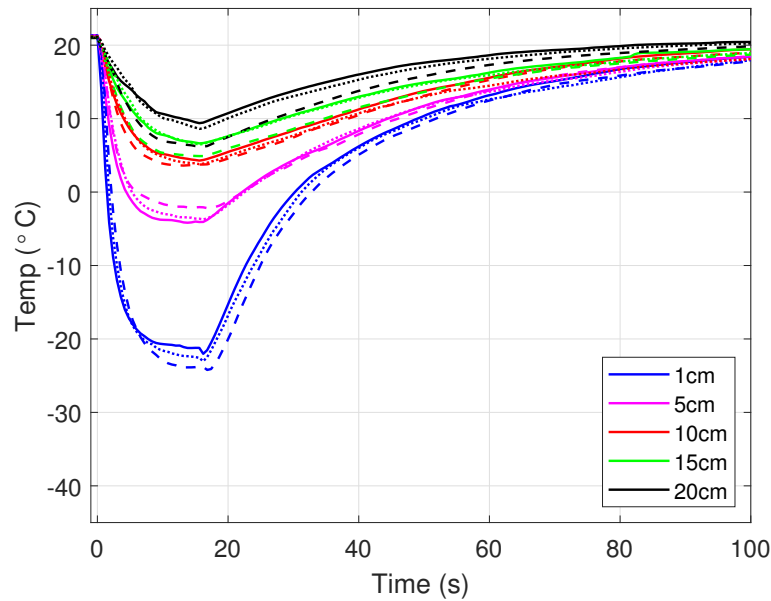


Figure 3.23: T-type thermocouple readings for three runs with thermocouples axially positioned at 1cm, 5cm, 10cm, 15cm and 20cm after actuation of can 1D. Bold line is the first run, dashed line is the second run and dotted line the third run.

is lower than -10 (arbitrarily small threshold), this actuation point is then plotted at time $t=0$.

In Figure 3.23 the temperature measured by the insulated thermocouples is shown for a set of three runs. The spray is actuated for approximately 17-20 seconds in order to reach a steady temperature. This spray time is due to the insulated thermocouples taking time to conduct the temperature through the insulation and to the thermocouple wires. Each run is consistent with the others, showing confidence in repeatability.

Position and Type Influence

To investigate the influence of the thermocouples themselves on the flow and the resultant temperature readings, two runs are performed with the full deodorant product (1D). The first set takes the distance of the nozzle to the first thermocouple to be 1 cm and a second set to have a distance of 5 cm to the first thermocouple. The 5 cm distance is chosen to compare with the readings from the

Setup	Nozzle position	First thermocouple position
1	At tip	1 cm
2	At tip	5 cm
3	Below Tip	1 cm
4	Below Tip	5 cm

Table 3.5: Nozzle position and first thermocouple position for the four different setups tested.

second thermocouple of the 1 cm set. As well as this, the vertical alignment of the nozzle changes as the can is actuated (decreasing after actuation), the influence of nozzle height on the insulated thermocouple is also investigated by another set of two runs by positioning the can such that the nozzle orifice is aligned with the tip of the thermocouple before actuation and also after actuation. This gives us 4 variations, seen in Table 3.5. This allows comparison of vertical height sprayed at the insulated thermocouple and thermocouple flow impingement influence on the readings.

For each set of n results, for the setups given in Table 3.5, the minimum temperature measurement of each thermocouple is taken. From this a mean (μ_m) and corrected sample standard deviation (σ) is calculated following the definitions,

$$\mu_m = \frac{1}{3} \sum_{n=1}^3 \min(T_n) \quad \text{and} \quad \sigma = \sqrt{\frac{1}{2} \sum_{n=1}^3 |\min(T_n) - \mu_m|^2}. \quad (3.11)$$

These are then plotted for the different axial positions and can be seen in Figure 3.24, which also shows that depending on the position of the nozzle after actuation the measured minimum temperature value is different. A lower temperature reading is found for spraying at the tip of the insulated thermocouple compared to 1cm below it. The difference is due to the position of the thermocouple wires inside the insulated thermocouple and the thermal conduction of the insulation. If the can was actuated for a longer period of time these values would converge to some common value, however the current set-up doesn't allow for this due to limited number of cans available for testing.

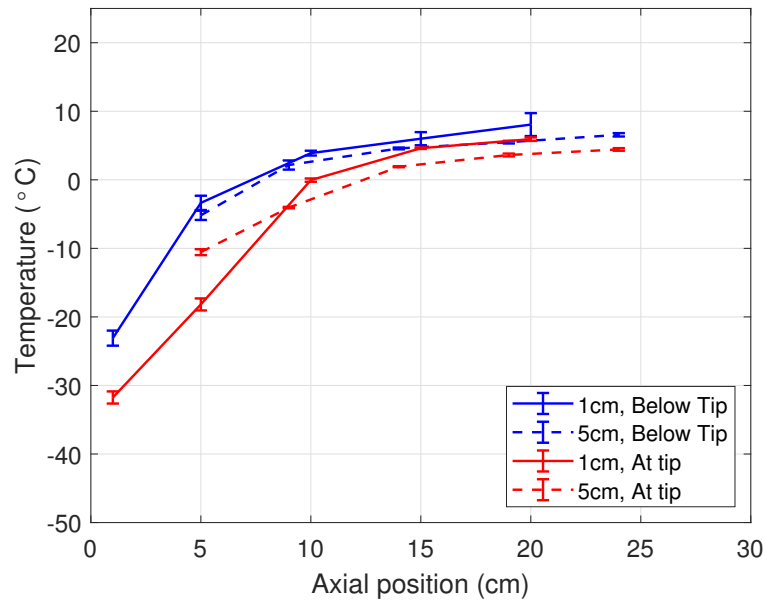


Figure 3.24: Mean minimum thermocouple temperature for nozzle position at the tip (Red) of the thermocouple or 1 cm below (Blue), with the first thermocouple positioned at either 1 cm from the nozzle (Solid) or 5 cm (dashed) using can 1D.

The dashed lines in Figure 3.24 represent the temperature results from moving the entire thermocouple set by 4 cm so that the first thermocouple is at a position of 5 cm and the distances between the thermocouples remain the same. The thermocouple bodies are shown to influence the flow itself and in turn the temperature readings from them. The experiment is performed with bare thermocouples to investigate the sensitivity of the equipment but also the difference in temperature measurements. Figure 3.25a shows the temperature readings for the insulated thermocouples and bare thermocouples. The time it takes to reach steady state is considerably quicker for the bare thermocouples as there is no need for thermal conduction through the insulation. This change results in a decrease in the required spraying time by a factor of 5. The results show good agreement close to the nozzle for the 1cm case. The bare thermocouples have less impact on the flow as they are smaller and therefore less intrusive, and as a result the thermocouples downstream also show good agreement with the 5cm case. Future experiments are performed with the bare thermocouples.

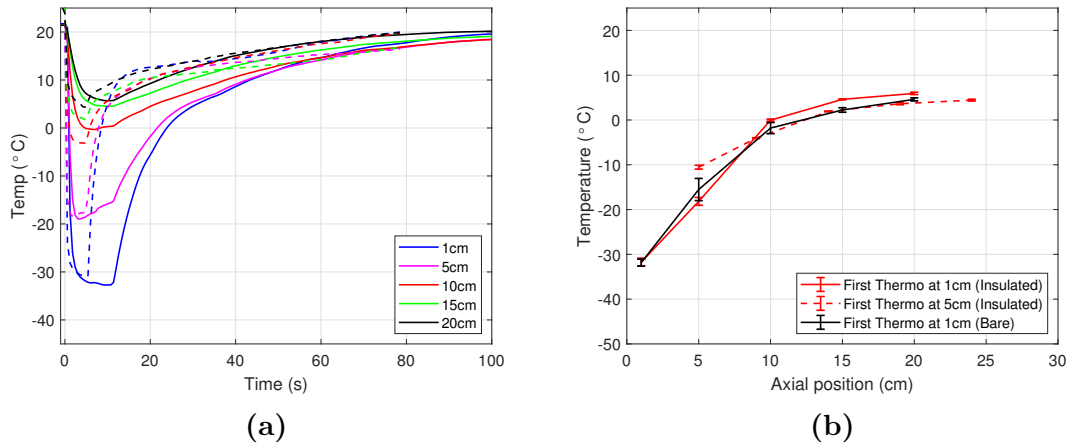


Figure 3.25: (a) Full time series of temperature measurements for both insulated (solid) and bare (dashed) T-type thermocouples using can 1D. (b) Mean minimum values of temperature from a set of 3 experiments with both bare and insulated T-type thermocouples at different axial positions using can 1D.

3.3 Results

In this section the results from each of the experimental methodologies is discussed. Firstly the schlieren results, then the Spraytec results and finally the thermocouple results.

3.3.1 Schlieren Imaging Results

Various spray features were investigated using the schlieren experiments, including the development of the spray and identifying key phases in the spray process. As well as this the spray angle for the different nozzle types and formulations was measured.

Spray Angle Results

The angles measured for a single frame and the mean frame for each of the different aerosol cans are shown in Table 3.6. The standard deviation is also given. The aerosol cans containing water sprayed the entire water contents of the can within a single actuation making repeatable results impossible to obtain. For

Can	μ_{single}	σ_{single}	μ_{mean}	σ_{mean}
1A	21.1	1.3	21.3	0.1
1B	-	-	-	-
1C	19.5	1.5	20.3	0.9
1D	20.8	2.4	22.2	1.1
2A	19.5	3.0	20.3	0.5
2B	17.8	2.7	20.1	0.4
2C	17.8	1.2	19.5	0.6
2D	18.4	2.8	18.9	2.9
2E	16.3	1.3	17.6	1.9

Table 3.6: Mean spray angle (μ) and standard deviation (σ) for an individual frame (single) and mean frame (mean) of schlieren videos for nine different formulations and two nozzle types.

this reason the statistics of these results are not provided. The spray angle measured from both the single and mean frame show that the sprays from the simple orifice nozzle tend to have a smaller spray angle compared to those generated from a swirl nozzle. The mean spray angles measured for the simple orifice nozzles were in the range of 16.3-20.3° depending on the formulation within the cans, whereas the swirl nozzles achieved a mean spray angle within the range 19.5-22.2°.

Performing a t-test on the spray angle measurements for the different nozzle types resulted in a t-score of 4.22 which for a system with 22 degrees of freedom statistically demonstrates a significance of 0.01% which is well within the standard 0.5% tolerance and therefore the nozzle type is to be deemed significant on the spray angles.

The spray angles measured using the mean frame had smaller standard deviations relative to the equivalent single frame measurements. This variation is due to the method by which the single frame was picked to be measured. The single frame could be selected anywhere between cavitation and no cavitation, whereas for the mean frame, since frames were averaged over, this resulted in a smoothing of the spray boundary and thus the pulsing had less of an effect. The pulsing spray was more prominent for the simple orifice nozzles where the largest standard deviations are observed.

Spray Stage Results

Three repeats were performed for each aerosol can and an example frame from each stage for each can is given in the following figures. The generation stage can be seen in Figure 3.26, the fully-developed stage in Figure 3.27 and the collapse stage in Figure 3.28. Here the frames selected to represent the stages are taken from key locations of the smoothed zero count, example seen in Figure 3.9. For the generation stage the middle frame of the steep positive gradient is chosen. For the fully activated stage the N_{Mid} frame is taken and for the collapse stage the middle frame of the steep negative gradient is taken. The automatic sampling method leads to slight differences for the different stages between the aerosol cans.

The generation stage frames captured in Figure 3.26, for most cases, show a less dense initial release which is then followed by a denser cloud of vapour. The initial less dense release is due to the vapour phase tap (VPT) located within the aerosol can. When the can is actuated the VPT opens which allows some of the vapour mixture at the top of the aerosol can to be released. The vapour release alone is observed in Figures 3.26b and 3.26h.

The initial vapour release is then followed by the denser liquid product propellant mixture and can be observed in Figures 3.26c, 3.26d, 3.26e, 3.26g and 3.26i. The dense product is quite noticeable relative to the gaseous release due to how dense this spray region is. The light is not just refracted but completely blocked, resulting in strong dark regions where the spray is most dense. The centre of the product bulk moves fastest and can be seen to have progressed the furthest through the spray providing a typical spray penetration shape. In Figure 3.26e there is an off-axis disturbance possibly resulting from an asymmetric release relative to the other cans.

For cans 1A and 2B the generation stage capture is towards the final parts of this stage and shows more of the transition between generation and fully developed

stage, this can be seen in Figures 3.26a and 3.26f. There does not appear to be any clear discernible qualitative difference in the spray generation between formulation or nozzle type within this stage.

The fully developed stage for the different aerosol cans can be seen in Figure 3.27. Taking the swirl nozzle cans shown in Figures 3.27a, 3.27b, 3.27c and 3.27d some differences can be observed in the sprays. The propellant only can, Figure 3.27a has an wider spray close to the nozzle compared to that of when alcohol is added in cans 1C and 1D, Figures 3.27c and 3.27d respectively. This could be due to the less volatile nature of the alcohol resulting in reduced cavitation within the nozzle.

Figure 3.27a shows that the schlieren technique was able to capture some of the entrainment into the spray cone from the ambient, which can be seen close to the top right of the aerosol can. As the propellant is evaporating, the aerosol can cools making the air close to it begin to cool as well. This increases its density and therefore means that it is slightly visible with the schlieren technique.

The aerosol can with water (1B), Figure 3.27b, has a considerably different spray structure to the other cans with the water being atomised into larger droplets which are easily visible and in a considerably wider spray angle. With the aerosol cans containing water, after carrying out a single schlieren experiment the aerosol can was not able to generate this structure again which is believed to be due to the lack of water remaining inside the can.

The simple orifice nozzle aerosol cans show a wider spray region close to the nozzle for the aerosol can with only the propellant, similar to that of the swirl nozzle aerosol cans. The can with only the active, AACH, is expected to have a similar spray structure as it does not contain any of the less volatile D5 fluid. This was found not to be the case. This could possibly be due to the frame selection method, where a frame was selected when cavitation was not occurring, or because

the AACH is influencing the nozzle flows. Further study into how the active affects the nozzle flow is needed.

Close to the nozzle for all of the sprays there is a dense region due to the high concentration of the aerosol can contents. Moving downstream from the nozzle the concentration drops as the ambient is entrained and the spray becomes increasingly visible. Across the interface boundary of the spray region and ambient the shear effects generate Kelvin Helmholtz instabilities which are visible for all of the aerosol cans. The turbulent structures within the spray region can be identified clearly using the schlieren technique.

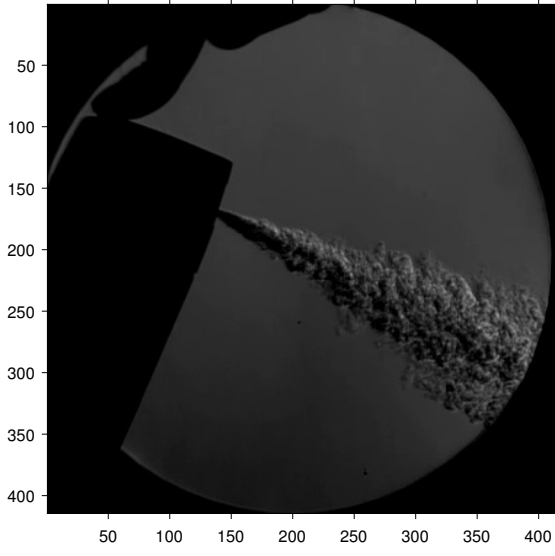
The spray collapse stage occurs after releasing the actuator, as shown in Figure 3.28. As the actuator is released the internal spring decompresses, closing the valve and the VPT. This stops the flow of product from exiting the can. The momentum of the spray rapidly decreases to a continuously decaying gaseous jet. Inside the aerosol can's head however remains remnants of product and propellant which have not been fully ejected. The remaining propellant evaporates and a flow of this now gaseous propellant leaves the aerosol can producing additional gaseous jets. These are not visible to the naked eye but are highlighted by the schlieren technique.

The nozzle type plays an important role in the structure of these final gaseous jets. For the swirl nozzles the momentum quickly dissipates close to the nozzle resulting in a weak jet which is convected away due to ambient room flows. This is seen in Figures 3.28a, 3.28b, 3.28c and 3.28d.

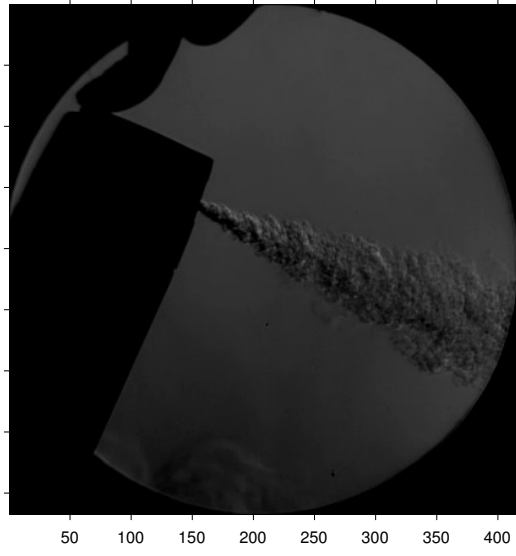
The simple orifice aerosol cans result in dense laminar jets of the propellant. Due to the automatic selection of frames the collapse is captured at different points throughout this stage for the different formulations. However, comparison between the videos reveals that similar to the generation stage there is not a clear observable difference between the cans, and the same behaviour is observed for each aerosol

can. Figure 3.28g shows the initial momentum decay as the actuator is released, which leads into a release of a thin laminar jet seen in Figure 3.28i which is followed by a larger jet release seen in 3.28e 3.28f which then dissipates as in 3.28h, which is seen in all videos for the simple orifice nozzle cans.

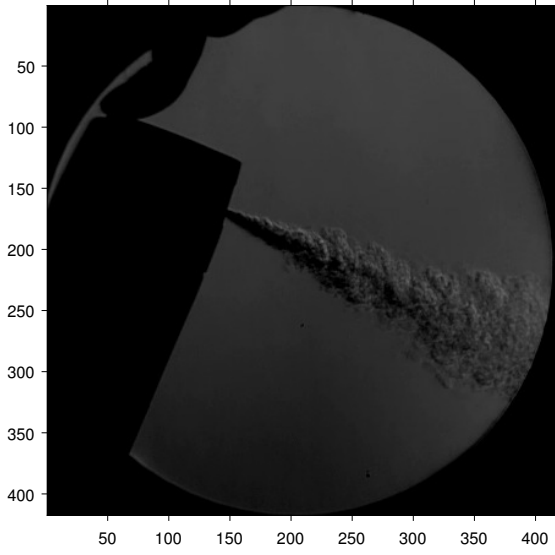
The different jets that are released may be due to the different propellant constituents vaporising within the can at different rates and thus releasing at different times. The thin jet could be due to the propane vaporising first which is then followed by the denser butane and isobutane jet where a sinuous interaction on the upper jet surface is observed. Since the jet fall due to negative buoyancy, they are denser than the ambient, which supports this possibility as the propellants are denser than the ambient. They also have a stronger momentum compared to that of the swirl nozzle and are not easily convected away by the ambient flow.



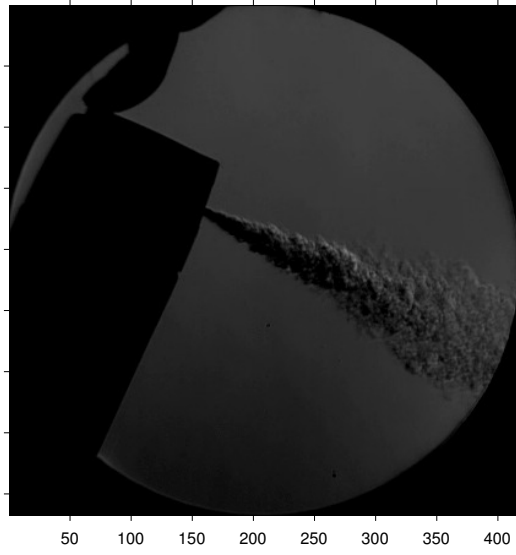
(a)



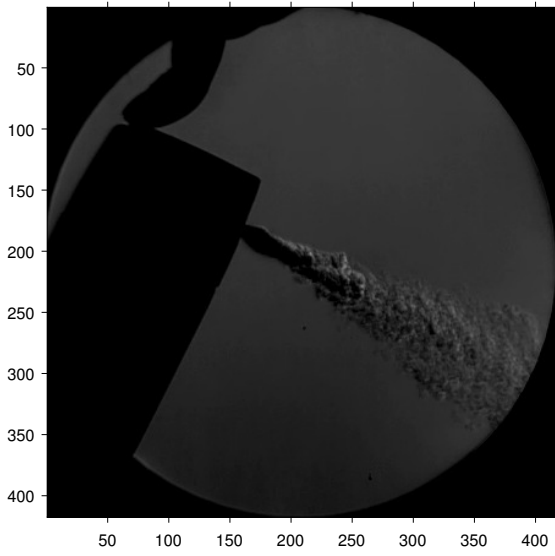
(b)



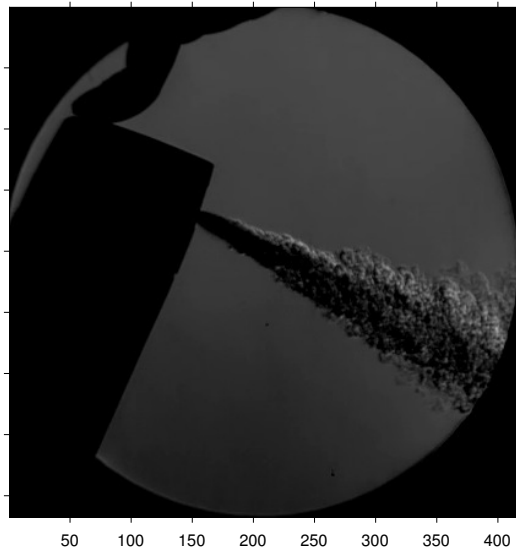
(c)



(d)



(e)



(f)

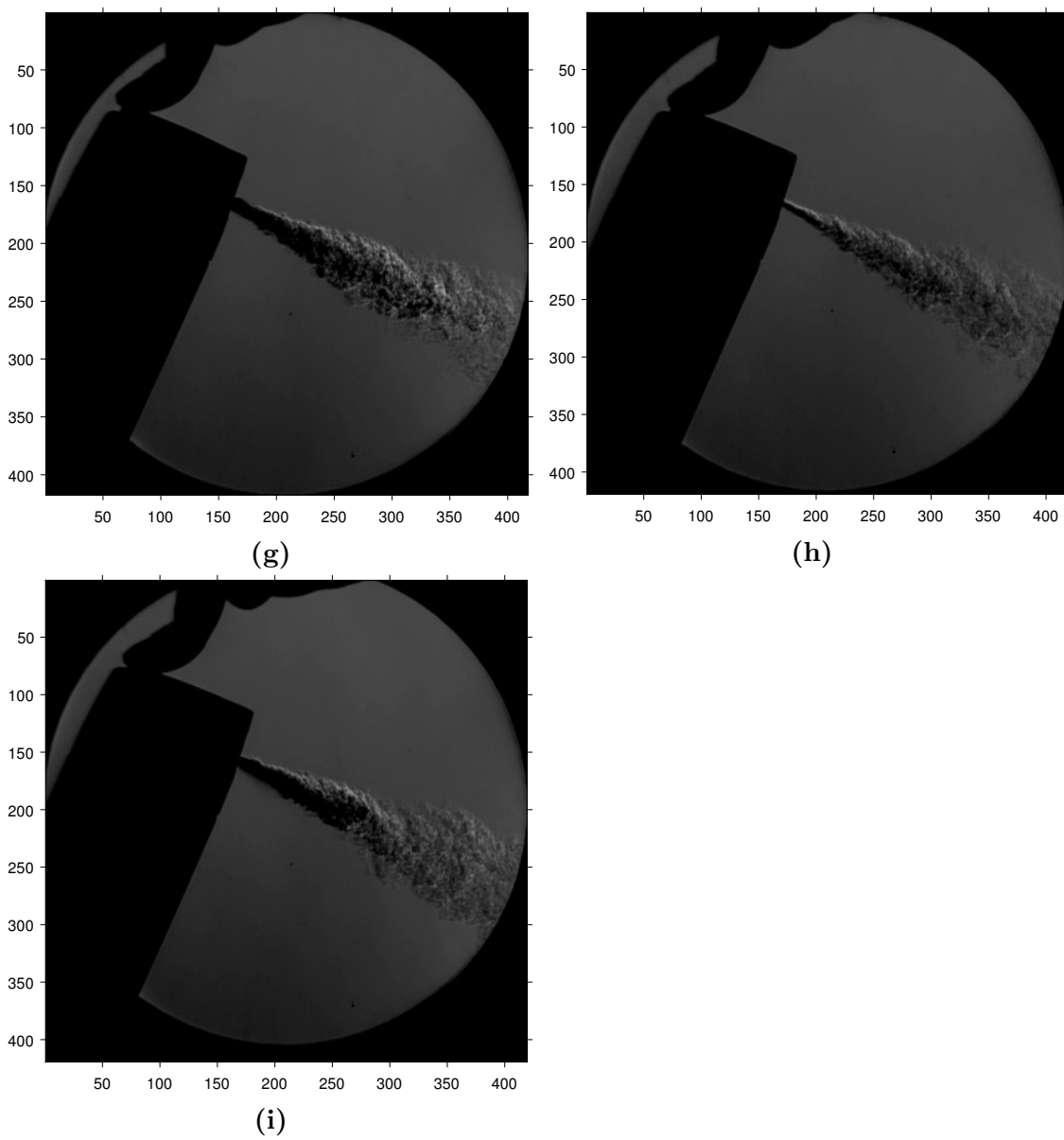
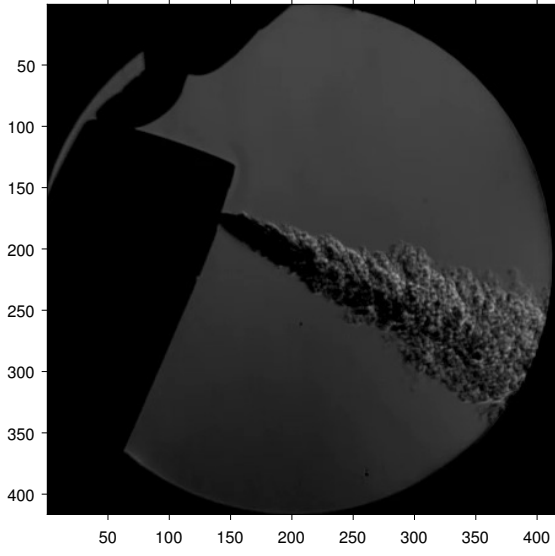
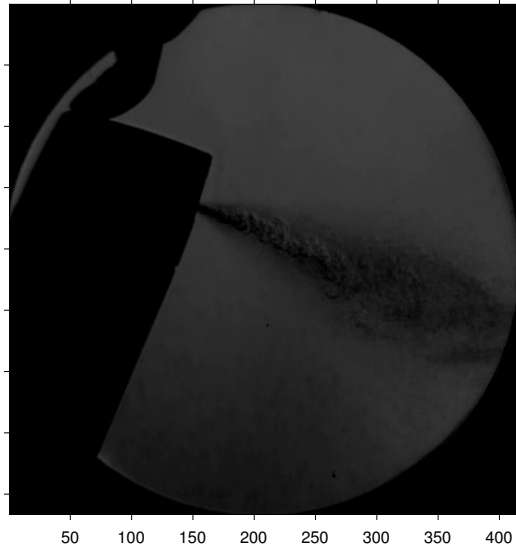


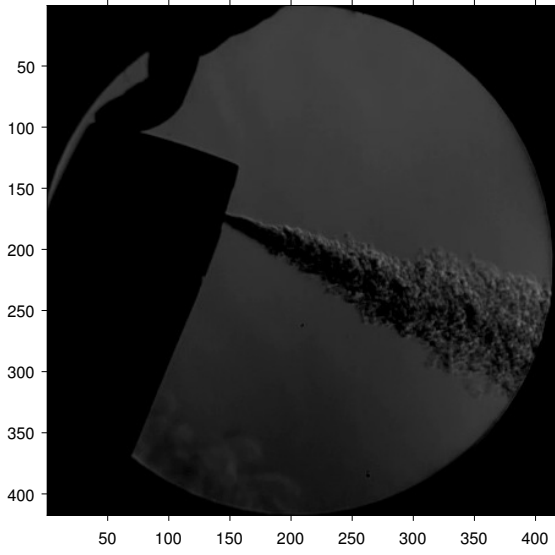
Figure 3.26: The spray generation phase for aerosol cans (a) 1A, (b) 1B, (c) 1C, (d) 1D, (e) 2A, (f) 2B, (g) 2C, (h) 2D and (i) 2E.



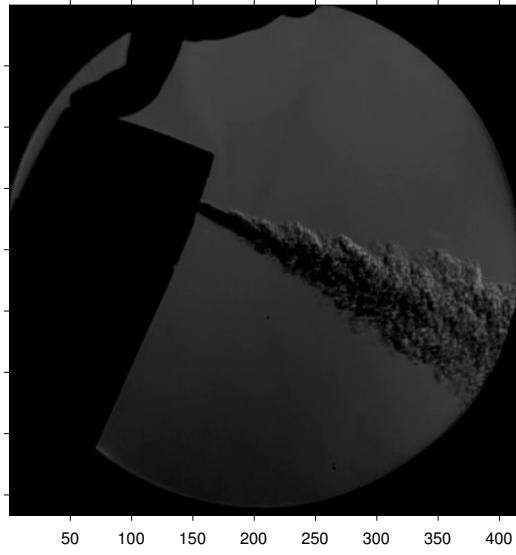
(a)



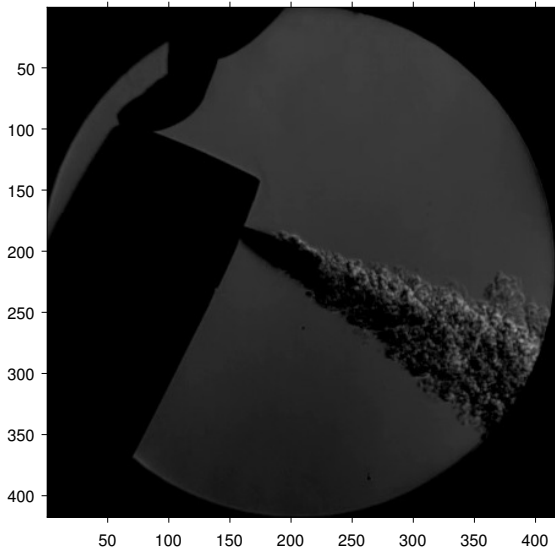
(b)



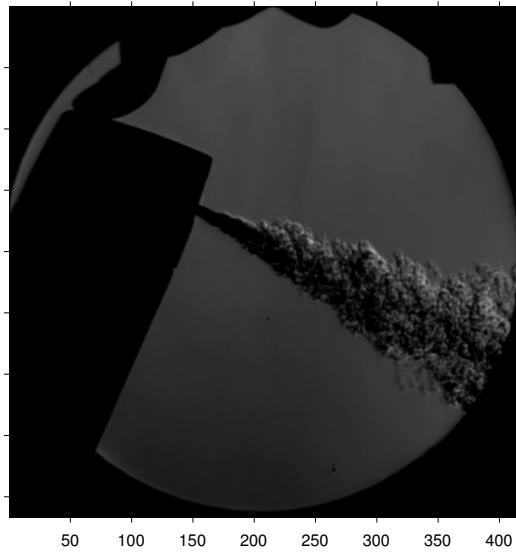
(c)



(d)



(e)



(f)

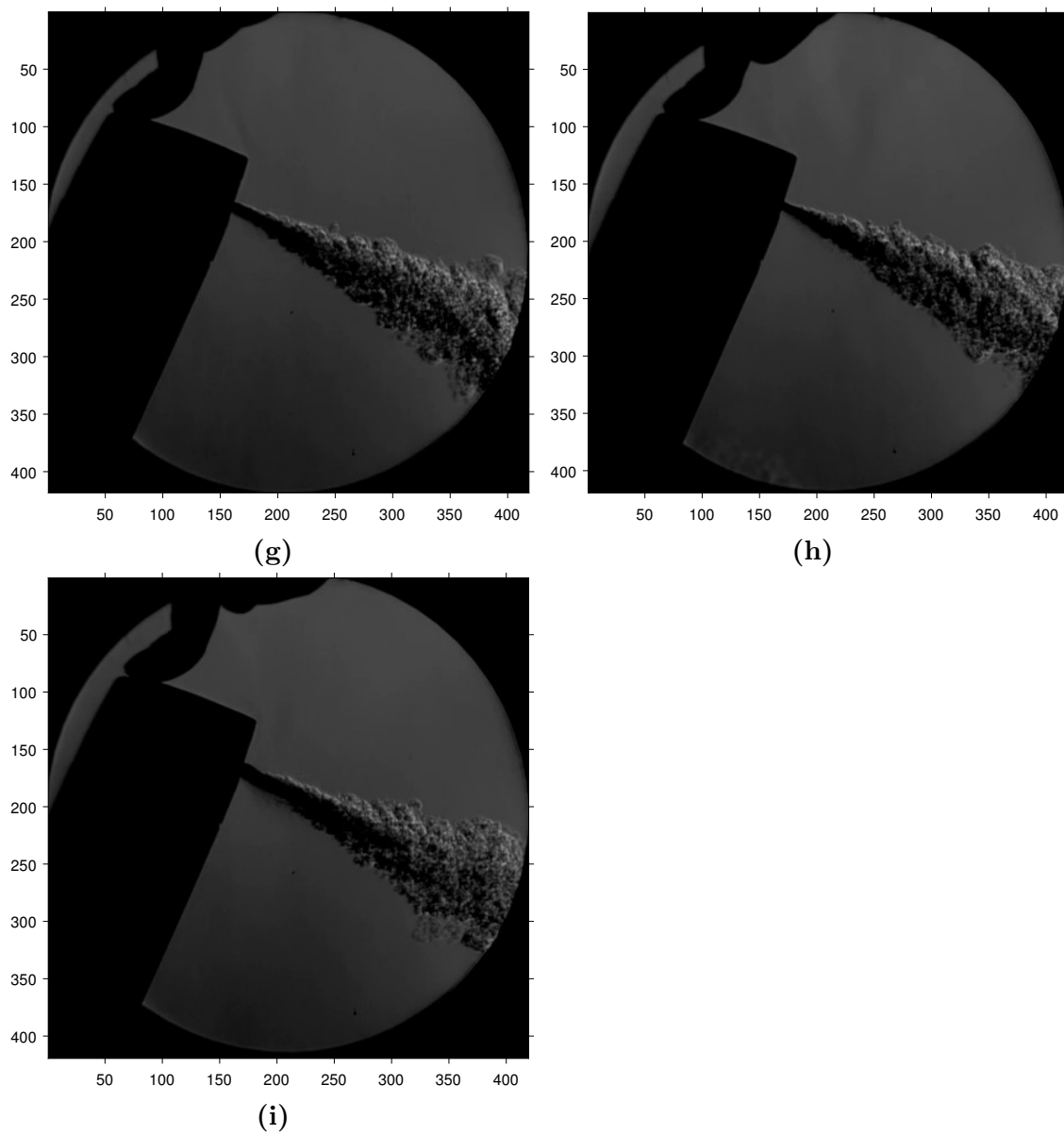
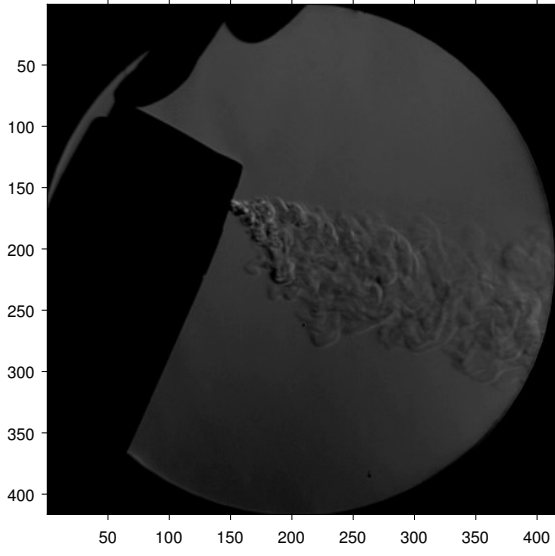
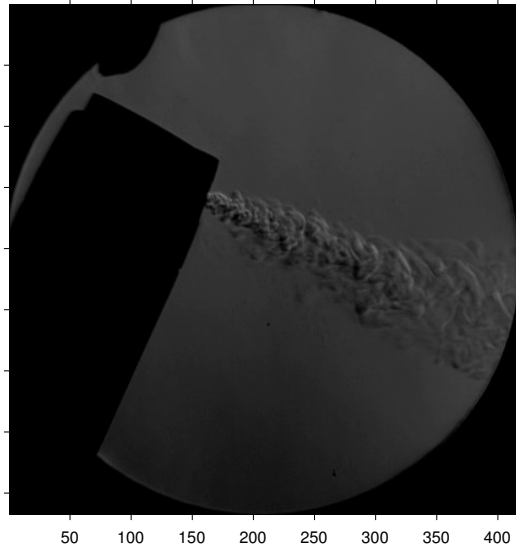


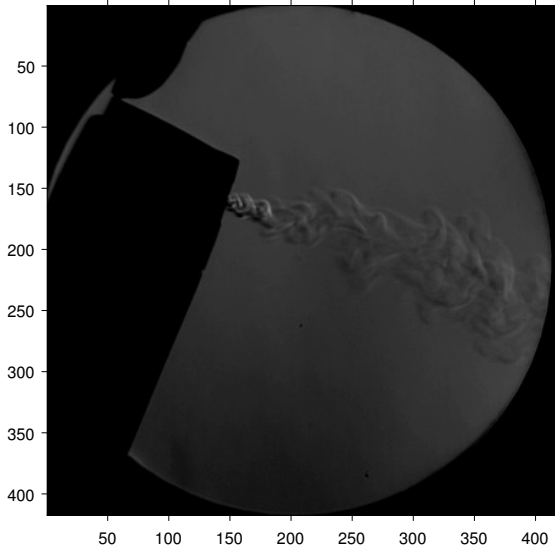
Figure 3.27: The fully activated phase for aerosol cans (a) 1A, (b) 1B, (c) 1C, (d) 1D, (e) 2A, (f) 2B, (g) 2C, (h) 2D and (i) 2E.



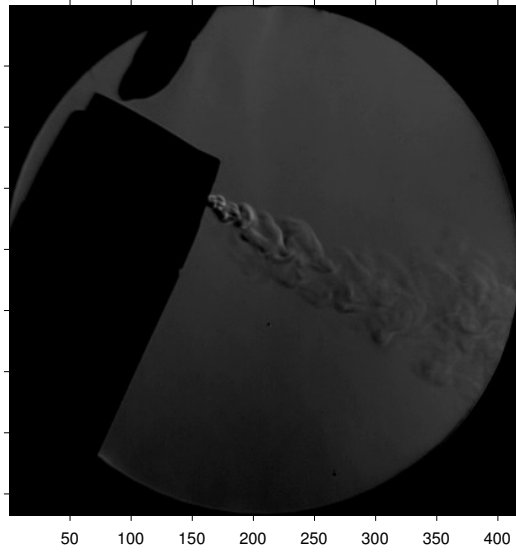
(a)



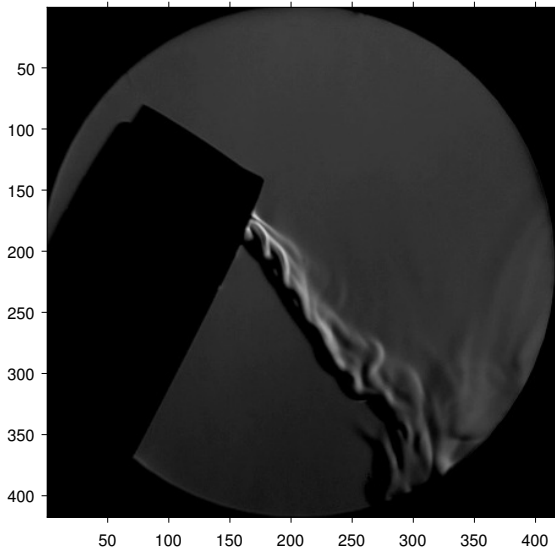
(b)



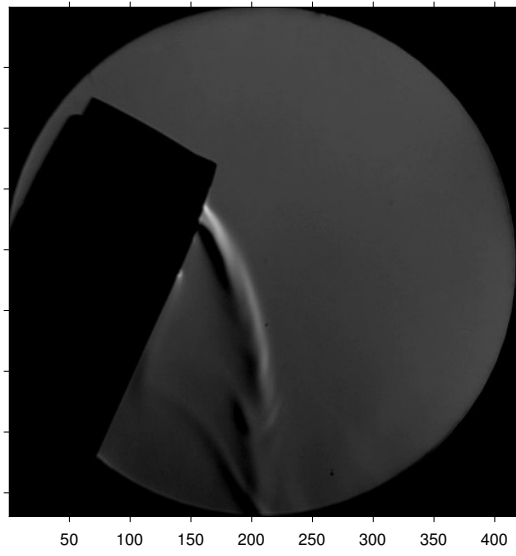
(c)



(d)



(e)



(f)

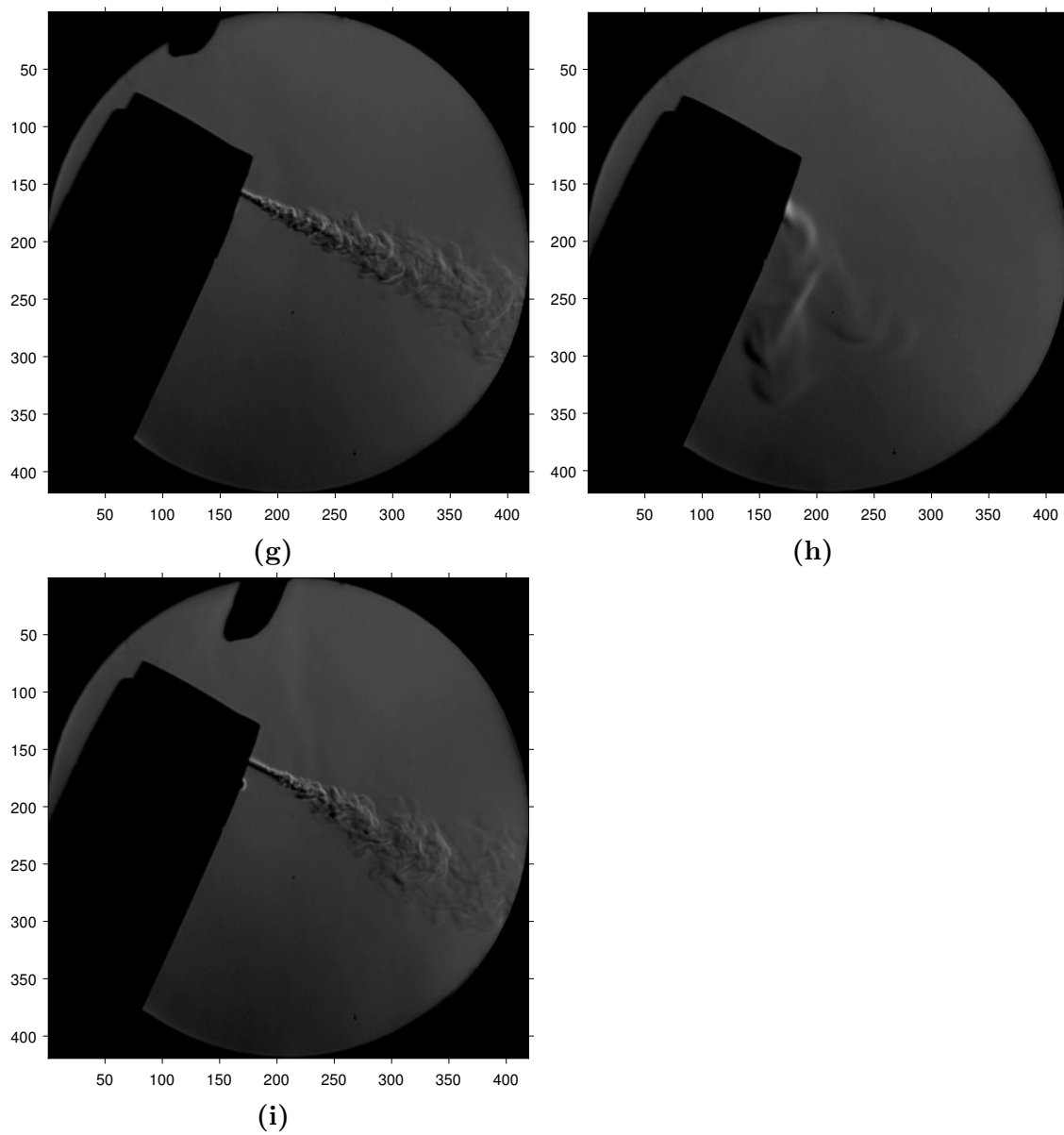


Figure 3.28: The collapse phase for aerosol cans (a) 1A, (b) 1B, (c) 1C, (d) 1D, (e) 2A, (f) 2B, (g) 2C, (h) 2D and (i) 2E.

3.3.2 Determining Droplet Size Results

The spraytec experiments were performed over several days. The ambient conditions were recorded and are presented here. For the PSDs measured the corresponding particle statistics are given. The CSDs are compared for each axial position and then a comparison for particular cans at these axial distances are compared. For the distributions measured the results of fitting the log-normal, Gamma and Rosin Rammler distributions are provided including the fitted parameters.

Ambient Conditions and Mass Flow

The ambient conditions for the each runs were recorded and can be found in Table 3.7. Temperature and humidity were not controlled during the experiments but were recorded for further information. Note due to the time needed to perform each experiment they were performed over 1 week, and as a result the ambient conditions vary. Cans 1A, 1B, 1C, 1D and 2D were tested on the same day; cans 2B, 2C and 2E on another day; and 2A on its own day.

Can	$T_\mu(^{\circ}C)$	T_σ	$RH_\mu(\%)$	RH_σ	$\Delta M_\mu(g)$	ΔM_σ
1A	21.8	0.0594	50.6	0.252	1.71	0.0885
1B	22.4	0.0647	44.3	2.50	1.67	0.225
1C	22.0	0.113	50.2	0.574	1.47	0.0907
1D	21.7	0.307	51.2	0.880	1.50	0.103
2A	19.4	0.0405	25.5	0.163	2.84	0.196
2B	21.0	0.342	56.8	0.834	2.86	0.100
2C	20.7	0.103	59.0	0.194	2.91	0.129
2D	22.5	0.0560	41.7	0.505	2.96	0.159
2E	21.6	0.0758	55.1	0.605	3.07	0.214

Table 3.7: The arithmetic mean (μ) and standard deviation (σ) of temperature (T), relative humidity (RH) and mass sprayed (within 2 seconds) (ΔM) for the Spraytec experiments for all aerosol cans.

Ambient temperature measurements for all experiments were within the range 19.4 – 22.5°C with little deviation between measurements for the respective aerosol cans. The relative humidity ranged from 25.5-59.0 % with small standard

deviations between the aerosol cans. The relative humidity on the day of aerosol can 2A was considerably lower than the other experiment days. The standard deviation of RH for aerosol can 1B was greatest, which was a result of the evaporating water from the droplets influencing the local RH measurements. Overall the temperature and relative humidity variations for the different cans were small.

The change in mass of the different formulations can be seen in Table 3.7. There is a clear separation of mass flow between the nozzle types, with 1 referring to swirl nozzle cans and 2 to simple orifice nozzle cans. The average mass flow between the 18 runs (6 axial positions x 3 repeats) for each aerosol can type can be seen in Table 3.7 as well as the standard deviation between measurements. The results clearly show the impact of nozzle type, with an average mass flow of 0.793 g/s for the swirl nozzles and 1.46 g/s for the simple orifice nozzles which is an increase of 85%. The nozzle geometry is believed to be the main cause of this as the pressure drop characteristics will control the overall flowrate.

Particle Statistics Results

For different axial distances the particle statistics are plotted and can be seen in Figures 3.29, 3.30, 3.31 and 3.32. Note aerosol can 1B is not included as there were insufficient cans to perform repeats. There is a clear separation between aerosol cans 1C and 1D and the remaining cans. The SMD shown in Figure 3.29 increases over axial distance with a swirl nozzle and with the inclusion of alcohol; cans 1C and 1D. This increase is not observed where pure propellant is used (1A). At sufficient axial distances the gradient of $D_{3,2}$ tends to zero with the values eventually levelling off. The two SMD limits are approximately 13.5 μm and 2.2 μm showing close to an order of magnitude difference with the main distinction being formulation. The greatest change in SMD occurs in the range 5-10 cm, the range where the evaporation of droplets is believed to be greatest for aerosol cans where the SMD decreases. On the other hand, for cans 1C and 1D, an increase in droplet size is observed. This

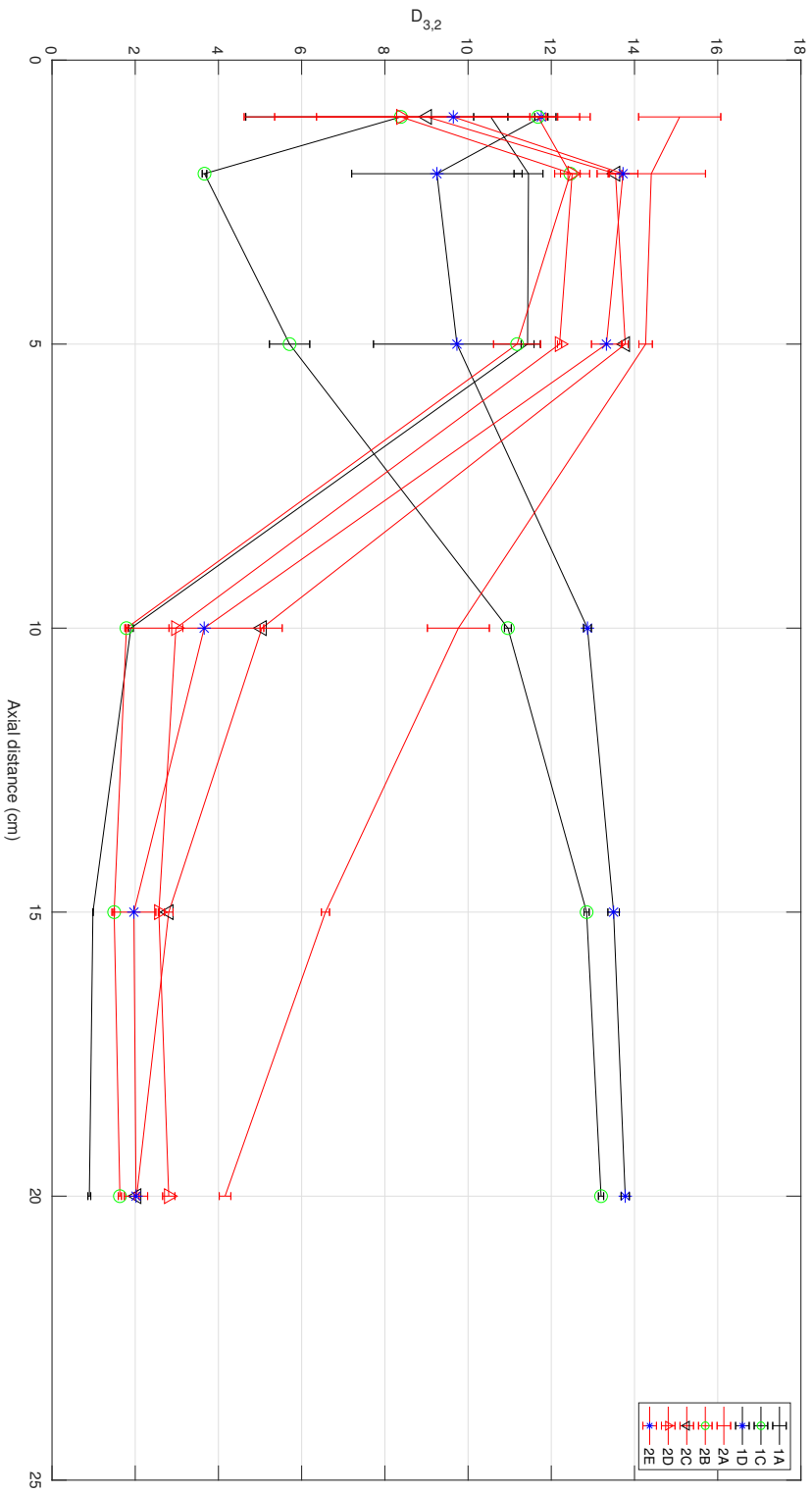


Figure 3.29: Axial distance evolution of D_{32} for the different aerosol cans tested. The swirl nozzle cans are represented in black and the simple orifice nozzles represented in red.

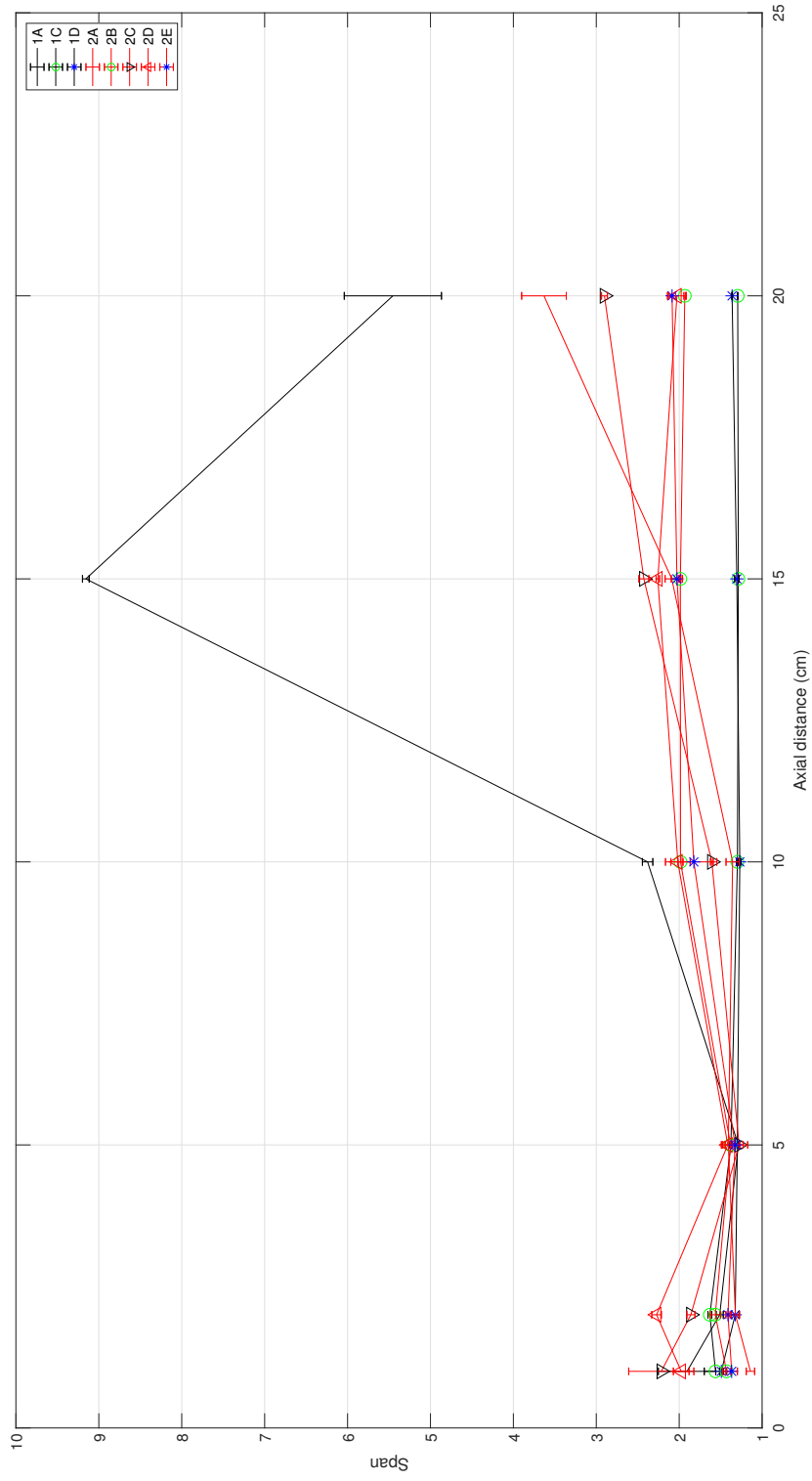


Figure 3.30: Axial distance evolution of distribution Span for the different aerosol cans tested. The swirl nozzle cans are represented in black and the simple orifice nozzles represented in red.

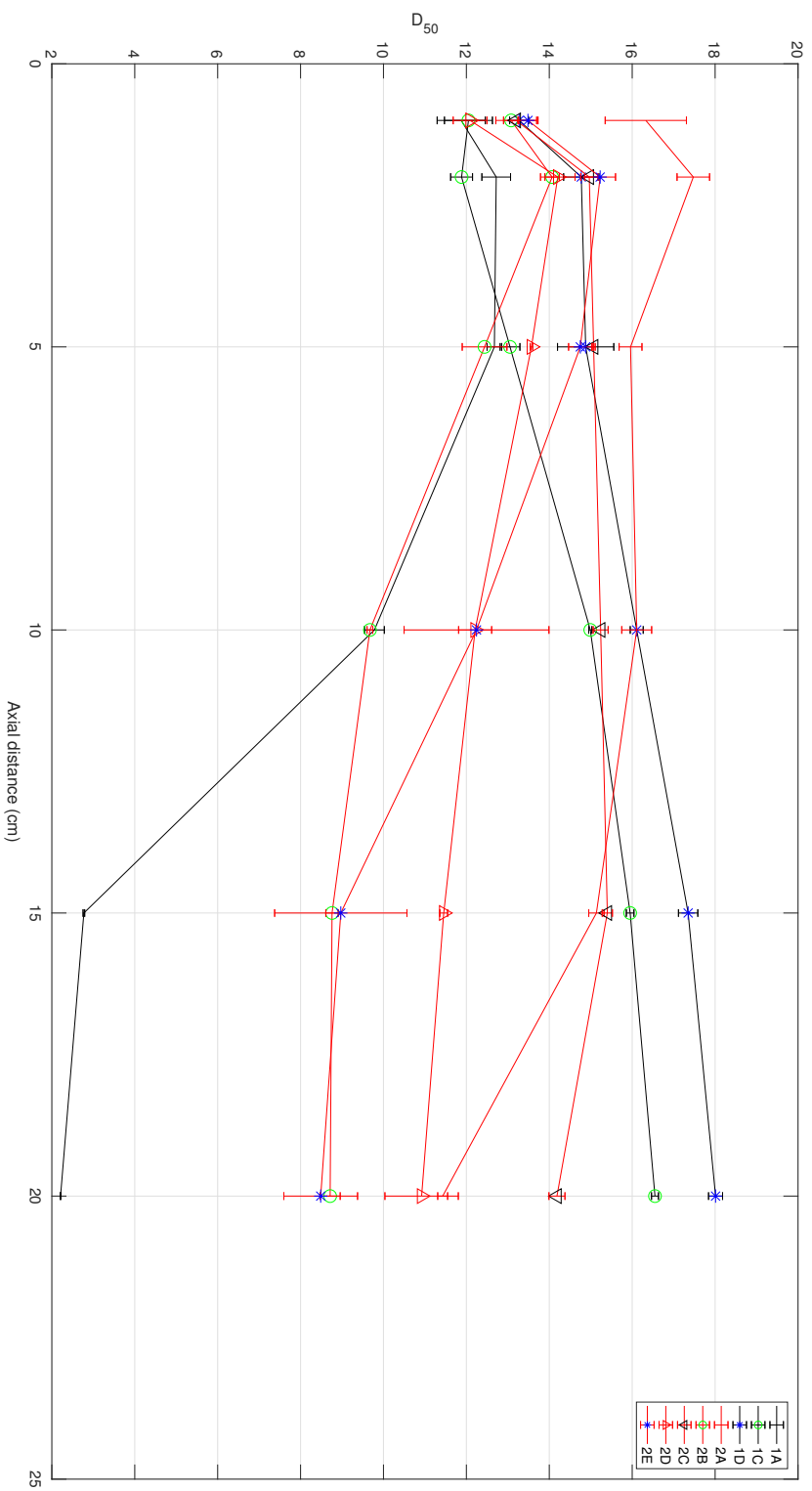


Figure 3.31: Axial distance evolution of D_{50} for the different aerosol cans tested. The swirl nozzle cans are represented in black and the simple orifice nozzles represented in red.

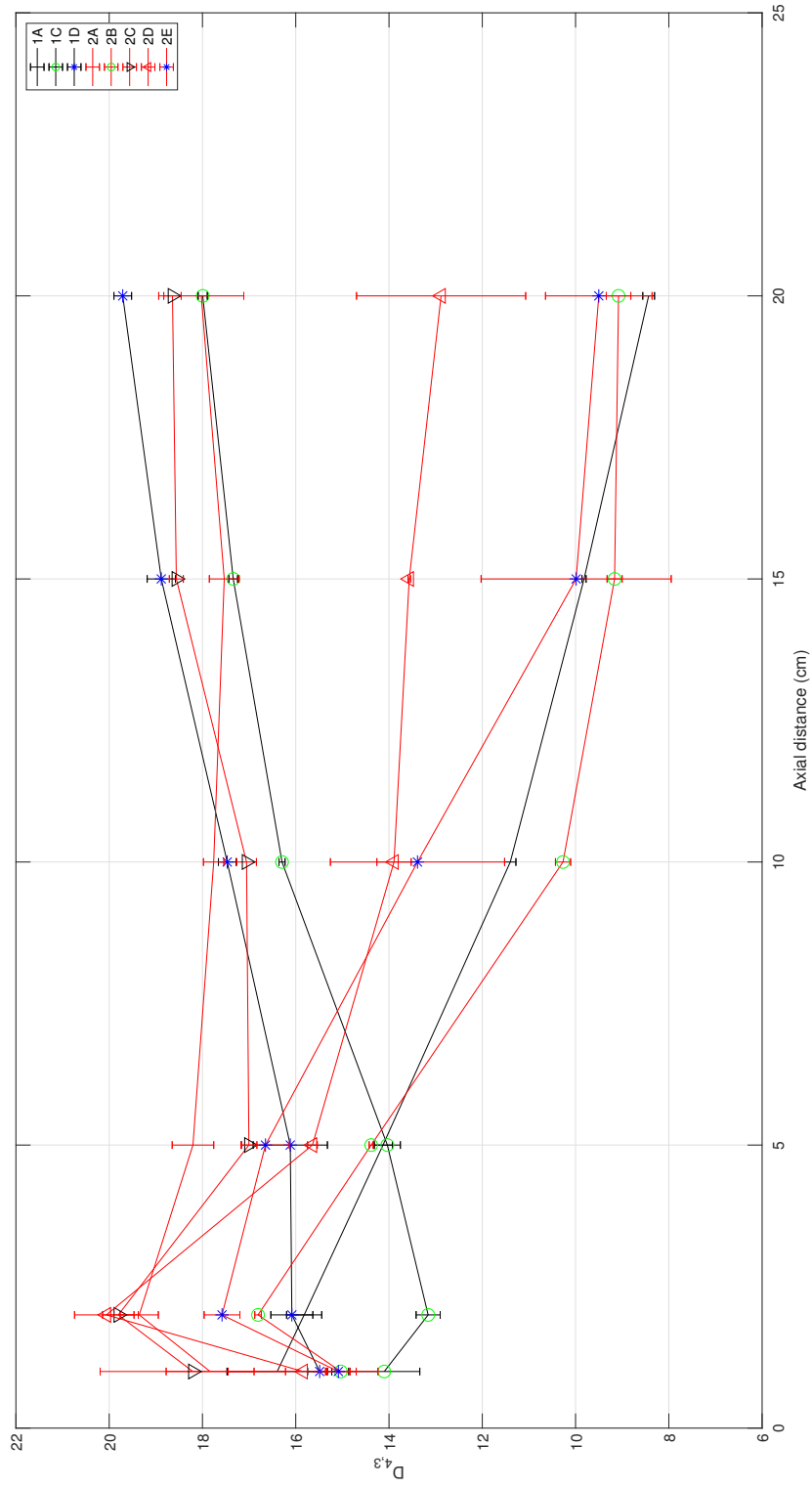


Figure 3.32: Axial distance evolution of D_{43} for the different aerosol cans tested. The swirl nozzle cans are represented in black and the simple orifice nozzles represented in red.

is physically possible due to condensation of water vapour in the ambient onto the droplets, or potentially coalescence of the droplets as discussed in Chapter 2.

The span of the distributions for the different axial positions can be seen in Figure 3.30. Aerosol cans 1C and 1D again tend to a similar value whereas aerosol can 1A is substantially different at 15 cm relative to the other aerosol cans. The main difference here is the presence of alcohol in the formulation of aerosol cans 1C and 1D, this decreases the evaporation rate of the droplets whereas for the pure propellant formulation the greater evaporation rate results in a greater span. The remaining cans (2A, 2B, 2C, 2D and 2E) are the simple orifice nozzle cans, which show similar trends between their span evolution with a slightly increasing trend.

Figure 3.31 shows the evolution of D_{50} and that the median droplet diameter generated is consistent at 1 cm from the nozzle exit between all but one of the aerosol cans, with a value of approximately $13 \mu\text{m}$. The clear outlier at 1 cm is seen with aerosol can 2A, the simple orifice nozzle with pure propellant. The physical breakup mechanism for this is not clear as the other simple orifice cans initially behave similarly to the others. One possible reason may lie in the ambient conditions, which are given in Table 3.7. Aerosol can 2A was performed on a different day where the ambient RH was considerably different to the other days. This lower RH can impact evaporation rate but further investigation with controlled RH is needed to determine if RH is a controlling factor.

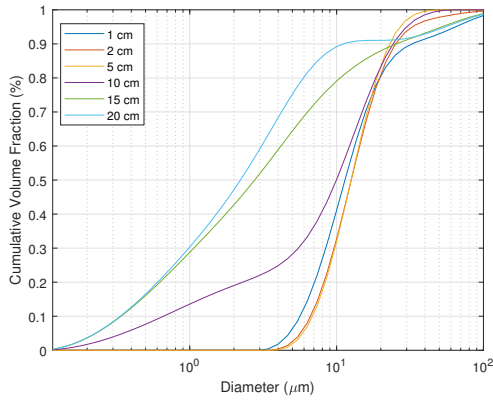
The volume mean diameter shows little change for aerosol cans 2A and 2C with the initial $D_{4,3}$ similar to that at the final axial position. This can be seen in Figure 3.32. Again aerosol cans 1C and 1D show an increasing trend whereas aerosol can 1A shows a decreasing trend. Aerosol cans 2A and 2C achieve a similar $D_{4,3}$ to that of aerosol cans 1C and 1D at 20 cm, whereas aerosol cans 2B and 2E achieve a similar $D_{4,3}$ to aerosol can 1A at 20 cm. Aerosol can 2D achieves a $D_{4,3}$ between the two sets.

Axial Variation

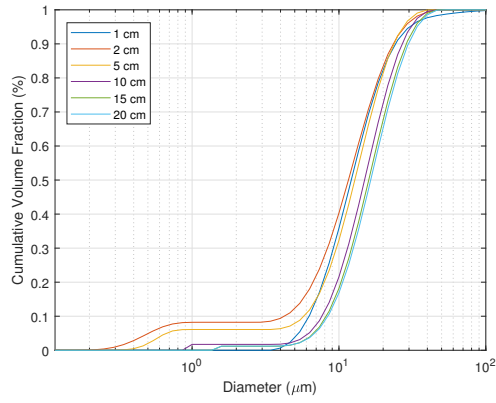
For each formulation the CSD of one experimental run is plotted for each axial position investigated, and can be seen in Figure 3.33. There is a clear separation for the evolution of CSD for the aerosol cans where the propellant is the only liquid content, as seen in Figures 3.33a, 3.33d, and 3.33f. The pure propellant aerosol cans have a distinct shift of CSD where the droplets appear to evaporate to considerably smaller sizes along the axial distances. The nozzles influence where this change occurs, starting at a smaller axial distance of 10 cm for the swirl nozzle (Figure 3.33a) and a longer distance of 15 cm for the simple orifice nozzle (Figure 3.33d). The active (aerosol can 2C) appears to influence the evaporation also, with smaller particle sizes measured at axial positions 10, 15 and 20 cm relative to the pure propellant (aerosol can 2A).

The influence of the additional components, for the swirl nozzle aerosol cans, on the droplet sizes generated can also be seen from the CSDs plotted in Figure 3.33. Comparing Figure 3.33a and Figure 3.33b shows that the addition of alcohol changes the nature of CSD evolution. From the CSD it appears that there is an increase in droplet size with a shift of the CSD from left to right. At axial distances of 2 cm and 5 cm there is a lower mode measured which brings the distribution slightly lower, but the increasing particle size trend is still observed. For aerosol can 1D, the full product, the same trend in increasing particle size can be observed. The shape and trend of the CSD agrees with what was seen in the particle statistic measures.

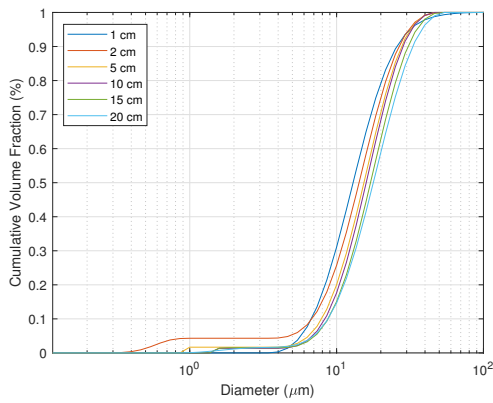
For the simple orifice nozzle aerosol cans the lower mode appears more often in the measurements, believed to be due to increased entrainment of the ambient. There is however consistency with the lower mode appearing at 10, 15 and 20 cm. The lower mode also consistently measures approximately 10-20% of the volume distribution.



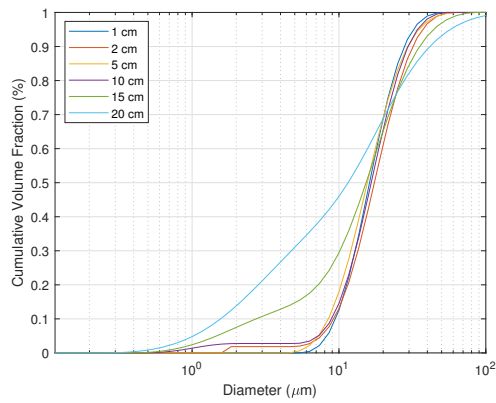
(a) Can 1A



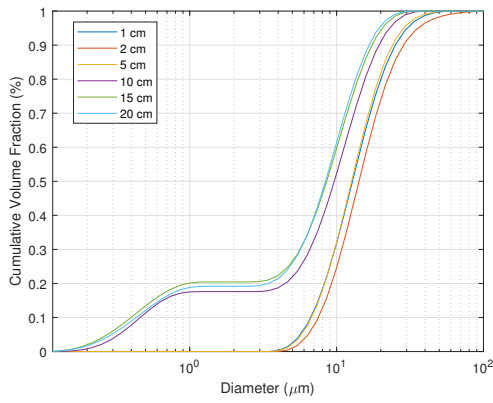
(b) Can 1C



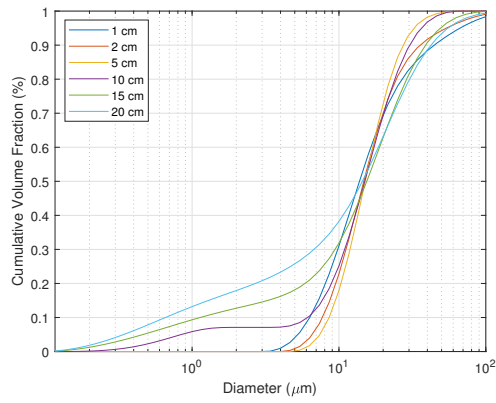
(c) Can 1D



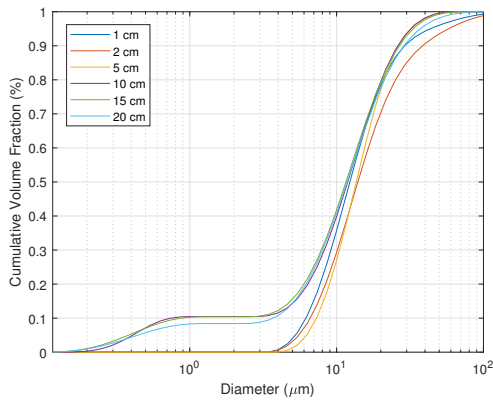
(d) Can 2A



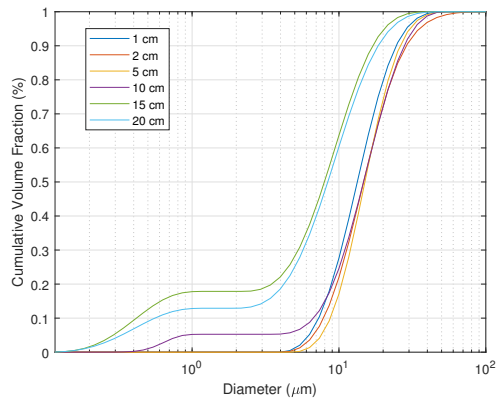
(e) Can 2B



(f) Can 2C



(g) Can 2D



(h) Can 2E

Figure 3.33: The CSD variation at varying axial positions of 1, 2, 5, 10, 15, 20 cm for the cans (a) 1A, (b) 1C, (c) 1D, (d) 2A, (e) 2B, (f) 2C, (g) 2D and (h) 2E.

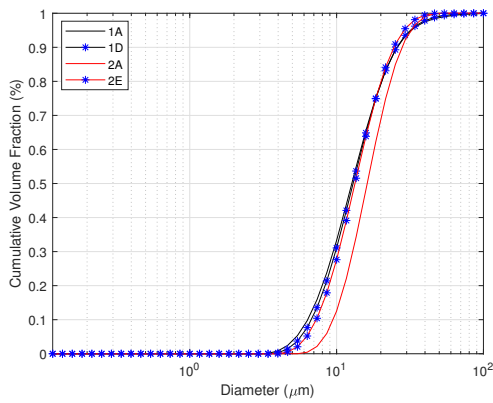
Variation Between Cans

Comparisons of the CSD for aerosol cans 1A, 1D, 2A and 2E at the different axial positions of 1, 2, 5, 10, 15 and 20 cm are shown in Figure 3.34. Here the black lines represent the aerosol cans with a swirl nozzle and the red lines represent the aerosol cans with a simple orifice nozzle. The lines without blue stars are for the propellant formulations and the lines with blue stars are the full product formulations.

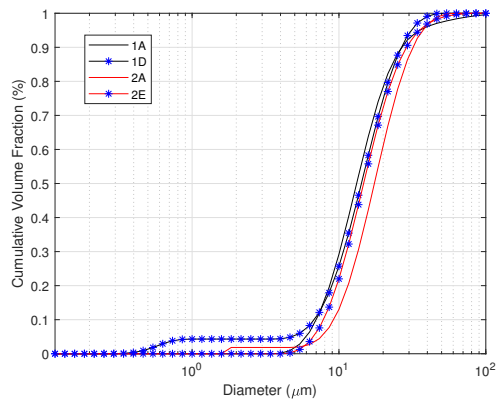
At 1 cm the CSD measured is relatively consistent for cans 1A, 1D and 2E with a difference seen for aerosol can 2A. Aerosol can 2A is noted to have been tested on a day with a considerably different RH but the effects of this at 1 cm are not expected to play a dominant effect on the CSD. At 2 cm similar CSD profiles can be seen. At 5 cm the CSD profiles for all cans have a similar form with slight differences seen for aerosol can 1A.

At 10 cm the evaporation effects on the CSD can be observed for aerosol can 1A with a tail extending to the smaller droplet sizes. The remaining cans still maintain a similar profile. At 15 cm the evaporation effects can now be seen now for aerosol can 2A and the lower mode is present for aerosol can 2E, shifting the main mode left as seen in the CSD comparison. At 20 cm the propellant aerosol cans (1A and 2A) now both have further evaporation effects but what can be also seen is larger droplets, due to further beam steering that is not accounted for with the detector cut off range used.

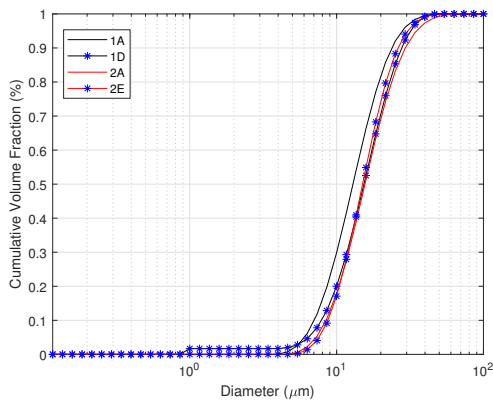
The CSD for aerosol can 1D retains a similar profile as seen at 1 cm, whereas aerosol can 2E shows the presence of the lower mode and therefore appears to result in finer droplets at 20 cm. Discerning whether this is an artefact due to ambient contaminants or due to droplets generated from the can is difficult with the current approach.



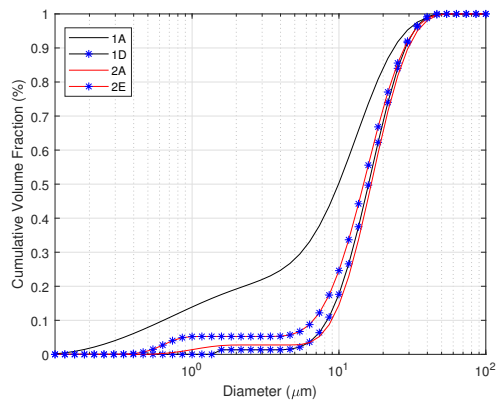
(a) At 1 cm



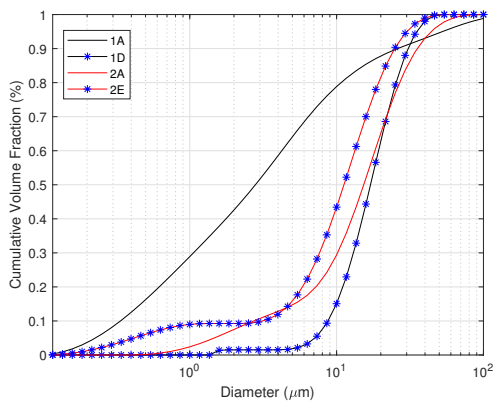
(b) At 2 cm



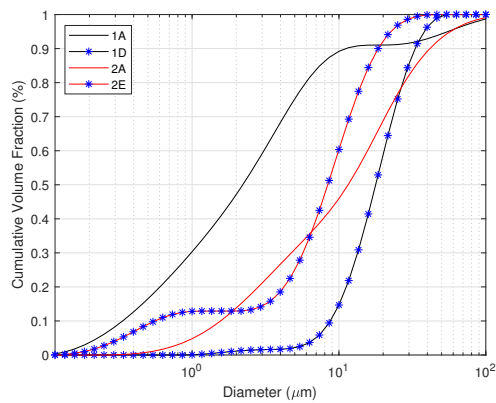
(c) At 5 cm



(d) At 10 cm



(e) At 15 cm



(f) At 20 cm

Figure 3.34: The CSD variation for aerosol cans 1A, 1D, 2A and 2E axial positions (a) 1 cm, (b) 2 cm, (c) 5 cm, (d) 10 cm, (e) 15 cm and (f) 20 cm. Black lines represent swirl nozzle and red lines a simple orifice nozzle. Solid lines are propellant formulations and blue circles are product formulations.

Fitting Distribution Results

For each repeat the fitting parameters are calculated. The arithmetic mean of the parameters for the given aerosol can and axial distance is calculated and the associated standard deviation is also calculated. These values for the different formulations and axial distances are also calculated to capture any variability in the size distributions and can be found in Table 3.8. Aerosol can 1B measurements are not included as only a single measurement is available.

For aerosol can 1D, Figure 3.35 shows the resulting distribution fits at 1 cm against the normalised PDF and the distribution fits using the mean parameters against the same normalised PDF. For this particular aerosol can at this axial distance the Log-normal distribution provides an excellent fit to the normalised PDF, as seen in Figure 3.35a. There is slight deviation at the start of the distribution but the peak is captured accurately as well as the tail of the distribution. The Gamma distribution provides a good fit as well but over-predicts the peak of the distribution and under-predicts the tail of the distribution. The worst performing fit is the Rosin-Rammler distribution with an even greater over-prediction of the distribution peak and under-prediction of the tail.

Figure 3.35b shows the fitted distributions using the mean parameters of the repeats for aerosol can 1D at the same axial location of 1 cm. The performance of the mean parameters is compared to the repeats of the experiment. The Log-normal mean distribution fit captures all of the repeats falling between the measured normalised PDFs. The mean Rosin-Rammler and Gamma distributions capture the height of the peak of run 1 but the location is shifted. The RR and Gamma distributions over-predict the diameter of the peak and also under-predict the tail as they did for the individual fit.

The mean fits as well as the normalised experimental results for the different axial positions are shown in Figures 3.36, 3.37, 3.38, 3.39, 3.40, 3.41, 3.42 and

	1cm			2cm			5cm			10cm			15cm			20cm									
	$k_{r\mu}$	$k_{r\sigma}$	λ_μ	$k_{r\mu}$	$k_{r\sigma}$	λ_μ	$k_{r\mu}$	$k_{r\sigma}$	λ_μ	$k_{r\mu}$	$k_{r\sigma}$	λ_μ	$k_{r\mu}$	$k_{r\sigma}$	λ_μ	$k_{r\mu}$	$k_{r\sigma}$	λ_μ							
1A	2.21	0.21	22.78	1.89	2.46	0.05	21.21	0.54	2.72	0.01	19.37	0.36	2.22	0.05	22.02	0.31	1.39	0.00	41.87	0.28	1.29	0.03	42.83	2.53	
1B	-	-	-	-	-	-	-	-	-	-	-	-	-	-	-	-	-	-	-	-	-	-	-	-	-
1C	2.50	0.02	20.22	0.40	2.54	0.02	20.40	0.38	2.74	0.00	20.65	0.37	2.73	0.02	23.21	0.19	2.73	0.00	24.61	0.16	2.73	0.00	25.61	0.17	
1D	2.48	0.03	21.82	0.67	2.73	0.04	22.97	0.41	2.76	0.01	22.98	1.12	2.77	0.03	24.68	0.44	2.72	0.05	26.96	0.73	2.64	0.01	28.62	0.36	
2A	2.97	0.11	23.59	1.23	2.69	0.07	27.11	0.36	2.58	0.08	25.45	1.12	2.72	0.12	25.22	0.30	2.22	0.08	30.09	1.15	1.64	0.05	43.77	4.47	
2B	2.10	0.22	27.99	5.35	2.25	0.03	27.37	0.75	2.76	0.08	22.76	0.41	2.52	0.01	26.04	0.38	2.11	0.04	34.66	0.77	1.93	0.01	40.17	0.60	
2C	2.55	0.06	21.02	0.53	2.42	0.08	23.71	0.62	2.61	0.17	19.72	0.15	2.65	0.06	17.39	0.46	2.70	0.01	15.92	0.38	2.73	0.03	15.40	0.56	
2D	2.26	0.15	22.85	1.79	2.02	0.02	30.26	1.50	2.57	0.04	21.62	0.28	2.38	0.02	22.69	0.57	2.25	0.02	22.89	0.03	2.34	0.29	21.24	4.25	
2E	2.66	0.05	21.21	1.04	2.58	0.04	24.16	0.64	2.70	0.25	22.83	1.67	2.56	0.08	21.17	2.24	2.46	0.13	17.00	3.91	2.43	0.10	15.97	2.22	
	Log-normal																								
1A	μ_μ	μ_σ	σ_μ	σ_σ	μ_μ	μ_σ	σ_μ	σ_σ	μ_μ	μ_σ	σ_μ	σ_σ	μ_μ	μ_σ	σ_μ	σ_σ	μ_μ	μ_σ	σ_μ	σ_σ	μ_μ	μ_σ	σ_μ	σ_σ	
1A	2.99	0.07	0.64	0.08	2.93	0.03	0.55	0.02	2.84	0.02	0.48	0.00	2.96	0.01	0.62	0.02	3.49	0.01	1.25	0.00	3.32	0.04	1.26	0.03	
1B	-	-	-	-	-	-	-	-	-	-	-	-	-	-	-	-	-	-	-	-	-	-	-	-	
1C	2.88	0.02	0.54	0.01	2.89	0.02	0.53	0.01	2.91	0.02	0.48	0.00	3.02	0.01	0.48	0.01	3.08	0.01	0.48	0.00	3.12	0.01	0.48	0.00	
1D	2.95	0.03	0.54	0.01	3.01	0.02	0.48	0.01	3.01	0.05	0.47	0.00	3.09	0.02	0.47	0.01	3.17	0.02	0.48	0.01	3.23	0.01	0.50	0.00	
2A	3.05	0.06	0.43	0.02	3.18	0.01	0.49	0.02	3.11	0.04	0.52	0.02	3.11	0.01	0.48	0.03	3.27	0.04	0.61	0.03	3.70	0.10	1.06	0.05	
2B	2.92	0.02	0.53	0.02	3.03	0.02	0.56	0.02	2.86	0.00	0.51	0.05	2.73	0.02	0.50	0.01	2.65	0.02	0.49	0.00	2.61	0.04	0.48	0.01	
2C	3.16	0.15	0.68	0.09	3.17	0.02	0.61	0.01	3.01	0.01	0.47	0.02	3.13	0.01	0.53	0.00	3.40	0.02	0.67	0.02	3.56	0.02	0.76	0.01	
2D	2.99	0.07	0.62	0.05	3.24	0.04	0.71	0.01	2.95	0.01	0.52	0.01	2.98	0.03	0.58	0.01	2.98	0.00	0.62	0.01	2.90	0.20	0.60	0.09	
2E	2.93	0.05	0.50	0.01	3.06	0.03	0.52	0.01	3.01	0.06	0.49	0.06	2.92	0.11	0.52	0.02	2.68	0.21	0.55	0.04	2.63	0.14	0.56	0.03	
	Gamma																								
1A	$k_{g\mu}$	$k_{g\sigma}$	θ_μ	θ_σ	$k_{g\mu}$	$k_{g\sigma}$	θ_μ	θ_σ	$k_{g\mu}$	$k_{g\sigma}$	θ_μ	θ_σ	$k_{g\mu}$	$k_{g\sigma}$	θ_μ	θ_σ	$k_{g\mu}$	$k_{g\sigma}$	θ_μ	θ_σ	$k_{g\mu}$	$k_{g\sigma}$	θ_μ	θ_σ	
1A	3.50	0.60	6.25	1.52	4.27	0.19	4.66	0.24	5.23	0.02	3.46	0.08	3.43	0.15	6.08	0.35	1.56	0.00	24.34	0.18	1.46	0.05	25.08	2.18	
1B	-	-	-	-	-	-	-	-	-	-	-	-	-	-	-	-	-	-	-	-	-	-	-	-	
1C	4.38	0.07	4.33	0.06	4.50	0.09	4.24	0.05	5.29	0.01	3.65	0.07	5.24	0.10	4.14	0.11	5.26	0.01	4.38	0.02	5.22	0.01	4.59	0.04	
1D	4.34	0.10	4.70	0.25	5.26	0.15	4.09	0.06	5.36	0.03	4.01	0.22	5.38	0.10	4.29	0.15	5.19	0.20	4.86	0.31	4.89	0.02	5.47	0.08	
2A	6.31	0.51	3.51	0.11	5.15	0.28	4.93	0.29	4.69	0.28	5.09	0.51	5.24	0.48	4.53	0.43	3.51	0.28	8.12	0.91	1.92	0.09	22.31	3.33	
2B	4.58	0.24	4.29	0.31	4.13	0.28	5.38	0.47	4.81	0.66	3.89	0.56	4.92	0.22	3.31	0.24	5.12	0.02	2.91	0.08	5.26	0.11	2.74	0.13	
2C	3.19	0.57	8.47	3.15	3.64	0.08	7.00	0.33	5.43	0.32	3.94	0.31	4.46	0.05	5.45	0.12	3.11	0.11	10.52	0.59	2.59	0.03	14.84	0.34	
2D	3.64	0.47	5.95	1.15	2.97	0.05	9.40	0.55	4.68	0.15	4.32	0.20	3.97	0.06	5.34	0.06	3.54	0.05	6.03	0.08	3.89	0.97	5.45	2.08	
2E	4.99	0.18	3.98	0.31	4.72	0.14	4.78	0.18	5.21	0.98	4.24	1.12	4.61	0.32	4.29	0.16	4.23	0.44	3.85	1.34	4.14	0.34	3.65	0.75	

Table 3.8: Fit parameters averaged over for their means and standard deviations for the Rosin-Rammler, Log-Normal and Gamma distributions for aerosol cans 1A, 1C, 1D, 2A, 2B, 2C, 2D, 2E at axial positions of 1 cm, 2 cm, 5 cm, 10 cm, 15 cm and 20 cm.

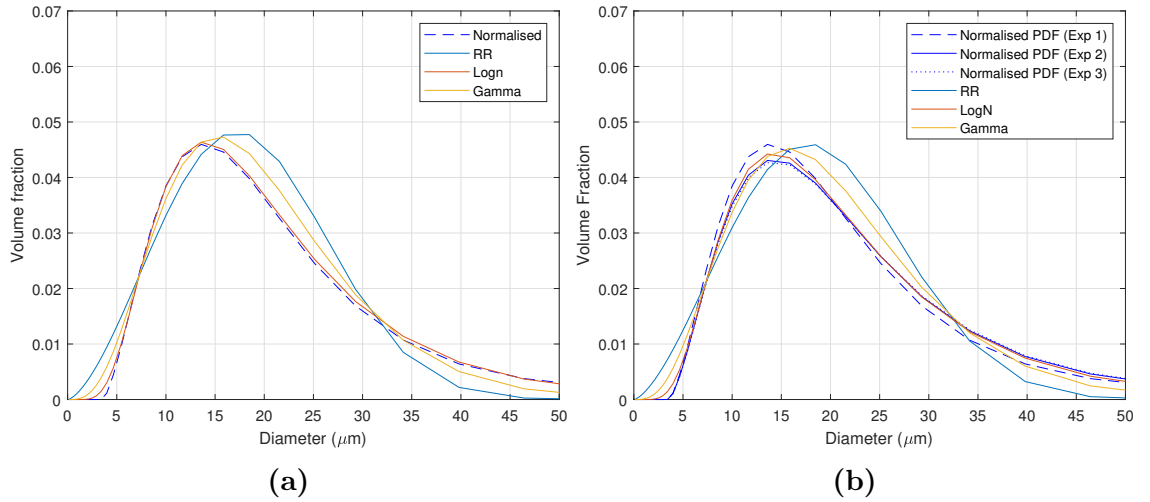


Figure 3.35: For aerosol can 1D at axial position of 1cm the (a) Normalised PDF plotted with fitted distributions Rosin-Rammler ($k_r = 2.52, \lambda = 21$), Log-normal ($\mu = 2.92, \sigma = 0.535$), Gamma ($k_g = 0.535, \theta = 4.42$); (b) Normalised PDF for repeated experiments plotted with mean parameter distributions Rosin-Rammler ($k_r = 2.48, \lambda = 0.67$), Log-normal ($\mu = 2.95, \sigma = 0.54$), Gamma ($k_g = 4.34, \theta = 4.70$).

3.43 for aerosol cans 1A, 1C, 1D, 2A, 2B, 2C, 2D, and 2E respectively. For nearly all cases the mean parameters calculated for the Log-normal or Gamma distributions provide good fits to the normalised PDFs. The cases where the fits do not perform as well are now discussed.

Aerosol cans 1A, 2C and 2D show significant deviation to the normalised PDFs at an axial position of 1 cm. Where there is deviation between the distributions the mean parameter fit tries to capture features such as the peak location and distribution tail across the three repeats. This results in the significant deviation observed.

For aerosol cans 1A, 2A and 2C, the aerosol cans where the only liquid content is the propellant, the normalisation process of eliminating the small mode impacts the resultant PDF. This can be seen for large axial distances where the evaporation effects are seen with the distribution. For some distributions the fitting was unsuccessful, where they reached the 10^4 iteration limit. For example for aerosol can 1A at an axial distance greater than 10 cm the form of the PDF did not fit with a unimodal distribution.

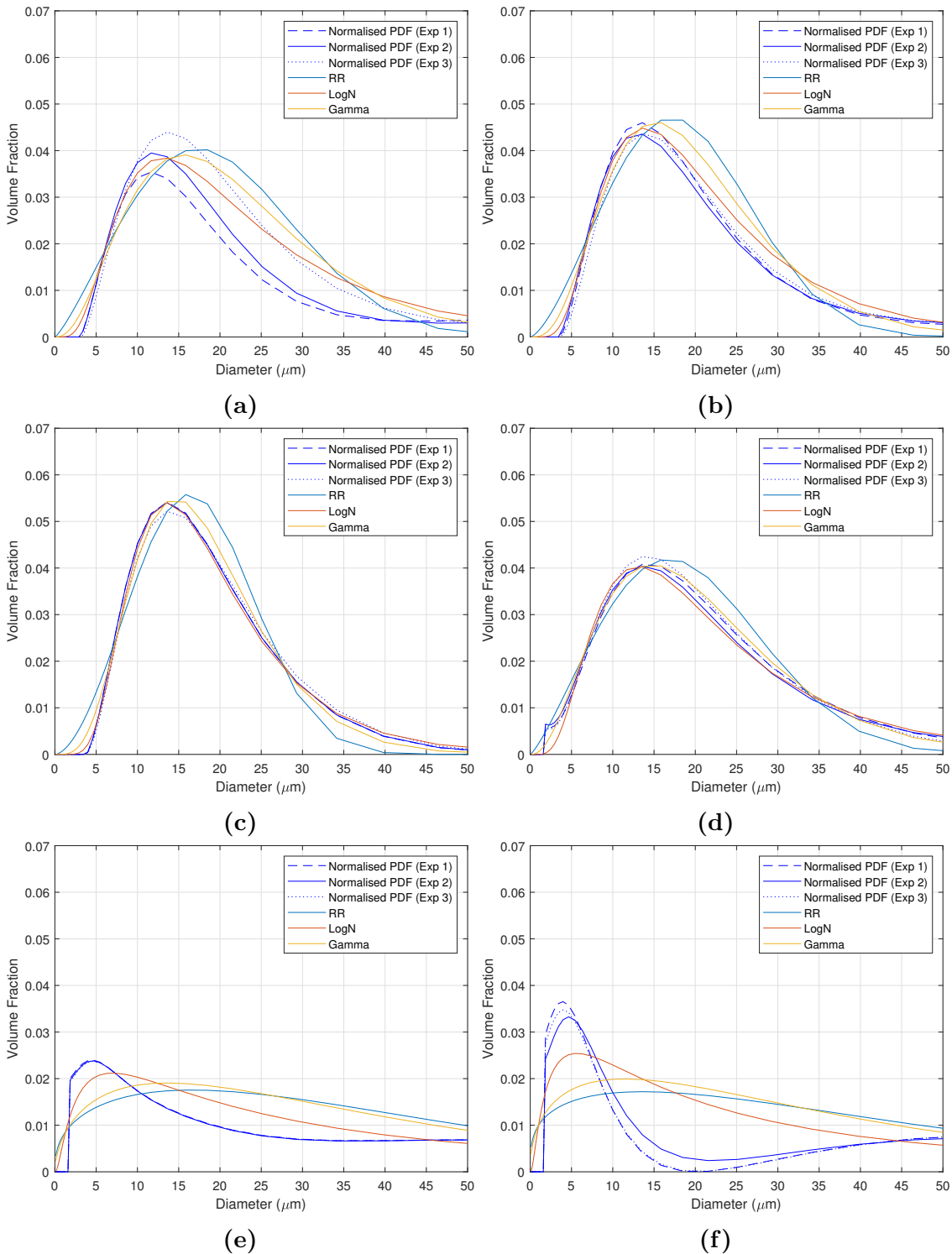


Figure 3.36: Normalised PDF for aerosol can 1A (Propellant) showing each repeat and the mean parameter fits of the Rosin-Rammler, Log-Normal and Gamma Distributions for axial distances (a) 1 cm, (b) 2 cm, (c) 5 cm, (d) 10 cm, (e) 15 cm, (f) 20 cm.

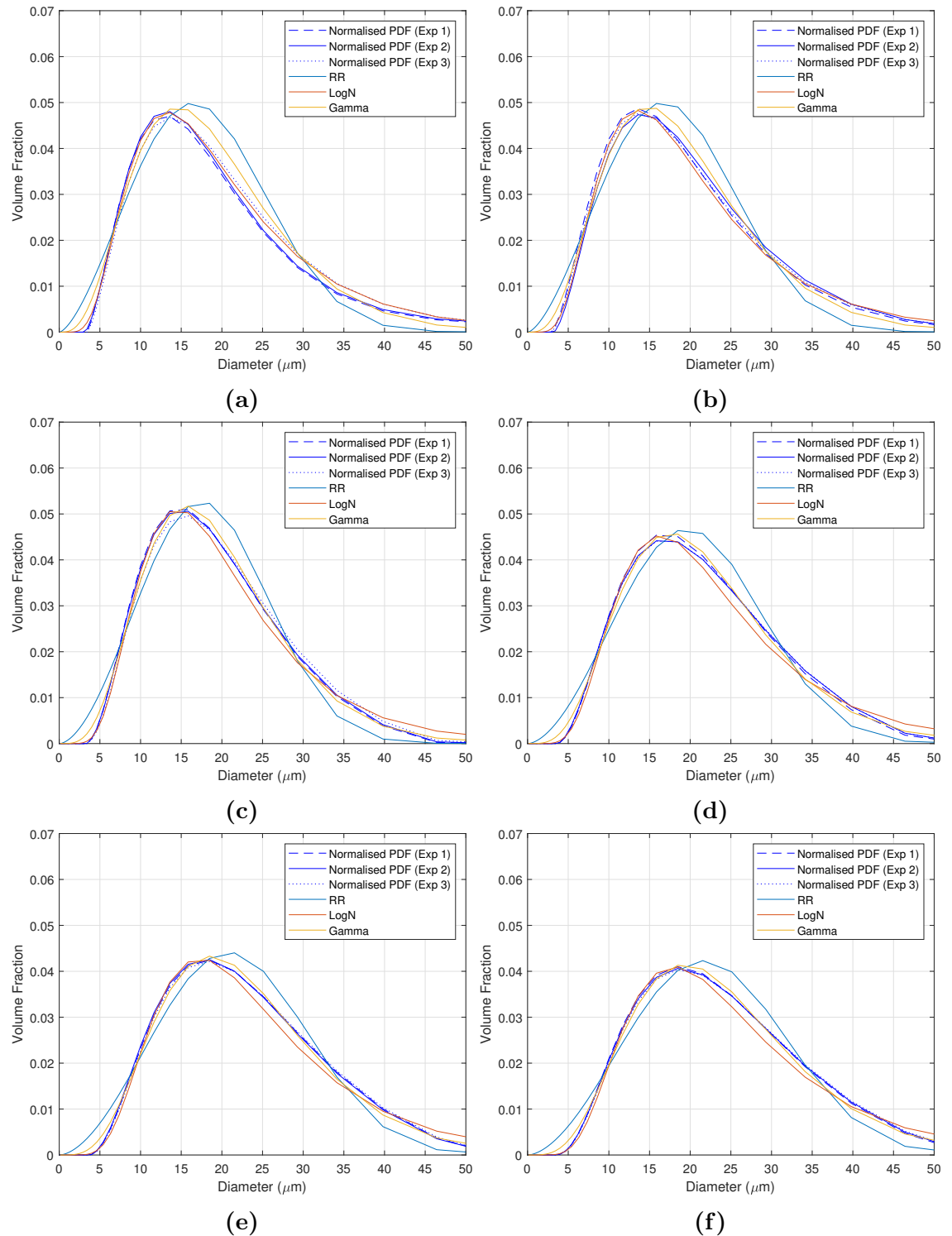


Figure 3.37: Normalised PDF for aerosol can 1C (Alcohol + Propellant) showing each repeat and the mean parameter fits of the Rosin-Rammler, Log-Normal and Gamma Distributions for axial distances (a) 1 cm, (b) 2 cm, (c) 5 cm, (d) 10 cm, (e) 15 cm, (f) 20 cm.

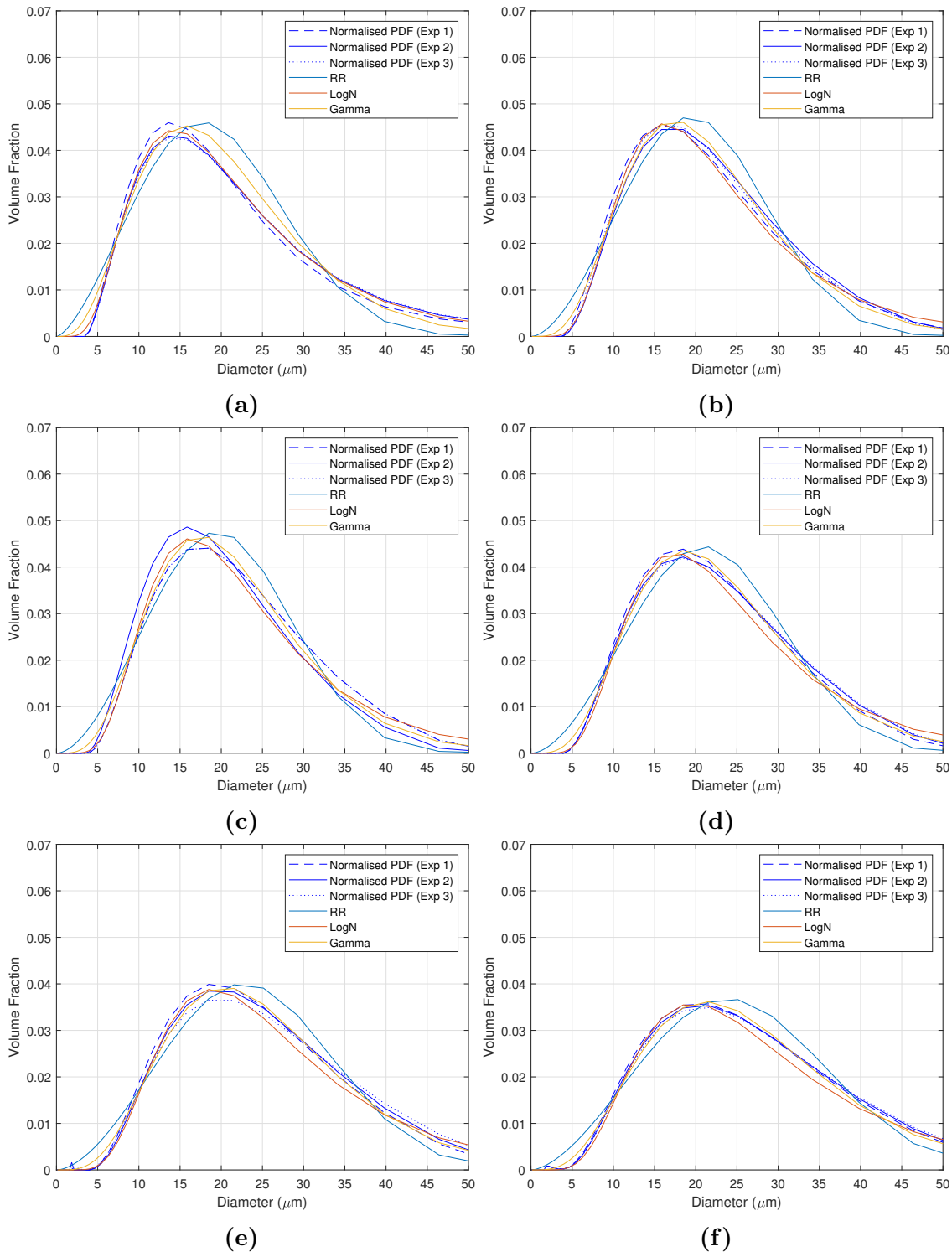


Figure 3.38: Normalised PDF for aerosol can 1D (Full Product) showing each repeat and the mean parameter fits of the Rosin-Rammler, Log-Normal and Gamma Distributions for axial distances (a) 1 cm, (b) 2 cm, (c) 5 cm, (d) 10 cm, (e) 15 cm, (f) 20 cm.

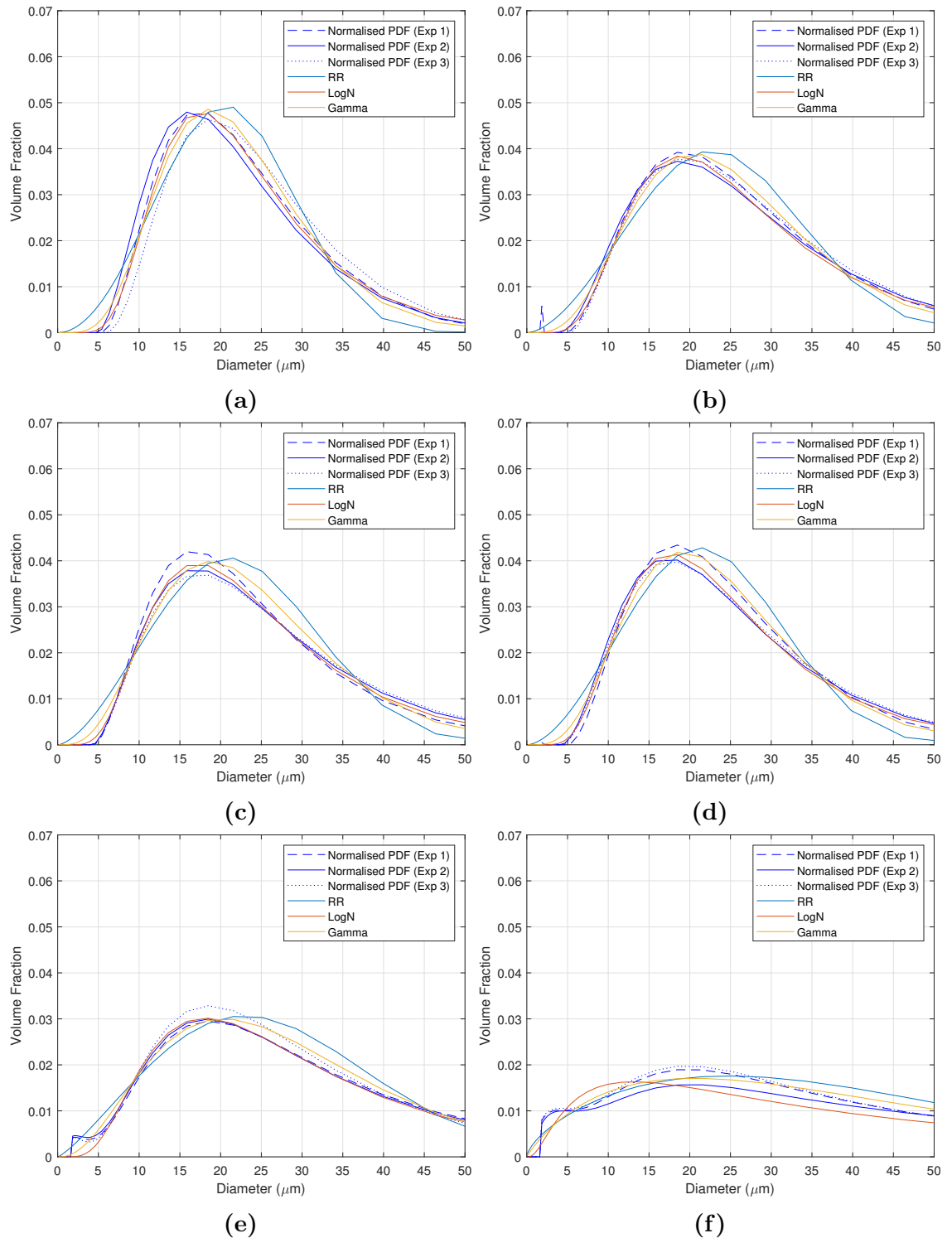


Figure 3.39: Normalised PDF for aerosol can 2A (Propellant) showing each repeat and the mean parameter fits of the Rosin-Rammler, Log-Normal and Gamma Distributions for axial distances (a) 1 cm, (b) 2 cm, (c) 5 cm, (d) 10 cm, (e) 15 cm, (f) 20 cm.

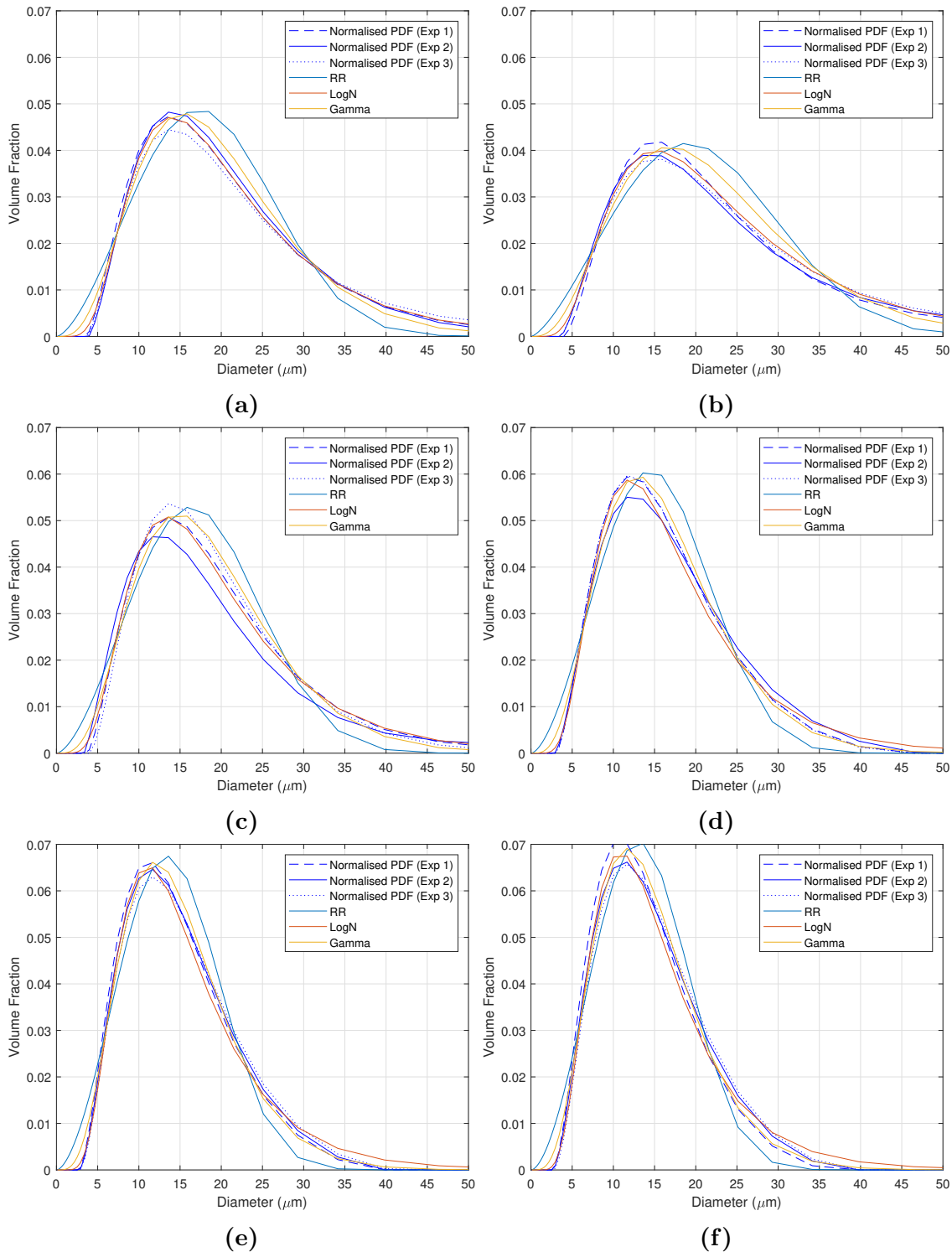


Figure 3.40: Normalised PDF for aerosol can 2B (D5 + Propellant) showing each repeat and the mean parameter fits of the Rosin-Rammler, Log-Normal and Gamma Distributions for axial distances (a) 1 cm, (b) 2 cm, (c) 5 cm, (d) 10 cm, (e) 15 cm, (f) 20 cm.

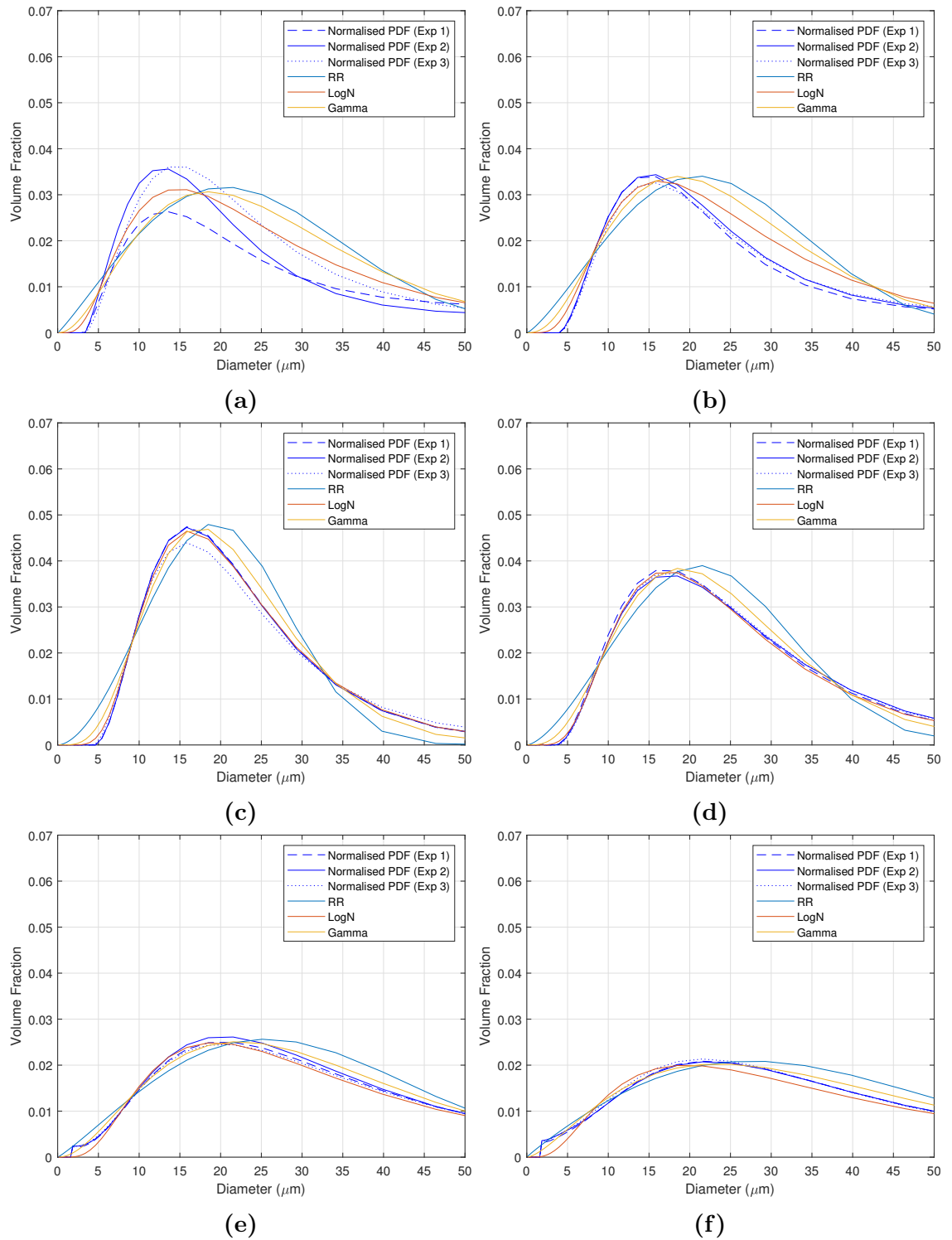


Figure 3.41: Normalised PDF for aerosol can 2C (Active + Propellant) showing each repeat and the mean parameter fits of the Rosin-Rammler, Log-Normal and Gamma Distributions for axial distances (a) 1 cm, (b) 2 cm, (c) 5 cm, (d) 10 cm, (e) 15 cm, (f) 20 cm.

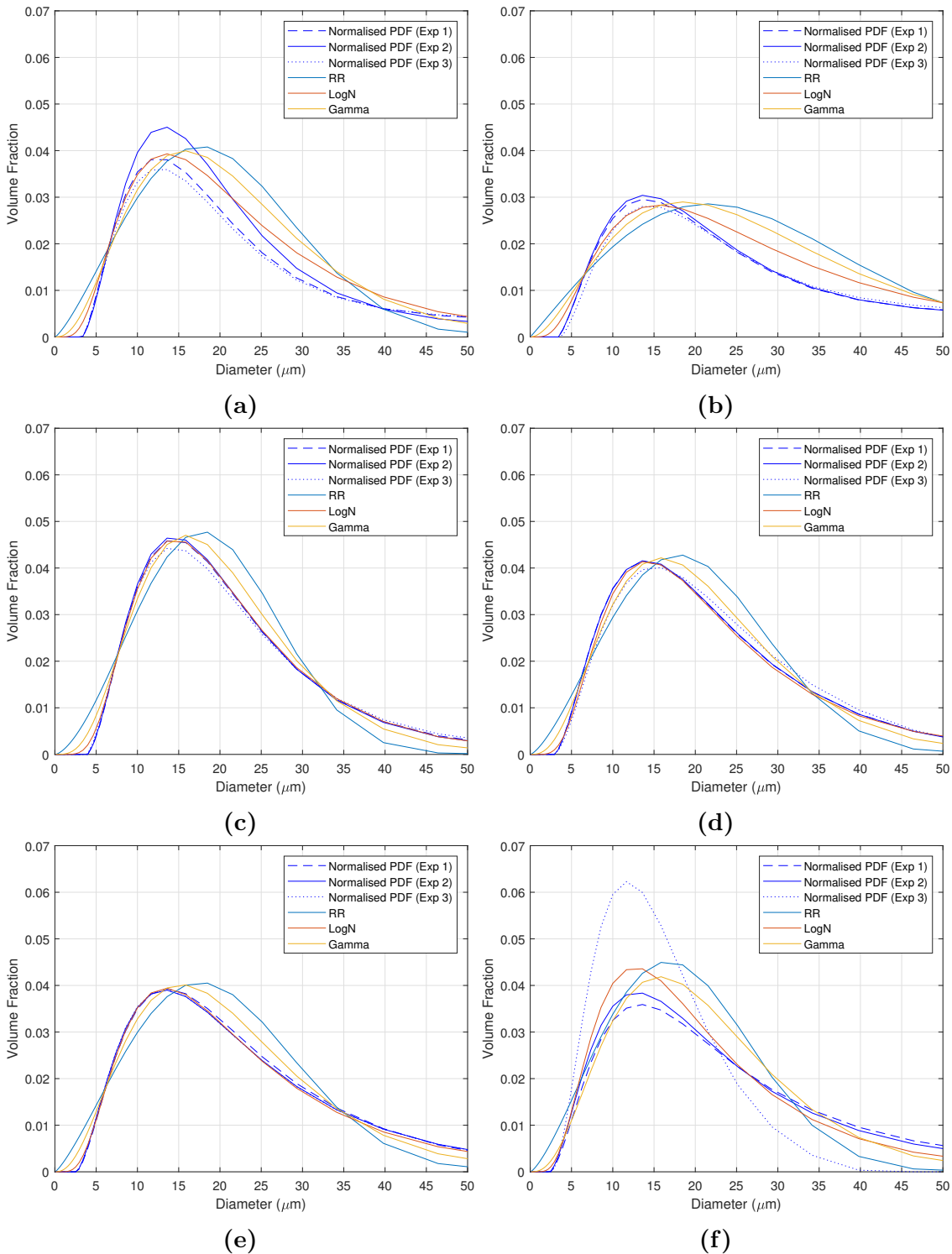


Figure 3.42: Normalised PDF for aerosol can 2D (Slurry + Propellant) showing each repeat and the mean parameter fits of the Rosin-Rammler, Log-Normal and Gamma Distributions for axial distances (a) 1 cm, (b) 2 cm, (c) 5 cm, (d) 10 cm, (e) 15 cm, (f) 20 cm.

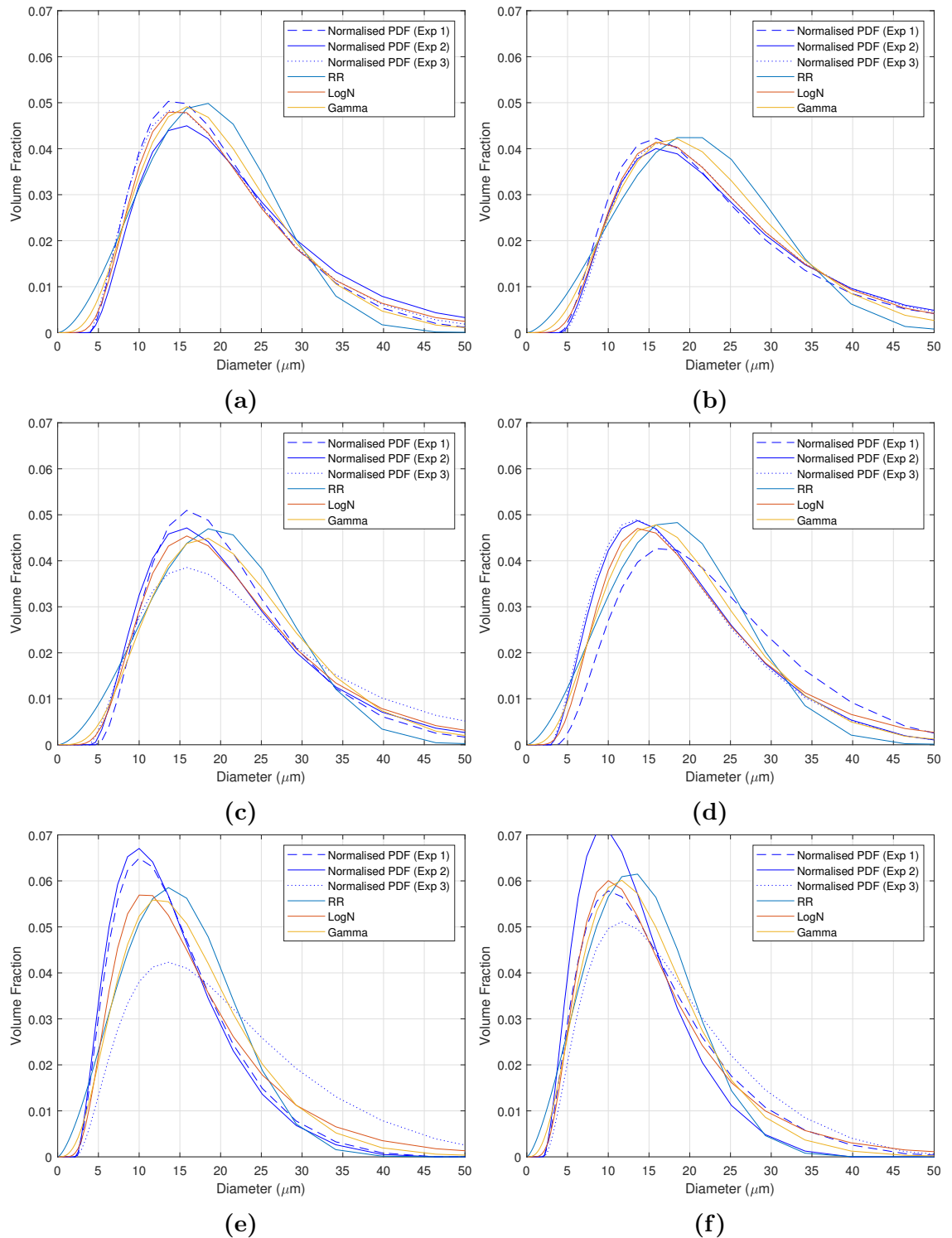


Figure 3.43: Normalised PDF for aerosol can 2E (Full Product) showing each repeat and the mean parameter fits of the Rosin-Rammler, Log-Normal and Gamma Distributions for axial distances (a) 1 cm, (b) 2 cm, (c) 5 cm, (d) 10 cm, (e) 15 cm, (f) 20 cm.

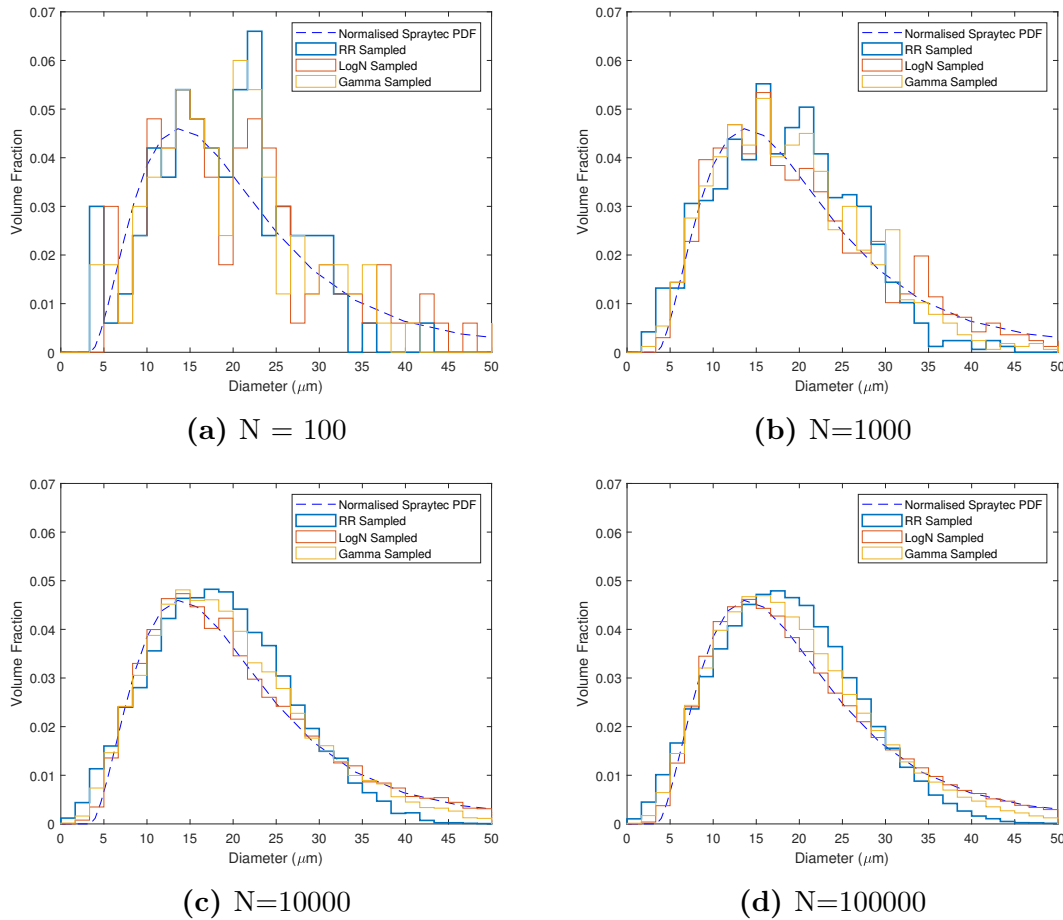


Figure 3.44: Normalised PDF for aerosol can 1D at 1cm and the resultant PDFs after sampling from the fitted Rosin-Rammler, Log-Normal and Gamma distributions with (a) 100, (b) 1000, (c) 10000 and (d) 100000 uniformly distributed points.

Sampling From Fitted Distributions results

For values of N equal to 100, 1000, 10000 and 100000 the resulting sampled distributions are plotted with the normalised PDF for aerosol can 1D at 1 cm which is shown in Figure 3.44. From Figure 3.44 it can be seen that a small value of $N=100$ gives a widely varying sampled PDF for all distributions. As N increases the sampled distribution tends closer to the distributions fitted and therefore the normalised measured PDF. At $N=10000$ the Log-normal distribution is seen to trace the normalised Spraytec PDF with excellent agreement. This method of sampling from the fitted distributions allows for the generation of a set of particle sizes which can then be injected into numerical CFD models and is representative of the PSD expected from a deodorant-type aerosol can.

3.3.3 Spray Temperature Measurements Results

Here the temperature profiles measured for each of the tested aerosol cans is presented showing variations due to nozzle type and formulation.

Temperature Profiles

The time-varying temperature for the propellant aerosol cans 1A and 2A can be seen in Figure 3.45b. These were picked to compare nozzle influence as they only differ by nozzle and have the same contents. The can is actuated until an approximate steady temperature is observed (approximately 5 s), at which point the actuator is released and the thermocouples tend to thermal equilibrium with the ambient. In Figure 3.45a, for the swirl nozzle, a sudden decrease in temperature can be observed on the thermocouple positioned at 10 cm at the time the actuator is released. This is likely due to slight misalignment with the centreline of the thermocouple tip. From Figure 3.45a the alignment of the centreline impacts the temperature recording. For the 5 cm and 10 cm thermocouples ice can be seen to form on the thermocouples during the experiments. This is due to the entrainment of water vapour from the ambient and such low temperatures that are observed for those thermocouples. During the warm up period of the thermocouples after actuation the energy goes into changing phase as observed with the constant temperature value at 0°C.

The mean minimum temperatures for the repeated runs and the standard deviation for cans 1A and 2A can be seen in Figure 3.46. Here additional runs were performed to provide further data points of the centreline temperature and increased spatial resolution. For the additional runs the first thermocouple was positioned at 3cm but the spacing was kept consistent with the previous measurements.

Figure 3.46 shows that the thermocouples positioned at 5cm reach a lower temperature than the thermocouples at 1cm or 3cm, and at a temperature below

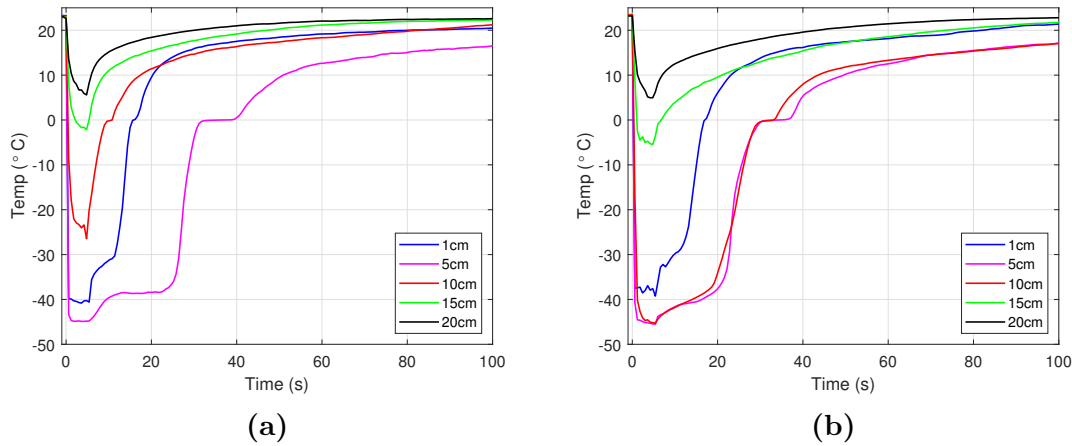


Figure 3.45: Time series of bare thermocouples for aerosol cans (a) 1A swirl nozzle with propellant and (b) 2A plain nozzle with propellant.

the boiling point of propane. The additional cooling was first believed to be due to the Joule-Thomson effect, where the gas experiences a drop in pressure through the orifice, however this cooling is still observed further downstream where warm ambient air has been entrained, and so this effect is not considered to be the dominant cooling effect.

Within the initial core region of the cone the liquid evaporation is in an environment saturated with the same vapour constituents of the product propellant mix. As ambient air is entrained into the spray the saturation pressure drops and this results in the additional cooling. The temperature decreases following the saturation pressure curve. This lower temperature can also be observed in Figure 3.45. The centreline temperature is consistent for both nozzles up to 7 cm, where the momentum of the jet dominates the flow. However, the simple orifice nozzle shows a deeper jet penetration than the swirl nozzle. The swirl induced within swirl nozzles enhances momentum decay of the jet which could be a possible cause for this. The thermocouples positioned at 17 cm, 20 cm and 22 cm reach the same temperature suggesting the centreline temperature reaches a point where the initial spray generation plays less influence far downstream from the nozzle and is mainly affected by the ambient.

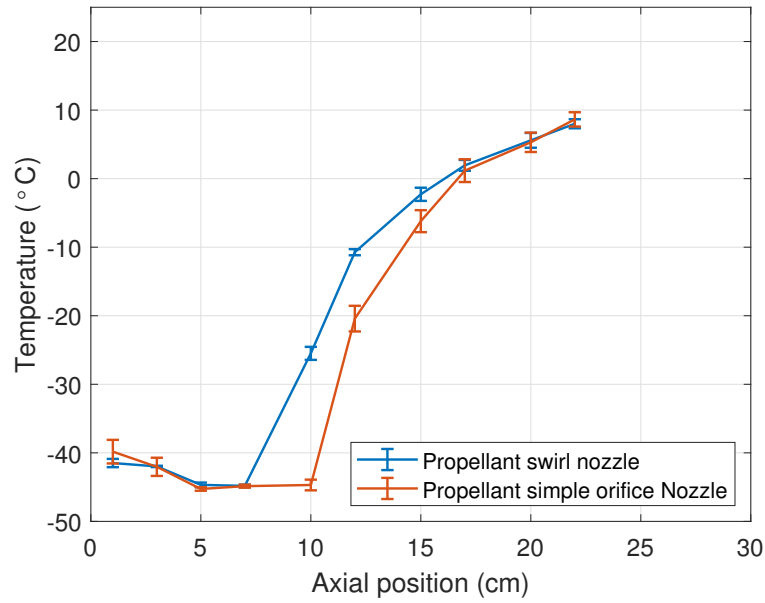


Figure 3.46: Average centreline temperature profile and their standard deviations at axial positions: 1, 3, 5, 7, 10, 13, 15, 17, 20 and 22 cm for aerosol cans 1A (Blue) and 2A (Orange).

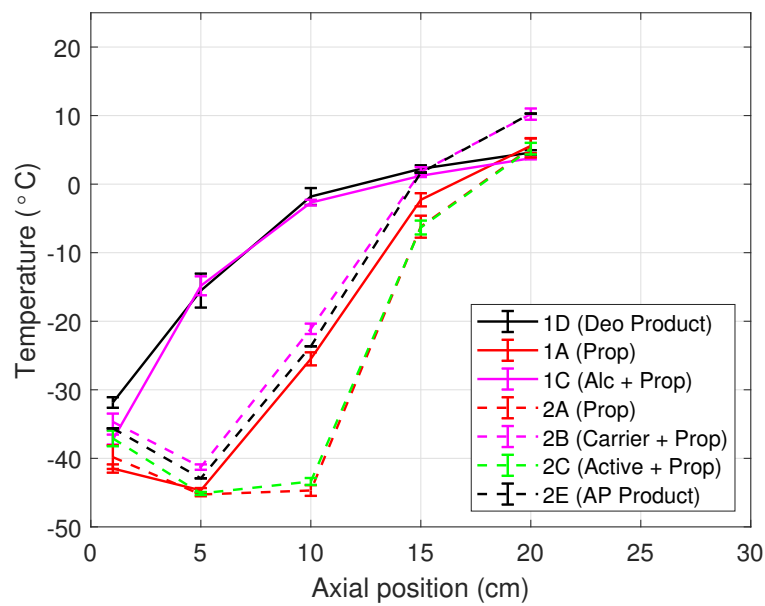


Figure 3.47: Centreline temperature at different axial positions for all the aerosol cans tested.

Figure 3.47 shows the centerline temperature for all the aerosol cans tested except can 1B (Prop+water). This can is not included in the results as after the first spray there was no water remaining in the can and thus resulted in a spray equivalent to that of 1A (Prop). The black lines in Figure 3.47 represent the full product cans where a clear difference in centreline temperature can be observed between 1D (black solid) and 2E (black dashed). The centreline temperature for 1D decays after exiting the nozzle whereas for 2E the centreline temperature continues to decrease. A possible explanation of this is that 2E exhibits greater evaporation of the propellant or less entrainment of the ambient, resulting in additional cooling or less mixing of warm ambient air.

Looking at 1A, 1C and 1D the effects due to the addition of alcohol can be seen. The pure propellant aerosol can (1A) has increased flashing and as a result a colder spray. The inclusion of alcohol alters the vapour pressure and as a result the change in centreline temperature decay is significant. Similar centreline temperature decay profiles can be seen for the propellant with alcohol (1C) and the full deodorant product (1D). A difference can be observed in the initial temperature at 1cm which may be a result of the additional components in 1D.

A similar observation of the effects of an additional less volatile fluid can be seen by looking at the centreline decay of 2A, 2B and 2E. The centreline temperature remains colder for a greater distance for the pure propellant can (2A). After the inclusion of carrier fluid D5 (2B) the centreline temperature begins to warm at a shorter axial distance. This is then comparable to the centreline temperature for the full AP product (2E). Note the exact point at which warming is observed is dependant on the spatial resolution of the data. Here only five thermocouple measurements are used and as such give a poor estimate of the change in temperature gradient. Further experiments would be needed to determine the exact axial distance at which a positive temperature gradient is first observed. The centreline temperatures of 2A and 2C, seen in figure 3.47, show that the inclusion of the active

(AACH) appears to have little affect on the centreline temperature.

3.4 Summary

The schlieren, Spraytec and thermocouple experiments performed have all provided insight into the complex nature of the sprays generated from deodorant-type aerosol cans. In particular the different formulations of the aerosol cans tested here, as well as the effects of nozzle type on the spray generated. The individual experiments help in understanding how different factors impact the spray generation, but the combination of the three paints a more detailed picture of this process. The experimental techniques allowed for investigation into the impact of typical deodorant-type ingredients on the spray generation and resultant sprays. The main conclusions of the schlieren, Spraytec and thermocouple experiments are detailed here.

The schlieren technique is an incredibly useful tool and was used to investigate the qualitative features of sprays generated for different formulations. The technique was able to capture the density differences within the spray which would otherwise be near impossible to observe with the naked eye. Three distinct spray stages were identified: spray generation stage, fully-developed stage and collapsing stage.

Using the Sobel edge detection filter the spray region was identified and extracted from the recorded video and post-processed. Quantitative data such as spray angle was measured using a single frame and mean frame averaged over a section of the video. From these representative frames the spray angle was measured. The carrier jet from the simple orifice nozzle resulted in a smaller spray angle relative to the swirl nozzle ranging from $16.3 - 20.3^\circ$ and $19.5 - 22.2^\circ$ respectively, believed to be due to the internal nozzle flow dynamics and differing mass flow rates.

Turbulent structures within the spray are identifiable and show the typical features of the spray structure, such as the turbulent eddies generated due to KH instabilities across the interface and the gaseous carrier jet and product jets during

actuation.

The volume based PSD through the spray was measured at axial positions of 1 cm, 2 cm, 5 cm, 10 cm, 15 cm and 20 cm using the Malvern Spraytec. The results provided a look at the evolution of PSD throughout the spray cone. Distribution statistics such as the Span, D_{50} , $D_{3,2}$ (SMD) and $D_{4,3}$ were calculated for the different formulations. Here increasing trends of the SMD with respect to axial distance were found for the swirl nozzle, where the contents were alcohol+propellant and the full product. This contrasts with the simple orifice nozzle where all formulations showed a decreasing trend.

For the pure propellant formulations the influence of nozzle type can be determined. Droplet evaporation effects on the centreline temperature were clearly observed but the evaporation effects on the measured distributions were observed at different axial positions, appearing at 10 cm for the swirl nozzle and 15 cm for the simple orifice nozzle. This increase in axial distance for the observed evaporation effects agrees with the increased axial distance at which point the centreline temperature begins to increase, as measured by the thermocouple experiments.

Other temperature measurements provide an insight into the influence of typical additional care product fluids, such as alcohol and D5, and the antiperspirant ingredient AACH on the evaporation of droplets. The data clearly shows that the centreline temperature is influenced greatly by the additional fluid and propellant mix with a temperature decay occurring at a reduced axial distance. This is believed to be due to alteration of the vapour pressure of the fluid as the additional fluids are less volatile.

Most importantly the experimental results provide a new dataset for the spray characteristics of sprays generated from deodorant-type aerosol cans. The schlieren videos provide insight into the sprays and their structure as they propagate from the nozzle. The PSD measurements provide an input condition for simple

numerical models as well as a validation set for more complex models where flash atomization is captured. The temperature measurements also provide a validation set for spray temperature profiles due to evaporation of droplets consisting of an LPG blend and mixtures including additional fluids like alcohol and D5.

Chapter 4

Species Transport of a Single Phase Gaseous Jet

4.1 Introduction

This chapter discusses the approach to producing a validated CFD model of a steady single phase carrier jet. Model validation is the process of determining if a model is able to reliably predict reality. Comparing model predictions against experimental measurements is a key step in validating a numerical model. The process of producing a robust CFD model is complex: the relevant physics and the physical equations which describe them are identified; next a representative geometry is generated for the problem; then a computational mesh is generated which is capable of resolving the important length scales of the problem. This process is detailed in this chapter. The numerical model is then used to investigate the effect of the ambient flow conditions and inlet conditions on the resultant flow.

4.1.1 Problem Motivation

The product from an aerosol can is a mixture of different compounds along with an alkane propellant mixture. The pressure inside the aerosol can is around 4-6 atm depending on the blend of propellant used, as detailed in Chapter 2, Section 2.2. This internal pressure is much larger relative to the outside ambient pressure of 1 atm. At these high pressures the propellant in the aerosol can exists in liquid form at room temperature which gives the aerosol can a long usage lifetime. Once the actuator of the can is pressed the high pressure contents of the can tend to the low pressure ambient. To aid the breakup of the liquid some aerosol cans have a vapour phase tap (VPT) installed, which allows for the vapour phase inside the aerosol can to also be ejected alongside the liquid propellant product mixture. This vapour phase along with the already evaporating propellant is what forms the carrier jet for the product.

The first stage of analysis is to produce a numerical model to represent the gaseous propellant carrier jet. The jet will affect the transportation of the droplets, which will be included within the overall physics of the model in the subsequent chapter. It is important to first generate a model which is able to capture the carrier flow, which then forms the base component for the numerical model. The numerical model is then validated against the experimental work of [Gouldin et al. \(1986\)](#) and [Schefer \(1987\)](#) where a gaseous propane jet is released into a co-flow. The schlieren experimental results detailed in Chapter 3 also provide spray angle data for further model validation.

4.2 Relevant Physics

The overall aim of the final CFD model is to be able to predict the carry-over of droplets after impinging onto a surface at a distance of approximately $\mathcal{O}(10^{-1} \text{ m})$.

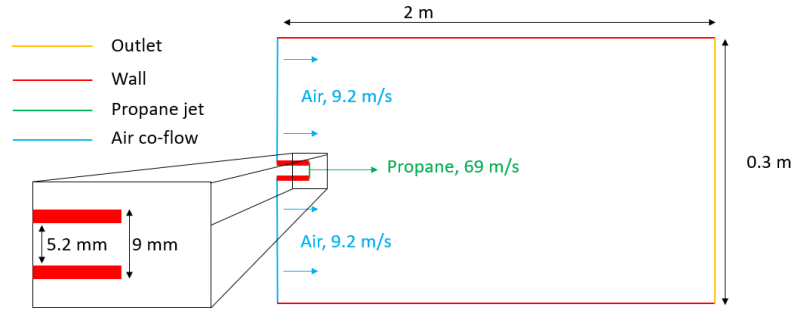


Figure 4.1: Cut through schematic of the square wind tunnel used in the [Schefer \(1987\)](#), not to scale.

The nozzle of a deodorant-type aerosol can is of size $\mathcal{O}(10^{-3} \text{ m})$ and the droplets generated are of mean size $\mathcal{O}(10^{-5} \text{ m})$, as shown in the Malvern Spraytec experiments detailed in Chapter 3. As discussed in Chapter 2, modelling over such a range of length scales can be computationally expensive to fully resolve the physics and so a balance of model fidelity and computational cost needs to be found. For this reason, only the flow field downstream of the nozzle exit is considered and therefore the internal upstream flow, flashing behaviour and internal can physics are not captured.

[Schefer \(1987\)](#) provides a database of experimental results of a gaseous propane jet released into co-flow of air. Velocity data for both axial and radial positions are given for axial positions 4D, 15D, 30D and 50D, where D is the nozzle inner diameter (ID) and axially data is collected up to 80D. The propane mixture fraction is also given for the same axial and radial positions. The velocity data is collected using laser doppler velocimetry (LDV) for both the seeding particles in the co-flow air stream and those in the propane stream. The propane mixture fraction is calculated using a combination of Rayleigh and Raman scattering systems.

The experiments detailed in [Schefer \(1987\)](#) were performed within a forced-draft vertical wind tunnel of streamwise length 2 m and cross-section $0.3 \text{ m} \times 0.3 \text{ m}$, with a schematic shown in Figure 4.1. The gaseous propane jet is injected into the tunnel through a nozzle of outer-diameter (OD) 0.009 m and inner-diameter (ID) 0.0052 m, with a maximum jet velocity of 69 ms^{-1} and a bulk velocity of 53 ms^{-1} .

Around the nozzle a co-flow of air is present, moving in the streamwise direction at a velocity of 9.2 ms^{-1} . The temperature of both the propane jet and the co-flow are at 294 K. Here the Reynolds number is equal to

$$\text{Re} = \frac{\rho UL}{\mu} = 1.8 \times \frac{69 \times 0.0052}{8.04 \times 10^{-6}} \approx 8 \times 10^5. \quad (4.1)$$

An initial model is constructed to replicate the experimental set up of [Schefer \(1987\)](#). The numerical model must to be able to track the individual components of the air-propane mixture, to capture how the propane jet mixes with the ambient. As the fluids are inherently miscible the case is still considered to be a single phase flow. For the transport of propane and the different components of air, a non-reacting species transport model is used. Convection-diffusion equations for the i^{th} species' mass fraction (Y_i), detailed in Section [2.5.4](#), are used to model the transport of the propane and air mixture.

4.3 Turbulence Model Study

Due to the high Reynolds number of the release the flow is considered turbulent. The velocity and mass fraction data of [Schefer \(1987\)](#) allow turbulence model validation for the carrier jet flows. The turbulence models investigated were the Standard, RNG and Realizable $k - \varepsilon$ models as well as the $k - \omega$ and $k - \omega$ SST models. Only 2-equation RANS models are used in order to keep the computational cost of the simulation low, but it is acknowledged that more computationally expensive, higher fidelity models such as the Reynolds Stress Model (RSM) or LES may more accurately model the turbulence of this problem.

There have been several studies investigating turbulence models for turbulent jets. [Celis et al. \(2005\)](#) investigated the 2 equation RANS models as well as the RSM and found that the standard, realizable $k - \varepsilon$ models and the $k - \omega$ SST model

gave best performance. Ghahremanian and Moshfegh (2011) similarly found that the $k-\omega$ SST model performed well. Som et al. (2012) and Rostampour et al. (2022) investigated combustion and compared a RANS approach to using LES and found that both approaches were able to predict spray features such as spray penetration and mixture fraction. LES however was able to predict the spray structure more accurately, resolving the turbulent structures. Som et al. (2012) recognises however that this increased accuracy does come at a significantly higher computational cost.

The remainder of this section will detail the geometry and mesh generation procedure, the prescription of boundary conditions, a mesh sensitivity study and the results from the turbulence model comparison.

4.3.1 Geometry Generation

The geometry is generated using ANSYS DesignModeller, a geometry creation tool which allows for parametric designs. The geometry is constructed to closely resemble that of Schefer (1987). A cuboid of size $0.3\text{ m} \times 0.3\text{ m} \times 1\text{ m}$ is made with a 0.0052 m diameter circle projected on to one of the square faces to represent the inner diameter of the nozzle. The projected circle is used to represent a nozzle of zero wall thickness. A 1 m streamwise length is used instead of 2 m to further reduce computational cost.

An O-grid style meshing strategy was used to structure the mesh within the jet region. An O-grid style mesh results in the mesh having regions looking like the letter “O” (Khare et al., 2009). This structure allows for edge sizings and biases to be allocated in important zones, near the nozzle zone and throughout the jet region. Symmetry of the problem allows for further reduction of the computational cost, and so only a quarter of the domain is simulated, with symmetry planes used to account for this.

The geometry generation procedure can be seen in Figure 4.2. The proce-

dure is as follows:

- ① A gaseous propane jet entering a co-flow of air in a wind tunnel, the experimental set up from [Schefer \(1987\)](#) to be simulated.
- ② A $0.3 \text{ m} \times 0.3 \text{ m} \times 1 \text{ m}$ cuboid (green) represents the wind tunnel, a cylinder (blue) of radius 0.025 m and cuboid (grey) $0.015 \text{ m} \times 0.015 \text{ m} \times 1 \text{ m}$ are introduced for the O-grid style mesh structure. This represents the whole domain. A circle of radius 0.0026 m is projected onto the upstream face to represent the nozzle inlet.
- ③ A quarter of the full domain is separated out using two symmetry planes given in red. The two planes go through the centre of the domain, separating it into quarters.
- ④ One of the quarter sections is used to represent the domain.
- ⑤ The regions of the domain are now assigned labels. The nozzle region (N), the grey inner region (I), the blue middle region (M) and the green outer region (O). The dividing lines (D_{ij}) between the regions are also assigned, with D_{ij} representing the dividing line between regions i and j .
- ⑥ The mesh is then constructed in such a way that the jet region has the highest resolution with increasing cell size away from the jet.

4.3.2 Boundary Conditions

Before simulating the flow, boundary conditions must be prescribed at the inlet, outlet, symmetry and wall boundaries. As only a quarter of the domain is simulated the two inner sides are prescribed as symmetry boundaries. A symmetry boundary imposes a zero normal velocity and zero flux of all variables on the boundary. The downstream boundary is prescribed as a zero pressure outlet and the upstream

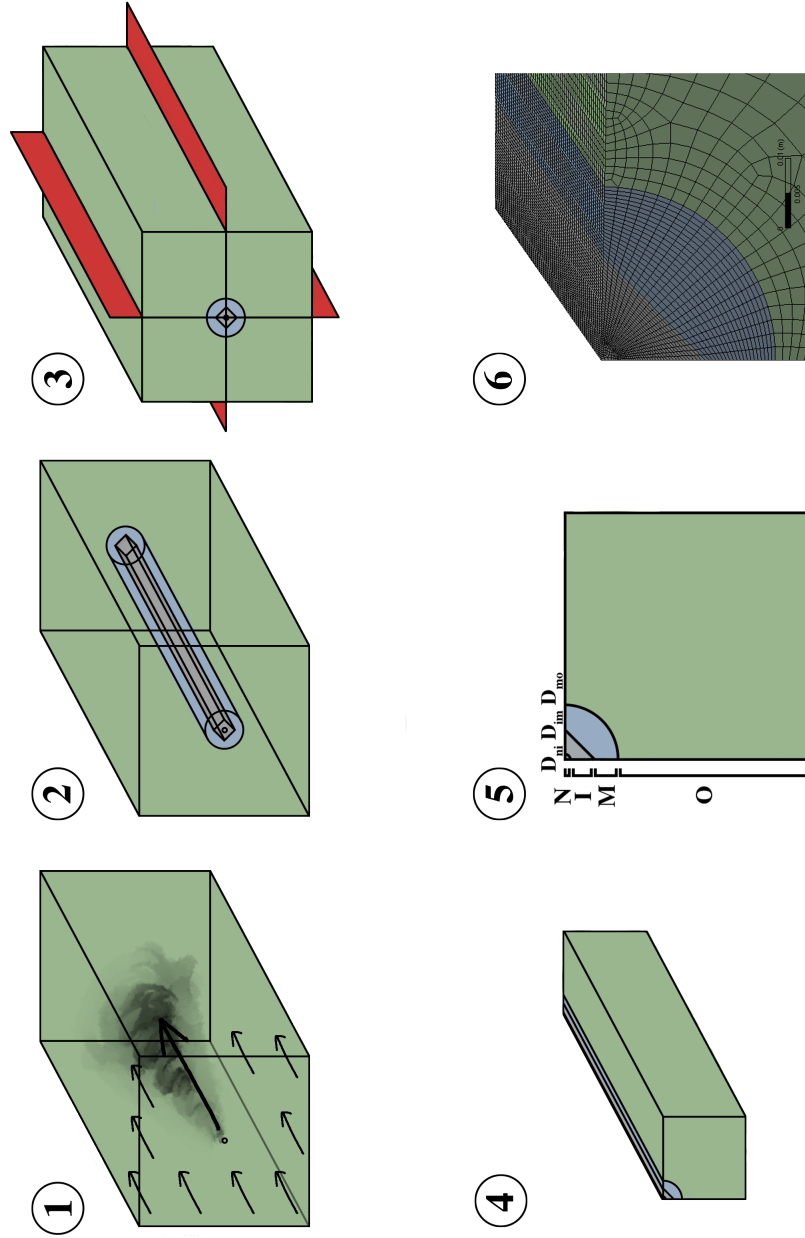


Figure 4.2: The geometry generation process: 1) The problem to be simulated, 2) The full geometry created, 3) The splitting of the geometry by symmetry planes, 4) The final geometry used, 5) The assignment of regions and dividing lines, 6) The resulting mesh. Further detail can be found within section 3.4.1.

boundary is split into two boundaries: N and $R = I \cup M \cup O$. The boundary N represents the propane inlet and R the co-flow inlet. The remaining boundaries are prescribed as no-slip walls where a zero-velocity condition is prescribed.

Both the nozzle inlet N and co-flow boundary R require mass flow/velocity, species mass fractions and temperature conditions prescribed. As the release conditions for a deodorant can are not well characterised, and the final aim is to have a model for this scenario, the boundary conditions are prescribed as top hat profiles for this problem. This is to determine how well the turbulence models can capture the experimental values with limited information available. Using limited detail for the flow conditions, N is prescribed as a velocity inlet with a uniform velocity of 69 m/s, to match the peak velocity measured in the experiments; a propane mass fraction of 1, to represent a pure release of gaseous propane; and a release temperature of 294 K. For the co-flow, a velocity inlet is prescribed with a uniform velocity of 9.2 m/s, a mass fraction 0.78:0.22 of Nitrogen to Oxygen to represent air and a temperature of 294 K. The outer boundaries are prescribed as walls. The uniform velocity profile at the nozzle is a simplified form of the inlet condition. [Gouldin et al. \(1986\)](#) simulates this experimental setup using a profile found from a fully developed turbulent pipe flow.

The simulations for the mesh sensitivity study use the $k - \varepsilon$ realizable model and the boundary conditions detailed previously. At the inlets, turbulence boundary conditions for k and ε are needed. There are four possible options within Fluent for prescribing the turbulence parameters:

1. Defining k and ε
2. Defining turbulence intensity (I) and Hydraulic Diameter (H_d)
3. Defining turbulence intensity and turbulent length scale (l)
4. Defining turbulence intensity and viscosity ratio $\left(\frac{\mu_t}{\mu}\right)$

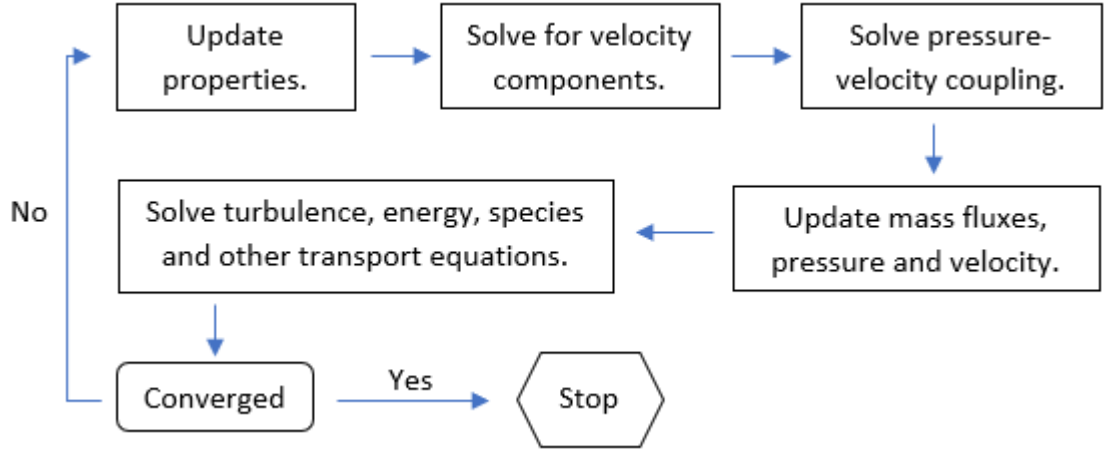


Figure 4.3: Starting at Update properties, the pressure-based solution algorithm employed in Ansys Fluent v19.2.

For a fully developed duct flow the turbulence intensity is taken as,

$$I = 0.16 Re_{H_d}^{-\frac{1}{8}}, \quad \text{with} \quad Re_{H_d} = \rho \frac{U H_d}{\mu} \quad (4.2)$$

where Re_{H_d} is the Reynolds number with the length scale taken as the hydraulic diameter [Ansys \(2009\)](#). In these simulations the turbulence intensity and hydraulic diameter are used to define the turbulence at the boundaries as they are easily attainable. For the propane inlet, using Eq. (4.2), the turbulent intensity $I = 3\%$ is defined with a hydraulic diameter of $H_d = 0.0052$ m. Following the same method the turbulence boundary conditions for co-flow are prescribed with a turbulent intensity of $I = 2\%$ and hydraulic diameter $H_d = 0.3$ m.

4.3.3 Numerical Schemes

ANSYS Fluent solves the governing equations using a finite volume method (FVM). Each mesh cell is treated as a finite volume where the flux between adjacent cells is equal and opposite. This approach is considered conservative for each finite volume. The numerical algorithm for the pressure-based solver follows the flow diagram in [Figure 4.3](#).

The base pressure velocity coupling algorithms implemented in Fluent v19.2 are the SIMPLE (Semi-Implicit Method for Pressure Linked Equations), SIMPLEC (Semi-Implicit Method for Pressure Linked Equations-Consistent) and PISO (Pressure-Implicit with Splitting of Operators) (Ansys, 2009). The PISO algorithm is suggested for transient problems whereas the SIMPLE and SIMPLEC algorithm are suggested for steady-state problems. As we are simulating a steady-state flow the SIMPLE algorithm is used for the simulations but it is noted that the SIMPLEC algorithm can in some cases improve convergence time.

For increased accuracy the momentum, turbulent kinetic energy (TKE), turbulent dissipation rate (TDR), species and energy equations are spatially discretised using a second order upwind discretisation. To calculate gradients the least-squares cell based method is used.

4.3.4 Mesh Independence

Meshes are generated within Ansys Meshing (within Ansys workbench v19.2), an automated mesh generation software which allows for cells size alteration and generation of biases needed for mesh refinement. A “number of divisions” for the nozzle (N), inner (I), middle (M) and outer (O) regions are applied for the cross-sectional edges (cs), streamwise edges (sw) and dividing edges (D). For the coarse mesh these are set to $N_{cs} = 20$, $I_{cs} = 30$, $M_{cs} = 20$, $O_{cs} = 50$, $I, M, O_{sw} = 400$ and $D_{NI} = D_{IM} = D_{MO} = 20$. This is to ensure element sizes are smaller than the nozzle radius in order to obtain reasonable resolution of the jet (Abraham, 1997). The edges are also prescribed linear biases to generate a mesh which is finer towards the jet centre to ensure higher resolution of the jet region. The mesh structure can be seen in Figure 4.4.

The mesh used to solve the governing equations plays an important role in terms of accuracy and stability of the solution. Three meshes are generated a

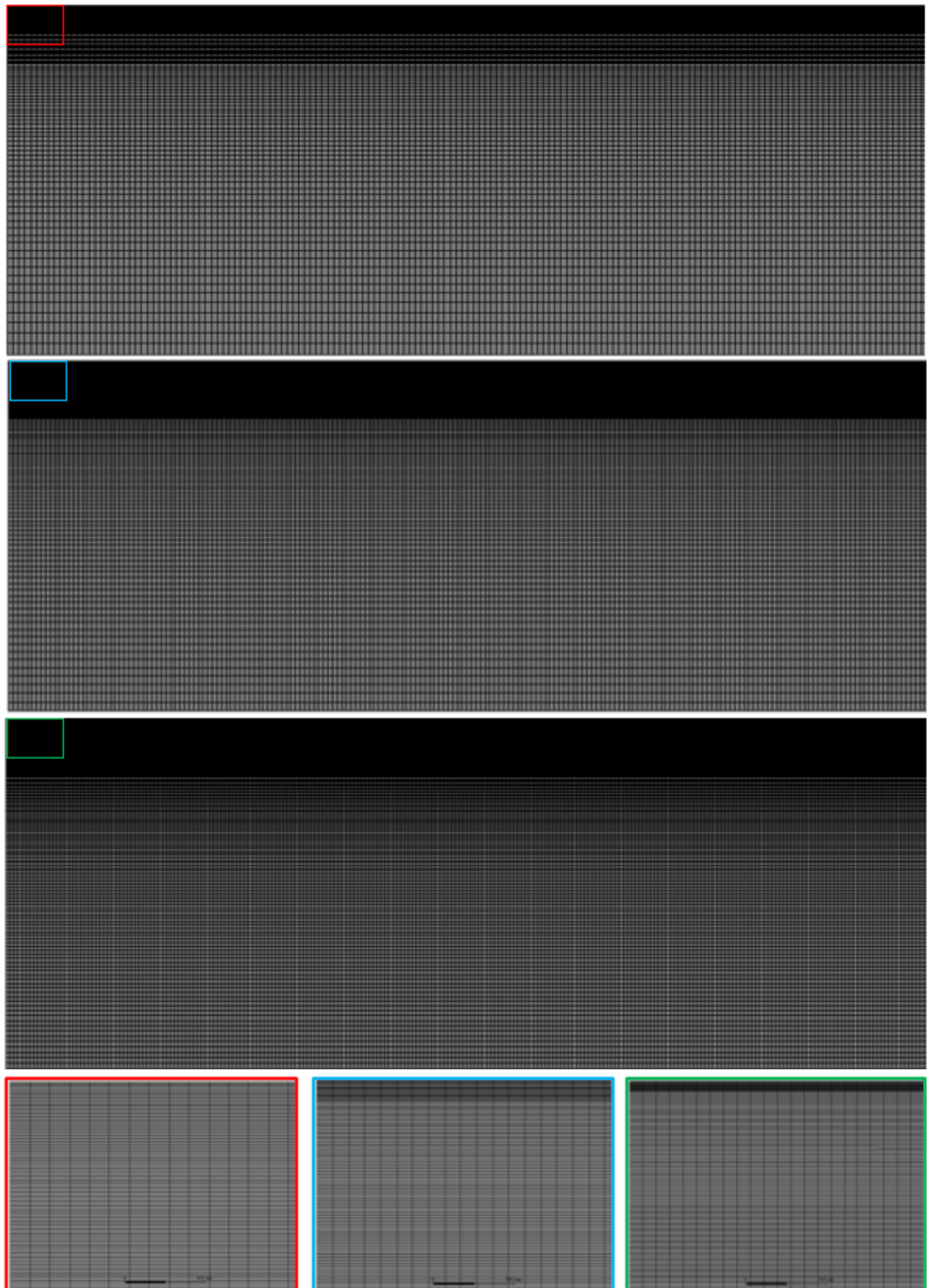


Figure 4.4: Symmetry plane view of the meshes generated for the carrier jet mesh sensitivity study, top to bottom: Coarse, Medium and Fine. A close up of the nozzle mesh region for the coarse (red), medium (blue) and fine (green) meshes.

	N_{cells}	$Skew_{avg}$	$Orth_{avg}$	Asp_{avg}	N_{cs}	I_{cs}	M_{cs}	O_{cs}	D_{NI}	D_{IM}	D_{MO}	sw
Coarse	852400	0.17	0.96	4.7	20	30	20	50	20	20	20	400
Medium	1710576	0.18	0.95	6.9	25	38	25	63	25	25	25	504
Fine	3847800	0.16	0.96	7.4	40	60	40	100	40	40	40	600

Table 4.1: This table shows the number of cells (N_{cells}), average cell skewness, average orthogonal quality and average aspect ratio for each of the three meshes generated. The number of divisions for the geometrical regions are also included in the table.

coarse, medium and fine mesh, achieved by refining parts of the mesh until the finer mesh has twice as many computational cells. This is done in order to test that the model predictions are not dependent on the mesh the equations are being solved on, which is known as mesh independence. The corresponding number of divisions, along with mesh quality statistics, can be found in Table 4.1. A view of the meshes generated using these sizings can be found in Figure 4.4.

The mesh quality statistics examined are the skewness ($Skew_{avg}$), orthogonal quality ($Orth_{avg}$) and the aspect ratio (Asp_{avg}). Tolerance levels for these mesh quality statistics can be found in [Ansys \(2009\)](#). Skewness is a measure of how close the cell is to an ideal cell of the same volume. Values of skewness range between 0 and 1 with values less than 0.33 acceptable. Orthogonal quality measures the relationship between centroids of adjacent cells. Values of orthogonal quality range between 0 and 1 with values close to 1 being acceptable. Aspect ratio measures the amount of stretching of a cell with values less than 10 being acceptable. For each mesh generated the three mesh quality measures are deemed to be at acceptable levels.

Solutions are said to converge once residuals drop below a tolerance of at least $\mathcal{O}(10^{-6})$, and once monitor points $M_{1,2,3,4}$ placed within the domain at positions (x,y,z) ($M_1=(0.1,-0.1,0)$, $M_2=(0.1,0,0)$, $M_3=(0.2,-0.1,0.1)$ and $M_4=(0.15,-0.05,0.05)$) asymptote. The monitor points were positioned to capture flow both within and outside of the jet region. Examples of the residuals for the last 500 iterations can be seen for the coarse mesh in Figure 4.5. The residuals are still decreasing so the simulation could be deemed to have not fully converged. Velocity

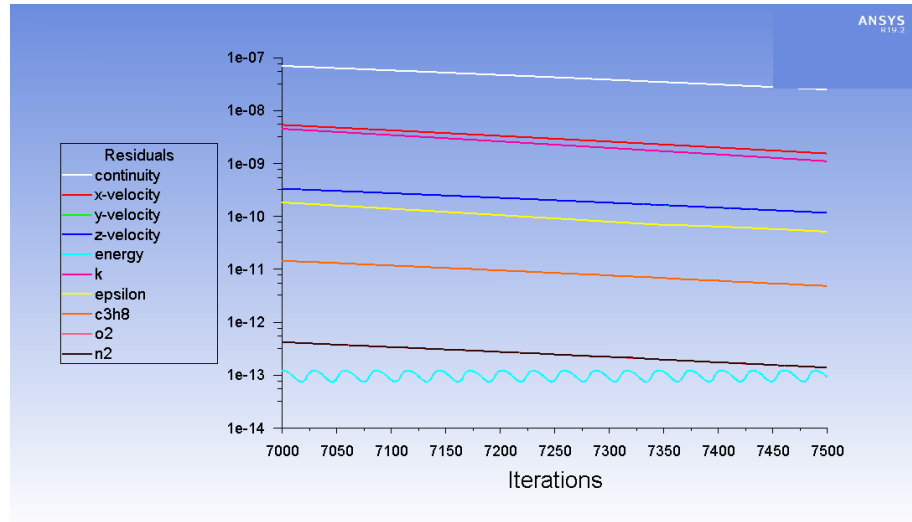


Figure 4.5: Residuals for the coarse mesh from iterations 7000-7500.

magnitude and propane mass fraction are measured at the monitor points for each iteration. There is little difference between each iteration and so it is assumed the final result is representative of the steady-state solution. Note there are oscillations in the energy residual but at a level of $\mathcal{O}(10^{-13})$ this is not deemed to impact the results. It does however point to possible transient features as the solution oscillates between possible predictions.

Axial velocity (U or u) and propane mass fraction values are compared for each of the meshes at non-dimensional axial positions ($X_d = X/d$), $X_d = 4$, $X_d = 30$ and along the centerline (denoted subscript c). The comparisons can be found in Figure 4.6. Analysis of the mean percentage error between meshes is calculated for the axial velocity predictions and a mean absolute error is calculated for the mass fraction predictions, shown in Table 4.2. The change in axial velocity of the jet is within a 1% tolerance for each mesh as is the radial spread of propane for the different axial positions investigated. For the remainder of the report the coarse mesh is used for its reduced computational cost and is able to capture the desired flow variables.

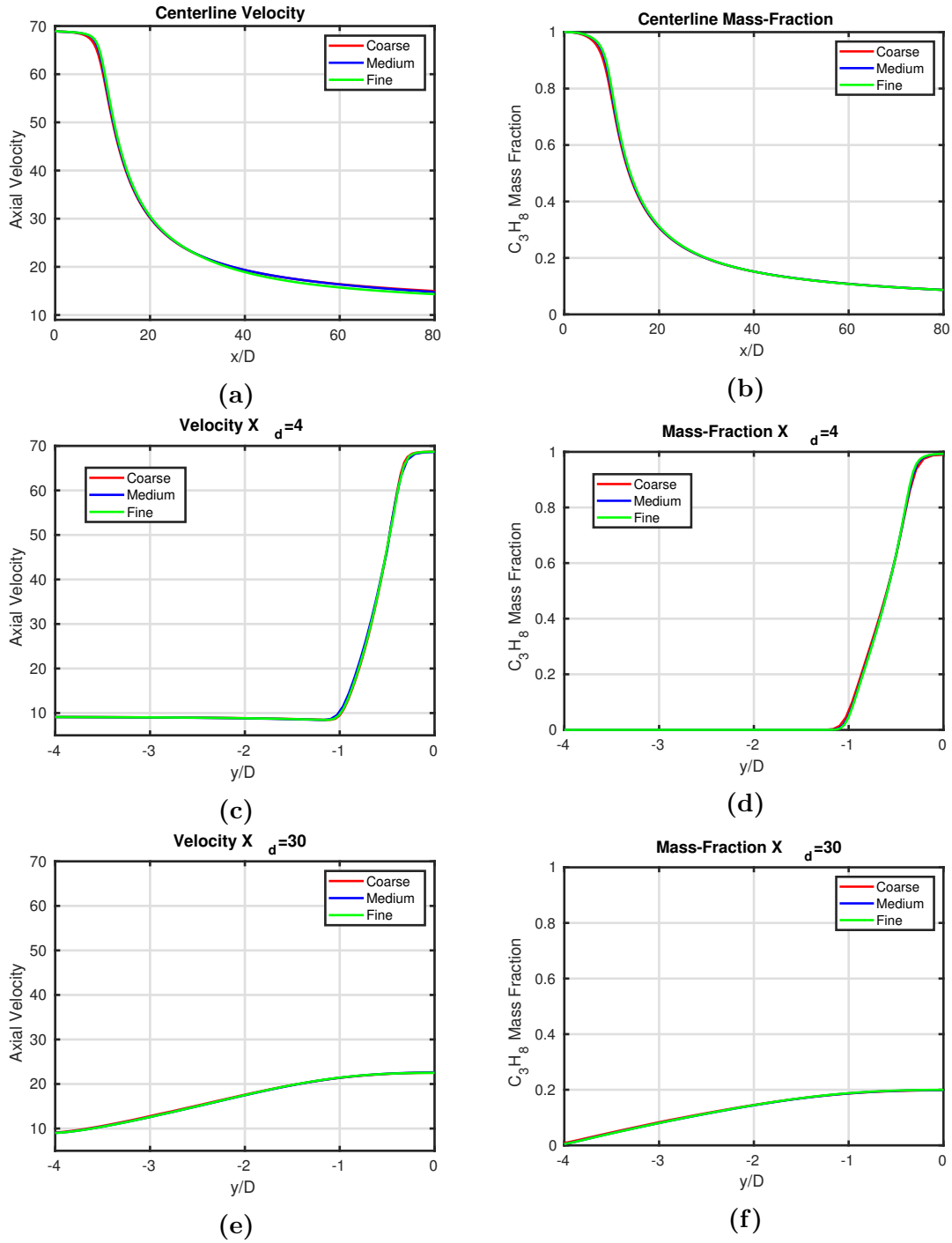


Figure 4.6: The axial velocity [(a),(c),(e)] and propane mass fraction [(b),(d),(f)] values along the centreline and for axial positions $X_d = 4$ and 30. Values are shown for the the coarse (red), medium (blue) and fine (green) mesh.

	V_c	$X_d = 4$	$X_d = 30$	MF_c	$X_d = 4$	$X_d = 30$
Coarse v Medium	2.40×10^{-3}	2.90×10^{-3}	4.50×10^{-3}	1.70×10^{-3}	6.43×10^{-4}	9.64×10^{-4}
Medium v Fine	2.20×10^{-3}	2.70×10^{-3}	5.16×10^{-4}	1.20×10^{-3}	3.00×10^{-4}	3.28×10^{-5}

Table 4.2: This table shows the errors between the coarse, medium and fine meshes. The percentage error for axial velocity is shown on the left hand side and the mean absolute error for the mass fraction on the right hand side. The errors are calculated for along the centerline and at axial positions $X_d = 4$ and 30.

4.3.5 Results

In this section the results of the simulations of the 2-equation turbulence models are investigated (standard, RNG and realizable $k - \varepsilon$ models along with the $k - \omega$ and $k - \omega$ SST models). The coarse mesh is used for each case and the boundary conditions discussed in the previous sections are used.

Flow Comparison

Here the velocity field and propane mass fraction fields are compared across the centre plane over the domain with the symmetry boundary shown. Velocity magnitude contours are seen in Figure 4.7 and propane mass fraction contours seen in Figure 4.8. The velocity contours do not show a great deal of difference on first inspection but looking closely there are several differences that are noticeable between the flows. The jet core region decays significantly quicker for the $k - \omega$ models than the $k - \varepsilon$ models. The RNG model appears to have the greatest radial spread whereas the $k - \omega$ model has the least. The $k - \omega$ models are more sensitive to the initial conditions and so the lack of well-defined turbulence profiles across the inlets could possibly be the cause of this significant decay.

The propane mass fraction contours, shown in Figure 4.8, show clearer differences between the turbulence model predictions. The wider spread of the propane jet predicted by the RNG model results in a greater dispersion of propane species and smaller propane mass fraction values at the centre of the domain. The $k - \omega$ model predicts an expanding nozzle release which is more indicative of compressible

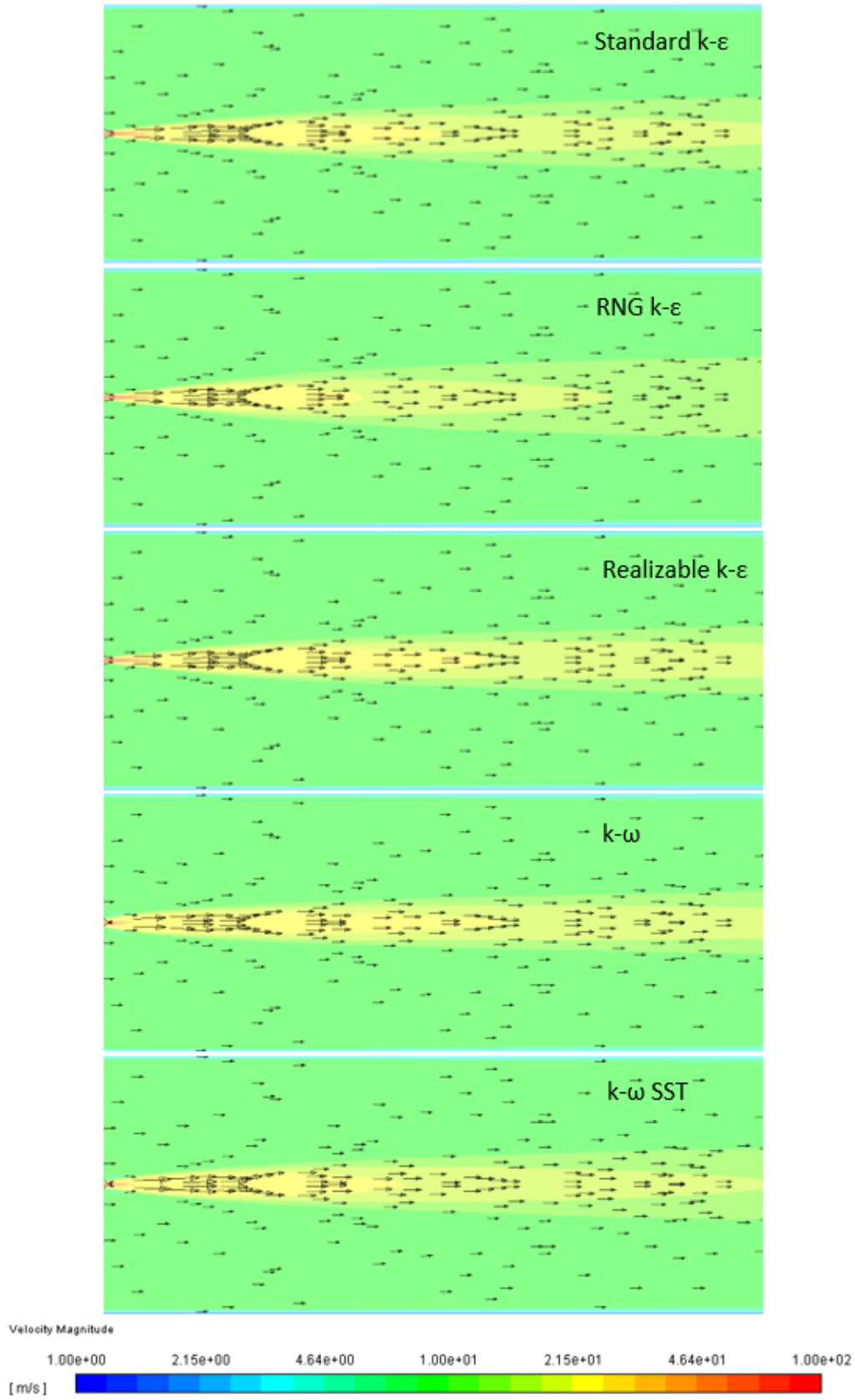


Figure 4.7: Velocity contours and vectors for the different turbulence models investigated, top to bottom: standard, RNG and realizable $k-\epsilon$ and $k-\omega$ and $k-\omega$ SST.

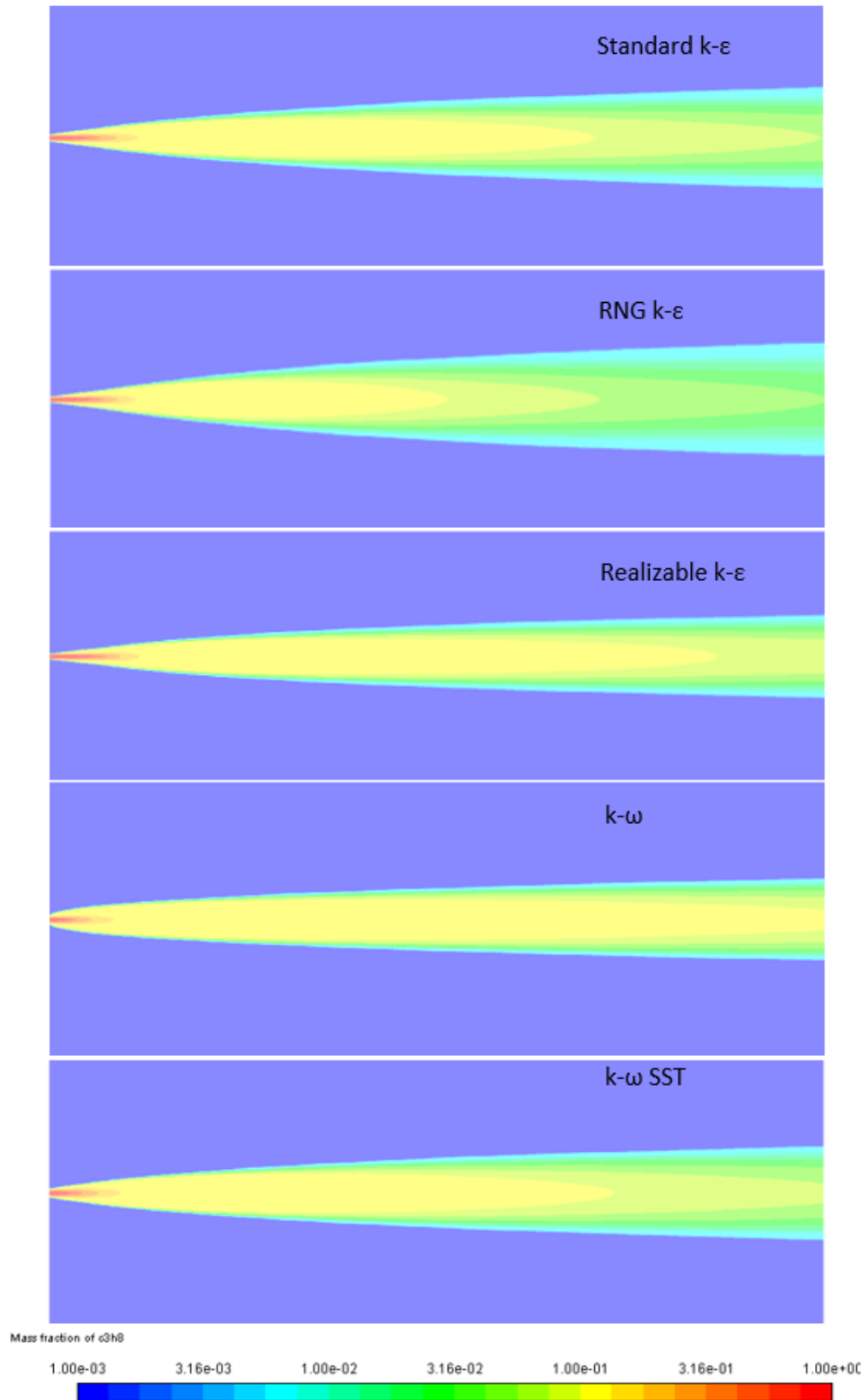


Figure 4.8: Propane mass fraction contours for the different turbulence models investigated, top to bottom: standard, RNG and realizable $k-\epsilon$ and $k-\omega$ and $k-\omega$ SST.

effects from supersonic flows. This same phenomenon is not present in predictions of the $k - \varepsilon$ variants. As the Mach number ($M = \frac{U}{c} = \frac{69}{258} \approx 0.28$), which represents the ratio of flow velocity to the speed of sound in the medium, is less than 0.3, compressible effects are not considered to be present. Furthermore, due to $M < 1$ the flow is considered a subsonic flow, therefore the predictions of the $k - \omega$ models do not appear to accurately represent this scenario.

Quantitative Comparison

To compare with [Schefer \(1987\)](#) the propane mixture fraction (Z) is calculated within CFD Post (a post processing software for CFD simulations), and is defined as,

$$Z = \frac{S y_{Prop} - y_{Oxy} + 1}{S + 1}, \quad \text{with} \quad S = \frac{s Y_{Prop,0}}{Y_{Oxy,0}} \quad \text{and} \quad s = \frac{32 \left(m + \frac{n}{4}\right)}{12m + n}. \quad (4.3)$$

Here $y_{prop} = Y_{Prop}/Y_{Prop,0}$ and $y_{oxy} = Y_{Oxy}/Y_{Oxy,0}$ are the normalised propane and oxygen mass fractions respectively, with $Y_{Prop,0} = 1$ and $Y_{Oxy,0} = 0.22$ the inlet mass fractions. For propane (C_3H_8) the constants m and n are taken as $m = 3$ and $n = 8$ giving $s = \frac{40}{11}$. Using this, the mixture fraction across the entire domain can be calculated.

The axial velocities and propane mixture fraction for the non-dimensional axial positions $X_d = 4, 15$ and 30 are compared with the axial velocity and propane mixture fraction results from [Schefer \(1987\)](#). This can be seen in [Figure 4.9](#). The same variables are compared along the centreline of the jet and can be found in [Figure 4.10](#) along with shear Reynolds stress profiles at the aforementioned axial positions. The shear Reynolds stresses are also calculated in CFD post following [Eq. \(2.46\)](#), in particular

$$-\overline{u'v'} = \frac{\mu_t}{\rho} \left(\frac{du}{dy} + \frac{dv}{dx} \right). \quad (4.4)$$

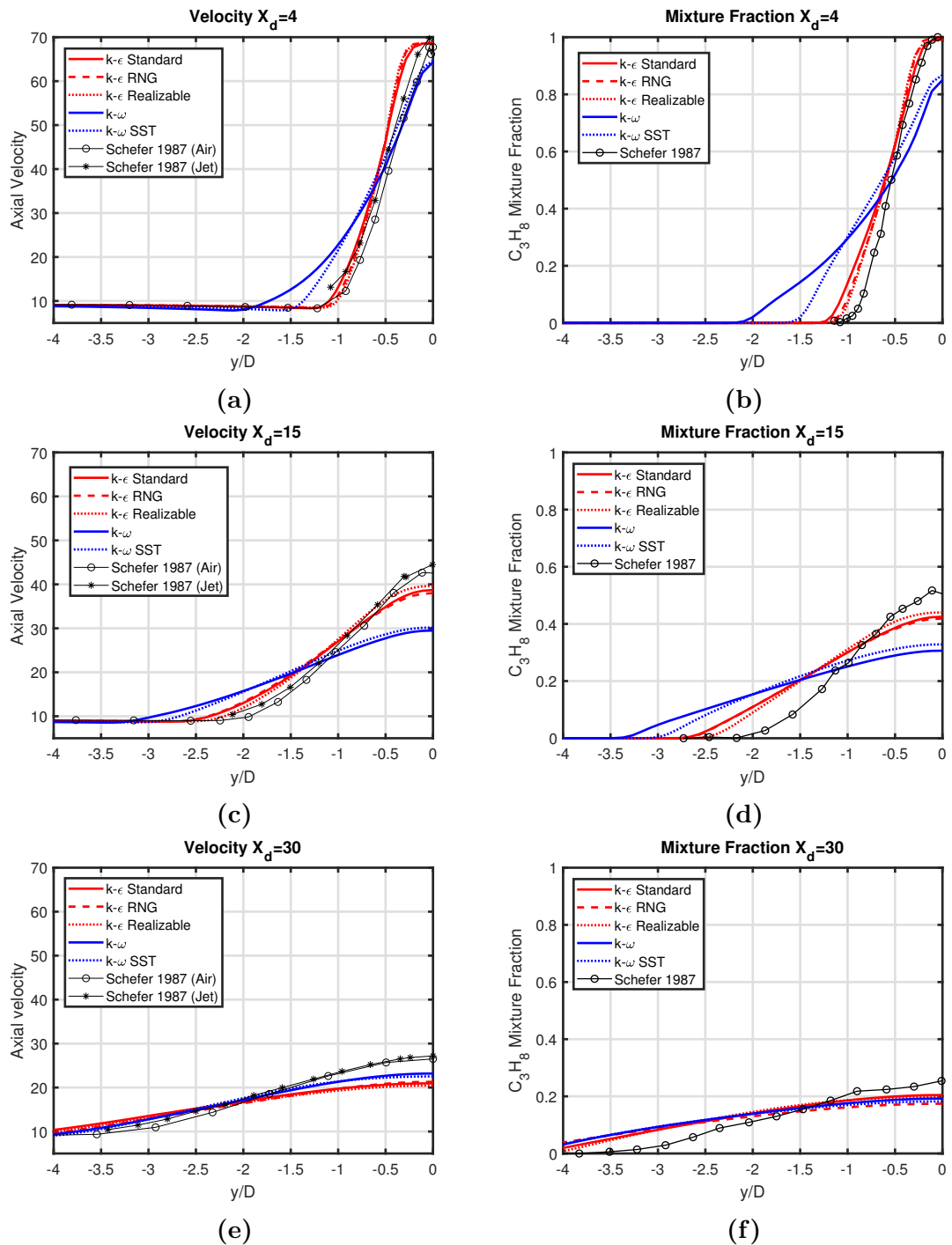


Figure 4.9: Velocity [(a),(c),(e)] and mixture fraction [(b),(d),(f)] profiles for the tested turbulence models and experimental results of Schefer (1987). Data is plotted for axial positions $x_d = 4, 15$ and 30 . $k - \epsilon$ turbulence models are in red and $k - \omega$ turbulence models in blue.

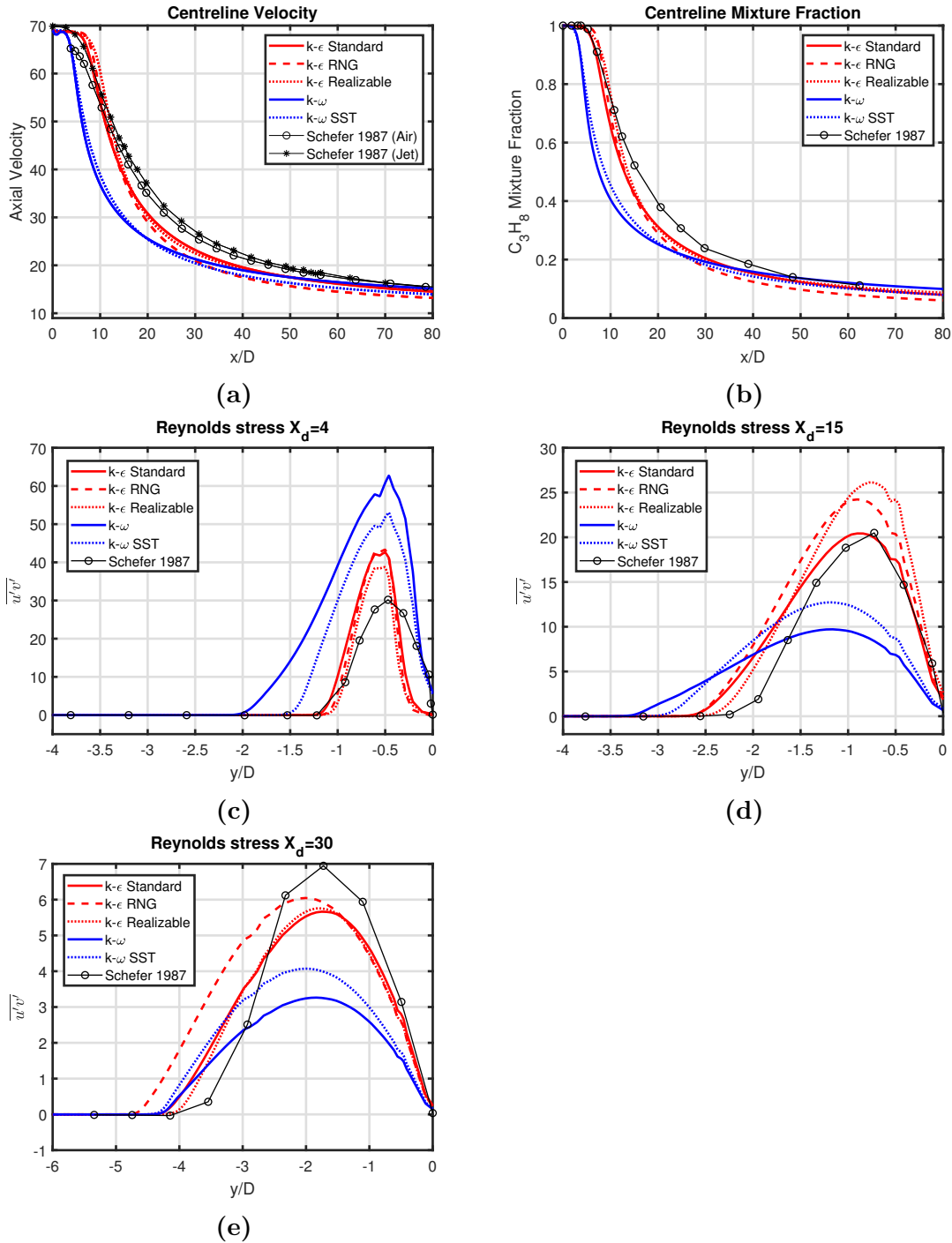


Figure 4.10: Centerline velocity (a) and propane mass fraction (b) for the investigated turbulence models and experimental data from Schefer (1987). Shear Reynolds stress profiles ($\overline{u'v'}$) [(c),(d),(e)] for the investigated turbulence models and the experimental data of Schefer (1987) at the axial positions $x_d = 4, 15$ and 30 . $k - \epsilon$ turbulence models are in red and $k - \omega$ turbulence models in blue.

Momentum Decay

Figures 4.9a, 4.9c and 4.9e show a clear difference in $k - \varepsilon$ based models compared to $k - \omega$ based models. All $k - \varepsilon$ models seem to predict a similar velocity profile. Comparing the realizable and RNG model to the experimental results shows that the realizable model appears to predict a better spreading of the jet and the RNG model appears to overpredict the spreading. The $k - \omega$ models show an even greater initial spreading rate of the jet which is likely due to increased sensitivity to the boundary conditions and a higher generation of TKE (due to differences in the TKE production term) and as a result a greater dissipation of the turbulence. Another consequence of this is the increased rate of the $k - \omega$ models to tend towards the mean stream velocity as seen in the centerline velocity plot (Figure 4.10a).

The radial spread of mixture fraction, seen in Figures 4.9b, 4.9d and 4.9f, has a similar trend to that of the numerical velocity profiles, as seen in Figure 4.9. This is due to the link between the velocity field and the convective term within the species transport equations Eq. (2.71). The comparison of mixture fraction to that of the experimental data is quantitatively different, but qualitatively shows good agreement in terms of trend. The uniform inlet profile used results in a greater propane mass flow rate than what is observed in the experiments, hence why there appears to be a greater mass of propane if the radial profiles are integrated over.

Shear Reynolds Stress

The shear Reynolds stress $\overline{u'v'}$ is calculated in CFD post. The results for each turbulence model are compared and can be seen in Figures 4.10c, 4.10d and 4.10e. Initially all turbulence models show an over-prediction compared to the experimental results of Schefer (1987), however, this is likely due to the inaccurate initial condition prescribed. The $k - \varepsilon$ models give similar agreement but the closest agreement to the experimental data is from the realizable model predictions.

The $k - \omega$ model predicts the largest shear Reynolds stress close to the nozzle. This agrees with the greater momentum decay already discussed because the shear Reynolds stress is comparable to an effective turbulent viscosity. The $k - \omega$ SST model results in predictions between the $k - \omega$ and standard $k - \varepsilon$ predictions which is expected due to the blending involved within the model's formulation. The $k - \varepsilon$ models vary considerably downstream but show promising predictions relative to the experimental results.

4.3.6 Boundary Condition and Parameter Studies

In this section model parameters and boundary conditions are varied to investigate their impact on the quantities measured. In particular, turbulent Schmidt number variations are investigated on the diffusion of species as well as the influence of the wall boundary on the jet profile up to a non-dimensional axial distance of $X_d = 30$.

Sc_t Dependence

The mixture fraction results show that all the turbulence models over predicted the decay and dispersion of propane species relative to the experimental results of [Schefer \(1987\)](#). Prescribing a more accurate inlet condition may account for this difference, but another possible cause is the use of a fixed turbulent Schmidt number ($Sc_t = \frac{\nu_t}{D_t}$). Sc_t gives the ratio of turbulent transport of momentum and the turbulent transport of mass, and is a parameter in the diffusion term of the species transport equation, Eq. [2.71](#).

The default value of Sc_t in ANSYS Fluent for the $k - \varepsilon$ realizable model is $Sc_t = 0.7$ ([Ansys, 2009](#)) and is believed to be from the work of [Spalding \(1971\)](#), which was chosen to ensure agreement with experiments. [Tominaga and Stathopoulos \(2007\)](#) discusses that the turbulent schmidt number can vary through a boundary layer, likely due to changes in turbulence levels and therefore turbulent diffusion of

quantities, and that optimum values of Sc_t are in the range of 0.2-1.3. However, these values were used in engineering problems relating to atmospheric dispersion problems. He et al. (1999) investigated Sc_t effects for jets in a crossflow ranging values from 0.2-1.5 and found, by comparison with experiments, that a value of $Sc_t = 0.2$ was more accurate.

Simulations are performed taking the realizable simulation setup described previously and varying Sc_t from 0.5 to 0.9. The model predictions are extracted from Fluent and postprocessed in MATLAB. Figure 4.11 shows the centreline mixture fraction, and radial profiles of mixture fraction at non-dimensional axial positions $X_d = 4, 15$ and 30 . For the centreline decay, the results show that by increasing Sc_t the point at which the mixture fraction begins to decay is delayed. The radial profiles plotted show that there is a slight difference within the jet core region and after the steep decay. At $X_d = 15$ the mixture fraction profile shows that for the case where $Sc_t = 0.9$, and thus molecular diffusivity is lower, a better prediction of the mixture fraction profiles can be found.

These results show that when species transport is involved, not only does a good representation of the velocity field need to be found, but also an adequate Sc_t parameter for species diffusion is needed. A default value of $Sc_t = 0.7$ may not be adequate and ideally a variable Sc_t implementation may be best to capture local deviations within the flow.

Wall Boundary Influence

The current model is built for an enclosed system confined between walls. This is to evaluate the effects of wall enclosures on model predictions of a free jet issuing into an domain with open boundaries. An investigation into the boundary condition is carried out to see how allowing entrainment from the side affects the generation of the carrier jet. To investigate the wall effects the same setup is used as defined previously. The wall boundary conditions as well as the co-flow inlet

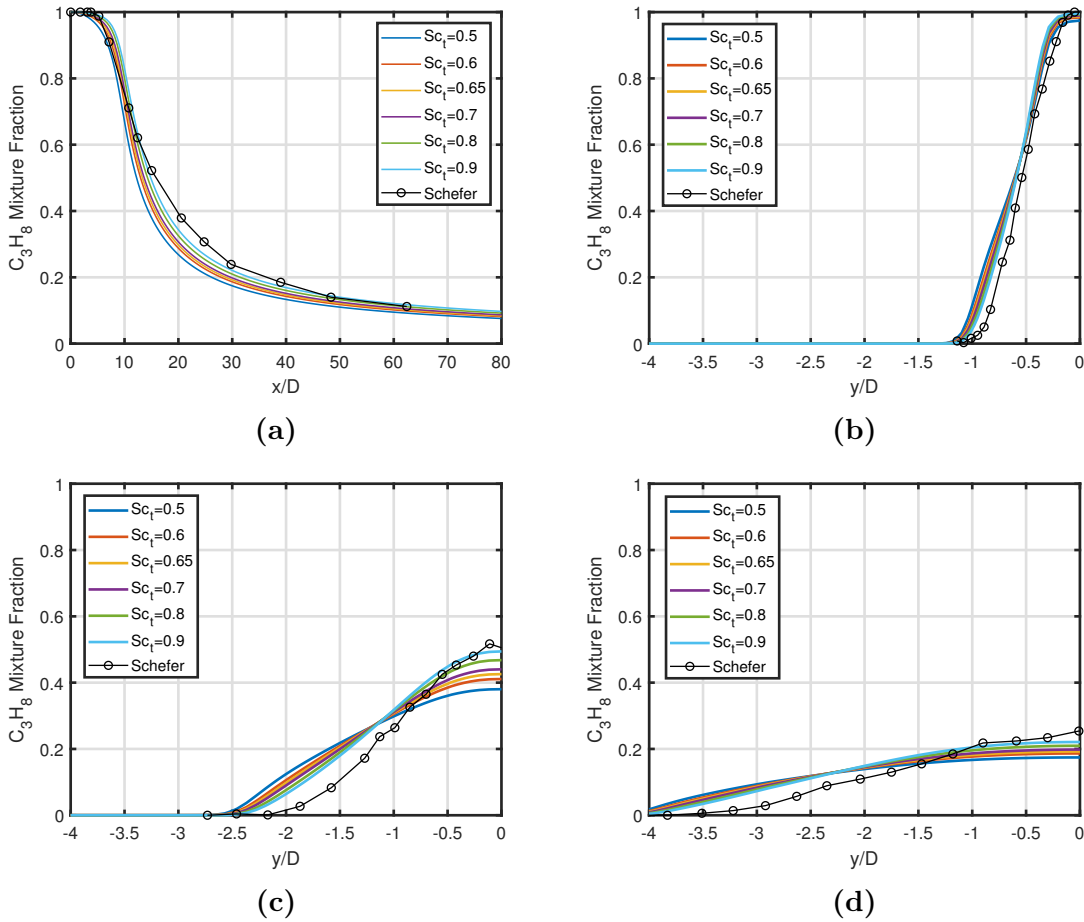


Figure 4.11: Propane mixture fractions plotted for varying turbulent Schmidt number ranging from $Sc_t=0.5$ to $Sc_t=0.9$. Mixture fractions are plotted (a) along the centreline, and radially at axial distances (b) $x_d = 4$, (c) $x_d = 15$ and (d) $x_d = 30$.

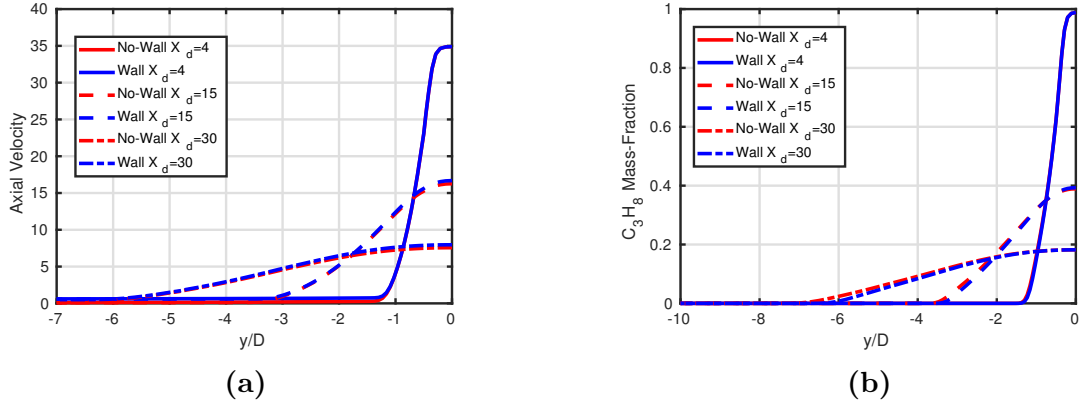


Figure 4.12: (a) Radial velocity profiles for both the Wall and No-Wall case at axial positions $X_d = 4, 15$ and 30 (b) Radial propane mass fraction profiles for both Wall and No-Wall cases at the same axial positions.

condition are now prescribed as pressure outlets which allow for backflow. The propane velocity inlet condition is now assigned as a uniform velocity of 35 m/s. The results are compared with the base case before the walls are reassigned. For all these cases the air is assumed initially quiescent.

The velocity and propane mass fraction are analysed for the standard axial positions previously mentioned. The results can be found in Figure 4.12. Up to a distance of 30 nozzle diameters in the axial direction, the effect of having no-wall does not play a significant role on the momentum decay of the jet. When the jet is confined between walls the air becomes entrained in a way which results in a flow similar to a co-flow close to the jet. This is not observed for the no-wall case. The presence of the co-flow reduces the entrainment, due to a smaller relative velocity, and in turn reduces the decay of the jet. Figure 4.12b shows that having no walls allows for what seems like a greater diffusion of propane radially.

Self-Similarity

The no-wall case is simulated for velocities $U=50, 40, 35$ and 30 m/s following the same strategy detailed above. Within the self-similar region of a jet's development the radial velocity profiles are said to be self-similar as discussed in section 2. The equations for the velocity profile similarity solution and centerline

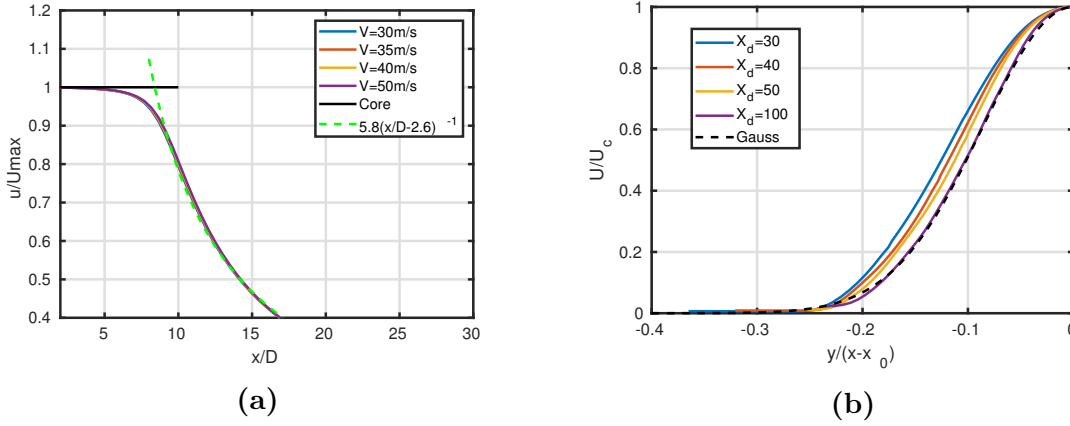


Figure 4.13: (a) Data fit for the centerline decay within the transitional region. Here the decay rate is given as $\beta \approx 5.8$ and the virtual origin $x_0 \approx 2.6$. The core level is denoted by the black line and the fit to scaled axial velocity is denoted by the dashed green line. (b) The self similar profiles of the numerical solution for a range of axial positions $x_D = 30, 40, 50$ and 100 . The Gauss error function with $\beta = 5.8$ and $x_0/D = 2.6$ is also plotted for comparison and is given by the dashed line.

velocity decay are

$$\frac{U}{U_c} = e^{-\ln(2)\zeta^2}, \quad \text{with} \quad \zeta = \beta \frac{y}{x - x_0} \sqrt{\frac{2}{\ln 2}}, \quad \text{and} \quad (4.5)$$

$$\frac{U_c}{U_i} = \beta \frac{d}{x - x_0}, \quad (4.6)$$

respectively. The self-similar profile requires a decay coefficient (β) and virtual origin (x_0). These can be approximated by fitting (4.6) to the normalised centerline decay shown in Figure 4.13a. The fit can be seen in Figure 4.13a on top of the normalised centreline velocity. Note that the centreline velocity decay appears to be independent of the velocity inlet condition prescribed. Here the decay coefficient is found to be $\beta \approx 5.8$ with a virtual origin at $x_0/D \approx 2.6$. The decay coefficient is found smaller than expected where a value $\beta = 6.5$ is usually found for uniform inlet profiles (Xia and Lam, 2009). These values however are similar to that found by Xia and Lam (2009).

Normalised radial velocity profiles are plotted against the self-similar velocity profile with $\beta = 5.8$ and $x_0/D = 2.6$. The self-similarity of the radial profiles

can be observed in Figure 4.13b. The velocity profiles show slight deviations for the axial positions $X_d = 30, 40$ and 50 . This makes detecting exactly where the self-similar region begins difficult. A larger axial position of $X_d = 100$ is investigated and found that the numerical solution gives excellent agreement to the analytic Gauss error function solution but is considerably larger than the predicted start of the self-similar region at $x_d > 20$.

4.3.7 Conclusion

Applying a boundary condition more representative of the experiments would allow for better agreement to the experimental results of Schefer (1987). However, the aim of these simulations was to find a turbulence model which when given limited information on boundary conditions can provide a reasonable prediction to the expected flow field. Other parameters such as the turbulent Schmidt number have been shown to influence the diffusion of species. The model predictions can be improved by increasing its value to $Sc_t = 0.9$ but care is needed when tuning parameters as the changes may be accounting for other model deficiencies.

Overall the 2-equation RANS models show promise in modelling a hydrocarbon gaseous free jet issuing into air. The $k - \varepsilon$ turbulence models show a more accurate prediction to the experimental data over the $k - \omega$ models where limited boundary information is used. The $k - \omega$ models appear to perform poorly in this case, with the $k - \omega$ SST model giving substantial deviation from the experimental results. The $k - \omega$ model also gave poor predictions for velocity and mixture fraction. As the $k - \omega$ SST model uses a blend of the $k - \omega$ model near the walls and $k - \varepsilon$ in the bulk, this deviation is likely due to near boundary effects not being accurately captured by the numerical model. Ghahremanian and Moshfegh (2011) found good agreement with the $k - \omega$ SST model when modelling free turbulent round jets, however the current problem methodology does not appear appropriate for a $k - \omega$ model.

Here no $k - \varepsilon$ model clearly outperformed the others, agreeing with the results of [Montazeri et al. \(2015\)](#). The $k - \varepsilon$ realizable model achieved slightly better predictions of jet spreading and ensures realizability with its formulation of a variable C_μ . For this reason the realizable $k - \varepsilon$ turbulence model is used for all future simulations detailed in this work.

4.4 Aerosol Can Carrier Jet

This section details the generation of an axisymmetric model of a aerosol can single-phase gaseous carrier jet. An axisymmetric methodology was also used by [Kelsey Kelsey \(2001\)](#) for a flashing propane jet and showed good agreement to the experimental data of [Allen \(1999\)](#). The knowledge gained from the turbulence model study was used to aid in construction of this model. The axisymmetric geometry and mesh generation are first described, then the boundary conditions used to represent the carrier jet are detailed. Finally the model predictions are compared to the experimental results detailed in Chapter 3, and a study of different ambient conditions on jet variables is discussed.

4.4.1 Geometry Generation

A 2D axisymmetric geometry is generated in ANSYS design modeller to represent a carrier jet from a nozzle of diameter 0.5 mm issuing into an open area. To have a separation between the nozzle and external flow boundary, a nozzle length of 20 mm is defined. The domain length and height are defined as 300 mm and 100 mm respectively. This domain length results in a distance of 280 mm from the nozzle to the boundary downstream. [Figure 4.14](#) shows the domain generated, detailing the boundary conditions that are applied. Further detail on boundary conditions is given in [Section 4.4.3](#).

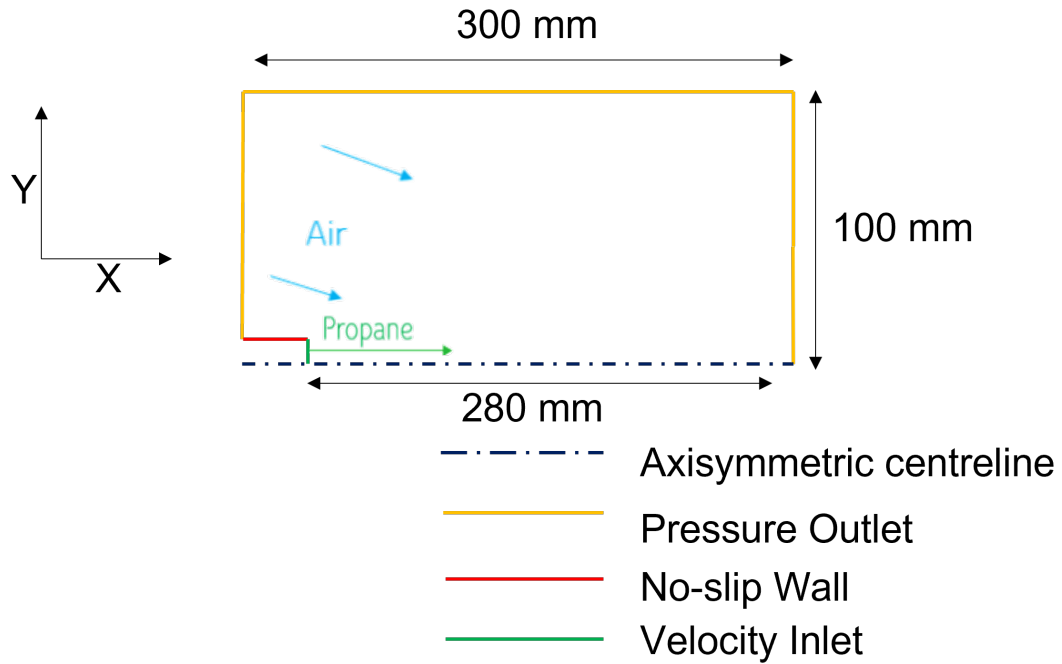


Figure 4.14: Domain schematic showing lengths and boundary conditions applied. Note this is not to scale.

4.4.2 Mesh Generation

The geometry is split into five rectangles to allow for mesh sizings to be applied through the domain. The location of the five rectangles can be seen in Figure 4.15. The domain is separated in this way to allow for refining the mesh within the jet region and to reduce the number of cells in the regions further away from the jet. The number of mesh cells needed to resolve the nozzle is taken as 20. This is taken from the coarse mesh sizing found in Table 4.1, where the coarse mesh was found to give comparable results to the medium and fine meshes.

The five rectangular zones have vertical (V) and horizontal (H) sizings applied to them. The sizings and bias factors for each of the five zones can be found in Table 4.3. The Bias factors are chosen to avoid spurious jumps between cell sizes and to keep a fine mesh towards the centre of the jet and coarser cells away from the jet.

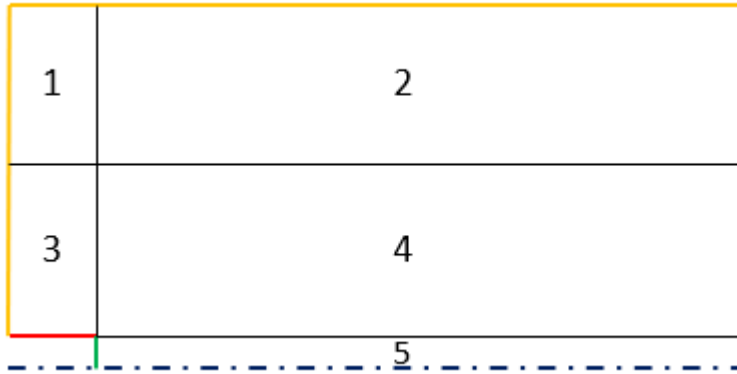


Figure 4.15: Illustration to show the separation of the 2D axisymmetric domain into five rectangles.

	1V	1H	2V	2H	3V	3H	4V	4H	5V	5H
Size (mm)	1	0.5	1	0.15	0.25	0.5	0.25	0.15	0.0125	0.15
Bias factor	4	40	4	10	20	40	20	10	1	10

Table 4.3: Horizontal (H) and vertical (V) cell sizings defined on the five rectangular regions along with the corresponding bias factors.

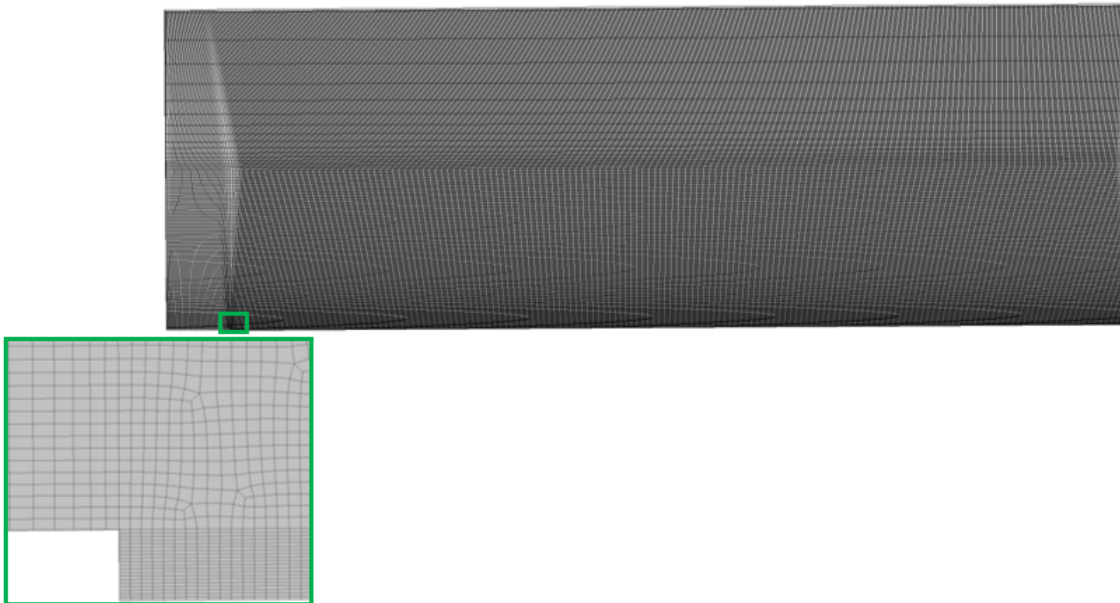


Figure 4.16: The computational mesh constructed and zoom in of the near-nozzle region for the axisymmetric domain.

4.4.3 Boundary Conditions

Boundary conditions need to be applied to the boundaries of the domain before the flow can be simulated. The nozzle is prescribed as a velocity inlet where the velocity of the carrier jet is assumed to be approximately equal to that of the liquid product that would be issuing out of the nozzle. The velocity is assumed to be the maximum exit velocity for the simple orifice flipped relation, Eq. (2.18), and the pressure swirl nozzle Eq. (2.20)

$$U_{exit} = \max \left(\frac{\dot{m}}{\rho_l C_{ct} A}, k_v \sqrt{\frac{2(P_{inj} - P_{amb})}{\rho_l}} \right). \quad (4.7)$$

The liquid density ρ_l is approximated by taking an LPG blend of propane, butane and iso-butane with approximate mass fractions of 20%, 45% and 35% respectively. These constituent mass fractions give an approximate liquid density (kg/m^3) of $(493 \times 0.2) + (572 \times 0.45) + (563 \times 0.35) \approx 553 \text{ kg/m}^3$. Using Eq. (4.7) with values: $P_{inj} = 4.5 \text{ atm}$, $\dot{m} = 0.0015 \text{ kg s}^{-1}$, $C_{ct} = 0.611$ (fully flipped), $A = \pi 0.00025^2$ gives an exit velocity of $U_{exit} \approx 25 \text{ ms}^{-1}$.

These relations use the density of the liquid and do not account for the flashing vapour phase, therefore a representative density lower than the liquid density would be more applicable to calculate the exit velocity. For a lower density and to maintain the same mass flow rate an increase in exit velocity is needed. Therefore an exit velocity of approximately $U_{exit} \approx 30 \text{ ms}^{-1}$ may be assumed. For a single component liquid, the fraction vaporised can be calculated from (Lees, 2012)

$$X = \frac{c_p (T_u - T_d)}{h_{fg}}, \quad (4.8)$$

where c_p is the specific heat capacity, T_u the upstream temperature, T_d the saturation temperature at the downstream pressure and h_{fg} the latent heat of vaporisation. For propane this gives a flash vapour fraction of approximately $X = \frac{2200(293.15 - 231)}{426000} =$

0.32. This gives a release density of approximately 335 kg/m^3 and results in a maximum velocity of 37 ms^{-1} . Following a methodology for calculating the flash vapour fraction for a multi-component liquid would be more robust but this demonstrates that an exit velocity of $U_{exit} \approx 30 \text{ ms}^{-1}$ is appropriate.

The injection temperature is initially set as room temperature (293.15 K) and the effects of varying ambient temperature and relative humidity (RH) on the species fractions within the jet are investigated. The ambient conditions for the cases investigated are given in Table 4.4.

	Ambient Temperature ($^{\circ}\text{C}$)	Relative Humidity
Case 1	20	40
Case 2	40	20
Case 3	40	40
Case 4	40	80

Table 4.4: Ambient temperature and relative humidity conditions for the four cases simulated.

Relative humidity is defined as the ratio of partial pressure due to water vapour divided by the saturation vapour pressure of water at that temperature (T),

$$\text{RH} = \frac{P_{par}^{H_2O}}{P_{sat}(T)}. \quad (4.9)$$

For a given ambient temperature T [$^{\circ}\text{C}$] the SVP [kPa] of water can be found from Buck's equation

$$P_{sat}(T) = 0.61121 \exp \left(\left(18.678 - \frac{T}{234.5} \right) \left(\frac{T}{257.14 + T} \right) \right). \quad (4.10)$$

To achieve the required relative humidity for the different cases the mole fraction of water vapour to exhibit the correct partial pressure must be calculated. This is achieved by first calculating the partial pressure needed for the given temperature T,

$$P_{par}^{H_2O} = \frac{\text{RH}}{100} \times P_{sat}(T) \quad (4.11)$$

where Buck's equation is used to calculate the saturation vapour pressure at that temperature. The ambient pressure is set to atmospheric pressure and thus the mole fraction (X_{H_2O}) of water vapour needed to achieve the desired partial pressure and therefore the desired relative humidity is calculated as,

$$X_{H_2O} = \frac{P_{par}^{H_2O}}{P_{atm}}. \quad (4.12)$$

Two further axisymmetric simulations are performed using the same setup described previously but where the injection temperature is set as either 241.15 K or 231.15 K (-31.15 °C, -41.15 °C), the approximate temperature measured for the Deodorant formulation and propellant aerosol can. This is to compare the carrier jet centreline predictions with the experimental measures from the thermocouple experiments detailed in Chapter 3.

4.4.4 Results

The results from the different simulations are discussed in this section. First the different ambient temperature and relative humidity conditions and their effect on the species fractions within the jet are discussed. Following this are the comparisons of the axisymmetric gaseous jet model with the schlieren and spray temperature experimental results detailed in Chapter 3.

Ambient Effects

The ambient temperature and relative humidity conditions, given in Table 4.4, describe the ambient conditions the carrier jet issues into. Figure 4.17 shows the relative humidity contours for the four different cases simulated. All four cases show that the relative humidity directly at the nozzle exit is equal to zero. This is because there is no water vapour being released from the nozzle and therefore no partial pressure due to water vapour.

Comparing case 1 and case 3 the ambient relative humidity is set as 40%, however, the ambient temperature for case 1 is 20 °C and for case 3 is 40 °C. Even though the relative humidity is the same, the amount of water vapour within the ambient is greater. This is because the saturation vapour pressure for water is greater at 40 °C than it is at 20 °C and therefore to achieve the same RH, a greater partial pressure due to water vapour is needed. For these cases, the temperature of the carrier jet was set to 20 °C. For case 1, where the ambient temperature is set as the same temperature, the entrained ambient air into the jet increases the water vapour mass fraction and results in an increase in jet relative humidity which tends towards the ambient RH but not greater than it.

Entrainment of the ambient into the jet for Cases 2,3 and 4, where the ambient temperature is 40 °C and the jet temperature is 20 °C, results in a jet RH greater than the RH within the ambient. This is due to the saturation vapour pressure of water decreasing as it is entrained from the warm ambient to the colder carrier jet, but the partial pressure from water vapour remains a similar value.

Case 4, where the ambient RH is equal to 80%, results in a jet RH which is greater than 100% which represents a region of supersaturation. These conditions result in condensation of water within the supersaturated region. If the ambient jet temperature was lower the RH would be even greater and would also increase the resultant condensation.

Spray Angle

The spread of the jet is important for the dispersion of the spray and resultant coverage of a target surface. Figure 4.18a shows the propane mass fraction contours predicted by the axisymmetric carrier jet model compared to the mean schlieren frame for aerosol can 1A taken from the experiments in Chapter 3. There is good qualitative agreement between the CFD prediction and experimental results.

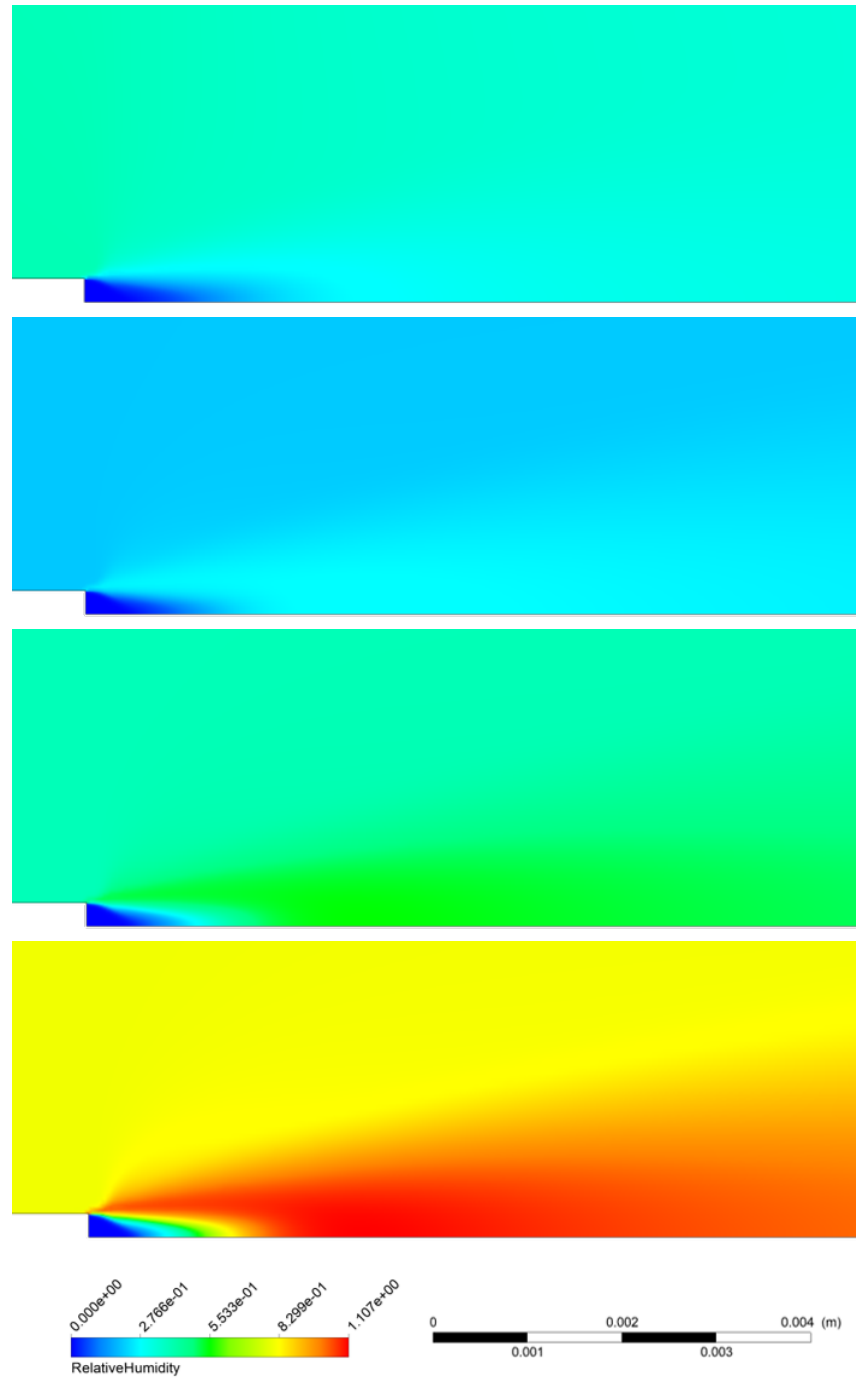


Figure 4.17: Relative humidity contours plotted for four different combinations of ambient temperature (T) and relative humidity (RH), top to bottom: T=20 °C RH=40% (case 1), T=40 °C RH=20% (case 2), T=40 °C RH=40% (case 3), T=40 °C RH=80% (case 4).

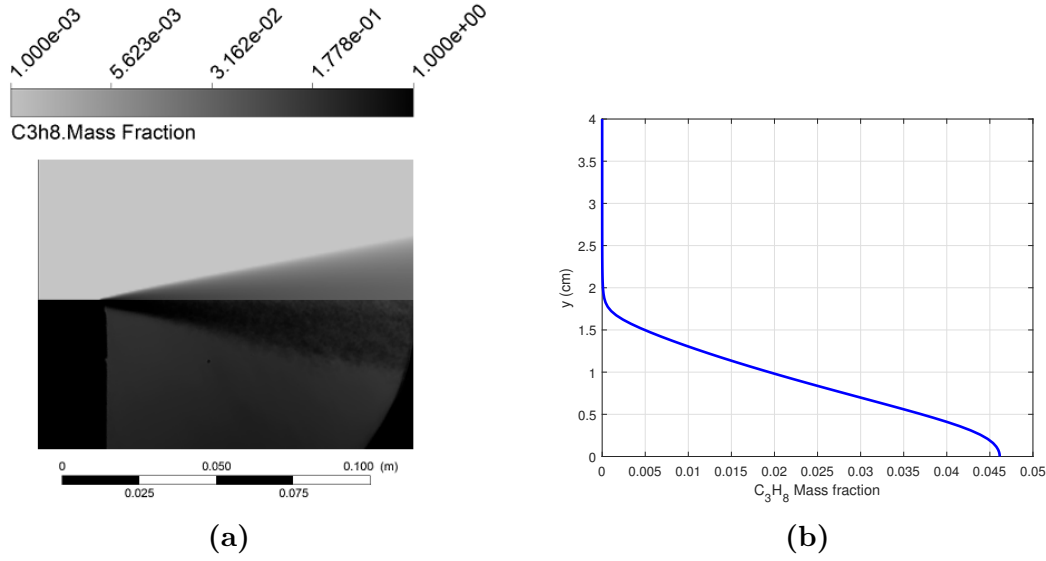


Figure 4.18: (a) Comparison of the CFD predicted propane mass fraction field to a mean schlieren frame for aerosol can 1A. (b) Radial propane mass fraction profile at an axial position of 10 cm.

To calculate the spray angle predicted by the CFD model, the radial profile of propane mass fraction is extracted from the CFD carrier jet model predictions at an axial position of 10 cm. The boundary between the carrier jet and the ambient is determined to be approximately where the propane mass fraction decreases to 0.001, an arbitrary cut off small enough to distinguish between the jet and ambient.

Figure 4.18b shows the radial profile of propane mass fraction at 10 cm. At 10 cm the radial distance from the centreline where the mass fraction reaches 0.001 is found to be at $y \approx 1.75$. This results in a spray half angle of

$$\frac{\theta}{2} = \arctan\left(\frac{1.8}{10}\right) \approx 10.2^\circ \quad (4.13)$$

and therefore a full spray angle of approximately $\theta \approx 20.4^\circ$. This spray angle falls within the range of spray angles observed for the different formulations and nozzle type. This demonstrates that the model is able to give a representation of the averaged fully-developed spray stage observed in the schlieren experiments. A simple representation of the inlet conditions is used and no clear distinction of nozzle type has been implemented, therefore achieving a spray angle within the measured

ranges is promising for a simple asymmetric model.

The velocity profiles of the carrier jet are taken as the self similar form from the analytic model of Reichardt (1942), as was done previously. Using the decay constant of Xia and Lam (2009) ($\beta = 6.5$) with Eq. (4.5), and taking the edge of the spray region to be the point at which the velocity is $U = 0.001U_c$, gives a predicted spray half angle of 15° . Here the decay coefficient would need to be approx $\beta \approx 10$ to achieve a spray half angle of 10.2° .

Bird et al. (2006) derives the formula for the mean axial velocity of a turbulent jet,

$$U = \frac{\nu_t}{z} \frac{2C_3^2}{[1 + \frac{1}{4}(C_3r/z)^2]^2} \quad (4.14)$$

where C_3 was determined experimentally to be $C_3 = 15.1$ and is also related to the flow of momentum J , and turbulent viscosity ν_t by the expression,

$$C_3 = \sqrt{\frac{3}{16\pi}} \sqrt{\frac{J}{\rho \nu_t}}. \quad (4.15)$$

As a uniform profile is assumed at the inlet of the carrier jet model, the rate of momentum flow is calculated as

$$J = \pi r_0^2 \rho U^2 = \pi \times 0.0005^2 \times 1.8 \times 30^2 = 0.0013 \text{ kg m s}^{-2}. \quad (4.16)$$

Substituting this into Eq. (4.15) the turbulent viscosity can be approximated, which is then used with Eq (4.14). The edge of the spray is calculated again using the same criteria as before, resulting in a spray half angle of 30° , a considerable overprediction of the spray half angle found experimentally.

Bird et al. (2006) finds that the eddy viscosity model used here is good at predicting the profile near the centreline but worse at the edge of the jet and therefore our criteria for determining the spray boundary may not be appropriate

here. The Prandtl mixing length theory has been shown to give better agreement to the experiments of Reichardt (1942) for velocities near the jet edge (Bird et al., 2006).

Temperature

Simulations where the carrier jet inlet is initialised with a temperature of either 231 K or 241 K were performed. Figure 4.19 shows the centreline temperature profiles for both of these simulation cases and also shows the centreline temperature measured from the thermocouple experiments described in Chapter 3.

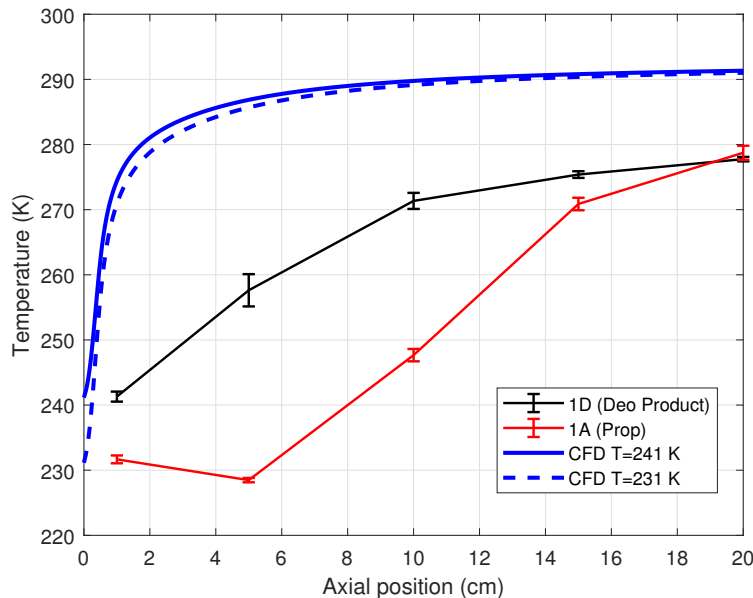


Figure 4.19: Centreline temperature predicted by the axisymmetric CFD models with initial jet temperature of $T=241$ K and $T=231$ K compared to the the measured centreline temperature for aerosol cans 1D (Deo) and 1A (Prop).

Figure 4.19 shows that as the warm ambient air is entrained the warm up of the carrier jet is not representative of measurements taken from the thermocouple experiments. This is true for both simulation predictions. These results show that there is a thermodynamic process not captured in the current model. The evaporation process of the spray droplets and transport of these droplets through the carrier jet are believed to be the key thermodynamic processes. The carrier jet model alone

is insufficient to capture the jet temperature accurately, and coupling of the droplet evaporation with the carrier jet is therefore important. Droplet evaporation and its impact on temperature predictions are covered in the subsequent chapter.

4.5 Summary

The development of the steady-state carrier jet model is discussed in detail throughout this chapter. The turbulence model study investigated five two-equation RANS turbulence models, the standard, RNG and realizable $k - \varepsilon$ turbulence models and the $k - \omega$ and $k - \omega$ SST turbulence models, and their applicability to a gaseous propane jet issuing into a co-flow. The aim of this study was to determine the appropriate turbulence model for capturing the velocity field and species fields where limited boundary information is used for the case setup.

The performance of the $k - \omega$ models was below what was initially expected but these differences are believed to be due to these models being more sensitive to the initial conditions. The $k - \varepsilon$ models performed well, achieving good predictions for both the velocity field and mass fraction down the centreline of the jet, and also achieved good predictions radially for the different axial positions investigated. The RNG model showed a greater decay of centreline velocity and species fraction whereas the standard and realizable model predicted very similar profiles. Due to the more robust formulation and good predictions of important variables the realizable model was chosen for future simulations.

Variations between the model species mass fraction predictions and the experimental data led to the influence of the turbulent Schmidt number on the species mass fraction fields being investigated. There was a clear influence due to this parameter, where the maximum value investigated $Sc_t=0.9$ gave improved predictions to the experimental results. This tuning of turbulent Schmidt number was not taken further as it would be tuning to specific scenarios rather than increasing the wider

understanding of model limitations.

An axisymmetric domain setup was chosen to further reduce the computational cost of the simulation. A study into the effects of ambient temperature and relative humidity was performed to investigate how they influence the environment within the spray region. It was shown that hot, humid ambient environments when entrained into the cooler jet environment can result in supersaturated conditions within the cold spray region. Relative humidity conditions greater than 100% result in condensation and this will influence the change in droplet size.

Conditions of that similar to deodorant-type aerosol cans were also simulated. The steady-state model predictions showed good agreement to the carrier jet dispersion with a predicted spray angle falling within the range found from the schlieren experiments. The predicted spray angle was in the range of both the swirl nozzle measurements and simple orifice measurements. The carrier jet flow has a zero angular velocity component and therefore may not be representative of that flow condition.

The gas jet inlet was also simulated with a temperature similar to that measured from the thermocouple experiments for both the swirl and simple orifice nozzles. The predictions showed that the entrainment of the ambient resulted in considerable warm-up of the jet region which was not measured within the experiments. The carrier jet model alone is not capable of capturing this reduced warm-up and is believed to be due to droplet evaporation, which maintains a colder jet region for a greater axial distance.

The results presented in this chapter show that an axisymmetric, RANS, steady-state carrier jet model is capable of accurately predicting a gaseous free jet. The numerical model provides a solid base for further model development and shows viability as a tool to aid in understanding of how ambient conditions can influence the spray region and the conditions spray droplets are subject to during their transport

from the nozzle to their destination.

Chapter 5

Spray Impingement and Droplet Carry-Over

5.1 Introduction

Understanding the impingement of personal care products sprays on the target surface is important for determining the efficiency of spray application methods and to aid in design improvements. For example, it supports understanding droplet size, carry-over from surfaces and deposition patterns. This chapter looks to introduce an impingement surface and to couple droplet transport with the carrier jet model described in Chapter 4. The previous CFD results described in Chapter 4 provide confidence in the CFD model's predictions for the variation of momentum of species within the steady-state carrier jet.

Here the impingement of droplets, representative of sizes generated from deodorant-type aerosol cans, is investigated. First a numerical study of ambient condition effects on droplet evaporation is detailed. Then an optimisation-type study is performed to understand the influence of geometric properties of the impingement surface on the efficiency of sprays generated from deodorant-type aerosol cans. The

following chapter describes the steps of this process, detailing the design of experiments (DoE) of the parameters of interest and the resultant capture efficiency for different droplet sizes.

5.2 Droplet Dynamics

This section looks at the evaporation of droplets and the impact ambient conditions can play on their evaporation. First the governing equations, detailed in Chapter 2, are revisited. Then the implementation of the equations into MATLAB is described. Finally the results from varying ambient conditions such as ambient temperature and ambient relative humidity are given.

5.2.1 Governing equations

The base equations solved for droplet transport and evaporation are given in this section with further detail such as definitions and model differences given in Chapter 2. The implementation of these equations into MATLAB and the physical properties of the liquid are then described.

Force Balance

The change in droplet velocity is related to the forces acting on the droplet. Here the force balance equation accounts for the drag on the droplet, influence of gravity and also allows for any additional forcing terms,

$$\frac{du_{p,i}}{dt} = F_D (u_i - u_{p,i}) + g_i \frac{(\rho_p - \rho)}{\rho_p} + \frac{F_i}{\rho_p}. \quad (5.1)$$

The drag force for spherical particles is given as,

$$F_D = \frac{18\mu C_D \text{Re}}{\rho_p d_p^2} \frac{1}{24} \quad \text{with} \quad \text{Re} = \frac{\rho |\mathbf{u} - \mathbf{u}_p| d_p}{\mu} \quad (5.2)$$

where the drag coefficient C_D is a function of Reynolds number and is given by the [Morsi and Alexander \(1972\)](#) correlation,

$$C_D = a_1 + \frac{a_2}{\text{Re}} + \frac{a_3}{\text{Re}^2} \quad (5.3)$$

where the coefficients a_i for $i=1,2,3$ are taken from [Morsi and Alexander \(1972\)](#) and are given in Table 5.1. These coefficients are fit to experimental data for ranges of Reynolds numbers.

	a_1	a_2	a_3
$\text{Re} < 0.1$	0	24	0
$0.1 < \text{Re} < 1$	3.69	22.73	0.0903
$1 < \text{Re} < 10$	1.222	29.1667	-3.8889
$10 < \text{Re} < 100$	0.6167	46.5	-116.67
$100 < \text{Re} < 1000$	0.3644	98.33	-2778
$1000 < \text{Re} < 5000$	0.357	148.62	-47500
$5000 < \text{Re} < 10000$	0.46	-490.546	578500
$10000 < \text{Re} < 50000$	0.5191	-1662.5	5416700

Table 5.1: [Morsi and Alexander \(1972\)](#) coefficients a_i determined by the value of the Reynolds number.

Droplet evaporation

Evaporation can be modelled using models such as the Maxwell evaporation model and Stefan-Fuchs evaporation model as discussed in Chapter 2, and are given by,

$$\frac{dm_p}{dt} = -A_p M_w N \quad (5.4)$$

and

$$\frac{dm_p}{dt} = -k_c A_p \rho \ln(1 + B_m) \quad (5.5)$$

respectively.

Assuming constant density and using the substitution $m_d = \rho V_d$ allows the Maxwell mass transfer equation to be transformed into ordinary differential equation with respect to the droplet's diameter. Following this substitution gives,

$$\frac{dm_p}{dt} = \rho_p \frac{dV_p}{dt} = \frac{1}{6} \pi \rho_p \frac{d(d_p(t)^3)}{dt} = \frac{1}{2} \pi \rho_p d_p^2 \frac{d(d_p)}{dt} = -\pi d_p^2 M_w N, \quad (5.6)$$

$$\implies \frac{d(d_p)}{dt} = -\frac{2}{\rho_p} M_w N. \quad (5.7)$$

This results in the Maxwell model and Stefan-Fuchs model in terms of the droplet diameter,

$$\frac{d(d_p)}{dt} = -\frac{2}{\rho_p} M_w k_c (C_s - C_\infty) \quad (5.8)$$

and

$$\frac{d(d_p)}{dt} = -2k_c \frac{\rho}{\rho_p} \ln(1 + B_m) \quad (5.9)$$

respectively.

Droplet heat transfer

Droplet heat transfer is modelled following the ODE

$$m_p c_p \frac{dT_p}{dt} = \underbrace{h A_p (T_\infty - T_p)}_{Convective} + \underbrace{\varepsilon_p A_p \sigma (\theta_R^4 - T_p^4)}_{Radiation} + \underbrace{\frac{dm_p}{dt} h_{fg}}_{Latent loss}. \quad (5.10)$$

As the ambient temperature is significantly less than 1000 K it is assumed that the temperature change due to radiative effects is significantly small (Sazhin, 2006) and can be ignored. This assumption simplifies the heat transfer equation to,

$$m_p c_p \frac{dT_p}{dt} = h A_p (T_\infty - T_p) + \frac{dm_p}{dt} h_{fg}. \quad (5.11)$$

For further detail on these equations the reader is directed back to Chapter 2, Section 2.4. Different substances of interest for the purpose of this study are water for model verification, and propane and butane, the main propellants in personal

	Water	Propane	Butane	Units
D_m , Mass diffusivity	2.22×10^{-5}	1.22×10^{-5}	9.81×10^{-6}	m^2/s
P_{sat} , Saturation vapour pressure	2.34×10^3	8.59×10^5	2.08×10^5	Pa
M_w , Molecular weight	1.80×10^{-2}	4.41×10^{-2}	5.81×10^{-2}	kg/mol
c_p , Specific heat capacity	4.19×10^3	2.2×10^3	1.68×10^3	J/kg/K
h_{fg} , Latent heat of evaporation	2.26×10^6	4.26×10^5	3.86×10^5	J/kg

Table 5.2: Thermophysical properties at approximately 293 K for water, propane and butane.

care products. The thermophysical properties of these substances can be found in Table 5.2. The mass diffusivities of propane and butane are taken from Elliott and Watts (1972). The saturation vapour pressure (SVP) for water, propane and butane are calculated from Buck's equation and the Antoine equations defined in Section 2.2 of Chapter 2 respectively. The constant pressure liquid specific heat capacity of water, propane and butane are taken from Chase (1998), Goodwin (1978) and Aston et al. (1940) respectively. The molecular weight is calculated for each substance. The latent heat of evaporation for water, propane and butane are taken from Datt (2011), Majer and Svoboda (1986) and Stephenson and Malanowski (1987) respectively. The values in Table 5.2 are taken at approximately room temperature, but note that these properties are temperature dependent.

5.2.2 Numerical Implementation

The ODEs governing droplet momentum, evaporation and temperature change are solved using MATLAB's inbuilt ODE solver `ode45`. The solver requires the system to be written in the form $\frac{dX}{dt} = X' = f(X, t)$. For our governing equations the system is written as six ODEs for the droplet position, $\mathbf{x} = (x_p, y_p)$, droplet velocity

$\mathbf{u}_p = (u_p, v_p)$, droplet diameter d_p and droplet temperature T_p

$$X' = \begin{bmatrix} x_p \\ u_p \\ y_p \\ v_p \\ d_p \\ T_p \end{bmatrix}' = \begin{bmatrix} u_p \\ F_D (U - u_p) \\ v_p \\ F_D (V - v_p) + g \frac{(\rho_p - \rho)}{\rho_p} \\ -\frac{2}{\rho_p} M_w k_c (C_s - C_\infty) \\ \frac{1}{m_p c_p} \left(h A_p (T_\infty - T_p) + \frac{dm_p}{dt} h_{fg} \right) \end{bmatrix}. \quad (5.12)$$

This system uses Maxwell's model for droplet evaporation. If the Stefan-Fuchs model is used the system is given by,

$$X' = \begin{bmatrix} x_p \\ u_p \\ y_p \\ v_p \\ d_p \\ T_p \end{bmatrix}' = \begin{bmatrix} u_p \\ F_D (U - u_p) \\ v_p \\ F_D (V - v_p) + g \frac{(\rho_p - \rho)}{\rho_p} \\ -2k_c \frac{\rho}{\rho_p} \ln(1 + B_m) \\ \frac{1}{m_p c_p} \left(h A_p (T_\infty - T_p) + \frac{dm_p}{dt} h_{fg} \right) \end{bmatrix}. \quad (5.13)$$

During the solution process the change in diameter with respect to time is calculated. The temperature change requires the change in droplet mass which is calculated following the ODEs given by (5.4) and (5.5) respectively for the two system of ODEs. The solver integrates through time using an adaptive Runge-Kutta time-stepping scheme. Further detail about the `ode45` solver can be found in [Moler \(2008\)](#) and [Shampine and Reichelt \(1997\)](#).

The ODE governing change in droplet diameter requires calculation of the mass transfer coefficient, k_c . This can be approximated from the Ranz-Marshall correlation for the Sherwood number ([Ranz and Marshall, 1952](#)),

$$\text{Sh} = \frac{d_p k_c}{D_m} = 2 + 0.6 \text{Re}_d^{\frac{1}{2}} \text{Sc}^{\frac{1}{3}} \quad \implies \quad k_c = \frac{D_m}{d_p} \left(2 + 0.6 \text{Re}_d^{\frac{1}{2}} \text{Sc}^{\frac{1}{3}} \right). \quad (5.14)$$

The droplet Reynolds number is calculated each time step following Eq. (5.2), where the updated droplet diameter and droplet velocity are used. The mass diffusivity (D_m) is taken from Table 5.2 and, along with the density and viscosity of air ($\rho = 1.225 \text{ kg m}^{-3}$, $\mu = 1.85 \times 10^{-5} \text{ kg m}^{-1}\text{s}^{-1}$), is used to calculate the Schmidt number.

The Maxwell evaporation requires the concentration of vapour at the surface of the droplet and the concentration of vapour within the ambient. The ambient temperature is defined as T_∞ and does not change through the solution. The initial droplet temperature is set as $T_{p,0}$ but evolves in time when heat transfer is accounted for. The concentration of vapour within the bulk (C_∞) and at the surface of the droplet (C_s) are calculated assuming the ideal gas law and are given by

$$C_\infty = \frac{\text{RH} P_{sat}(T_\infty)}{100 RT_\infty} \quad \text{and} \quad C_s = \frac{P_{sat}(T_p)}{RT_p}, \quad (5.15)$$

where RH is used to denote the saturation of species in the ambient relative to how much can be held in the ambient (equilibrium saturation). If the species is water, then this is known as relative humidity.

The Stefan-Fuchs model requires calculation of the Spalding mass transfer number (B_m) which is given by

$$B_m = \frac{Y_\infty - Y_s}{Y_s - 1}, \quad (5.16)$$

where Y_∞ and Y_s are the mass fraction of evaporating species in the ambient and at the surface of the droplet. These are calculated using,

$$Y_\infty = \frac{P_{partial}}{P_{atm}} \frac{M_w}{M_{w,Total}} \quad \text{and} \quad Y_s = \frac{P_{sat}(T_p)}{P_{atm}} \frac{M_w}{M_{w,Total}}, \quad (5.17)$$

with M_w the molecular weight of the evaporating species and $M_{w,Total}$ the combined molecular weight of the evaporating species and the ambient (air, $M_{w,air} = 2.9 \times 10^{-2} \text{ kg/mol}$).

The change in droplet temperature requires the calculation of the heat transfer coefficient h . This can be approximated from a Ranz-Marshall correlation for the Nusselt number (Ranz and Marshall, 1952),

$$\text{Nu} = \frac{hd_p}{k} = 2 + 0.6\text{Re}^{1/2}\text{Pr}^{1/3} \quad \implies \quad h = \frac{k}{d_p} \left(2 + 0.6\text{Re}^{1/2}\text{Pr}^{1/3} \right). \quad (5.18)$$

The droplet Reynolds number is calculated following Eq. 5.2 whereas the Prandtl number is approximated to be 0.7, which for gases is a standard assumption Rapp (2017). The specific heat capacity (c_p) is also needed and is taken from Table 5.2.

5.2.3 Verification

The governing equations are implemented into MATLAB and therefore verification steps are taken to ensure that they have been implemented correctly. For these verification tests water droplets are used. The implementation of the force balance equations is verified by comparing the y-velocity predictions to the terminal settling velocity of the droplets of that size. Droplets of sizes 10-100 μm are initialised with a horizontal velocity of 1 ms^{-1} . The horizontal velocity component of the droplets tends to zero (the ambient velocity) with the smaller droplets' horizontal velocity reducing quicker than that of the larger droplets. This is expected due to the smaller relaxation time of the small droplets.

For the vertical velocity component of the force balance the predicted velocities at long times are compared to that of the Stokes droplet terminal settling velocity (V_t) given by,

$$V_t = \frac{gd^2}{18\mu} (\rho_l - \rho). \quad (5.19)$$

The droplets with diameter less than 40 μm show exact agreement to the terminal Stoke's settling velocity, verifying the code implementation. As the droplet size increases, Eq. (5.19) does not capture the true terminal settling velocity as the

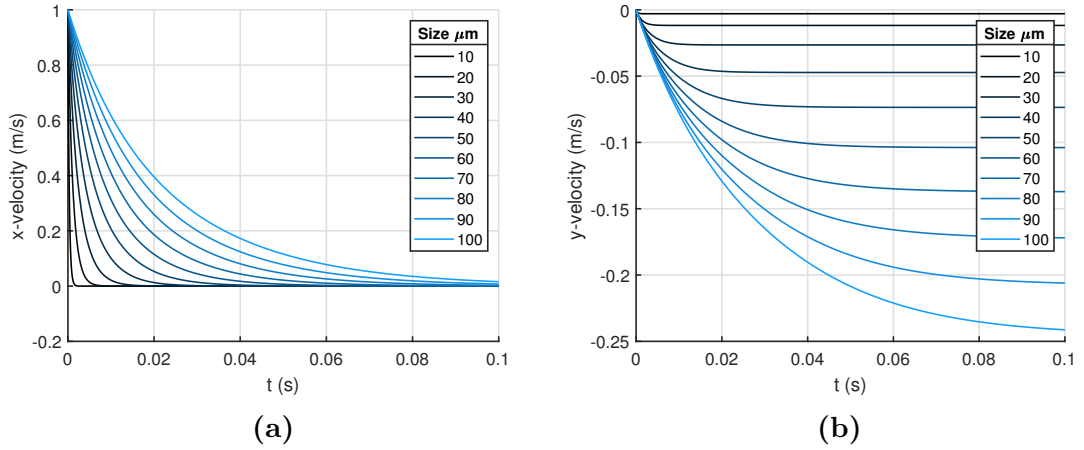


Figure 5.1: X velocity and Y velocity plot against time for the release of different size droplets with initial velocity $u = 1 \text{ ms}^{-1}$ prescribed in the x-direction into quiescent air.

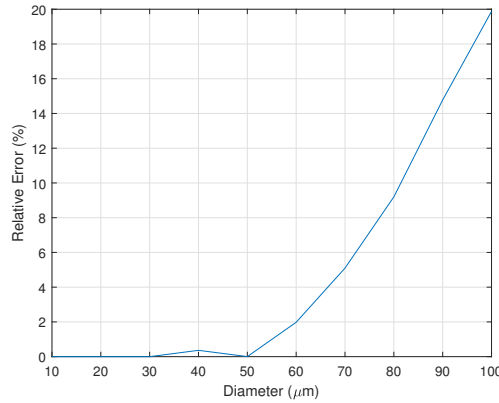


Figure 5.2: Relative error of the implemented model predictions to the settling velocity Eq. (5.19) for droplets sizes 10-100 μm .

drag coefficient behaves differently than what is represented by Eq. (5.19), but good agreement is found for small droplets and the relative error can be seen in Figure 5.2. For the Newtonian drag regime the settling velocity becomes an implicit function as shown in Hinds (2012).

To verify the implementation of the heat and mass transfer equations the predictions are compared to the d^2 law (detailed in Chapter 2, Section 2.4.4) and the wet bulb temperature, also known as the adiabatic saturation temperature. A stationary droplet with an initial diameter of 12 μm and temperature of 293.15 K is initialised into a quiescent environment with a relative humidity of 50% and temperature 293.15 K. Figure 5.3a shows the square of the diameter decaying linearly

with time, satisfying the d^2 law. The wet bulb temperature is taken from the psychrometric chart for water vapour and is estimated to be approximately 286.8 K for the ambient conditions modelled. The predictions from the implemented model are shown in Figure 5.3b and give the wet bulb temperature as 286.7 K, showing good agreement with the expected value.

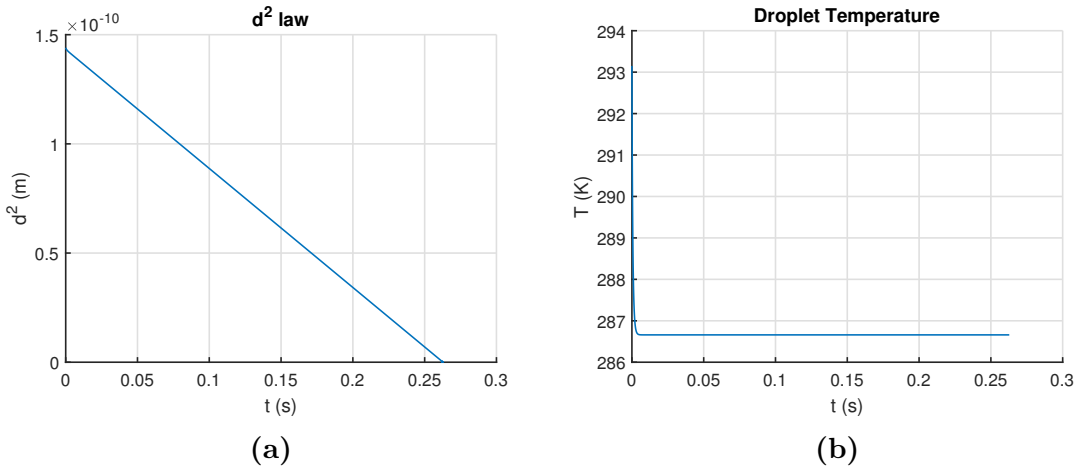


Figure 5.3: For a $12 \mu\text{m}$ diameter water droplet within a quiescent environment with an ambient temperature of 293.15 K and RH=50%, (a) d^2 against time and (b) droplet temperature (T) against time.

The same verification test was performed for the Stefan-Fuchs implementation which accounts for the advection of vapour away from the droplet. The comparison between the implementations is shown in Figure 5.4. Inclusion of the species advection results in an increase in the time it takes for the droplet to evaporate. The wet-bulb temperature achieved when advection of vapour from the droplet is included slightly increases, due to the slightly lower evaporation rate.

5.2.4 Results

Here the numerical droplet model implemented into MATLAB is used to investigate how ambient effects such as temperature and relative humidity influence the evaporation of droplets, in particular water droplets. First the influence of droplet size and inclusion of the droplet heat transfer is investigated. Then the model is applied

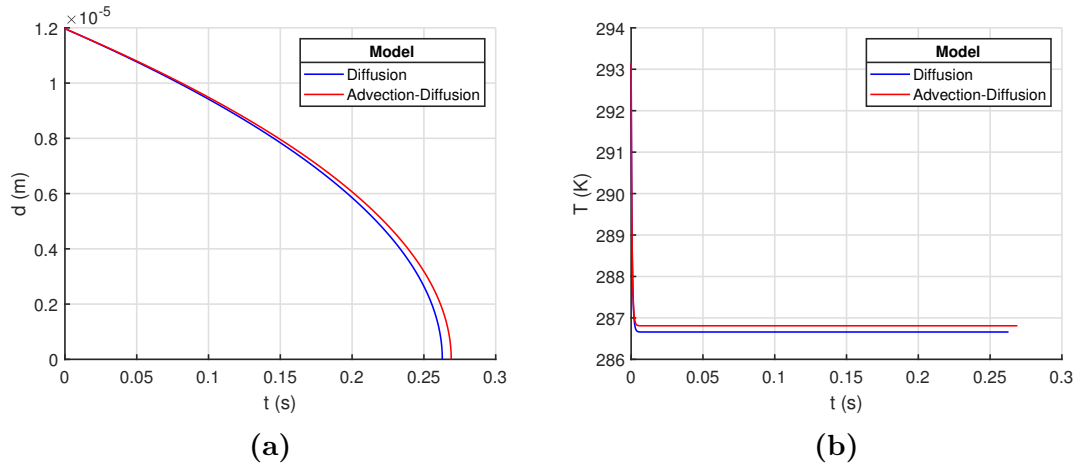


Figure 5.4: For a 12 μm diameter water droplet within a quiescent environment with an ambient temperature of 293.15 K and RH=50%, (a) droplet diameter (d) against time and (b) droplet temperature (T) against time are plotted for both the Maxwell (diffusion) model and Stefan-Fuchs (advection-diffusion) model.

to propane droplets where an equivalent ambient saturation fraction is used to that of relative humidity.

Ambient Condition Influence

Droplets of size ranging from 10-100 μm are initialised at room temperature 293.15 K into a quiescent environment also at room temperature and with a relative humidity of 50%. To compare the influence of incorporating droplet temperature variations, initially the change in droplet temperature is not accounted for, but the momentum and Maxwell mass transfer equations are solved. Figure 5.5 shows the diameter change in time. Water droplets with a diameter less than 30 μm evaporate within less than a second, whereas an increase in droplet size results in droplets staying present for longer periods of time.

The vertical velocity of the droplets during their evaporation is plotted in Figure 5.5. The droplets reach their terminal velocity and then as they evaporate their diameter decreases, resulting in a decrease to their terminal velocity. This trend is captured within the model. The classification between droplets evaporating and ones depositing as they have a sufficient settling velocity can be categorised by

the Wells curve (Wells, 1934) and has been used extensively in recent work looking at exhaled respiratory droplets.

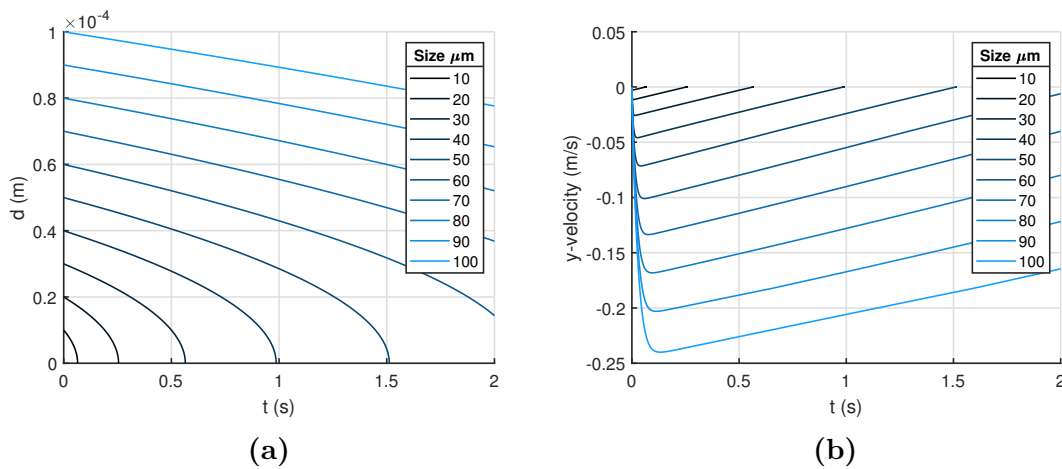


Figure 5.5: Plots against time of (a) droplet diameter and (b) the droplet vertical velocity. Droplets evaporate with an assumed constant temperature of 293.15 K in an ambient of temperature 293.15 K and 50% RH.

The same size droplets are modelled with the same initial droplet and ambient conditions, but now droplet temperature is allowed to change in time. The resultant droplet diameter in time and settling velocity are given in Figure 5.6. The droplets cool due to the latent heat of evaporation, this cooling results in a reduction in evaporation rate and therefore droplets persist for longer. For example, a 30 μm droplet is predicted to take 0.55 s to evaporate fully, however, when the droplet is allowed to cool it is predicted to take approximately 1.5 s, approximately 3 times longer than before. This reduction in evaporation is also seen in the decrease of rate of terminal settling velocity as the droplets evaporate.

Ambient conditions also impact the evaporation of the droplet, in particular the temperature of the ambient and the saturation of species vapour in the ambient (RH). To first investigate the effects of RH a droplet with initial diameter of 12 μm is initialised at room temperature into an ambient also at room temperature, but four RH conditions are simulated, RH at 20, 40, 60 and 80%. The results can be seen in Figure 5.7. As RH increases there is a greater concentration of species already in the ambient. This results in a decrease of species diffusion from the droplet surface

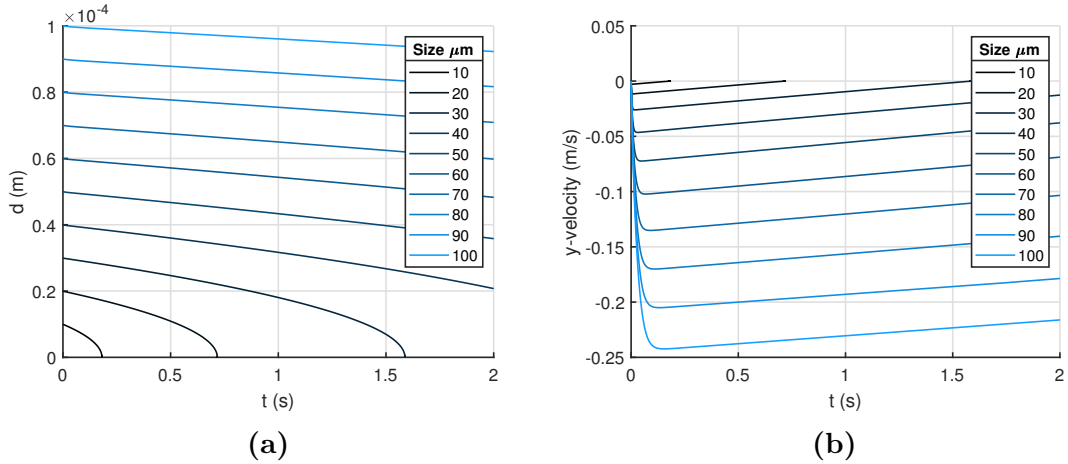


Figure 5.6: Plots against time of (a) droplet diameter and (b) the droplet vertical velocity. Droplets evaporate allowing with an initial temperature of 293.15 K in an ambient of temperature 293.15 K and 50% RH, droplet temperature is allowed to change.

into the ambient and therefore the rate of droplet evaporation decreases.

The effect of varying ambient temperature is captured by simulating a droplet with an initial diameter of 12 μm and droplet temperature 293.15 K, in a room with a RH of 50%, but where the ambient temperature is given values of 278.15, 283.15, 293.15 and 303.15 K.

The higher ambient temperatures result in an increased droplet evaporation rate. This is because the wet bulb temperature achieved for the higher temperatures is much greater and therefore the concentration of vapour at the surface of the droplet is greater, enhancing the diffusion of the vapour into the ambient.

The model predictions show that droplet evaporation for simple scenarios is still complex and heavily dependent on ambient conditions. Room environments have varying flow velocities, ambient temperature and RH levels which have been shown to influence droplet evaporation. Increasing RH results in a decrease in evaporation rate and increasing temperature results in an increase in evaporation rate, showing that these ambient conditions compete against one another and that only knowing one of these conditions is insufficient to determine droplet evaporation rate.

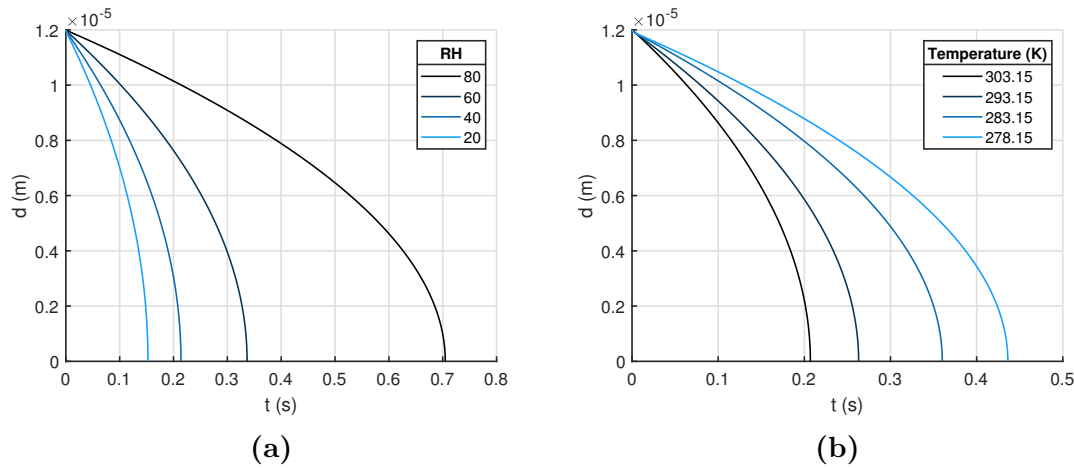


Figure 5.7: A water droplet of initial diameter $12 \mu\text{m}$ is initialised with a temperature of 293.15 K into a quiescent ambient with (a) fixed ambient temperature of 293.15 K but varying relative humidity (RH) or (b) a fixed RH of 50% with varying ambient temperature.

Droplets of Propellant

The previous work looked at water droplet evaporation and the impact of ambient conditions on the droplet evaporation. Here the same governing equations are used to determine the evaporation of propane droplets in conditions representative of what would be experienced during their flight when issued from a deodorant-type aerosol can. This system of equations is not appropriate to determine boiling of droplets however, and therefore the conditions which can be investigated are restricted to ambient temperatures at or below the boiling point of the propellant. Temperatures within the carrier jet have been shown experimentally to be much lower than the ambient temperature and even drop below the boiling point of propane at ambient pressures so this assumption is valid close to the nozzle. Numerically, the mass fraction of gaseous propellant, and thus propellant vapour pressure, varies through the carrier jet. More precisely, the mass fraction of gaseous propellant decreases away from the nozzle.

Propane is more volatile (ability of a substance to vaporise) than water, which is because the vapour pressure of propane at a given temperature is greater than the associated vapour pressure of water. To demonstrate this, droplets of

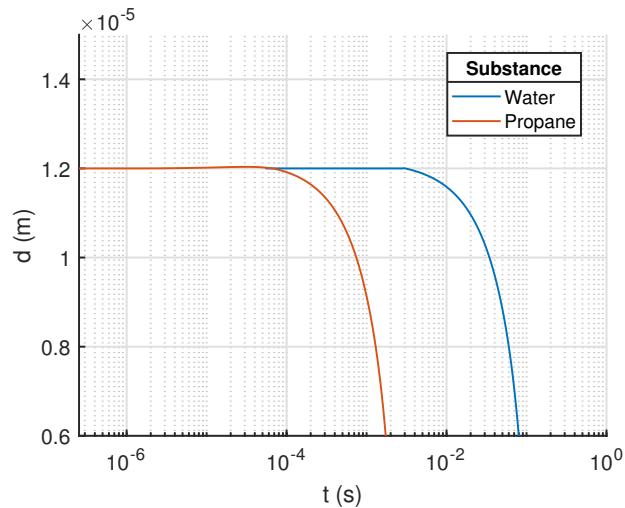


Figure 5.8: Log-log plot of droplet diameters against time for a water droplet and propane droplet initialised at 10 K less than the liquids' boiling points (-52°C and 90°C respectively).

propane and water are simulated at a temperature 10 K below their boiling points (-52°C and 90°C respectively), into an ambient of the same temperature (-52°C and 90°C respectively) and with a ambient saturation fraction of 50% respectively. Droplet mass and heat transfer are modelled as described previously. The droplet diameter with respect to time is plotted for both cases in Figure 5.8.

The dependency of the propellant on the ambient conditions holds for the same reasoning as discussed for water droplets. Figure 5.9 shows the minimum droplet temperature reached (equivalent to the wet bulb temperature of water) for different ambient propane saturation fractions. This shows that if a propellant droplet, in particular a pure propane droplet, is in an ambient of temperature 231.15 K then the temperature of the droplet can cool to a temperature lower than the boiling point of the of droplet at a 100% saturation fraction. Comparing this to the experimental temperature plots explains why, close to the nozzle, the temperature measured decreases below the boiling point of the most volatile component.

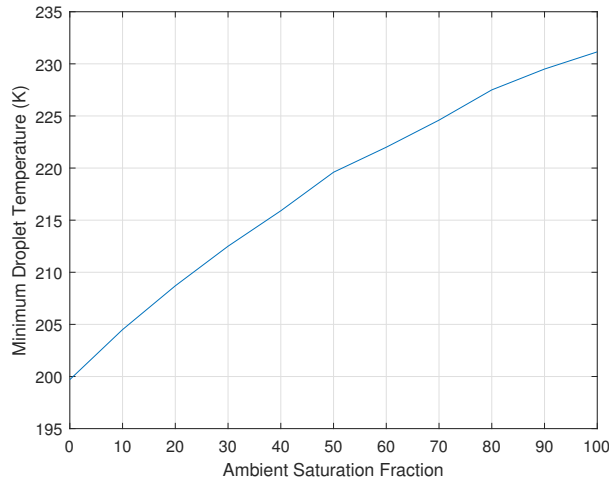


Figure 5.9: Minimum droplet temperature achieved against the ambient saturation fraction due to propane droplet vaporisation in an ambient temperature of 231.15 K.

5.2.5 Coupling Discrete and Continuous Phases in Fluent

In this section the droplet discrete phase is coupled with the Eulerian axisymmetric carrier jet model detailed in Chapter 4, Section 4.4. This is done to understand how the presence of the droplets impacts the carrier jet. Numerically three phase systems are difficult to capture (Wareing et al., 2014), therefore a simpler two-phase approach is used. First the continuous source terms are described including the momentum, mass and heat source. Then additional droplet physics are detailed, including potential breakup and turbulent dispersion. Finally the centreline temperature due to the presence of propane droplets is compared to the experimental measurements.

Continuous Source Terms

This droplet model is coupled with the Eulerian continuous axisymmetric carrier jet model within Fluent, allowing for two-way coupling where the droplet temperature and ambient temperature influence each other. The momentum source

(Ansys, 2009) from the droplets into the continuous phase is given by,

$$\mathbf{F} = \left(\frac{18\mu C_D \text{Re}}{\rho_p d_p^2 24} (\mathbf{u}_p - \mathbf{u}) \right) Q_p \Delta t, \quad (5.20)$$

where Q_p is the particle mass flow rate. Note that gravity is not accounted for in this model as the axisymmetric assumption does not allow for it in this circumstance. However, the droplets are assumed to reach the impingement surface before gravity is able to have a substantial effect.

The heat source term (Ansys, 2009) between the phases is given by,

$$Q = \frac{Q_p}{m_{p,0}} \left[- (m_{p,in} - m_{p,out}) h_{fg} - m_{p,out} \int_{T_{ref}}^{T_{p,out}} c_p dT + m_{p,in} \int_{T_{ref}}^{T_{p,in}} c_p dT \right], \quad (5.21)$$

where $m_{p,in}$ and $T_{p,in}$ are the mass and temperature of the droplet entering the computational cell and $m_{p,out}$ and $T_{p,out}$ the mass and temperature of the droplet leaving the cell.

The final source term is that of evaporated species vapour for species component i from the discrete phase into the continuous phase (Ansys, 2009) which is given by,

$$S_i = \frac{\Delta m_p}{m_{p,0}} Q_p. \quad (5.22)$$

Note each droplet which passes through a computational cell will contribute to each of the three source terms. Further detail on the individual terms and their implementation can be found in Ansys (2009).

Droplet Breakup

Droplet breakup is not considered in this model but it is noted that close to the nozzle the Weber number for a propane droplet is given as $\frac{\rho v^2 L}{\gamma} = \frac{498 \times 8^2 \times 12 \times 10^{-6}}{0.007} \approx 55$. As the We number is sufficiently large close to the nozzle, secondary breakup may possibly occur. To temporally resolve this, a time-step sufficiently small would

be required as the droplets are assumed to eject with such high velocities. Away from the nozzle where the droplet velocity has sufficiently decayed results in a significant reduction in We . The droplet size measurements from Chapter 3 show little change of the PSD up to 5 cm, at which point the jet velocity has decayed to approximately 3 ms^{-1} . This results in $We \approx 8$ which is below the critical Weber number for the occurrence of breakup (Pilch and Erdman, 1987).

The RANS turbulence model averages the temporal nature of the flow and so the turbulent fluctuations are not given and only a mean velocity is found. The effects of flow turbulence on the dispersion of the particles are therefore modelled through stochastic tracking via the Discrete Random Walk (DRW) model. Stochastic tracking allows for particle trajectories to be computed from not only the mean flow velocity but also the turbulent fluctuations.

Turbulent Dispersion

The DRW model (Ansys, 2009) is a stochastic approach to determine the fluctuating contribution and uses the TKE to determine an isotropic fluctuation. Here a normally distributed random number given by ζ is used and the turbulent velocity components are given as

$$u' = v' = w' = \zeta \sqrt{\frac{2k}{3}}. \quad (5.23)$$

This turbulent fluctuation is applied to the droplet during the minimum time of the eddy lifetime or eddy crossing time, at which point a new value of the random number is used for ζ . Including a turbulent velocity fluctuation on droplets is crucial for accurate predictions for the turbulent dispersion of droplets. Figure 5.10 shows the impact of not including this turbulent fluctuation on the droplet trajectories, resulting in the droplets staying on their initial trajectories.

To determine the influence of propane droplet evaporation on the temper-

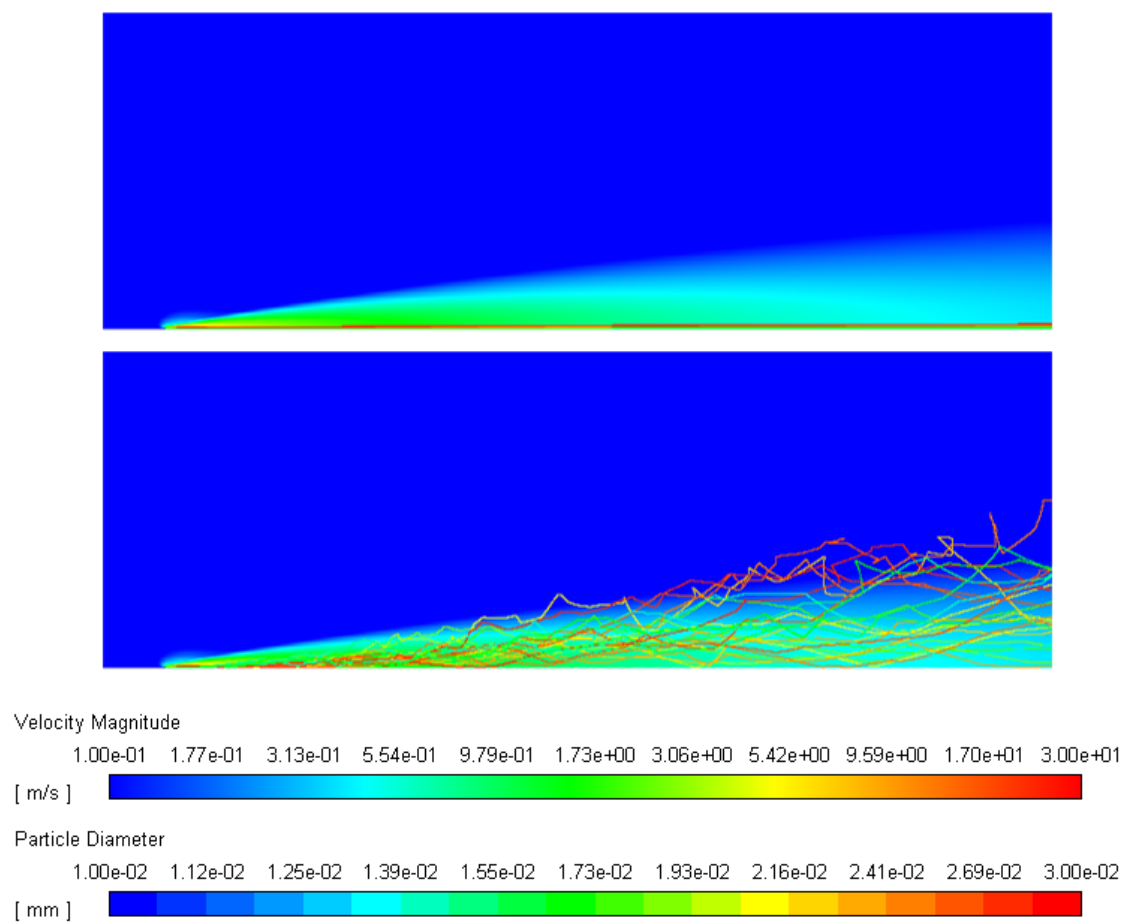


Figure 5.10: Contours of velocity magnitude for the continuous phase as well as particle trajectories coloured by particle diameter top: without turbulent dispersion and bottom: with turbulent dispersion.

ature field of the jet, a material property for propane is defined within Fluent. This is defined using the properties given in Table 5.2 and the saturation vapour pressure taken from that defined in Chapter 2, Section 2.2. The initial atomization of the can contents is assumed to have occurred at the nozzle exit. Here 25 streams of droplets of size 15-50 μm are linearly distributed across the nozzle plane from $y=0$ mm to $y=0.25$ mm, with an axial velocity equal to that of the carrier jet, (30 ms^{-1}) and with temperature of 231 K, a temperature below the boiling point of propane at ambient pressure. The total mass flow is defined as $1 \times 10^{-6} \text{ kg/s}$ for each of the 25 streams. Experimentally the mass flow rate was measured at 0.75 g/s however this lower mass flow was chosen as higher values resulted in unphysical temperatures. This is not fully representative of the size distribution or droplet components but is simulated to demonstrate the effects of droplet evaporation on the temperature field.

The influence of droplet evaporation on the centreline temperature along with the experimental temperature measurements for aerosol cans 1A and 1D are plotted in Figure 5.11. Including droplet evaporation and therefore an additional contribution to the energy/temperature of the carrier jet results in a delayed warm up of the carrier jet. This additional cooling results in closer agreement to the experimental data. The initial temperature condition case of $T=231 \text{ K}$ gives closer agreement to the temperature plots where a lower temperature was measured. This is a consequence of not resolving the inner nozzle flows and achieving an accurate source term for the different releases. The results do show that good agreement can still be found with limited information but fully representative sizes and multi-component droplets would be more representative of sprays generated from deodorant-type aerosol cans.

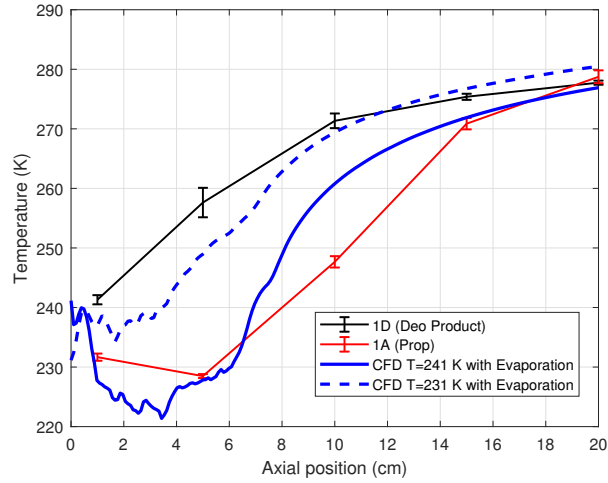


Figure 5.11: Centreline temperature predicted by the axisymmetric CFD models with initial jet temperature of $T=241$ K and $T=231$ K with the inclusion of propane droplet vaporisation, compared to the the measured centreline temperature for aerosol cans 1D (Deo) and 1A (Prop).

5.3 Capture Efficiency and Carry-Over

In this section the axisymmetric carrier jet model coupled with the droplet model are used to investigate the efficiency of deodorant-type sprays on curved surfaces. A parameterised impingement surface is introduced into the axisymmetric spray model and used to determine the capture efficiency (E), where a ratio of impinged droplets (N_{Imp}) to injected droplets (N) is used,

$$E = \frac{N_{Imp}}{N}. \quad (5.24)$$

When the capture efficiency is equal to 0, no droplets have impinged the surface, whereas a capture efficiency of 1 equates to all of the droplets impinging onto the surface. The droplet fraction which carries-over (C) from the target surface can be calculated as $C = 1 - E$. This number is of interest as it gives insight into the number of droplets which can then be inhaled and cause respiratory discomfort. When a large capture efficiency is predicted, a lower carry-over of droplets is present.

First sensitivity studies are performed to understand droplet count and

mesh influence on the capture efficiency predictions. A study on the influence of standoff distance and surface shape on the capture efficiency of these sprays is then performed and the results are presented.

5.3.1 Design Of Experiments

A curved impingement surface is generated and positioned at a standoff distance (D) away from the nozzle. The impingement surface is built to represent an axilla/underarm like surface. The curved surface is parameterised by a radius of curvature (R) and surface height (H). Here a high value for the radius of curvature represents a raised arm and a lower value represents an arm which is not raised as much. The surface height provides an adjustable parameter to the surface area of the underarm. A schematic of the geometry is given in Figure 5.12 showing the curved surface, its defined parameters and the boundaries of the domain. For a given radius of curvature (R) and surface height (H) the necessary angle (θ) from the axisymmetric centreline to the edge of the curved surface is given by

$$\theta = \tan^{-1} \left(\frac{H}{R} \right), \quad (5.25)$$

and is used to automatically adjust the geometry generation to the prescribed parameters.

The values of standoff distance and surface height are limited to a range intended to be representative of reality. The axilla size has been shown to vary between genders and within genders (Cowan-Ellsberry et al., 2008). The median axilla surface area for male and female participants was measured as 135.5 cm² and 64.5 cm² respectively by Cowan-Ellsberry et al. (2008). Taking this, and assuming a circular cross section, the range of radius can be approximated as 4-7 cm which gives us an approximation for our axilla size. For standoff distance personal care product manufactures recommend a standoff distance of approximately 15 cm. It is assumed

regression (Rasmussen and Williams, 2005), support vector machines (Kaya, 2019) and neural networks (Pedro Souza de Oliveira et al., 2022). The response surface surrogate modelling approach was selected because the design space only consists of two design variables and it is therefore assumed that a more complicated approach is not necessary to represent the design space.

A design of experiments (DoE) provides a tool to efficiently select a limited amount of simulations in order to cover the design space of interest. Here the parameters which constitute the design space are the axilla size (H), the standoff distance (D) with a fixed axilla radius of curvature of 7.5 cm. Due to limited data on underarm curvature a value of 7.5 cm is chosen to provide a surface with sufficient curvature and is also larger than the maximum axilla size studied, 7 cm.

The design of experiments procedure is able to provide n design points within the design space. Typically, the minimum number of design points should be at least 10 for each design variable (Harrell, 2001). However, due to restrictions in computational cost, a total count of 10 design points is generated which is noted to be below the recommended minimum. In order to achieve reasonably good coverage over the design space the latin hypercube algorithm is used to generate the 10 design points. Here each of the variable ranges are divided into 10 equal intervals. Then a point is sampled from each of the 10 intervals. This is performed 100 times and to achieve good coverage of the design space the minimum of the distance between design points is maximised. The chosen set of design points can be seen in Figure 5.13.

For each of the design points (H,D), monodisperse propane droplets of size 10 μm , 15 μm , 20 μm and 25 μm are initialised at the nozzle exit using the propane material property defined in Section 5.2. The initial droplet positions span the nozzle orifice linearly between $y=0$ mm to $y=0.25$ mm. The droplets are initialised with the same velocity and temperature as the carrier jet, 30 ms^{-1} and 231 K. Further simulations are performed where 1000 droplet diameters are sampled from the log-

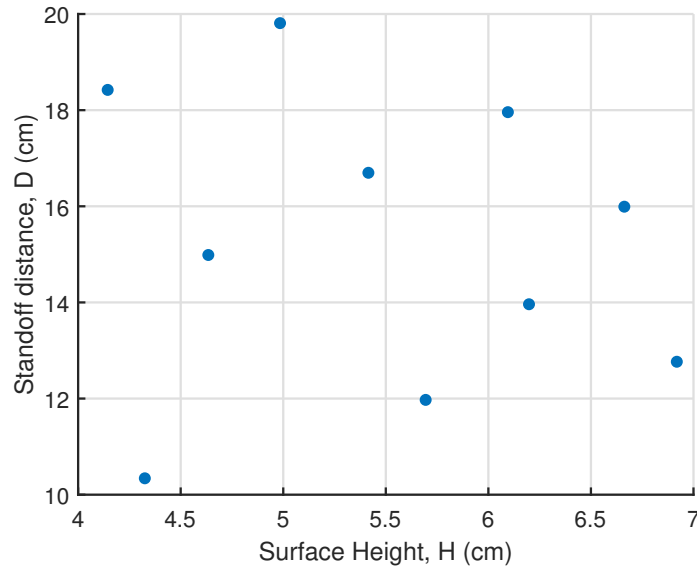


Figure 5.13: The design space coverage for surface height (H) and standoff distance (D) resulting from a design of experiments.

normal PSD of aerosol can 1D (full product). Here two simulations are run, one with droplets initialised at initial position $y=0$ mm and the other where the droplets are initialised at $y=0.25$ mm. This is determine the effect of initial droplet position on the capture efficiency. For all of these simulations the droplets are not considered to evaporate, keeping a fixed size which is similar to the PSD observed for aerosol can 1D. A conservative approach for droplet impingement is used where droplets which come into contact with the surface are considered to stick to the surface. First a mesh sensitivity is performed and is described in the following section.

5.3.3 Mesh Generation and Sensitivity

The mesh is constructed within ANSYS meshing following a similar approach detailed in Chapter 4, Section 4.4.2 for the free axisymmetric propane jet. In this section the detail of the mesh used for the new domain with an impingement surface is described. Due to the presence of the impingement surface another mesh sensitivity study is performed and the results of the study are detailed here. A schematic of the domain showing the mesh zones is given in Figure 5.14. To resolve the near

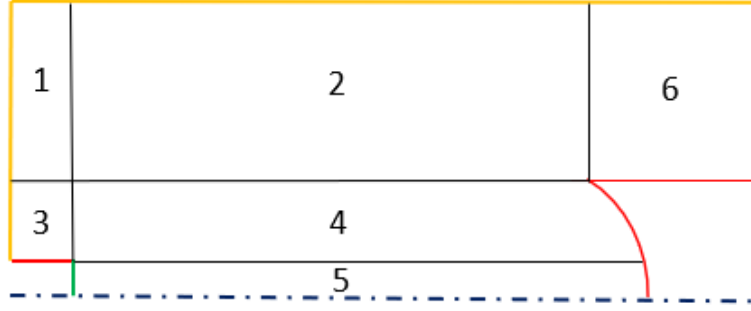


Figure 5.14: Mesh zones

	Edge Sizings (mm)		
	Coarse	Medium	Fine
1V	1	1	0.5
1H	1	0.5	0.2
2V	1	1	1
2H	0.5	0.5	0.5
3V	0.5	0.25	0.1
3H	0.5	0.5	0.2
4V	0.5	0.25	0.1
4H	0.5	0.15	0.1
5V	0.075	0.05	0.025
5H	0.2	0.15	0.1
6V	0.5	0.5	0.5
6H	1	0.5	0.5

Table 5.3: Horizontal and vertical edge sizings (mm) for the six mesh zones for the coarse, medium and fine mesh.

wall flow the enhanced wall-treatment method is used.

Three meshes are constructed for the sensitivity study. Due to the varying standoff distance and surface height, biases are not used but element sizes are prescribed on each of the surfaces to avoid unwanted cell skewness. The horizontal and vertical edge sizings for each of the zones for the coarse, medium and fine mesh can be found in Table 5.3.

Sensitivity

The presence of the impingement surface changes the flow structure and therefore another sensitivity study is performed. The meshing zones and a close-

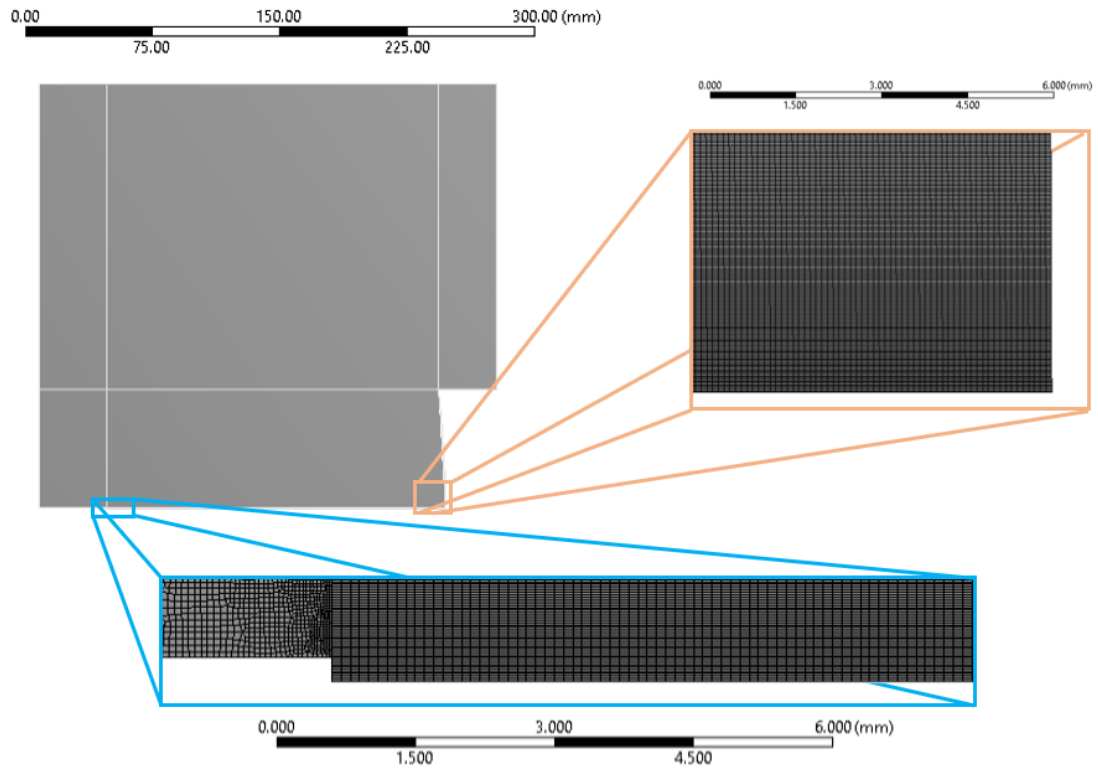


Figure 5.15: Schematic of the geometry split into mesh zones, and a zoom in of the mesh near the nozzle region and near the curved impingement surface for the fine mesh.

up of the mesh near to the nozzle and impingement surface are given in Figure 5.15 for the fine mesh. In the near nozzle region the mesh is refined to achieve acceptable resolution of the jet release. Close to the impingement surface a fine mesh is needed in order to resolve the boundary layer close to the wall, which will impact the velocities the droplets close to the wall experience.

Droplet Count Sensitivity

To determine the number of droplets needed to achieve a constant capture efficiency 15 μm droplets are injected, with the total number injected (N) varying from 10 to 20000. Figure 5.16 shows that the capture efficiency asymptotes to an efficiency of 85% which is first achieved at approximately 200 droplets.

Fluctuations of the efficiency measure are due to the stochastic nature of the DRW turbulent dispersion model as well as changes in initial droplet location

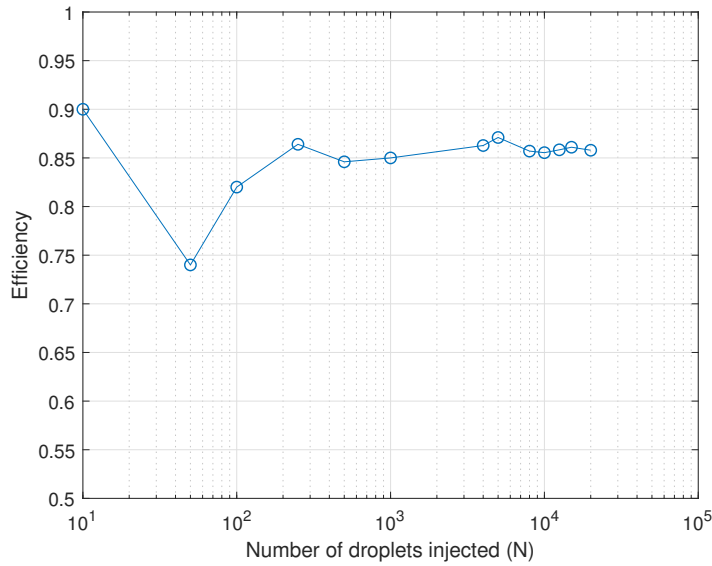


Figure 5.16: For droplets of size $15 \mu\text{m}$ the droplet efficiency is measured against the total number of droplets injected into the domain (N).

and the resultant droplet trajectories. Note that the DRW has been shown to give over predictions of deposition due to the isotropic nature of the turbulent velocity prescribed [Parker et al. \(2008\)](#).

Mesh Sensitivity

CFD results are sensitive to the quality of the mesh as described previously. To provide evidence of mesh independence, sensitivity analysis is performed on the bounds of the DoE but including variation in radius of curvature. It is assumed that if the bounds are found to be mesh independent then we can assume that same meshing strategy will also be mesh independent for the values within that range. For the first sensitivity study $R = 7.5 \text{ cm}$, $H = 4 \text{ cm}$ and $D = 10 \text{ cm}$ and for the second sensitivity $R = 600 \text{ cm}$, $H = 7 \text{ cm}$ and $D = 20 \text{ cm}$. Note the increase in radius of curvature from 7.5 cm to 600 cm results in a flatter surface.

This work was undertaken on ARC4, part of the High Performance Computing facilities at the University of Leeds, UK. The simulations were run in parallel using 40 computational cores which may be distributed across multiple nodes depending on availability at the time. Information on total cell count and simulation

		Cell count	CPU time	Wall-clock	Iterations	Iteration/s	Time to converge
R75	Coarse	120000	270:33:10	06:48:32	70000	4.30	04:31:04
	Medium	200000	210:06:48	05:17:40	90000	5.54	04:31:00
	Fine	540000	285:39:27	07:11:51	105500	4.07	07:11:51
R600	Coarse	323000	174:02:48	04:23:28	90000	6.67	03:44:45
	Medium	610000	271:08:14	06:50:04	70000	4.29	04:32:05
	Fine	1600000	954:06:46	23:59:59	168000	1.94	23:59:59

Table 5.4: Information on simulation time for the coarse medium and fine mesh for both the curved surface cases.

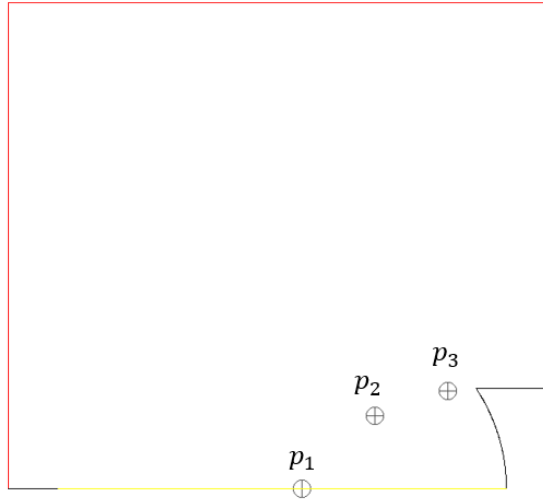


Figure 5.17: Monitor point locations (crosshairs) within the axisymmetric impingement simulation domain.

time for the different meshes is given in Table 5.4. For the $R = 7.5$ cm case the fine mesh performs iterations at a faster rate relative to the coarse mesh, and is able to perform approximately 1.5 times the number of iterations in a similar wall-clock time. The parallelisation of ANSYS Fluent onto HPC clusters is not trivial, and the distribution of cores across nodes can limit communication between the cores, resulting in different simulation times for the same case.

For all simulations three monitor points are positioned within the flow and used to aid in determining convergence. One is placed within the jet region (p_1) with the other two outside the jet region (p_2 , p_3). These can be seen in Figure 5.17. A surface monitor is also used on the impingement surface to measure the total pressure. To ensure convergence the simulation is ran until all residuals reach an order $\mathcal{O}(10^{-6})$ and the monitor points asymptote.

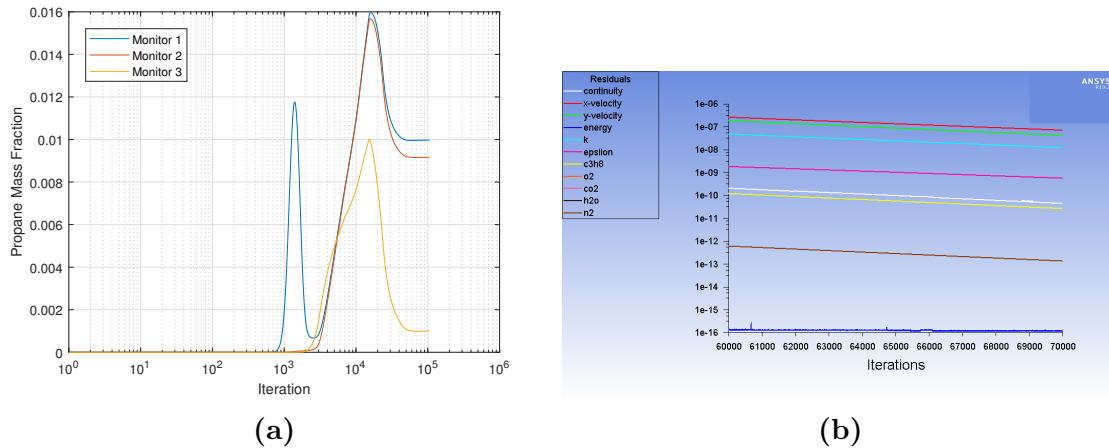


Figure 5.18: (a) Propane mass fraction at the monitor point locations plotted against log scale of iteration number, (b) Residual levels from iterations 60000-70000.

The mass fraction measured at the three monitor points, as well as simulation residuals, can be seen in Figure 5.18. The levelling off of the monitor points as well as acceptable tolerance levels of residuals provides confidence that the simulations have converged. For sensitivity study 1, qualitatively there is good agreement with the velocity contours and mass fraction contours between the 3 meshes. This can be seen in Figure 5.19 and 5.20 respectively.

The velocity contours in Figure 5.19 have an upper bound limited to 1 m/s, which makes contour visualisation of the velocity decay from the initial condition difficult using a linear scale and so log scaling of the contours is used. The entrainment of the ambient is visible close to the nozzle, with the region of increased velocity relative to the quiescent ambient. Figure 5.19 also shows the stagnation point at the centre of the surface where the impingement occurs. Due to the axisymmetric assumption and absence of gravity influence, the buoyancy due to temperature differences of the jet is not modelled here, however, the momentum of the jet will dominate over buoyancy effects as seen in the observations from the schlieren experiments detailed in Chapter 3. The horizontal momentum is transferred to radial momentum after impingement and generates a jet after leaving the surface.

The mesh sensitivity results, seen in Figure 5.21, show that capture ef-

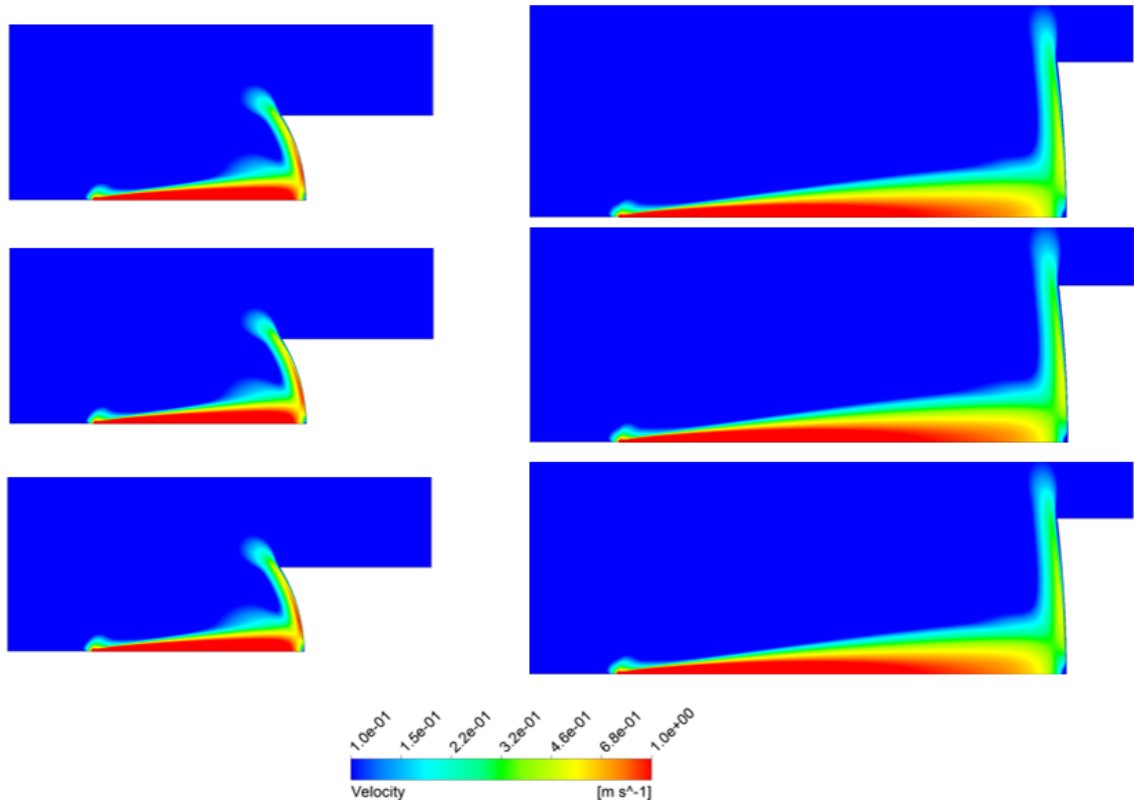


Figure 5.19: Velocity contours with log scaling for the, top to bottom: Coarse, Medium and Fine mesh for left: $R=7.5$ cm case and right: $R=600$ cm case.

efficiency is influenced by mesh size, with droplet size influencing this sensitivity. Despite this the influence is not that significant and therefore the model is assumed to be capturing the physics at work. The capture efficiency measure follows a tanh-like function, with the independent variable being droplet size. Across the span of droplet sizes the capture efficiency ranges from 0 to 1 and is dependent on geometrical properties.

The simulation time was of similar order across the three meshes. Good agreement for the velocity and mass fraction contours was achieved and there appears to be some sensitivity for the capture efficiency when the fine mesh is used. This is to ensure adequate resolution of the near-wall flow and to maintain a y^+ within the range of 1-5 near the curved impingement surface which is needed for use of enhanced wall treatment.

The contours of propane mass fraction shown in Figure 5.20 again identify

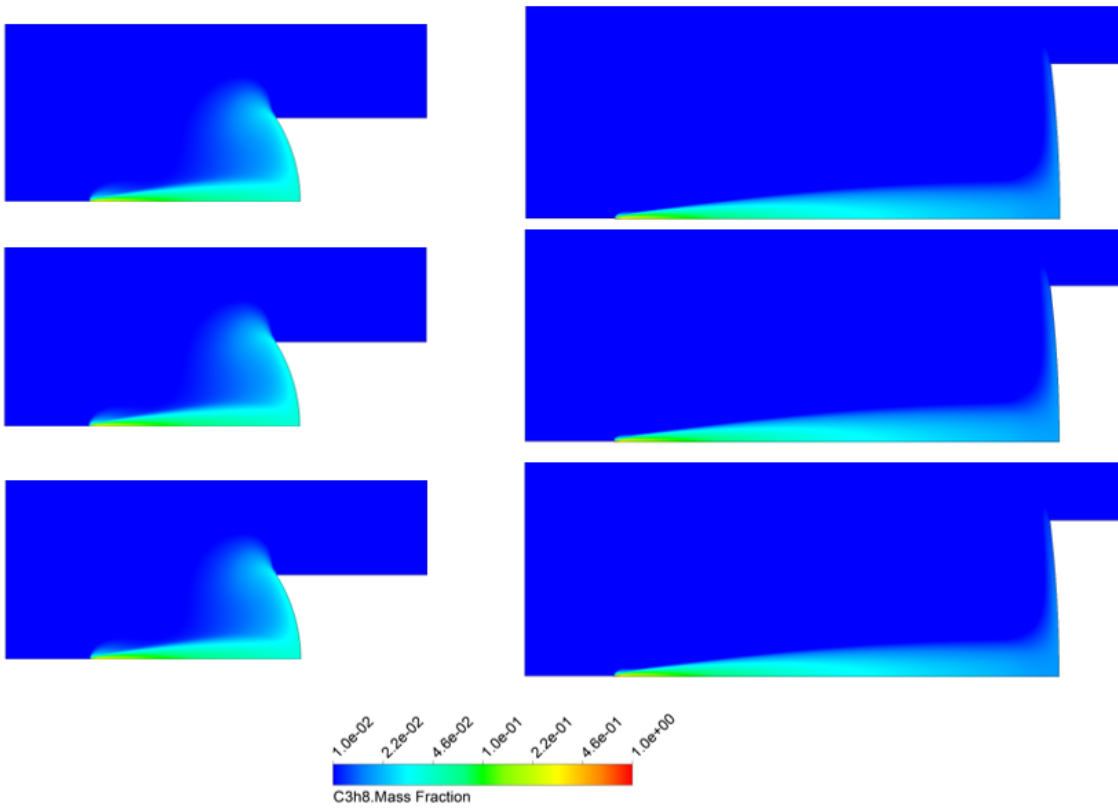


Figure 5.20: Propane mass fraction contours with log scaling for the, top to bottom: Coarse, Medium and Fine mesh for left: R=7.5 cm case and right: R=600cm case.

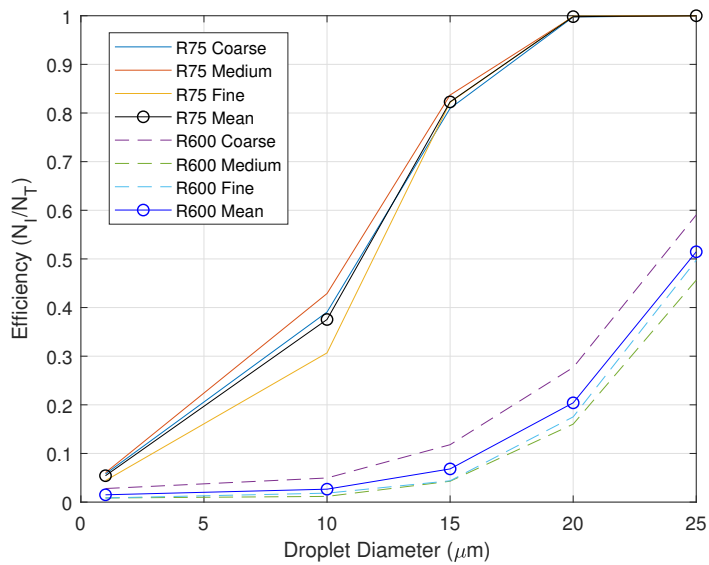


Figure 5.21: Mesh sensitivity of capture efficiency for the coarse, medium and fine mesh for both cases where R=7.5 cm and R=600 cm.

the strong jet region. The propane mass fraction field is dominated by the jet. The recirculation region, which occurs due to re-entrainment of the surface jet back into the main carrier jet, results in a region of high propane mass fraction between them.

5.3.4 Results

The capture efficiency is measured for each of the monodisperse sizes injected as well as the polydisperse sampled distribution from aerosol can 1D. A response surface is then fit to the design points and predicted capture efficiency. This is achieved by using MATLAB's `fit` function to fit a cubic polynomial (`poly23`) to the measured capture efficiencies. The polynomial is given by

$$f(H, D) = p_{00} + p_{10}H + p_{01}D + p_{20}H^2 + p_{11}HD + p_{02}D^2 + p_{21}H^2D + p_{12}HD^2 + p_{03}D^3, \quad (5.26)$$

where p_{ij} are the coefficients for corresponding terms H^iD^j . The coefficients found from fitting the response surface can be found in Table 5.5. Note the response surfaces do not capture physical processes and are merely a fit to the data.

	Monodisperse				Polydisperse	
	10 μm	15 μm	20 μm	25 μm	Centre	Edge
p00	1.84	1.592	0.9663	0.5483	-1.06	-8.47
p10	-0.1173	-0.118	-0.1383	-0.1123	1.41	4.188
p01	-0.1551	-0.06961	0.07858	0.1486	-0.06944	0.457
p20	-0.00665	0.003688	0.01156	0.0109	-0.06813	-0.1626
p11	0.03008	0.01821	0.01016	0.003285	-0.1412	-0.4431
p02	0.002078	-0.00144	-0.00877	-0.01066	0.02673	0.03824
p21	-7.38E-05	-0.00078	-0.00117	-0.00083	0.004726	0.01165
p12	-0.00076	-6.52E-05	0.000364	0.000408	0.003081	0.01088
p03	4.91E-05	3.78E-05	0.000125	0.000146	-0.0009	-0.00198

Table 5.5: Cubic equation coefficients p_{ij} for the capture efficiency response surfaces predicted for monodisperse droplet sizes and polydisperse droplet sizes initialised at the centre or at the edge of the carrier jet.

The resultant response surfaces for the monodisperse sizes of 10 μm , 15

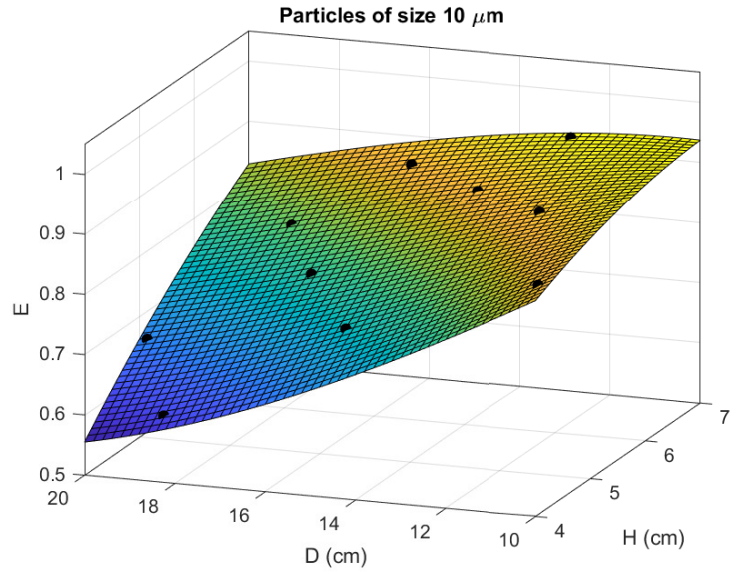
μm , $20 \mu\text{m}$ and $25 \mu\text{m}$ are given in Figure 5.22. Note for these cases that the efficiency (E) is plotted from 0.5 to 1, equating to a 50% and 100% capture efficiency respectively. The $10 \mu\text{m}$ droplets never appear to reach a capture efficiency of 1 with the surface beginning to level off at the extreme of $D=10 \text{ cm}$ and $H=7 \text{ cm}$. The maximum capture efficiency is expected at this extreme of the domain as it represents the smallest standoff distance and largest surface height. The other extreme of the domain, $D=20 \text{ cm}$ and $H=4 \text{ cm}$, gives the case where the nozzle is the greatest distance away from the impingement surface and also the smallest height of the surface. The extremes are termed “best” and “worst” respectively due to the largest and smallest capture efficiency achieved, where the aim is to deposit as much of the product as possible. Where capture efficiency is lowest determines where an increased carry-over of droplets occurs.

The reduction in capture efficiency is due to a smaller carrier jet velocity and therefore a smaller droplet velocity as the droplet approaches the wall. This small velocity allows the droplets to be able to react to the change in flow due to the presence of the surface. This can be captured by looking at the ratio of particle relaxation time t_0 to a representative flow time U/l , and is known as the Stokes number,

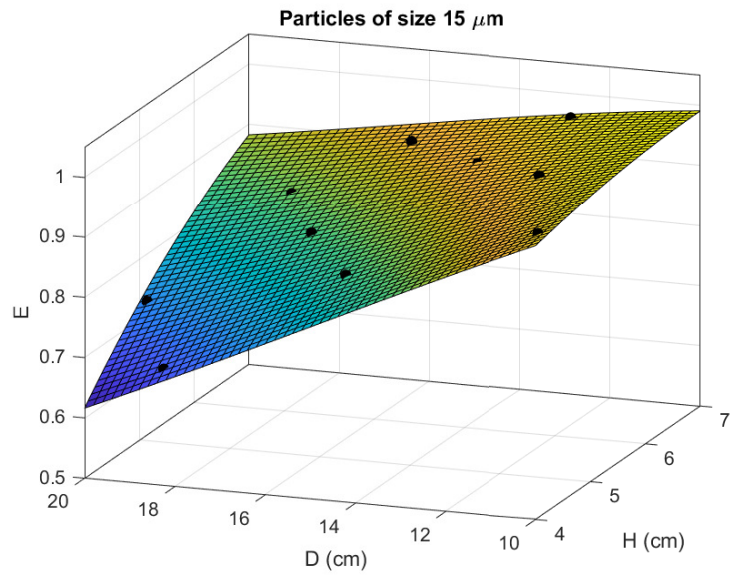
$$\text{St} = \frac{t_0 U}{l}, \quad \text{with} \quad t_0 = \frac{\rho_d d_d^2}{18\mu}. \quad (5.27)$$

For $\text{St} < 1$ the droplet will act as a tracer for the flow and for $\text{St} > 1$ the droplet will detach from the streamline and potentially impinge onto the target surface.

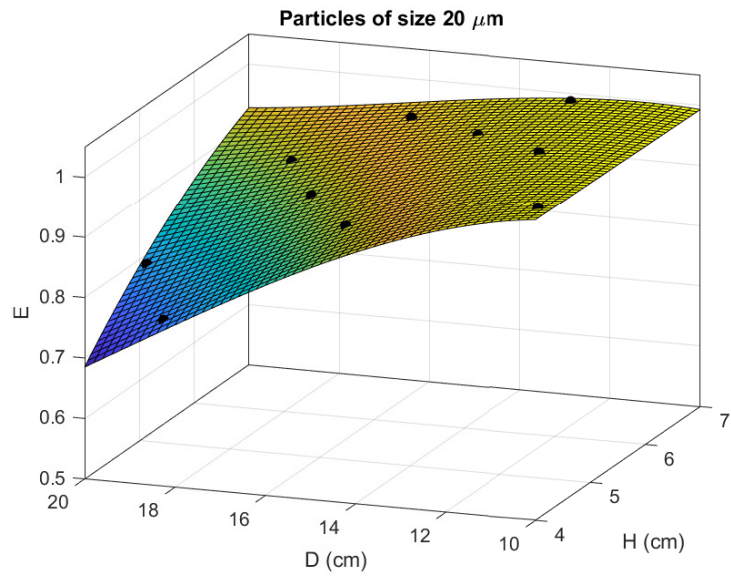
The flow length scale is taken as the height of the surface, $l = H$ and the flow velocity taken as a representative jet velocity. As the droplet diameter increases the droplet relaxation time increases, resulting in an increase in Stokes number and therefore a higher probability of impingement. As surface height increases the Stokes number again increases, resulting in an increase in impingement probability. As the standoff distance increases the jet velocity will be lower at the same relative position, resulting in a decrease in Stokes number and therefore a reduction in the probability



(a)



(b)



(c)

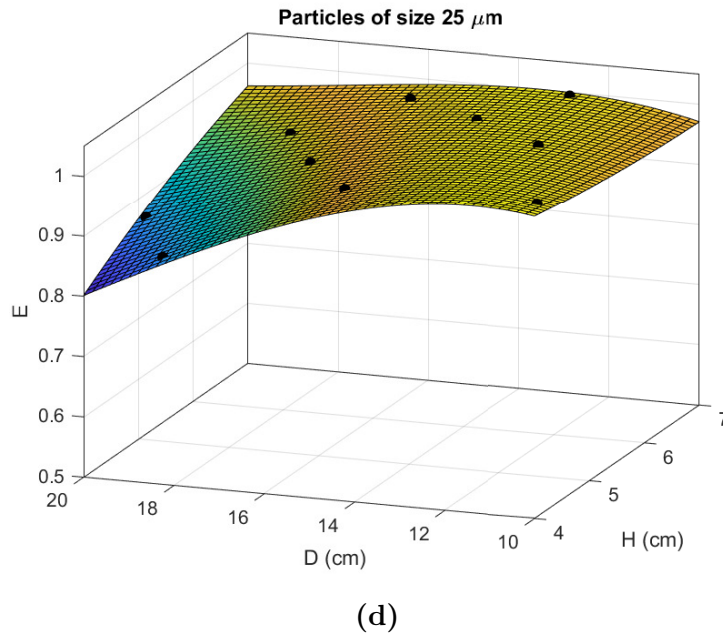
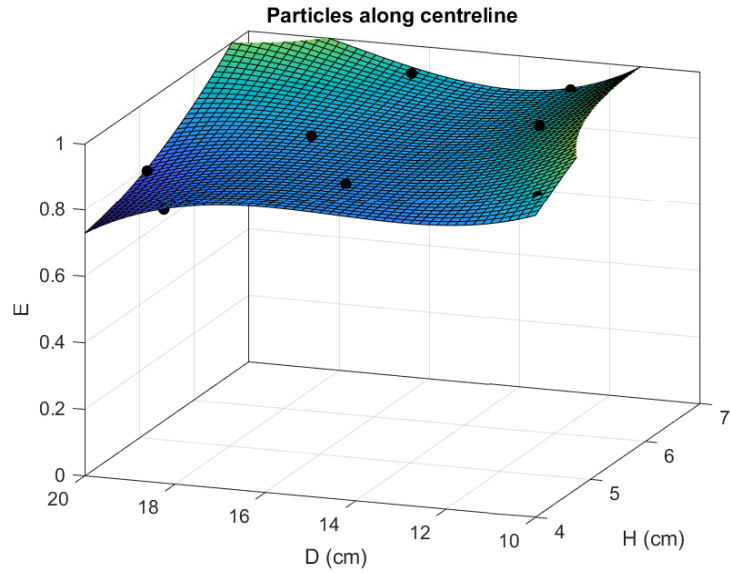


Figure 5.22: Response surfaces of capture efficiency (E) from varying the standoff distance (D) and surface height (H) for a surface with radius of curvature 75 mm generated for monodisperse sizes of (a) 10 μm , (b) 15 μm , (c) 20 μm and (d) 25 μm .

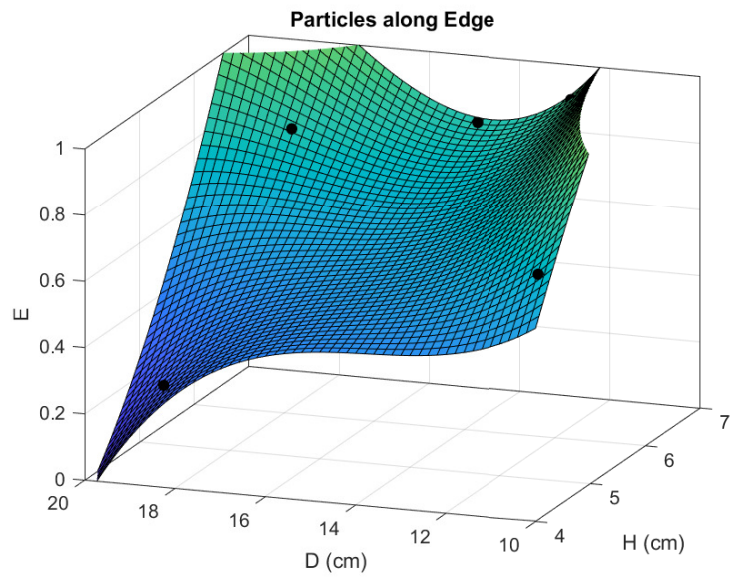
of droplet impingement.

At the worst extreme, the capture efficiency increases with increase in particle size as shown in Figure 5.22. The capture efficiency increases from 55% to 80% when the particle size changes from 10 μm to 25 μm . For a fixed surface height, decreasing the standoff distance results in an increase in capture efficiency for sizes 10 μm , 15 μm and 20 μm and all surface heights. Similarly, for a fixed standoff distance, increasing the impingement surface height results in an increase of capture efficiency.

The 25 μm response surface exhibits overturning near the best extreme, resulting in a reduction in the predicted capture efficiency. There are no limiting features preventing the response surface going above an unphysical capture efficiency of 1, therefore where values exceed 1, they are treated as a value of 1. The response surface has not been validated, but the shape of the surface in general appears to fit what is expected. To obtain an improved fit further design points should be generated, in particular at the extremes.



(a)



(b)

Figure 5.23: Response surfaces of capture efficiency (E) from varying the standoff distance (D) and surface height (H) for a surface with radius of curvature 75 mm generated for (a) droplets injected along the centreline, $y=0$ mm (b) injected at the nozzle edge, $y=0.25$ mm.

The polydisperse response surface fits can be seen in Figure 5.23. Note here the capture efficiency is plotted from 0 to 1. When droplets are initialised along the centreline a higher capture efficiency is seen relative to the droplets initialised at the edge of the spray. This is because the droplets initialised at the centre of the jet are within a high velocity carrier flow and approach the impingement surface with a continuing high velocity. When the droplets are initialised at the edge of the spray, however, they approach the impingement surface along the lower velocity region at the edge of the spray with some droplets entrained into the centre of the carrier jet.

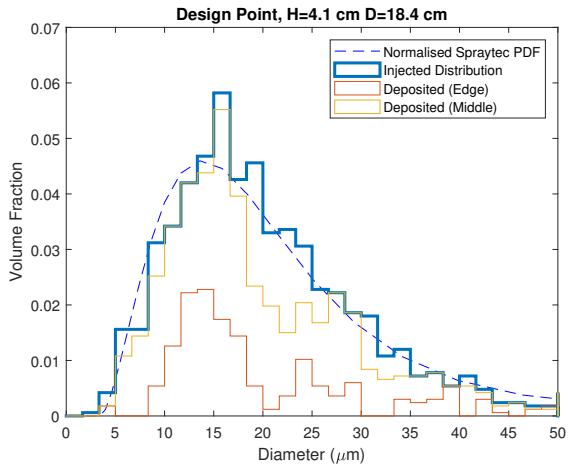
The shape of the response surface is similar but there appears to be a scaling factor which decreases as the design point approaches the worst case. The true value of the capture efficiency for the case of droplets initialised across the entire nozzle surface is predicted to be a value between the two cases. The response fit for this case also shows sensitivity to the number of design points used. Here 10 design points were used to generate the response surface, below the recommended minimum of 10 times the number of design variables. It would be beneficial to simulate additional design points to achieve coverage in the regions of steep gradients and at the extreme points of the design space.

Based on the response surfaces, the worst scenario for the polydisperse cases is still located at $D=20$ cm and $H=4$ cm. However, the best scenario for capture efficiency is predicted to occur at two locations, where $D=10$ cm and $H=7$ cm or where $D=20$ cm and $H=7$ cm. The capture efficiency is predicted to dip between these points, whereas previously it was found, for the monodisperse case, that the capture efficiency would monotonically decrease for an increase in standoff distance. This is likely due to count sensitivity for the design point case located near the region of the design space with $D=20$ cm and $H=7$ cm.

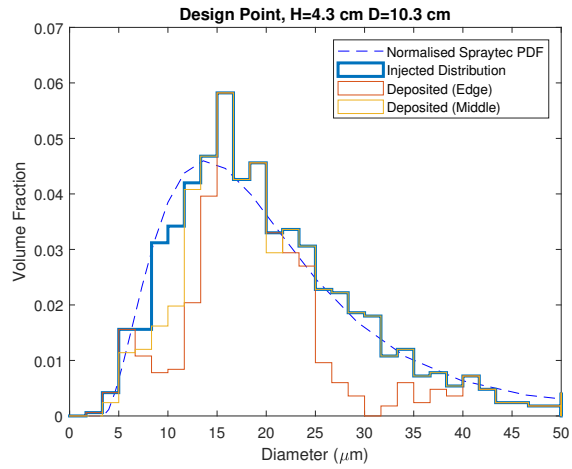
To understand the capture efficiency for the different droplet sizes throughout the distribution, the injected PSD is plotted along with the deposited droplet distribution for both the centreline and edge initialisation cases, shown in Figure

5.24. For most size bins, and nearly all cases, the fraction that deposits is greater when the droplets are initialised at the centreline rather than the edge. However there are still several size bins within cases where this does not hold, and the depositing fraction is predicted to be greater when initialised at the edge than at the centreline. This could be due to the flow of that particular case strongly entraining the droplets into the centre of the jet, or it could again be due to a limited number of droplets necessary to accurately predict the capture efficiency of that droplet size and therefore statistical. Further study on droplet sensitivity with respect to capture efficiency is needed.

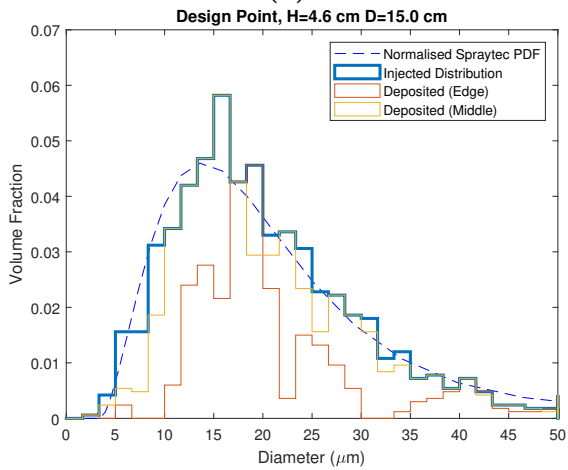
The fraction of large droplets nearly always deposit regardless of their initialisation. For the design point cases with a small surface height and large standoff distance, the centreline deposition is significantly larger than the edge case deposition. For cases with a large surface height and small standoff distance the deposition fractions for the different droplet sizes is comparable.



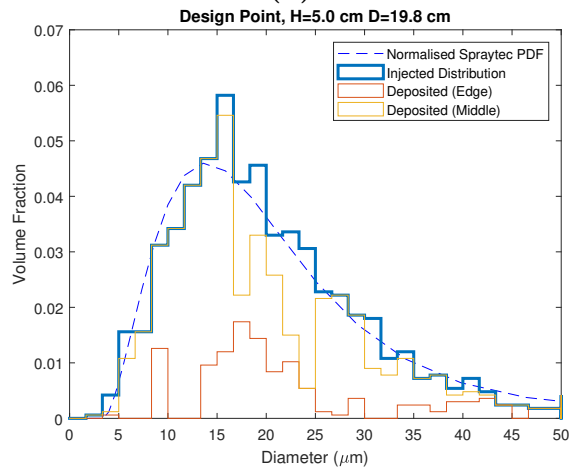
(a)



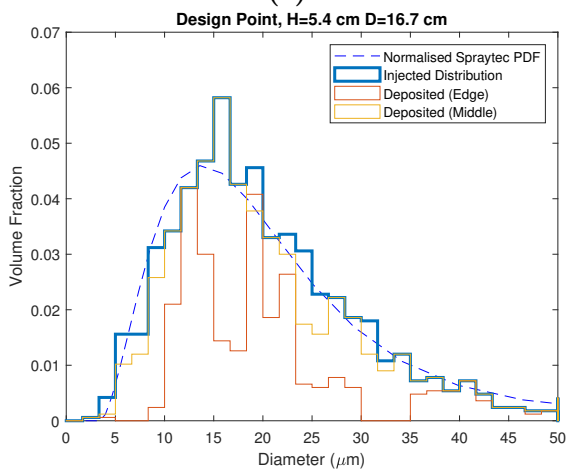
(b)



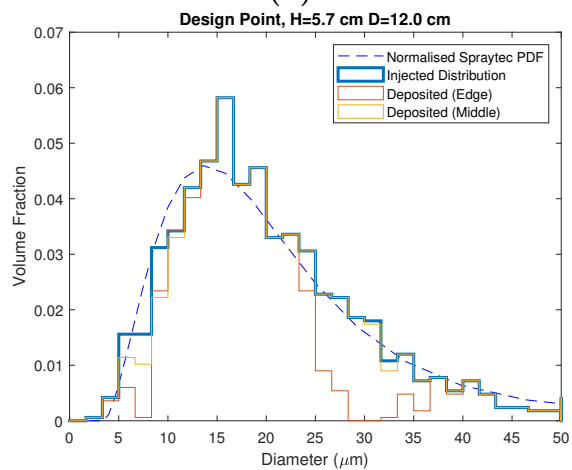
(c)



(d)



(e)



(f)

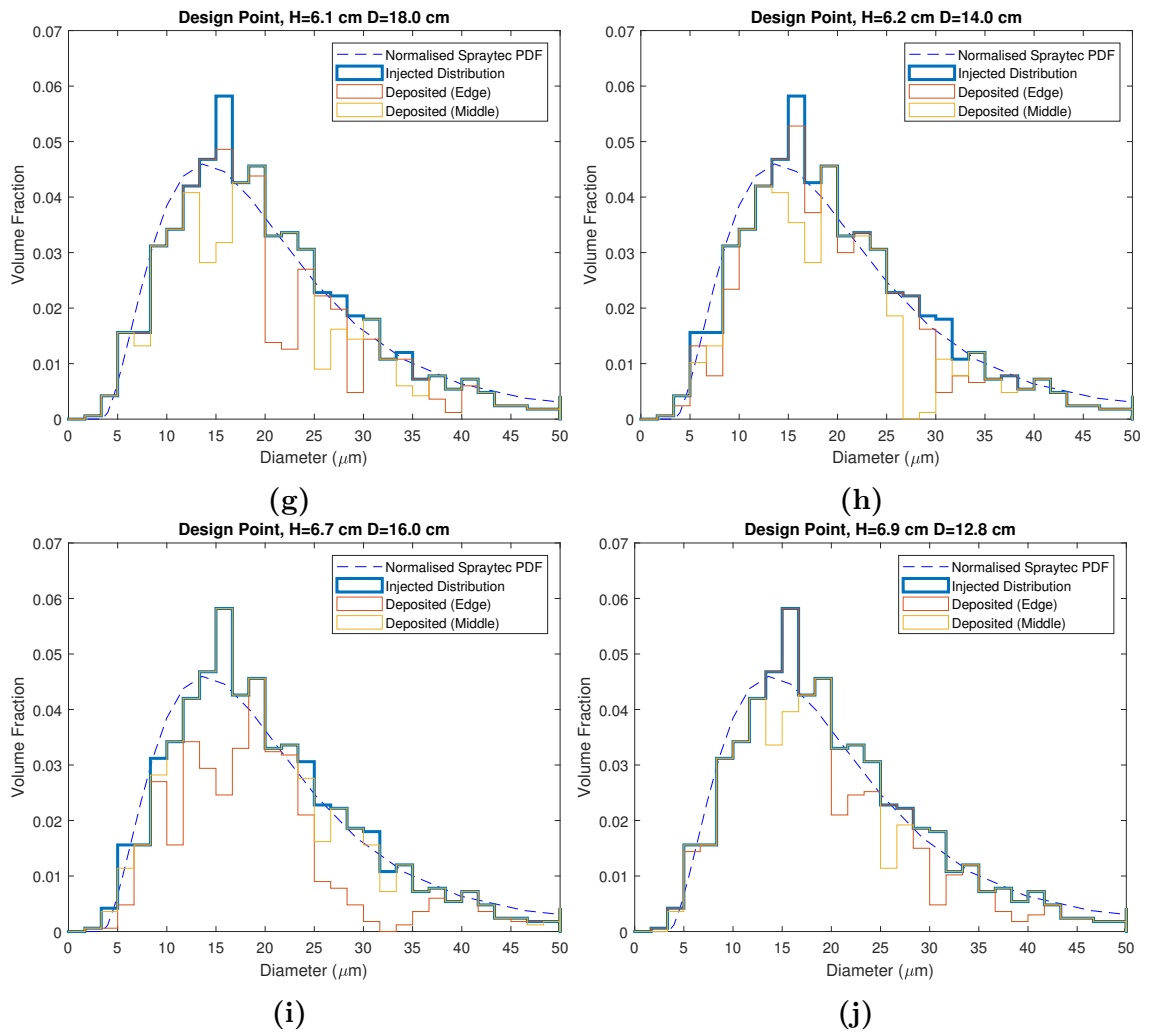


Figure 5.24: Injected particle size distribution for both the edge and centreline injections for design points (H,D) cm (a) (4.1,18.4) cm, (b) (4.3, 10.3) cm, (c) (4.6,15) cm, (d) (5,19.8) cm, (e) (5.4,16.7) cm, (f) (5.7,12) cm, (g) (6.7,16) cm, (h) (6.2,14) cm (i) (6.7,16) cm and (j) (6.9, 12.8) cm.

5.4 Summary

This chapter detailed the study of ambient effects on droplet dynamics including droplet transport and on droplet evaporation. A MATLAB implementation of the governing system of equations for droplet momentum, mass and heat transfer was detailed and the implementation was verified against the d^2 law and the wet bulb temperature for a given ambient temperature and relative humidity. The model was then used for water droplets and showed that warmer ambient conditions result in greater droplet evaporation rates and an increase in relative humidity, or ambient saturation fraction of the evaporating species, results in a lower droplet evaporation rate.

This model was then used for propane droplets. The evaporation of a 12 μm propane droplet compared to the same size of a water droplet was predicted to evaporate nearly two orders of magnitude faster. The impact of ambient saturation on the droplet temperature was investigated and showed that when a propane droplet is in an ambient of temperature 231 K, and with an ambient propane vapour saturation fraction less than 100%, that the droplet evaporation causes the droplet temperature to go lower than propane's atmospheric boiling point. Therefore, this should be considered when modelling alkane based aerosol cans.

The droplet evaporation was modelled within Fluent, coupling droplet transport and evaporation with the carrier jet model discussed in Chapter 4. Propane droplets were initialised at the nozzle exit and transported through the spray. The cooling of the jet was captured through the spray region. The predicted temperature along the centreline of the carrier jet showed good agreement with the temperature decay found experimentally in Chapter 3. This demonstrated that an axisymmetric carrier jet model, coupled with a discrete droplet phase, is able to accurately predict jet properties downstream from the nozzle.

The model was then used to investigate the effects of varying standoff distance and curved surface height (axilla size) on the capture efficiency or equivalently the fraction that does not carry-over from the impingement surface. A design of experiments was performed to generate 10 design points across the range of standoff distances and axilla sizes. A droplet count and mesh sensitivity were performed to determine the number of droplets needed to obtain a constant capture efficiency and to show that the computational mesh was adequately resolved to not impact the model predictions. The sensitivity study showed mesh independence but also showed that a flat surface results in a considerably lower capture efficiency relative to a curved surface. Therefore the shape of the surface also influences carry-over and capture efficiency, similar to the work of [Marple and Willeke \(1976\)](#), which showed that rectangular and circular impactor surfaces result in different efficiencies.

Non-evaporating monodisperse propane droplets, of sizes 10 μm , 15 μm , 20 μm and 25 μm were initialised across the nozzle orifice for the design points generated from the design of experiments with respect to a curved surface with a radius of curvature equal to 7.5 cm. The capture efficiency was measured for each of the design points and response surfaces were fit that determine the capture efficiency for a given standoff distance and surface height. The results showed that reducing the standoff distance (spraying closer to the surface) increased the capture efficiency, and that having a larger axilla also resulted in a greater capture efficiency.

Particle sizes were sampled from a log-normal fit of the particle size distribution measured experimentally in Chapter 3. The sizes were initialised at the centre of the nozzle and at the edge of the spray to determine initial location influence on capture efficiency. Droplets generated at the edge of the spray had a greater tendency to carry-over from the target surface whereas ones initialised at the centre of the spray generally achieved a greater capture efficiency. The results appeared to show sensitivity to the number of design points and insufficient droplet count. Further design points could also provide a way of validating the response surface

predictions.

With respect to capture efficiency of deodorant-type aerosol cans, the results appear to recommend spraying as close as possible to achieve the best capture efficiency, however, personal comfort (temperature, wetness), which is a key factor, is not considered in this model. The experimental temperature work showed that the deodorant-type sprays are capable of reaching temperatures as cold as -40°C . Such low temperatures are able to cause cryogenic burns (Camp et al., 2003) and care is needed when considering optimal spray standoff distances for alkane propellant based formulations.

This work assumed that if a droplet impinges onto the target surface then it would stick to it. This is a significant assumption and an area for future work. Nevertheless, the work provides a framework for such studies and allows comparative analysis. Further study is needed to understand the properties of the product propellant mix in order to determine the adhesion of the droplets onto the target surface and the potential changes in adhesion with the degree of evaporation of the droplet, impacting their overall fate.

Chapter 6

Conclusions and Outlooks

6.1 Summary

In this thesis sprays generated from deodorant-type aerosol cans were both experimentally and numerically investigated. A literature review was first performed to understand the current experimental and numerical methodologies for sprays, which identified that there has been limited work on deodorant-type sprays. The aim of the experimental work was then to generate an experimental data set of the features/properties of sprays generated from deodorant-type aerosol cans. This was achieved in Chapter 3. One aim of the numerical work was to produce a validated CFD model for the gaseous carrier jet, which was achieved in Chapter 4. Droplet transport was then coupled into the carrier jet model along with a curved impingement surface. This was then used to understand the impact of impingement surface topology on potential spray carry-over in Chapter 5. Each of the main pieces of work, from Chapters 3-5 are now summarised, followed by discussion of the successes and limitations of the work, as well as suggestions for future work.

6.1.1 Chapter 3 - Experimental Study of Spray Generation

Spray features from nine different aerosol cans were experimentally investigated. The differences between the nine cans were nozzle type (swirl or simple orifice) and can contents (propellant, propellant+alcohol, propellant+D5, propellant+ACH, full product). The spray features that were measured experimentally were the spray angle, captured with the schlieren technique; the particle size distributions, measured at different axial positions throughout the spray, using laser diffraction (Malvern's Spraytec); and measuring the spray temperature along the spray centreline, measured using thermocouples.

Schlieren

- The schlieren experiments took advantage of high speed photography to capture three distinct spray stages that occur when using a deodorant-type aerosol can. These stages were classified as the spray generation stage, fully-developed stage and collapse stage. During the generation phase a primary vapour release is initially observed, followed by a secondary release of the liquid product propellant mix. This transitions into the fully developed stage, where the spray oscillations at the nozzle are observed due to cavitation effects. Once the actuator is released, the spray collapses, and a low momentum vapour jet is released from the aerosol can nozzle.
- Using imaging processing, specifically edge detection algorithms, the spray angle for the different formulations and nozzles was measured using Image J. Here single frames and a representative mean frame were taken from the fully developed stage of the different nozzle type and formulation of aerosol can. The spray angles produced show a clear dependency on nozzle type, with the swirl nozzle aerosol cans achieving a mean frame spray angle in the range of $19.5 - 22.2^\circ$, and the simple orifice nozzles having a spray angle of $16.3 - 20.3^\circ$.

- The schlieren results demonstrate its ability to distinguish between vapour and product release. Schlieren proves to be a useful tool in understanding sprays generated from deodorant-type aerosol cans, capturing the spray features such as development and spray angle. Schlieren has potential to be used as a development tool to aid in future aerosol can design.

Particle Size Measurements

- Particle size distributions were measured at axial positions 1, 2, 5, 10, 15 and 20 cm for each of the different aerosol cans. Distribution statistics such as the distribution span and $D_{3,2}$ were measured. All of the simple orifice nozzle formulations showed a decreasing trend in $D_{3,2}$ for increasing axial distance, whereas for swirl nozzles, the addition of alcohol resulted in an increase in $D_{3,2}$ for a greater axial distance. This showed that components of the formulation play non-trivial roles in mass transfer of the droplets during their flight and that capturing the multicomponent behaviour of droplet evaporation is important.
- Fitting of Rosin-Rammler, Log-normal and Gamma distribution parameters was performed. The log-normal distribution achieved the best fits across the different formulations and nozzle types. The distributions provide the initial droplet size conditions for the numerical models for deodorant-type sprays and a way of validating the change in particle size distribution through the spray region.
- Laser diffraction measurements provide insight into the axial evolution of the particle size distribution and provides a route of comparing how product components influence the development of the distribution.

Temperature Measurements

- Centreline temperature measurements showed that the temperature of sprays generated from deodorant-type aerosol cans can drop to temperatures of approximately -40°C at an axial distance of 5 cm. Inclusion of additional liquid components resulted in warm up at a shorter axial position relative to the pure propellant formulations and their respective nozzle types. This is because the additional components alter the vapour pressure of the fluid, decreasing the rate of droplet evaporation.
- The high momentum of the release from the simple orifice nozzle results in a prolonged low temperature for a greater axial distance compared to the non pure propellant swirl nozzle formulations. This is because the swirl nozzles have an increased entrainment of the ambient and result in a warm up of the jet occurring at a shorter axial distance of approximately 7 cm relative to the 10 cm for the simple orifice nozzle.

6.1.2 Chapter 4 - Species Transport of a Single Phase Gaseous Jet

The generation of a validated CFD model for a gaseous propane jet was the aim of this chapter. The standard, RNG and realizable $k - \varepsilon$ models as well as the $k - \omega$ and $k - \omega$ SST turbulence models were investigated and compared to experimental data of a gaseous propane jet release. Following that, an axisymmetric model was detailed, which was compared to the experimental results in Chapter 3 and used to investigate the ambient effects on the species field through length of the spray.

- The $k - \omega$ variants performed poorly compared to the $k - \varepsilon$ variants with the main differences due to the sensitivity of the models to initial conditions. The RNG turbulence model predicted a greater momentum decay over the

standard and realizable models. The realizable model was deemed the best performing model due to its robust formulation and good agreement to both the jet velocity and the mass fraction results. The results show that this modelling approach is capable of capturing the physics of a carrier jet to an appropriate accuracy.

- The turbulent Schmidt number was investigated and showed that tuning of this parameter or implementing a variable turbulent Schmidt number could result in better predictions of the CFD model to experimental results.
- An axisymmetric model was constructed and compared to the experimental results. Good agreement was shown between the spray angle model predictions and the spray angle measured experimentally. A pure gaseous jet initialised at the temperatures observed in the experiments results in significant warm-up due to entrainment of warm ambient air. This showed a carrier jet model alone cannot capture the temperature field of the spray.
- Four different ambient conditions were simulated for varying temperature and relative humidity. It was shown that entrainment of warm humid air into the cold carrier jet results in supersaturated conditions, ideal for condensation of water vapour within the spray.

6.1.3 Chapter 5 - Spray Impingement and Droplet Carry-Over

The aim of this chapter was to understand the effects of ambient conditions on droplet evaporation and to couple a discrete phase model with the carrier jet model to investigate capture efficiency on a curved impingement surface was the aim of this chapter. A system of equations for droplet momentum, mass and temperature was numerically solved and the influence of varying droplet size, ambient temperature and ambient vapour saturation on droplet evaporation rate investigated. Response

surfaces were fit to simulation predictions of capture efficiency of monodisperse and polydisperse distributions when standoff distance and surface height were varied.

- For decreasing ambient saturation, a propane droplet was shown to evaporate down to a temperature cooler than the ambient, demonstrating that temperatures colder than propellant boiling points can be achieved and are dependant on the conditions the droplet is subjected to.
- Inclusion of propane droplets into the numerical model showed that their evaporation accounts for the prolonged cooling of the spray region as seen from the experimental temperature measurements. This is because the latent heat of evaporation results in a decrease in droplet temperature. The presence of this evaporating droplet is then accounted for in the source term for the energy equation as the droplet is transported through the carrier jet.
- The monodisperse capture efficiency results showed that larger droplets achieved a greater capture efficiency across the entire range of standoff distance and surface height. It was shown that a smaller standoff distance results in a greater capture efficiency, as does an increase in surface height. Therefore to reduce carryover a smaller standoff distance may be better, however, the comfort of the individual is not accounted for in this model and spraying at such close distances may cause harm due to the cold spray temperatures.
- The polydisperse capture efficiency results showed that the initial position of the droplet may impact the overall capture efficiency measured. In general, droplets initiated at the centre of the carrier jet achieve a greater capture efficiency to those initialised at the edge of the spray.

6.2 Future Work

The experimental results presented here provide an important data set for model validation of deodorant-type sprays but there still remains a gap in experimental data for these spray systems. The current form of the numerical model provides a tool for identifying key model components needed to capture deodorant-type sprays, as demonstrated through this thesis. Extensions to the numerical model are needed to fully represent a deodorant-type spray. Possible further work addressing these issues include:

Experimental

- *Droplet Properties* - The numerical model considered single-component droplets while noting that the droplets generated from deodorant-type aerosol cans are a mix of propellant and product. Measurements which accurately characterise the liquid properties before release and after evaporation should be performed, such as, mass fraction, viscosity and density measurements. The properties are necessary for understanding droplet evaporation rates and also the fate of droplet-wall interaction.
- *Additional Temperature Measurements* - The temperature measurements taken along the centreline of the spray are limited. Additional measurements should be taken at more axial positions for increased resolution of the data and to determine the point of warm up. Further measurements at varied radial distances should also be taken to provide insight into the extent of convection of heat across the spray region.

Numerical

- *Nozzle flow* - Flash atomization and cavitation within the nozzle should be investigated for the different nozzle types. The variable flows alter the dis-

charge coefficient and thus nozzle mass flow rate. Including accurate nozzle inflow conditions that are representative of flows from swirl nozzles and simple orifice nozzles should be investigated.

- *3D and Transient Model* - The current numerical model is a 2D steady-state axisymmetric model. To be able to present accurate geometries for an impingement surface a non-axisymmetric impingement surface should be included. The schlieren results showed that the spray is inherently transient therefore the model should also be extended to capture transient effects on spray generation and the subsequent droplet dynamics.
- *Droplet Deposition* - Currently deposition is assumed to occur if a droplet comes into contact with the impingement surface. Understanding the droplet properties and incorporating an impingement model which accounts for droplet adhesion could greatly influence the capture efficiency measured.
- *Turbulence Modelling* - The two-equation RANS turbulence modelling approach assumes isotropic turbulence which can result in an overprediction of droplet deposition when using the discrete random walk turbulent dispersion model. Anisotropic turbulence models such as the reynolds stress model (RSM) and large eddy simulation (LES) should be investigated to determine the impacts of anisotropy on capture efficiency predictions.
- *Surface Curvature Influence* - The design of experiments investigated the standoff distance and surface height. Investigating variations in surface curvature is necessary as a flatter surface was shown to result in a smaller capture efficiency during the mesh sensitivity study in Chapter 5.

Bibliography

- Abraham, J. (1997). What is Adequate Resolution in the Numerical Computations of Transient Jets? SAE Technical Paper 970051, SAE International, Warrendale, PA.
- AEROBAL (2022). High-grade premium packaging: Aluminium aerosol cans. <http://www.aerobal.org/>.
- Aerosol (2022). European Aerosol Federation (FEA: Federation Europeenne des Aerosols). https://www.aerosol.org/wp-content/uploads/2022/09/2021_FEA_European_Aerosol_Production_final.pdf.
- Ailaboina, A. and Saha, K. (2022). Modeling the spray characteristics of blended fuels for gasoline direct injection applications. *International Journal of Green Energy*, 0(0):1–16. Publisher: Taylor & Francis .eprint: <https://doi.org/10.1080/15435075.2022.2057801>.
- Al-Dirawi, K. H. and Bayly, A. E. (2020). An experimental study of binary collisions of miscible droplets with non-identical viscosities. *Experiments in Fluids*, 61(2):50.
- Allen, J. T. (1999). *Laser-based measurements of two-phase flashing propane jets*. PhD Thesis, University of Sheffield.
- Almohammed, N. and Breuer, M. (2019). Towards a deterministic composite collision outcome model for surface-tension dominated droplets. *International Journal of Multiphase Flow*, 110:1–17.

Andersson, B., Golovitchev, V., Jakobsson, S., Mark, A., Edelvik, F., Davidson, L., and Carlson, J. S. (2013). A Modified TAB Model for Simulation of Atomization in Rotary Bell Spray Painting. *Journal of Mechanical Engineering and Automation*, 3(2):54–61.

Ansys (2009). Ansys Fluent 12.0 user's guide. *Ansys Inc*, 15317:1–2498.

Antoine, Y., Lemoine, F., and Lebouch, M. (2001). Turbulent transport of a passive scalar in a round jet discharging into a co-flowing stream. *European Journal of Mechanics - B/Fluids*, 20(2):275–301.

Argyropoulos, C. D. and Markatos, N. C. (2015). Recent advances on the numerical modelling of turbulent flows. *Applied Mathematical Modelling*, 39(2):693–732.

Ashgriz, N., editor (2011). *Handbook of atomization and sprays: theory and applications*. Springer, New York, NY. OCLC: 731927924.

Ashgriz, N. and Poo, J. Y. (1990). Coalescence and separation in binary collisions of liquid drops. *Journal of Fluid Mechanics*, 221:183–204.

Aston, J. G., Kennedy, R. M., and Schumann, S. C. (1940). The Heat Capacity and Entropy, Heats of Fusion and Vaporization and the Vapor Pressure of Isobutane. *Journal of the American Chemical Society*, 62(8):2059–2063. Publisher: American Chemical Society.

Aston, J. G. and Messerly, G. H. (1940). The Heat Capacity and Entropy, Heats of Fusion and Vaporization and the Vapor Pressure of n-Butane1. *Journal of the American Chemical Society*, 62(8):1917–1923. Publisher: American Chemical Society.

Avedisian, C. T. (1985). The Homogeneous Nucleation Limits of Liquids. *Journal of Physical and Chemical Reference Data*, 14:695–729. ADS Bibcode: 1985JPCRD..14..695A.

- Bai, C. and Gosman, A. D. (1995). Development of Methodology for Spray Impingement Simulation. *SAE Transactions*, 104:550–568.
- BAMA (2023). BAMA: British Aerosol Manufacturers' Association.
- Beale, J. C. and Reitz, R. D. (1999). Modeling spray atomization with the Kelvin-Helmholtz/Rayleigh-Taylor hybrid model. *Atomization and Sprays*, 9(6).
- Beji, T., Zadeh, S. E., Maragkos, G., and Merci, B. (2017). Influence of the particle injection rate, droplet size distribution and volume flux angular distribution on the results and computational time of water spray CFD simulations. *Fire Safety Journal*, 91:586–595.
- Bellan, J. and Harstad, K. (1987). The details of the convective evaporation of dense and dilute clusters of drops. *International Journal of Heat and Mass Transfer*, 30(6):1083–1093.
- Bertholon, J.-F., Becquemin, M.-H., Roy, M., Roy, F., Ledur, D., Annesi-Maesano, I., and Dautzenberg, B. (2015). Particle Sizes of Aerosols Produced by Nine Indoor Perfumes and Deodorants. *International Journal of Environmental Monitoring and Analysis*, 3(6):377.
- Bhatia, B. and De, A. (2019). Flash Boiling in Sprays: Recent Developments and Modeling. *Journal of the Indian Institute of Science*, 99(1):93–104.
- Bhide, K. and Abdallah, S. (2022). High-Order Accurate Numerical Simulation of Supersonic Flow Using RANS and LES Guided by Turbulence Anisotropy. *Fluids*, 7(12):385. Number: 12 Publisher: Multidisciplinary Digital Publishing Institute.
- Bianchi, G. M., Minelli, F., Scardovelli, R., and Zaleski, S. (2007). 3D Large Scale Simulation of the High-Speed Liquid Jet Atomization.
- Bird, R. B., Stewart, W. E., and Lightfoot, E. N. (2006). *Transport Phenomena*. John Wiley & Sons. Google-Books-ID: L5FnNIIaGfcC.

- Blander, M. and Katz, J. L. (1975). Bubble nucleation in liquids. *AIChE Journal*, 21(5):833–848.
- Borgnakke, C. and Sonntag, R. E. (2022). *Fundamentals of Thermodynamics*. John Wiley & Sons. Google-Books-ID: KHITEAAAQBAJ.
- Bower, G., Chang, S. K., Corradini, M. L., El-Beshbeeshy, M., Martin, J. K., and Krueger, J. (1988). Physical Mechanisms for Atomization of a Jet Spray: A Comparison of Models and Experiments.
- Brown, J. S., Gordon, T., Price, O., and Asgharian, B. (2013). Thoracic and respirable particle definitions for human health risk assessment. *Part Fibre Toxicol*, 10:12.
- Buhmann, M. D. (2003). *Radial Basis Functions: Theory and Implementations*. Cambridge Monographs on Applied and Computational Mathematics. Cambridge University Press, Cambridge.
- Camp, D. F., Ateaque, A., and Dickson, W. A. (2003). Cryogenic burns from aerosol sprays: a report of two cases and review of the literature. *British Journal of Plastic Surgery*, 56(8):815–817. Publisher: Elsevier.
- Carruth, G. F. and Kobayashi, R. (1973). Vapor pressure of normal paraffins ethane through n-decane from their triple points to about 10 mm mercury. *Journal of Chemical & Engineering Data*, 18(2):115–126.
- Castleman, R. A. (1932). The Mechanism Of Atomization Accompanying Solid Injection. Technical Report 440, NACA.
- Celis, C., Barreto, C., Lopes, G., Carneiro, J., Abrantes, J., Barros, J., and Nieckele, A. (2005). Evaluation of Different Turbulence Models to Predict a Turbulent Free Jet.
- Chase, M. W. (1998). NIST-JANAF Thermochemical Tables, 4th Edition. *NIST*. Last Modified: 2017-02-19T20:02-05:00 Publisher: M W. Chase.

-
- Coleman, T. F. and Li, Y. (1996). An Interior Trust Region Approach for Nonlinear Minimization Subject to Bounds. *SIAM Journal on Optimization*, 6(2):418–445. Publisher: Society for Industrial and Applied Mathematics.
- Cowan-Ellsberry, C., McNamee, P. M., and Leazer, T. (2008). Axilla surface area for males and females: Measured distribution. *Regulatory Toxicology and Pharmacology*, 52(1):46–52.
- Cunningham, E. and Larmor, J. (1910). On the velocity of steady fall of spherical particles through fluid medium. *Proceedings of the Royal Society of London. Series A, Containing Papers of a Mathematical and Physical Character*, 83(563):357–365.
- Da Vinci, L. (1510). *Leonardo Da Vinci: The Codex Hammer Formerly The Codex Leicester : [exhibition] Royal Academy of Arts [London]*. Armand Hammer Foundation.
- Das, T. R., Reed, C. O., and Eubank, P. T. (1973a). PVT [pressure-volume-temperature] surface and thermodynamic properties of butane. *Journal of Chemical & Engineering Data*, 18(3):244–253.
- Das, T. R., Reed, C. O. J., and Eubank, P. T. (1973b). PVT [pressure-volume-temperature] surface and thermodynamic properties of isobutane. *Journal of Chemical & Engineering Data*, 18(3):253–262. Publisher: American Chemical Society.
- Datt, P. (2011). Latent Heat of Vaporization/Condensation. In Singh, V. P., Singh, P., and Haritashya, U. K., editors, *Encyclopedia of Snow, Ice and Glaciers*, Encyclopedia of Earth Sciences Series, pages 703–703. Springer Netherlands, Dordrecht.
- de Villiers, E., Gosman, A., and Weller, H. (2004). Large Eddy Simulation of Primary Diesel Spray Atomization.
- Delmaar, J. E. and Bremmer, H. J. (2009). *The ConsExpo Spray Model: Modelling and Experimental Validation of the Inhalation Exposure of Consumers to Aerosols from Spray Cans and Trigger Sprays*. RIVM. Google-Books-ID: 3irqZwEACAAJ.

-
- Dong, X., Zhu, H., and Yang, X. (2015). Characterization of droplet impact and deposit formation on leaf surfaces: Droplet impact and deposit formation on leaf surfaces. *Pest Management Science*, 71(2):302–308.
- Donnelly, R. J. and Glaberson, W. (1966). Experiments on the Capillary Instability of a Liquid Jet. *Proceedings of the Royal Society A: Mathematical, Physical and Engineering Sciences*, 290(1423):547–556.
- Eggers, J. and Villermaux, E. (2008). Physics of liquid jets. *Reports on Progress in Physics*, 71(3):036601.
- Elghobashi, S. (1994). On predicting particle-laden turbulent flows. *Appl. Sci. Res.*, 52(4):309–329.
- Elliott, R. W. and Watts, H. (1972). Diffusion of some Hydrocarbons in Air: a Regularity in the Diffusion Coefficients of a Homologous Series. *Canadian Journal of Chemistry*, 50(1):31–34.
- Fogliati, M., Fontana, D., Garbero, M., Vanni, M., Baldi, G., and Dond, R. (2006). CFD simulation of paint deposition in an air spray process. *JCT Research*, 3(2):117–125.
- Geng, L., Wang, Y., Wang, J., Wei, Y., and Lee, C.-f. F. (2020). Numerical simulation of the influence of fuel temperature and injection parameters on biodiesel spray characteristics. *Energy Science & Engineering*, 8(2):312–326. eprint: <https://onlinelibrary.wiley.com/doi/pdf/10.1002/ese3.429>.
- Ghahremanian, S. and Moshfegh, B. (2011). Numerical and experimental verification of initial, transitional and turbulent regions of free turbulent round jet.
- Goodwin, R. D. (1978). Specific Heats of Saturated and Compressed Liquid Propane. *Journal of Research of the National Bureau of Standards*, 83(5):449–458.

-
- Gordillo, J. M. and Prez-Saborid, M. (2005). Aerodynamic effects in the break-up of liquid jets: on the first wind-induced break-up regime. *Journal of Fluid Mechanics*, 541(-1):1.
- Gorokhovski, M. and Herrmann, M. (2008). Modeling Primary Atomization. *Annual Review of Fluid Mechanics*, 40(1):343–366.
- Gouldin, F. C., Schefer, R. W., Johnson, S. C., and Kollmann, W. (1986). Non-reacting turbulent mixing flows. *Progress in Energy and Combustion Science*, 12(4):257–303.
- Greco, G. (2018). *A computational investigation of jet-plate interaction noise using a Lattice-Boltzmann based method*. PhD Thesis.
- Grundmann, R. (2000). Technische Problemlsung, Verhandeln und umfassende Problemlsung. *Gesellschaftliche Komplexitt und kollektive Handlungsfhigkeit. Frankfurt am Main: Campus*, pages 154–182.
- Grnholm, T. and Annala, A. (2007). Natural distribution. *Mathematical Biosciences*, 210(2):659–667.
- Han, Z., Parrish, S. E., Farrell, P. V., and Reitz, R. D. (1997). Modeling atomization processes of pressure-swirl hollow-cone fuel sprays. *Atomization and Sprays*, 7(6).
- Han, Z. and Reitz, R. D. (1995). Turbulence Modeling of Internal Combustion Engines Using RNG - Models. *Combustion Science and Technology*, 106(4-6):267–295. Publisher: Taylor & Francis .eprint: <https://doi.org/10.1080/00102209508907782>.
- Harrell, F. E. (2001). *Regression Modeling Strategies: With Applications to Linear Models, Logistic Regression, and Survival Analysis*. Springer Science & Business Media.

- He, G., Guo, Y., and Hsu, A. T. (1999). The effect of Schmidt number on turbulent scalar mixing in a jet-in-crossflow. *International Journal of Heat and Mass Transfer*, 42(20):3727–3738.
- Heidenreich, S. and Bttner, H. (1995). Investigations about the influence of the Kelvin effect on droplet growth rates. *Journal of Aerosol Science*, 26(2):335–339.
- Heintzenberg, J. (1994). Properties of the Log-Normal Particle Size Distribution. *Aerosol Science and Technology*, 21(1):46–48.
- Helgeson, N. L. and Sage, B. H. (1967). Latent heat of vaporization of propane. *Journal of Chemical & Engineering Data*, 12(1):47–49. Publisher: American Chemical Society.
- Herwig, H. (2016). What Exactly is the Nusselt Number in Convective Heat Transfer Problems and are There Alternatives? *Entropy*, 18(5):198.
- Hinds, W. C. (2012). *Aerosol Technology: Properties, Behavior, and Measurement of Airborne Particles*. John Wiley & Sons. Google-Books-ID: qIkjyPXfWK4C.
- Hinze, J. O. (1955). Fundamentals of the hydrodynamic mechanism of splitting in dispersion processes. *AIChE Journal*, 1(3):289–295.
- Hnizdil, M., Chabicovsky, M., Raudensky, M., and Lee, T.-W. (2016). Heat Transfer during Spray Cooling of Flat Surfaces with Water at Large Reynolds Numbers. *Journal of Flow Control, Measurement & Visualization*, 4(3):104–113.
- Hochrainer, D., Hlz, H., Kreher, C., Scaffidi, L., Spallek, M., and Wachtel, H. (2005). Comparison of the Aerosol Velocity and Spray Duration of Respimat Soft Mist Inhaler and Pressurized Metered Dose Inhalers. *Journal of Aerosol Medicine*, 18(3):273–282.
- Hoffman, N., Galea, E. R., and Markatos, N. C. (1989). Mathematical modelling of fire sprinkler systems. *Applied Mathematical Modelling*, 13(5):298–306.

- Hussein, H. J., Capp, S. P., and George, W. K. (1994). Velocity measurements in a high-Reynolds-number, momentum-conserving, axisymmetric, turbulent jet. *Journal of Fluid Mechanics*, 258:31–75. Publisher: Cambridge University Press.
- Imperato, M., Kaario, O., Sarjovaara, T., and Larmi, M. (2016). Influence of the in-cylinder gas density and fuel injection pressure on the combustion characteristics in a large-bore diesel engine. *International Journal of Engine Research*, 17(5):525–533.
- Jones, W. P. and Launder, B. E. (1972). The prediction of laminarization with a two-equation model of turbulence. *International Journal of Heat and Mass Transfer*, 15(2):301–314.
- Joshi, S., Kadam, Y., and Ranade, S. (2021). A Parametric Study on the Taylor Analogy Breakup Model. In Prabu, T., Viswanathan, P., Agrawal, A., and Banerjee, J., editors, *Fluid Mechanics and Fluid Power*, Lecture Notes in Mechanical Engineering, pages 223–230, Singapore. Springer.
- Josserand, C. and Thoroddsen, S. (2016). Drop Impact on a Solid Surface. *Annual Review of Fluid Mechanics*, 48(1):365–391.
- Kadocsa, A. (2007). *Modeling of Spray Formation in Diesel Engines*. PhD thesis, Budapest University of Technology and Economics.
- Kaya, M. (2019). A CFD Based Application of Support Vector Regression to Determine the Optimum Smooth Twist for Wind Turbine Blades. *Sustainability*, 11(16):4502. Number: 16 Publisher: Multidisciplinary Digital Publishing Institute.
- Kelsey, A. (2001). CFD modelling of flashing jets: Simulation of flashing propane jets. *HSL report CM/00/02*.
- Kemp, J. D. and Egan, C. J. (1938). Hindered Rotation of the Methyl Groups in Propane. The Heat Capacity, Vapor Pressure, Heats of Fusion and Vaporization

-
- of Propane. Entropy and Density of the Gas. *Journal of the American Chemical Society*, 60(7):1521–1525. Publisher: American Chemical Society.
- Khare, A., Singh, A., and Nokam, K. (2009). Best practices in grid generation for CFD applications using HyperMesh.
- Kim, S.-E., Choudhury, D., and Patel, B. (1999). Computations of Complex Turbulent Flows Using the Commercial Code Fluent. In Salas, M. D., Hefner, J. N., and Sakell, L., editors, *Modeling Complex Turbulent Flows*, ICASE/LaRC Interdisciplinary Series in Science and Engineering, pages 259–276. Springer Netherlands, Dordrecht.
- Kong, S. C., Senecal, P. K., and Reitz, R. D. (1999). Developments in Spray Modeling in Diesel and Direct-Injection Gasoline Engines. *Oil & Gas Science and Technology*, 54(2):197–204.
- Kuhnke, D. (2004). *Spray wall interaction modelling by dimensionless data analysis*. phd, Shaker, Aachen. ISBN: 9783832235390.
- Kulkarni, P., Baron, P., and Willeke, K. (2011). *Aerosol Measurement: Principles, Techniques, and Applications, 3rd Edition*.
- Lacour, M. and Coultre, C. L. (1991). Spray-Induced Frostbite in a Child: A New Hazard with Novel Aerosol Propellants. *Pediatric Dermatology*, 8(3):207–209.
- Lamb, H. (1932). *Hydrodynamics. 6th edition*. C.U.P. Google-Books-ID: nOHRXwAACAAJ.
- Lane, W. R. (1951). Shatter of Drops in Streams of Air. *Industrial & Engineering Chemistry*, 43(6):1312–1317.
- Laplace, P. S. m. d. (1805). *Trait de mcanique ceste*. Chez J.B.M. Duprat. Google-Books-ID: _A8OAAAAQAAJ.

- Launder, B. E. and Sharma, B. I. (1974). Application of the energy-dissipation model of turbulence to the calculation of flow near a spinning disc. *Letters in Heat and Mass Transfer*, 1(2):131–137.
- Launder, B. E. and Spalding, D. B. (1974). The numerical computation of turbulent flows. *Computer Methods in Applied Mechanics and Engineering*, 3(2):269–289.
- Laurendeau, N. M. (2005). Statistical Thermodynamics by Normand M. Laurendeau. Publication Title: Cambridge Core.
- Lees, F. (2012). *Lees' Loss Prevention in the Process Industries: Hazard Identification, Assessment and Control*. Butterworth-Heinemann.
- Lefebvre, A. H. and McDonell, V. G. (2017). *Atomization and sprays*. CRC Press, Taylor & Francis Group, CRC Press is an imprint of the Taylor & Francis Group, an informa business, Boca Raton, second edition edition.
- Levich, V. G. (1962). *Physicochemical hydrodynamics*. Prentice-Hall, Englewood Cliffs, N.J.
- Lichtarowicz, A., Duggins, R. K., and Markland, E. (1965). Discharge Coefficients for Incompressible Non-Cavitating Flow through Long Orifices. *Journal of Mechanical Engineering Science*, 7(2):210–219. Publisher: IMECHE.
- Linstrom, P. J. and Mallard, W. G. (2001). The NIST Chemistry WebBook: A Chemical Data Resource on the Internet. *Journal of Chemical & Engineering Data*, 46(5):1059–1063. Publisher: American Chemical Society.
- Liu, A. B., Mather, D., and Reitz, R. D. (1993). Modeling the Effects of Drop Drag and Breakup on Fuel Sprays.
- Longest, P. W. and Hindle, M. (2008). Evaluation of the Respimat Soft Mist Inhaler using a Concurrent CFD and In Vitro Approach. *Journal of Aerosol Medicine and Pulmonary Drug Delivery*, 22(2):99–112.

-
- Loureiro, D. D., Reuttsch, J., Kronenburg, A., Weigand, B., and Vogiatzaki, K. (2020). Primary breakup regimes for cryogenic flash atomization. *International Journal of Multiphase Flow*, 132:103405.
- Majer, V. and Svoboda, V. (1986). Enthalpies of vaporization of organic compounds: a critical review and data compilation.
- Majithia, A. K., Hall, S., Harper, L., and Bowen, P. J. (2008). Droplet breakup quantification and processes in constant and pulsed air flows. Italy.
- Marinescu, I. D., Rowe, W. B., Dimitrov, B., and Ohmori, H. (2013). 8 - Fluid delivery. In Marinescu, I. D., Rowe, W. B., Dimitrov, B., and Ohmori, H., editors, *Tribology of Abrasive Machining Processes (Second Edition)*, pages 213–240. William Andrew Publishing, Oxford.
- Marple, V. A. and Willeke, K. (1976). Impactor design. *Atmospheric Environment (1967)*, 10(10):891–896.
- Marshall, A. and di Marzo, M. (2004). Modelling Aspects of Sprinkler Spray Dynamics in Fires. *Process Safety and Environmental Protection*, 82(2):97–104.
- Mehta, D., Krishnan, A., and Clemens, F. (2018). A Wall Boundary Condition for the Simulation of a Turbulent Non-Newtonian Domestic Slurry in Pipes. *Water*, 10:124.
- Menard, T., Beau, P. A., Tanguy, S., Demoulin, F. X., and Berlemont, A. (2006). Primary Break up modeling Part A: DNS, a tool to explore primary break up. Kyoto, Japan. Inst. Liq. Atom. Spray Syst.
- Menter, F. R. (1994). Two-equation eddy-viscosity turbulence models for engineering applications. *AIAA Journal*, 32(8):1598–1605.
- Merrington, A. C. and Richardson, E. G. (1947). The break-up of liquid jets. *Proceedings of the Physical Society*, 59(1):1.

- Mezhericher, M., Levy, A., and Borde, I. (2009). Modeling of Droplet Drying in Spray Chambers Using 2D and 3D Computational Fluid Dynamics. *Drying Technology*, 27(3):359–370.
- Moler, C. B. (2008). *Numerical Computing with MATLAB: Revised Reprint*. SIAM. Google-Books-ID: SNwTlee8hWAC.
- Montazeri, H., Blocken, B., and Hensen, J. (2015). Evaporative cooling by water spray systems: CFD simulation, experimental validation and sensitivity analysis. *Building and Environment*, 83:129–141.
- Morsi, S. A. and Alexander, A. J. (1972). An investigation of particle trajectories in two-phase flow systems. *Journal of Fluid Mechanics*, 55(2):193–208. Publisher: Cambridge University Press.
- Murzin, D. and Salmi, T. (2005). Chapter 9 - Mass transfer and catalytic reactions. In Murzin, D. and Salmi, T., editors, *Catalytic Kinetics*, pages 341–418. Elsevier Science, Amsterdam.
- Myers, R. H., Montgomery, D. C., and Anderson-Cook, C. M. (2011). *Response Surface Methodology: Process and Product Optimization Using Designed Experiments*. John Wiley & Sons. Google-Books-ID: F6MJere2POUC.
- Nasr, G. G., Yule, A. J., and Bendig, L. (2013). *Industrial Sprays and Atomization: Design, Analysis and Applications*. Springer Science & Business Media. Google-Books-ID: AuzjBwAAQBAJ.
- Nicholls, J. A. and Ranger, A. A. (1969). Aerodynamic shattering of liquid drops. *AIAA Journal*, 7(2):285–290.
- Nourian, A., Nasr, G. G., Yule, A. J., Goldberg, T., and Tulloch, G. (2015). Next generation of consumer aerosol valve design using inert gases. *Proceedings of the Institution of Mechanical Engineers, Part C: Journal of Mechanical Engineering Science*, 229(16):2952–2976. Publisher: IMECHE.

-
- Nurick, W. H. (1976). Orifice Cavitation and Its Effect on Spray Mixing. *Journal of Fluids Engineering*, 98(4):681–687.
- Ohnesorge, W. V. (1936). Die Bildung von Tropfen an Dsen und die Auflsung flssiger Strahlen. *ZAMM - Journal of Applied Mathematics and Mechanics / Zeitschrift fr Angewandte Mathematik und Mechanik*, 16(6):355–358.
- O'Rourke, P. J. (1981). Collective drop effects on vaporizing liquid sprays. Technical Report LA-9069-T, Los Alamos National Lab., NM (USA).
- O'Rourke, P. J. and Amsden, A. A. (1987). The Tab Method for Numerical Calculation of Spray Droplet Breakup.
- OrszagS, A., Yakhot, FlanneryW, S., Boysan, F., Choudhury, D., Maruzewski, J., and Patel, B. (1993). Renormalization Group Modeling and Turbulence Simulations.
- Otsu, N. (1979). A Threshold Selection Method from Gray-Level Histograms. *IEEE Transactions on Systems, Man, and Cybernetics*, 9(1):62–66. Conference Name: IEEE Transactions on Systems, Man, and Cybernetics.
- Parker, S., Foat, T., and Preston, S. (2008). Towards quantitative prediction of aerosol deposition from turbulent flows. *Journal of Aerosol Science*, 39(2):99–112.
- Patterson, M. A. and Reitz, R. D. (1998). Modeling the Effects of Fuel Spray Characteristics on Diesel Engine Combustion and Emission. SAE Technical Paper 980131, SAE International, Warrendale, PA.
- Pedro Souza de Oliveira, J., Victor Barbosa Alves, J., Neuenschwander Escosteguy Carneiro, J., de Andrade Medronho, R., and Fernando Lopes Rodrigues Silva, L. (2022). Coupling a neural network technique with CFD simulations for predicting 2-D atmospheric dispersion analyzing wind and composition effects. *Journal of Loss Prevention in the Process Industries*, 80:104930.

- Pilch, M. and Erdman, C. A. (1987). Use of breakup time data and velocity history data to predict the maximum size of stable fragments for acceleration-induced breakup of a liquid drop. *International Journal of Multiphase Flow*, 13(6):741–757.
- Plateau, J. (1850). Ueber die Grnze der Stabilitt eines flossigen Cylinders. *Annalen der Physik*, 156(8):566–569.
- Polanco, G., Hold, A. E., and Munday, G. (2010). General review of flashing jet studies. *Journal of Hazardous Materials*, 173(1):2–18.
- Poling, B. E., Prausnitz, J. M., and OConnell, J. P. (2001). *Properties of Gases and Liquids*. McGraw-Hill Education, 5th edition edition.
- Pope, S. B. (2000). Turbulent Flows. ISBN: 9780511840531 Publisher: Cambridge University Press.
- Pratt, W. K. (2001). *Digital Image Processing: PIKS Inside*. John Wiley & Sons, Inc., USA, 3rd edition.
- Ranz, W. and Marshall, W. (1952). Evaporation Form Drops. *Chem. Eng. Prog.*, 48:141–146.
- Rapp, B. E. (2017). Chapter 9 - Fluids. In Rapp, B. E., editor, *Microfluidics: Modelling, Mechanics and Mathematics*, Micro and Nano Technologies, pages 243–263. Elsevier, Oxford.
- Rasmussen, C. E. and Williams, C. K. I. (2005). *Gaussian Processes for Machine Learning*. MIT Press. Google-Books-ID: Tr34DwAAQBAJ.
- Rayleigh, L. (1878). On The Instability Of Jets. *Proceedings of the London Mathematical Society*, s1-10(1):4–13.
- Rayleigh, L. (1879). On the Stability, or Instability, of certain Fluid Motions. *Proceedings of the London Mathematical Society*, s1-11(1):57–72.

-
- Rayleigh, L. (1891). Some Applications of Photography. *Nature*, 44:249–254.
- Reichardt, H. (1942). *Gesetzmassigkeiten der freien Turbulenz*. VDI-Verlag.
- Reitz, R. (1978). Atomization and other breakup regimes of a liquid jet.
- Reitz, R. D. and Bracco, F. V. (1982). Mechanism of atomization of a liquid jet. *The Physics of Fluids*, 25(10):1730–1742.
- Rips, S. M. (1963). On a Feasible Level of Filling in of Reservoirs by Liquid Hydrocarbons. 8:610–613.
- Rosin, P. and Rammler, E. (1933). The Laws Governing the Fineness of Powdered Coal. 7(31):29–36.
- Rostampour, A., Shojaeefard, M. H., and Molaeimanesh, G. R. (2022). A comprehensive investigation of RANS and LES turbulence models for diesel spray modeling via experimental diesel schlieren imaging. *Proceedings of the Institution of Mechanical Engineers, Part C: Journal of Mechanical Engineering Science*, 236(15):8321–8337. Publisher: IMECHE.
- Rutland, D. F. and Jameson, G. J. (1971). A non-linear effect in the capillary instability of liquid jets. *Journal of Fluid Mechanics*, 46(2):267–271.
- Salvador, F. J., Gimeno, J., Pastor, J. M., and Mart-Aldarav, P. (2014). Effect of turbulence model and inlet boundary condition on the Diesel spray behavior simulated by an Eulerian Spray Atomization (ESA) model. *International Journal of Multiphase Flow*, 65:108–116.
- Sazhin, S. (2006). Advanced models of fuel droplet heating and evaporation. *Progress in Energy and Combustion Science*, 32:162–214.
- Sazhin, S. (2014). Spray Formation and Penetration. In Sazhin, S., editor, *Droplets and Sprays*, pages 9–48. Springer London, London.

- Schefer, R. W. (1987). Data Base for a Turbulent, Nonpremixed, Nonreacting Propane-Jet Flow. page 21.
- Schmidt, D. and Corradini, M. (1997). Analytical prediction of the exit flow of cavitating orifices. *Atomization and Sprays*, 7:603–616.
- Schmitt, F. G. (2007). About Boussinesq’s turbulent viscosity hypothesis: historical remarks and a direct evaluation of its validity. *Comptes Rendus Mecanique*, 335(9):617–627.
- Schneider, B. M. (2003). *Experimentelle Untersuchungen zur Spraystruktur in transienten, verdampfenden und nicht verdampfenden Brennstoffstrahlen unter Hochdruck*. PhD thesis, ETH. Zrich, Zrich.
- Settles, G. S. (2012). *Schlieren and Shadowgraph Techniques: Visualizing Phenomena in Transparent Media*. Springer Science & Business Media. Google-Books-ID: MB3qCAAAQBAJ.
- Settles, G. S. and Hargather, M. J. (2017). A review of recent developments in schlieren and shadowgraph techniques. *Measurement Science and Technology*, 28(4):042001.
- Shampine, L. F. and Reichelt, M. W. (1997). The MATLAB ODE Suite. *SIAM Journal on Scientific Computing*, 18(1):1–22. Publisher: Society for Industrial and Applied Mathematics.
- Sher, E., Bar-Kohany, T., and Rashkovan, A. (2008). Flash-boiling atomization. *Progress in Energy and Combustion Science*, 34(4):417–439.
- Sher, E. and Elata, C. (1977). Spray Formation from Pressure Cans by Flashing. *Industrial & Engineering Chemistry Process Design and Development*, 16(2):237–242. Publisher: American Chemical Society.

-
- Shih, T.-H., Liou, W. W., Shabbir, A., Yang, Z., and Zhu, J. (1995). A new k -epsilon eddy viscosity model for high reynolds number turbulent flows. *Computers & Fluids*, 24(3):227–238.
- Shinjo, J. (2018). Recent Advances in Computational Modeling of Primary Atomization of Liquid Fuel Sprays. *Energies*, 11(11):2971.
- Singhal, C., Murtaza, Q., and Parvej (2018). Simulation of Critical Velocity of Cold Spray Process with Different Turbulence Models. *Materials Today: Proceedings*, 5(9, Part 1):17371–17379.
- Sirignano, W. A. (2010). *Fluid Dynamics and Transport of Droplets and Sprays by William A. Sirignano*. Cambridge University Press.
- Sivakumar, S., Sangras, R., and Raghavan, V. (2012). Characteristics of Turbulent Round Jets in its Potential-Core Region. 6(1):7.
- Skripov, V. P., Kondor, R., and Slutzkin, D. (1974). *Metastable liquids*. Wiley ; Israel Program for Scientific Translations, New York, Chichester. OCLC: 16230076.
- Smagorinsky, J. (1963). General circulation experiments with the primitive Equations: 1. The basic experiment. *Monthly Weather Review*, 91(3):99–164.
- Smallwood, G. J. and Gulder, O. L. (2000). Views on the structure of transient diesel sprays. *Atomization and Sprays*, 10(3-5).
- Smolkov-Keulemansov, E. and Feltl, L. (1991). Chapter 10 - Gas chromatography. In Smolkov-Keulemansov, E. and Feltl, L., editors, *Comprehensive Analytical Chemistry*, volume 28 of *Analysis of Substances in the Gaseous Phase*, pages 223–462. Elsevier.
- Som, S., Senecal, P., and Pomraning, E. (2012). Comparison of RANS and LES Turbulence Models against Constant Volume Diesel Experiments.

-
- Sommerfeld, H., Koch, C., Schwarz, A., and Beck, A. (2021). High velocity measurements of particle rebound characteristics under erosive conditions of high pressure compressors. *Wear*, 470-471:203626.
- Sommerfeld, M. and Pasternak, L. (2019). Advances in modelling of binary droplet collision outcomes in Sprays: A review of available knowledge. *International Journal of Multiphase Flow*, 117:182–205.
- Soteriou, C., Andrews, R., and Smith, M. (1995). Direct Injection Diesel Sprays and the Effect of Cavitation and Hydraulic Flip on Atomization.
- Sou, A., Hosokawa, S., and Tomiyama, A. (2007). Effects of cavitation in a nozzle on liquid jet atomization. *International Journal of Heat and Mass Transfer*, 50(17):3575–3582.
- Spalding, D. B. (1971). Concentration fluctuations in a round turbulent free jet. *Chemical Engineering Science*, 26(1):95–107.
- Speak, G. S. and Walters, D. J. (1950). Optical considerations and limitations of the Schlieren method. Accepted: 2014-10-21T15:53:16Z.
- Stephenson, R. M. and Malanowski, S. (1987). Properties of Organic Compounds. In Stephenson, R. M. and Malanowski, S., editors, *Handbook of the Thermodynamics of Organic Compounds*, pages 1–471. Springer Netherlands, Dordrecht.
- Sun, Y., Guan, Z., and Hooman, K. (2019). Cavitation in Diesel Fuel Injector Nozzles and its Influence on Atomization and Spray. *Chemical Engineering & Technology*, 42(1):6–29.
- Taylor, G. I. (1963). *The Scientific Papers of Sir Geoffrey Ingram Taylor: Volume 3, Aerodynamics and the Mechanics of Projectiles and Explosions*. Cambridge University Press. Google-Books-ID: oXuyjeTDlxgC.
- Temkin, S. and Mehta, H. K. (1982). Droplet drag in an accelerating and decelerating flow. *Journal of Fluid Mechanics*, 116:297–313.

- Testik, F. Y., Barros, A. P., and Bliven, L. F. (2011). Toward a Physical Characterization of Raindrop Collision Outcome Regimes. *Journal of the Atmospheric Sciences*, 68(5):1097–1113. Publisher: American Meteorological Society Section: Journal of the Atmospheric Sciences.
- Thomson, G. W. (1946). The Antoine Equation for Vapor-pressure Data. *Chemical Reviews*, 38(1):1–39. Publisher: American Chemical Society.
- Tominaga, Y. and Stathopoulos, T. (2007). Turbulent Schmidt numbers for CFD analysis with various types of flowfield. *Atmospheric Environment*, 41(37):8091–8099.
- US EPA National Center for Environmental Assessment, W. D. (1997). Exposure Factors Handbook, Final Report. Reports & Assessments.
- Van Hoeve, W., Gekle, S., Snoeijer, J. H., Versluis, M., Brenner, M. P., and Lohse, D. (2010). Breakup of diminutive Rayleigh jets. *Physics of Fluids*, 22(12):122003.
- Versteeg, H. K. and Malalasekera, W. (2007). *An introduction to computational fluid dynamics: the finite volume method*. Pearson Education Ltd, Harlow, England ; New York, 2nd ed edition. OCLC: ocm76821177.
- Viegas, J. R., Rubesin, M. W., and Horstman, C. C. (1985). On the use of wall functions as boundary conditions for two-dimensional separated compressible flows. *AIAA, Aerospace Sciences Meeting*.
- Villermaux, E. (2006). Fragmentation. *Annual Review of Fluid Mechanics*, 39(1):419–446.
- Von Karman, T. H. (1931). Mechanical similitude and turbulence. NTRS Author Affiliations: NTRS Report/Patent Number: NACA-TM-611 NTRS Document ID: 19930094805 NTRS Research Center: Legacy CDMS (CDMS).
- Wareing, C. J., Fairweather, M., Falle, S. A., and Woolley, R. M. (2014). Validation of a model of gas and dense phase CO₂ jet releases for carbon capture and stor-

- age application. *International Journal of Greenhouse Gas Control*, 20:254–271.
Publisher: Elsevier.
- Wells, W. F. (1934). On air-borne infection: Study II. Droplets and droplet nuclei. *American Journal of Epidemiology*, 20(3):611–618.
- Wilcox, D. C. (1988). Reassessment of the scale-determining equation for advanced turbulence models. *AIAA Journal*.
- Wittner, M. O., Karbstein, H. P., and Gaukel, V. (2018). Pneumatic Atomization: Beam-Steering Correction in Laser Diffraction Measurements of Spray Droplet Size Distributions. *Applied Sciences*, 8(10):1738. Number: 10 Publisher: Multidisciplinary Digital Publishing Institute.
- Xia, P. and Lam, K. M. (2009). Velocity and concentration measurements in initial region of submerged round jets in stagnant environment and in coflow. *Journal Of Hydro-Environment Research*, 3(1):21–34.
- Yakhot, V., Orszag, S. A., Thangam, S., Gatski, T. B., and Speziale, C. G. (1992). Development of turbulence models for shear flows by a double expansion technique. *Physics of Fluids A: Fluid Dynamics*, 4(7):1510–1520.
- Yarin, A. (2006). Drop Impact Dynamics: Splashing, Spreading, Receding, Bouncing. *Annual Review of Fluid Mechanics*, 38(1):159–192.
- Yih, C.-S. (1967). Instability due to viscosity stratification. *Journal of Fluid Mechanics*, 27(2):337–352. Publisher: Cambridge University Press.
- Young, T. (1805). An Essay on the Cohesion of Fluids. *Philosophical Transactions of the Royal Society of London*, 95:65–87.
- Zou, Y. (2001). *Air jets in ventilation applications*. PhD thesis, KTH Royal Institute of Technology.